Unsteady Aerodynamics of Wings in Extreme Conditions

Bull, Samuel

Award date:
2020

Unsteady Aerodynamics of Wings in Extreme Conditions

submitted by

Samuel Charles Bull

A thesis submitted for the degree of Doctor of Philosophy

of the

University of Bath

Department of Mechanical Engineering

October 2019

Signature of Author.....

Samuel Charles Bull

Abstract

Leading-edge vortices (LEVs) can form over wings in unsteady flows across many engineering applications, from small unmanned vehicles to aircraft in gusts and manoeuvres. They create large overshoots in aerodynamic loads and exhibit significant non-linear characteristics. Knowledge of LEV behaviour is critical to informing predictive models, which can facilitate the development of technologies to either exploit or mitigate the effect of LEVs. In this thesis the effect of extreme unsteady wing motion is experimentally investigated to study vortex-wing/vortex-vortex interactions and a potential method to disrupt their formation.

The unsteady aerodynamics of an airfoil undergoing a single transient plunge manoeuvre was investigated. During motion the peak lift was found to be primarily due a build up of the circulatory component. Conversely the peak pitching moment magnitude was found to be primarily dependent on the added-mass force. The peak loads showed an increase with effective angle of attack amplitude, yet remained relatively insensitive to motion period. Significant loads oscillations were observed after the end of motion at post-stall angles of attack. These were shown to be caused by large-scale vortex shedding. The frequency of the first vortex shedding cycle was found to occur at the sub-harmonic of the airfoils static shedding frequency. After the first shedding cycle, the frequency displayed an asymptotic increase to the static shedding frequency within 10 to 15 convective times. A potential relationship between peak magnitude and subsequent shedding cycle frequency was found to follow a linear trend to a reasonable level of correlation, $R^2 = 0.70$.

The introduction of a second transient motion in the large-scale vortex shedding window produced a significant increase in peak lift and pitching moment. It was found that the loads response could be accurately estimated through linear superposition of the single motion response, which coincided with the merging of two distinct LEVs over the airfoil upper surface. Breakdown of this linear behaviour occurred when the separation distance between the two vortices reached the critical separation distance of a chord length, controlled through a time delay between the two

motions. To test this further, the linear superposition of a single sinusoidal cycle was compared against the true periodic experiment. It could predict the mean lift and amplitude reasonable well for lower frequencies, where weaker vortical flow was present.

The effect of Reynolds number change from $\mathcal{O}(10^4)$ to $\mathcal{O}(10^5)$ was investigated through equivalent water and wind tunnel measurements. The loads and flow-fields were qualitatively similar and only minor differences were observed, stemming from the unsteady shear layer behaviour. Unsteady pressure measurements revealed the maximum post-motion loads to occur when the chord-wise area exposed to the upper surface vortex was maximised, which coincided with the aftward movement of the lower surface stagnation region. LEV growth and convection rates were estimated from the approximate movement of a half-saddle point across the chord and shown to vary between 21 and 29%. The half-saddle marks the shedding of the upper surface vortex and subsequent loss of suction when it reaches the trailing-edge. The peak loads showed excellent agreement with equivalent water tunnel measurements at $Re = 20K$, adding confidence in the use of low Re measurements for the high Reynolds number applications.

The effect of a passively deployed mini-tab (flow fence) device at the airfoils leading-edge was investigated for lift and pitching moment suppression in periodic unsteady conditions. Depending on the frequency and the amplitude of the wing motion the mini-tab can delay LEV formation. This provides effective lift and moment alleviation for post-stall angles of attack at low reduced frequencies. In contrast, at low angles of attack the mini-tab can facilitate roll up, resulting in vortex shedding and lift/moment increase. The borderline between the two regions approximately scales with the Strouhal number based on amplitude, and in particular with the minimum effective angle of attack during the cycle. The transient response was studied through impulsively started plunging oscillations. During the first cycle, lift reduction is achieved for all frequencies within the range tested, which is highly beneficial for a device operating in a more realistic gust or manoeuvre scenario.

Acknowledgements

This work was supported by an Engineering and Physical Sciences Research Council studentship.

First and foremost I'd like to express my gratitude to Dr. David Cleaver, Professor Ismet Gursul and Dr. Nicola Chiereghin. David, your supervision and expertise has been critical to this project. Thank you for always making time to help guide and keep me on the right path. Ismet, your vision has elevated all of my findings and taught me so much in the process. Nicola, thanks for your patience, for bouncing ideas around with me and for instilling a methodical approach to the myriad of problems I experienced.

This project would not have been possible without the skill, knowledge and hard work of the technical staff. Vijay, John, Steve, Mark, Martin, Nick, Guy, Lee, Paul, Jack and Dan... without you, all I'd be left with is a pile of unfinished drawings.

I want to thank the Biomechanics Research office for taking me in upon my arrival at Bath, the kindness and friendship you all showed means a lot. I'm still not interested in bones or finite element modelling, but I do feel like an integral member of your group. Particular thanks goes to my house mates Laurie, Ollie and Ali for putting up with me in close quarters.

To my parents, your support made this possible for me, and I am always indebted to you. Michael, thanks for the many phone calls over the years, it's helped more than you know.

Last but not least, I want to express my gratefulness to Lucy; for her company during long nights of testing, for teaching me the importance of snacks and above all, for being an endless well of positivity when it came to this PhD.

List of Figures

2-1 Typical wake frequency spectra of a stalled NACA 0012 airfoil [8]. 7
2-2 Natural shedding frequency of wings with respect to the Strouhal number based on airfoil frontal area [9]. 8
2-3 Motion types of airfoil unsteadiness. 9
2-4 a) Diagram of starting vortex, and b) plot of Wagner's Function, taken from [13]. 11
2-5 Shed vortices from airfoil oscillating in pitch. 11
2-6 Evolution of airfoil wakes with increasing St_A, modified from [5, 26]. 14
2-7 Vortex ring structure, taken from [22]. 16
2-8 Sketch of vortex chain structure that prevents the deflected jet phenomena, taken from [34]. 16
2-9 Aerodynamic loads and corresponding flow features during a typical dynamic stall event, taken from [5]. 18
2-10 Time history of pressures across the airfoil chord during dynamic stall, taken from [40]. 20
2-11 Lift, pitching moment and drag plots showing the difference between dynamic stall regimes, taken from McCroskey [14]. 22
2-12 Three dimesnional LEV structures, taken from [53, 55]. 25
2-13 Leading-edge vortex formation due to plunge motion, taken from [63]. 28
2-14 Aerodynamic loads induced by leading-edge vortex, taken from [63]. 29
2-15 Peaks in lift due to vortex lock-in at a post-stall angle, taken from [8]. 32
2-16 Strouhal number effect on LEV circulation, taken from [77]. 33
2-17 (a Vortex shedding modes shown as a function of plunging amplitude and frequency, b) Colour plot of the normalised lift coefficient against plunging amplitude and frequency, taken from [8]. 34
2-18 a) Evolution of LEV arch structure on finite plunging wing, (b) associated lift coefficient, taken from [81]. 36
2-19 LEV distortion at the end of downstroke for various planforms, taken from [83]. . 36
2-20 LEV distortion on high aspect ratio wings, taken from [84]. 37
2-21 Representaion of various force mechanisms for unsteady massively separated flow during pitching motion, taken from [95]. 39
2-22 LEV circulation on pitching and surging wings, taken from [96]. 40
2-23 Lift of pitching and surging wings plotted on different time-scales, taken from [96]. 40
2-24 Normalised circulation histories of various flat plate geometries and planforms, taken from [97]. 41
2-25 Topological flow points during a) LEV growth stage and b) LEV shedding stage, taken from [99]. 43

2-26 Half-saddle tracking from surface pressure, a) half-saddle estimation b) diagrams of corresponding flow topology, taken from [101]. 43
2-27 Topological flow points during boundary layer eruption mechanism, taken from [99]. 45
2-28 Examples of post-motion vortex shedding from literature [101, 103, 106, 107]. . . 47
2-29 Combined benefits of a leading-edge droop and gurney flap configuration, taken from [112]. 49
2-30 Passive disturbance generators, a) circular, b) reverse wedge, c) forward wedge, taken from [116]. 50
2-31 Comparison of rigid and passively flexible plunging wings, taken from [117]. . . . 50
2-32 a) Diagram of rotating leading-edge cylinder, b) Comparison between off and on condition for rotating cylinder, taken from [123]. 52
2-33 a) Diagram of Zero-Net Mass Flux device (synthetic jet), taken from [131]. . . . 53

3-1 Water tunnel test rig, a) isometric view, b) front view. 76
3-2 Airfoil geometry, a) NACA 0012, b) NACA0012 with mini-tab, c) Flat plate with lower surface chamfer. 77
3-3 a) Airfoil plunging motion parameters, b) profile of effective angle of attack for transient plunging motion, c) profile of effective angle of attack for sinusoidal plunging motion. 78
3-4 Profile of effective angle of attack for, a) single transient motion, b) compound transient motion, c) single sinusoidal motion, d) periodic sinusoidal motion. . . . 79
3-5 a) Position accuracy of transient motion, b) induced plunge angle accuracy for transient motion, c) position accuracy for sinusoidal motion, d) induced plunge angle accuracy for sinusoidal motion. 80
3-6 Calibration curve for lift sensor. 80
3-7 a) Static lift coefficient, b) static pitching moment coefficient. 81
3-8 a) Typical magnitude of force exerted by wire, b) uncorrected and corrected lift time history. 82
3-9 a) Raw signal to filtered average signal, b) repeat variation, c) estimated uncertainty with average signal, d) estimated uncertainty. 83
3-10 a) Normalised velocity and spanwise vorticity plots, b) estimated expanded uncertainty, c) uncertainty distribution. 84
3-11 a) Plunging assembly with wing, b) Full rig diagram. 85
3-12 Tunnel view of full set-up. 86
3-13 a) Position accuracy of transient motion, b) induced plunge angle accuracy of transient motion. 87
3-14 Turbulence intensity vs. tunnel speed. 87
3-15 a) Wing cross-section, b) wing skin thickness trade-off, c) final wing cross-section design. 88
3-16 a) Top view diagram of in-situ pressure measurement system, b) transducer - PCB assembly. 89
3-17 a) Photo of in-situ pressure measurement system, b) photo of tubing. 90
3-18 a) Pressure map of upper surface displaying half-saddle convection, b) half-saddle convection speed estimation with uncertainty bounds. 91
3-19 Static pressure distributions. 92
3-20 a) Static lift coefficient, b) static pitching moment coefficient. 93

3-21 a) Unsteady air jet experiment: ON condition, b) Unsteady air jet experiment: OFF condition. 94
3-22 a) Resonance effect of tubing, b) Power Spectral Density of pressure transducers. 95
3-23 a) Average Power Spectral Density (PSD) with corrected average PSD, b) integrated PSD for corrected and uncorrected PSD, c) pressure amplitude error. . . . 96
3-24 a) Raw signal to filtered average signal, b) repeat variation, c) estimated uncertainty with average signal, d) estimated uncertainty. 97
3-25 a) Raw signal to filtered average signal, b) repeat variation, c) estimated uncertainty with average signal, d) estimated uncertainty. 98
3-26 Water tunnel and wind tunnel rig capabilities. 99

4-1 Profile of motion induce angle of attack, α_{pl}, for positive and negative motions with convective time $\tau = tU_\infty/c$. 121
4-2 NACA 0012 positive motion: a) Relative lift and b) relative moment coefficient time histories. $\alpha_0 = 0, 9, 15, 20, 25, 30°$, for $T = 2.22$, $\alpha_{pl,max} = +25°$. 122
4-3 NACA 0012 negative motion: a) Relative lift and b) relative moment coefficient time histories. $\alpha_0 = 0, 9, 15, 20, 25, 30°$, for $T = 2.22$, $\alpha_{pl,max} = -25°$. 123
4-4 $\alpha_0 = 9°$ for $T = 2.22$, $\alpha_{pl,max} = +25°$: a) relative lift, b) relative pitching moment with the added-mass estimation, c) phase-averaged normalized spanwise vorticity with streamlines. 124
4-5 $\alpha_0 = 15°$ for $T = 2.22$, $\alpha_{pl,max} = +25°$: a) relative lift, b) relative pitching moment with the added-mass estimation, c) phase-averaged normalized spanwise vorticity with streamlines. 125
4-6 $\alpha_0 = 20°$ for $T = 2.22$, $\alpha_{pl,max} = +25°$: a) relative lift, b) relative pitching moment with the added-mass estimation, c) phase-averaged normalized spanwise vorticity with streamlines. 126
4-7 $\alpha_0 = 15°$ for $T = 2.22$, $\alpha_{pl,max} = -25°$: a) relative lift, b) relative pitching moment with the added-mass estimation, c) phase-averaged normalized spanwise vorticity with streamlines. 127
4-8 Relative lift and pitching moment coefficient for L1/L2/L3 and M1/M2/M3 respectively with $\alpha_{pl,max}$ 128
4-9 a) Relative lift coefficient for L1, b) modified relative lift coefficient for M1 with $\alpha_{pl,max}$ across the α_0 range. 129
4-10 Timing information of L1/L2/L3 and M1/M2/M3 - a) $\alpha_o = 0°$, b) $\alpha_o = 9°$. . . . 130
4-10 (Continued) Timing information of L1/L2/L3 and M1/M2/M3 - c) $\alpha_o = 15°$, d) $\alpha_o = 20°$. 131
4-11 Modified Strouhal number from τ_{L3}-τ_{L2} for $\alpha_0 = 20°$ 132
4-12 a) Relative lift and b) Relative pitching moment of NACA 0012 and flat plate at $\alpha_0 = 20°$ for $T = 2.22\tau$ and $\alpha_{pl,max} = +25°$. 132
4-13 a,b) Positive motion, c,d) negative motion: Relative lift and pitching moment coefficient of NACA 0012 and flat plate for L1/L2/L3 and M1/M2/M3 with α_0 for $T = 2.22\tau$, $\alpha_{pl,max} = \pm 25°$ 133
4-14 a,b) Positive motion, c,d) negative motion: Timing information of NACA 0012 and flat plate for L1/L2/L3 and M1/M2/M3 with α_0 for $T = 2.22\tau$, $\alpha_{pl,max} = \pm 25°$ 134
4-15 Modified Strouhal number based on chord, $fcsin(\alpha_0)/U_\infty$, between successive post-motion lift peak timings for a) NACA0012 airfoil and b) flat plate. 135

4-16 Vortex shedding magnitude and frequency vs. τ : a) lift peak normalised by first lift peak, b) normalised peak lift coloured by α_0, c) frequency of shedding event normalised by static shedding frequency, b) normalised shedding frequency coloured by α_0. 136
4-17 a) Normalised peak lift against normalised shedding frequency, b) peak lift normalised by $2\pi\alpha_0 \cdot cos(\alpha_0) - C_{L,\alpha_0}$ against normalised shedding frequency. 137

5-1 Single transient motion, $T = 2.22$ and $\alpha_{pl,max} = 25°$; a) ΔC_L for single transient motion at $\alpha_0 = 5, 20°$, b) ΔC_M, c) key corresponding flow field development stages for $\alpha_0 = 20°$ 154
5-2 Compound transient motion, $T = 2.22$ and $\alpha_{pl,max} = 25°$; a) ΔC_L for compound motion with $\Delta\tau = 2.2$ at $\alpha_0 = 5, 20°$, e) ΔC_M for same compound motion case. . 155
5-3 Effect of second motion delay, $\Delta\tau$, on ΔC_L with corresponding flow field images. 156
5-4 Effect of second motion amplitude, $\alpha_{pl,max}$, on ΔC_L with corresponding flow field images for $\Delta\tau = 2.22$; a) Single motion, b) $\alpha_{pl,max} = 5°$, c) $\alpha_{pl,max} = 10°$, d) $\alpha_{pl,max} = 15°$, e) $\alpha_{pl,max} = 20°$, f) $\alpha_{pl,max} = 25°$. 157
5-5 Normalised correlation of linear superposition and experiment. 158
5-6 Four compound transient motions, a) $\Delta\tau = 0.5$, b) $\Delta\tau = 1.0$, c) $\Delta\tau = 1.5$, d) $\Delta\tau = 2.0$. 158
5-7 Sinusoidal motion, a) example of lift response for single sinusoidal motion with the linear superposition, b) mean lift and cycle amplitude extraction for sinusoidal motion. 159
5-8 Periodic sinusoidal comparison with linear superposition of single sinusoid lift response for, a) $k = 0.24$, b) $k = 0.47$, c) $k = 0.63$, d) $k = 0.94$, e) corresponding flow fields at $t/T = 0.25$ (quarter-cycle) for first 3 motion periods. 160
5-9 Periodic sinusoidal comparison with linear superposition of single sinusoid, a) normalised mean lift variation with τ, b) normalised cycle amplitude with tau, c) mean lift values against k at periodic condition, d) first harmonic of lift signal against k at periodic condition. 161

6-1 Comparison between $Re = 20K$ and $150K$ for a single plunging motion at $T = 5.0$ and $\alpha_{pl,max} = \pm 8°$ with $\alpha_0 = 0, 5, 10, 15°$. a) relative lift for positive motion, b) relative pitching moment for positive motion, c) relative lift for negative motion, d) relative pitching moment for negative motion. 176
6-2 Comparison between $Re = 20K$ and $150K$ for a single plunging motion at $T = 5.0$ and $\alpha_{pl,max} = \pm 8°$ with $\alpha_0 = 18, 20, 25, 30°$. a) relative lift for positive motion, b) relative pitching moment for positive motion, c) relative lift for negative motion, d) relative pitching moment for negative motion. 177
6-3 a) Chord-normal acceleration with relative lift coefficient, b) coefficient of pressure with τ for $\alpha_0 = 18°$, $T = 5.0$, $\alpha_{pl,max} = 8°$ - positive motion. 178
6-4 Comparison between $Re = 20K$ and $150K$; $\alpha_0 = 15°$, $T = 5.0$, $\alpha_{pl,max} = 8°$; a) relative lift coefficient, b) relative Pitching moment, c) velocity magnitude at select times. 179
6-5 Comparison between $Re = 20K$ and $150K$; $\alpha_0 = 15°$, $T = 5.0$, $\alpha_{pl,max} = -8°$; a) relative lift coefficient, b) relative Pitching moment, c) velocity magnitude at select times with select spanwise vorticity plots. 180

6-6 Comparison between $Re = 20K$ and $150K$; $\alpha_0 = 18°$, $T = 5.0$, $\alpha_{pl,max} = -8°$; a) relative lift coefficient, b) relative Pitching moment, c) velocity magnitude at select times with select spanwise vorticity plots. 181
6-7 Comparison between $Re = 20K$ and $150K$; $\alpha_0 = 20°$, $T = 5.0$, $\alpha_{pl,max} = -8°$; a) relative lift coefficient, b) relative Pitching moment, c) velocity magnitude at select times with select spanwise vorticity plots. 182
6-8 Pressure coefficient distribution at $Re = 150K$; corresponding to Figures 6-4,6-5, 6-6 and 6-7. 183
6-9 a) Relative lift, b) relative pitching moment and c) velocity magnitude plots at $Re = 150K$ for $\alpha_0 = 5, 10, 15°$, $T = 5.0$ and $\alpha_{pl,max} = 8°$. 184
6-10 Pressure coefficient distribution at $Re = 150K$; corresponding to the cases presented in Figure 6-9. 185
6-11 Pressure contour maps of the airfoil upper and lower surface. 186
6-12 Comparison between $Re = 20K, 100K$ and $150K$ at $T = 5.0$ and $\alpha_{pl,max} = \pm 6°$ with $\alpha_0 = 15°$. a) relative lift for positive motion, b) relative pitching moment for positive motion, c) relative lift for negative motion, d) relative pitching moment for negative motion. 187
6-13 Pressure contour maps of the airfoil upper and lower surface at $Re = 100, 150K$ for positive and negative motion. 188
6-14 Relative lift and pitching moment peaks comparison between $Re = 20K, 100K$ and $150K$ for $\alpha_0 = 15°$. a) L1/M1, b) L2/M2, c) Peaks superposed onto Figure 4-8 at $\alpha_0 = 15°$. 189

7-1 a) Static lift coefficient, b) static pitching moment coefficient and c) velocity magnitude plots for select α_0. 208
7-2 Example case: $\alpha_0 = 15°$, $A/c = 0.5$, $k = 0.24$; a) phase-averaged lift coefficient, b) phase-averaged pitching moment coefficient, c) normalised velocity and vorticity flow fields. 209
7-3 Lift performance of mini-tab. 210
7-4 Pitching moment performance of mini-tab. 211
7-5 Type A flow field - $\alpha_0 = 9°$, $A/c = 0.05$, $k = 0.94$: a) phase-average lift coefficient, b) phase-average pitching moment coefficient, c) normalised velocity magnitude with streamlines. 212
7-6 Type B flow field - $\alpha_0 = 15°$, $A/c = 0.5$, $k = 0.24$: a) phase-average lift coefficient, b) phase-average pitching moment coefficient, c) normalised spanwise vorticity. . 213
7-7 Type C flow field - $\alpha_0 = 3°$, $A/c = 0.5$, $k = 0.40$: a) phase-average lift coefficient, b) phase-average pitching moment coefficient, c) normalised velocity magnitude with streamlines. 214
7-8 Type D flow field - $\alpha_0 = 5°$, $A/c = 0.5$, $k = 0.94$: a) phase-average lift coefficient, b) phase-average pitching moment coefficient, c) normalised spanwise vorticity. . 215
7-9 Type D flow field - $\alpha_0 = 9°$, $A/c = 0.5$, $k = 0.47$: a) phase-average lift coefficient, b) phase-average pitching moment coefficient, c) normalised spanwise vorticity. . 216
7-10 Type D flow field - $\alpha_0 = 15°$, $A/c = 0.5$, $k = 0.63$: a) phase-average lift coefficient, b) phase-average pitching moment coefficient, c) normalised spanwise vorticity. . 217
7-11 Type D flow field - $\alpha_0 = 15°$, $A/c = 0.5$, $k = 0.94$: a) phase-average lift coefficient, b) phase-average pitching moment coefficient, c) normalised spanwise vorticity. . 218

7-12 LEV signature detection through modified pitching moment coefficient, $C_{M,mod}$: Baseline airfoil at $\alpha_0 = 7°$, $A/c = 0.5$, $k = 0.24$,0.31. 219
7-13 Contour plots of mini-tab lift performance with detected LEV formation boundaries and qualitative PIV flow field types. 220
7-14 Contour plots of mini-tab pitching moment performance with detected LEV formation boundaries and qualitative PIV flow field types. 221
7-15 Boundary of $\delta C_L = 0.0$. 222
7-16 Extracted minima/maxima of δC_L. 223
7-17 $\alpha_0 = 15°$, $A/c = 0.5$ - Lift and pitching moment response for impulsively started plunging oscillations at different k. 224
7-18 $A/c = 0.5$ - Transient lift and pitching moment performance. 225
7-19 $\alpha_0 = 15°$, $A/c = 0.5$, $k = 0.24$; a) transient lift coefficient, b) transient pitching moment coefficient, c) normalised velocity magnitude with streamlines. 226
7-20 $\alpha_0 = 15°$, $A/c = 0.5$, $k = 0.94$; a) transient lift coefficient, b) transient pitching moment coefficient, c) normalised vorticity magnitude. 227

List of Tables

3.1 Airfoil geometry parameters and associated uncertainties. 57
3.2 Parameters for transient motion and their associated uncertainties. 59
3.3 Parameters for multiple transient motions and their associated uncertainties. . . 60
3.4 Parameters for sinusoidal motions and their associated uncertainties. 60
3.5 Static load uncertainties. 61
3.6 Dynamic load uncertainties. 64
3.7 Parameters for transient motion and their associated uncertainties. 67
3.8 Static uncertainties. 72
3.9 Typical uncertainties for dynamic motion. 75

4.1 Transient studies used for data extraction. 117

Contents

Abstract i

Acknowledgements iii

List of Figures v

List of Tables xi

Contents xii

Subscripts xvi

Layout xvii

1 Motivation 1
- 1.1 Objectives . . . 3

2 Literature Review 5
- 2.1 Steady-State Stall . . . 5
- 2.2 Unsteady Aerodynamics . . . 6
- 2.3 Unsteady Conditions . . . 7
- 2.4 Wake Structures: Periodic Conditions . . . 10
  - 2.4.1 Effect on Aerodynamic Forces . . . 10
  - 2.4.2 Thrust Production . . . 12
  - 2.4.3 Deflected Jets . . . 14
  - 2.4.4 Finite Wing Effects . . . 15
- 2.5 Leading-Edge Structures: Periodic Conditions . . . 16
  - 2.5.1 Pitching . . . 17
  - 2.5.2 Plunging . . . 25
- 2.6 Leading-Edge Structures: Transient Conditions . . . 37
  - 2.6.1 LEV Formation and Growth . . . 38
  - 2.6.2 LEV Shedding . . . 42
  - 2.6.3 Added-Mass Effects . . . 44
  - 2.6.4 Reynolds Number Effects . . . 45
  - 2.6.5 Post-stall Vortex Shedding . . . 46
- 2.7 Flow Control Strategies . . . 47
  - 2.7.1 Passive Control . . . 48
  - 2.7.2 Active Control . . . 51

2.8 Literature Review Conclusions . . . 53

3 Experimental Methods 55
3.1 Introduction . . . 55
3.2 Water Tunnel . . . 55
3.2.1 Experimental Set-up . . . 55
3.2.2 Airfoil Geometry . . . 56
3.2.3 Airfoil Motions . . . 57
3.2.4 Loads Measurements . . . 60
3.2.5 Particle Image Velocimetry (PIV) Measurements . . . 64
3.3 Wind Tunnel . . . 66
3.3.1 Experimental Set-Up . . . 66
3.3.2 Wing Design . . . 68
3.3.3 Loads Measurements . . . 71
3.4 Rig Comparison . . . 75

4 Unsteady Aerodynamics of a Transient Plunging Airfoil 101
4.1 Summary . . . 101
4.2 Effect of Geometric Angle of Attack . . . 102
4.2.1 Force Measurements . . . 102
4.2.2 Flow Field Measurements . . . 105
4.3 Motion Period and Amplitude Effects . . . 110
4.4 Effect of Airfoil Geometry . . . 114
4.4.1 Conclusions . . . 119

5 Compound Transient Airfoil Motions and the Principle of Linear Superposition 139
5.1 Summary . . . 139
5.2 Canonical Case . . . 141
5.3 Effect of Convective Time Delay . . . 143
5.4 Effect of Second Motion Amplitude . . . 146
5.5 Correlation of Linear Superposition . . . 147
5.6 Additional Transient Motions . . . 148
5.7 Periodic Motion . . . 149
5.8 Conclusions . . . 152

6 Reynolds number effects 163
6.1 Summary . . . 163
6.2 Aerodynamic Loads . . . 164
6.3 Flow Field and Pressure Distribution Measurements . . . 166
6.4 Surface Pressure Analysis . . . 170
6.5 Additional Cases with Data Reduction . . . 173
6.6 Conclusions . . . 174

7 Loads Reduction Through Passive Device 191
7.1 Summary . . . 191
7.2 Static Lift and Pitching Moment . . . 192

7.3 Dynamic Loads and Mini-tab Performance . . . 193
7.4 Flow Field Types . . . 196
7.4.1 Type A . . . 196
7.4.2 Type B . . . 197
7.4.3 Type C . . . 198
7.4.4 Type D . . . 199
7.5 Flow Field Type Identification . . . 201
7.6 Transient Response . . . 204
7.7 Conclusions . . . 206

8 Conclusions **229**
8.0.1 Future Work . . . 231

Bibliography **233**

Appendix A **245**
A.1 Chapter 5 - Pitching Moment Responses . . . 246
A.2 Chapter 7 - LEV boundary sensitivity . . . 247

Appendix B **253**
B.1 Uncertainty Analysis . . . 253
B.2 Lift Coefficient Uncertainty: Water Tunnel . . . 253
B.2.1 Total Measured Lift Force Uncertainty . . . 254
B.2.2 Inertial Lift Force Uncertainty . . . 255
B.2.3 Wire Lift Force Uncertainty . . . 255
B.2.4 Aerodynamic Lift Force Uncertainty . . . 255
B.2.5 Aerodynamic Constant Uncertainty . . . 255
B.3 Pitching Moment Coefficient Uncertainty: Water Tunnel . . . 256
B.3.1 Total Measured Moment Uncertainty . . . 256
B.3.2 Inertial Moment Uncertainty . . . 257
B.3.3 Aerodynamic Moment Uncertainty . . . 258
B.4 Pressure Coefficient Uncertainty: Wind Tunnel . . . 258
B.4.1 Static Pressure Uncertainty . . . 258
B.4.2 Free-Stream Static Pressure Uncertainty . . . 259
B.4.3 Aerodynamic Constant Uncertainty . . . 260
B.5 Lift and Moment Uncertainty: Wind Tunnel . . . 261

Nomenclature

$a1$	First Fourier coefficient	
A	Peak-to-peak amplitude	m
AR	Aspect Ratio	
α_0	Geometric angle of attack	^{o}
α_{eff}	Effective angle of attack	^{o}
$\alpha_{eff,max}$	Maximum effective angle of attack	^{o}
α_{pl}	Induced angle of attack during plunging motion	^{o}
$\alpha_{pl,max}$	Maximum induced angle of attack during plunging motion	^{o}
b	Wing span	m
c	Chord length	m
C_L	Lift coefficient	
δC_L	Lift performance of mini-tab	
ΔC_L	Lift coefficient relative to static	
$\Delta C_{L,mod}$	Modified relative lift coefficient	
$\Delta C_{L,Pk}$	Peak relative lift coefficient	
C_M	Quarter-chord pitching moment coefficient	
$C_{M,mod}$	Modified quarter-chord pitching moment coefficient	
δC_M	Pitching moment performance of mini-tab	
ΔC_M	Quarter-chord pitching moment coefficient relative to static	
$\Delta C_{M,Pk}$	Peak relative quarter-chord pitching moment coefficient	
C_P	Pressure coefficient	
ΔC_P	Pressure coefficient relative to static	
f	Frequency	Hz
k	Reduced frequency	
$L1, L2, L3$	First, second and third peak in transient lift signal	
$M1, M2, M3$	First, second and third peak in transient pitching moment signal	
Re	Reynolds number	
St_A	Strouhal number based on amplitude	
St_c	Strouhal number based on chord	
$St_{c,mod}$	Strouhal number based on projected chord length	
t	Time	s
T	Motion period	
τ	Convective time	
$\tau_{C_{L,Pk}}$	Convective time for lift peak	
$\tau_{C_{M,Pk}}$	Convective time for pitching moment peak	
U_∞	Free-stream velocity	ms^{-1}
V_{pl}	Plunge velocity	ms^{-1}
$V_{pl,max}$	Maximum plunge velocity	ms^{-1}

Subscripts

A	First transient motion
α_0	Static (steady-state)
B	Second transient motion
eff	effective
$L1, L2, L3$	Specific: First, second and third peak in transient lift signal
$M1, M2, M3$	Specific: First, second and third peak in transient pitching moment signal
max	maximum
mod	modified
Pk	Generic: Peak in loads signal
pl	plunge

Layout

The figures in Chapters 3, 4, 5, 6 and 7 are presented as a set at the end of the each chapter. The reader is referred to the following pages for each figure set:

- **Chapter 3**:- p.76 to p.99
- **Chapter 4**:- p.121 to p.137
- **Chapter 5**:- p.154 to p.161
- **Chapter 6**:- p.176 to p.189
- **Chapter 7**:- p.208 to p.227

Chapter 1

Motivation

The field of unsteady aerodynamics is currently in an exciting stage. Researchers are pushing the boundaries of unsteady wing conditions, measurement techniques and diagnostic tools to unravel the complex flow fields that form and the forces they produce. To understand why, it is necessary to look back at where unsteady aerodynamics began. The field was birthed out of the necessity to predict an instability phenomenon known as flutter - where aerodynamic, elastic and inertial wing forces unfavourably combine to create catastrophic oscillations. The first recorded case of flutter was in 1916 [1], and by 1936 a generally applicable, unsteady aerodynamic theory was derived by Theodore Theordorsen [2]. The mathematical tool he developed has proved formidable and still remains valid in many applications to this date. This a textbook example of engineering methodology, to understand the salient features of a problem and boil it down into a model in order to aid design and development.

One of the key aspects of Thoerdorsen's theory (and many similar unsteady analytical models that followed [3]) is the underlying assumption of small amplitude oscillations, where the flow remains attached to the surface of the wing, allowing the forces to be readily described by linear equations. This assumption, although valid for many applications, severely limits the scope of the model, which can and will break down in more extreme unsteady conditions.

A prime example of an extreme unsteady condition is the phenomenon known as dynamic stall - first discovered on helicopter rotor blades during high speed, forward flight conditions. The key aspect of this phenomenon is the unsteady separation of the flow on the blade's upper surface followed by the formation and passage of a distinct rotating disturbance known as a Dynamic Stall Vortex (DSV). The DSV significantly augments aerodynamic loading, leading to large overshoots in blade lift and torque as well as considerable hysteresis. This results in severe vibrational loads and is a limiting factor in helicopter forward flight speed. Of course the primary aim for aerodynamicists at the time was to understand the core aspects of the problem in order to develop a predictive model; however this has proved especially laborious due to the severe non-linearity of massively separated, vortex dominated flow fields – a giant leap from the simplicity of Theordorsen's attached flow assumptions. Although many useful models were developed that could somewhat describe the air loads during dynamic stall, no single model prevailed in doing so without the use of multiple empirical inputs, limiting their scope to a handful of pre-defined conditions.

Since their discovery, DSVs have been documented in a wide range of engineering applications where extreme unsteady conditions occur and are more widely known as the generically termed Leading-Edge Vortex (LEV). LEV's have been found to occur on Micro Air Vehicles (MAVs), wind turbines, aircraft in gusts and manoeuvres and have recently been attributed to the remarkable agility and lift capabilities of insects and other biological flyers/swimmers. As a result of this, focus of late has shifted away from LEV behaviour in terms of specific conditions, i.e. periodic rotor blades, and has instead been placed on abstract canonical wing motions to simplify and distil the problem to better understand the underlying physics. Although LEV research is now stepping out of its infancy, a complete understanding of their behaviour is still lacking. Ultimately the goal is to have sufficient insight into LEV behaviour to inform an aerodynamic model, akin to Theordorsen's model, to cheaply and accurately predict loads in massively separated, vortex-dominated flows. Whether this goal is possible within the author's lifetime is unknown, but the road to it is paved with aerodynamic studies on all fronts – experimental, computational and analytical – to systematically probe the boundaries of understanding to un-

lock and explore new avenues of research.

This thesis aims to add to the current understanding of massively separated, unsteady aerodynamics with particular attention to LEV behaviour through experimental means. This will be achieved by addressing the following points, outlined in a recent LEV review by Eldredge and Jones [4].

- Further study of vortex-wing and vortex-vortex interactions during unsteady disturbances to better understand bulk flow field behaviour.
- A viable method to disrupt LEVs in order to alleviate the loads they create. Such a device would have far reaching benefits across many applications.

1.1 Objectives

The objectives of the study are:

- Investigate the aerodynamic response of an airfoil undergoing single transient plunge manoeuvres. Particular focus will be placed on post-stall angles of attack where large-scale vortex shedding can occur.
- Quantify the bulk flow field and loads response to multiple transient plunge manoeuvres at post-stall angles of attack. The effect of time delay between the motions will have a large effect due to the presence of large-scale vortex shedding.
- Determine the effect of a significant Reynolds number change on the aerodynamic response to transient plunge manoeuvres. This will be achieved through equivalent water and wind tunnel experiments.
- Assess the performance of a flow fence device for loads suppression during unsteady motion. The experiment will cover pre-stall, stall and post-stall conditions.

Chapter 2

Literature Review

This section is intended to give a brief overview of steady-state stall and unsteady aerodynamics in order to highlight gaps in understanding and introduce concepts that will be used when discussing the unsteady aerodynamics of airfoils and wings in extreme conditions.

2.1 Steady-State Stall

A very brief and general description of the mechanisms and trends for steady-state stall is given below. The reader is referred to [5, 6] for a more in depth discussion of the topic.

For an airfoil inclined in a free stream, there exists a maximum angle of inclination that maintains largely attached flow on the upper surface. When this angle is exceeded it results in a loss of lift and an increase in drag and nose-down pitching moment, the rate of which depend on the airfoil parameters, Mach number and Reynolds number of the flow; this phenomenon is known as steady-state or static stall and is primarily dependant on boundary layer behaviour. As the angle of inclination, or angle of attack (α_0), of the airfoil approaches stall, the adverse pressure gradient acting on the fluid over the airfoil's upper surface will increase and cause the boundary layer to progressively thicken. When the boundary layer can no longer overcome this pressure gradient, it will separate from the upper surface creating a reversal in the boundary layer [5]. A

fully stalled airfoil displays flow separation over the entire upper surface.

The lift coefficient, C_L, exhibits linear, or nearly-linear, behaviour up until the point of stall, after which the non-linearities of separated flow dominate. The quarter-chord pitching moment coefficient, C_M, tends to become more negative (nose-down) due to a shift in the centre of pressure on the airfoil. The pressure on the upper surface is more or less constant in the separated flow region which causes the centre of pressure to move aft. A higher Reynolds number can increase the maximum achievable lift coefficient. This is due to the increasing ratio between inertial and viscous effects which produce a thinner boundary layer, delaying the onset of separation [5].

2.2 Unsteady Aerodynamics

Unsteady aerodynamics refers to time-dependant aerodynamic behaviour. In reality, all flows are inherently unsteady, but often this unsteadiness is small and of no interest. In such cases it can be ignored and assumed to be in a quasi-steady state.

In the stall and post-stall regimes, the flow is no longer steady and exhibits unsteady behaviour giving rise to fluctuations in the aerodynamic forces. The source of the unsteadiness is the shedding of shear layers from the leading and trailing-edge which roll up to form vortices [7], see Figure 2-1. An example Power Spectral Density (PSD) of the wake of a stalled NACA 0012 profile is shown in Figure 2-1.

The frequency parameter in Figure 2-1 is shown in terms of the Strouhal Number based on the airfoil chord length, St_c. This is a non-dimensional frequency defined as the ratio of the vortex shedding frequency and free steam velocity according to:

$$St_c = \frac{fc}{U_\infty} \tag{2.1}$$

where f is the shedding frequency, c is the airfoil chord length and U_∞ is the free stream velocity. The PSD in Figure 2-1 shows a range of shedding frequencies present in the wake, however there

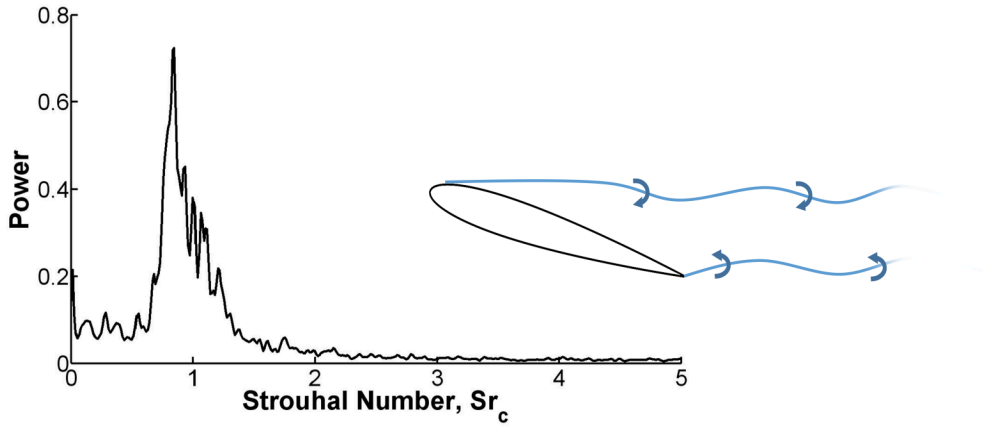

Figure 2-1: Typical wake frequency spectra of a stalled NACA 0012 airfoil [8].

is a clear dominant frequency at a St_c of around 0.9. This is the wakes fundamental or natural frequency and plays an important role in the lift force of oscillating airfoils in the stall and post-stall regime [7, 8].

The natural shedding frequency of wings in stall and post-stall conditions were measured by Rojratsirikul *et al.* [9], the results of which can be seen in Figure 2-2. They present the shedding frequency in terms of the Strouhal number based on the projected area of the chord, $c \cdot sin(\alpha_0)$, where reasonable collapse around a mean value of 0.17 can be observed for different airfoil shapes and wing aspect ratios, similar to study by Huang and Lin [10]. Although this data is for finite wings, they note that the shedding frequencies are very close to that of two-dimensional airfoils. Again, this fundamental frequency plays an important role in unsteady lift production.

2.3 Unsteady Conditions

Unsteady conditions can arise from various sources and become important when time dependant effects cause the aerodynamic forces to deviate considerably from their steady-state value. These sources include gusts, manoeuvres and any body/wing motion that is induced by these disturbances, both rigid body and flexible. From a kinematics point of view, four motion types of airfoil unsteadiness can be defined, see Figure 2-3. In Figure 2-3, pitch is defined as the change in α_0 over time through a rotation usually located at 1/4 chord, plunge is a vertical translation

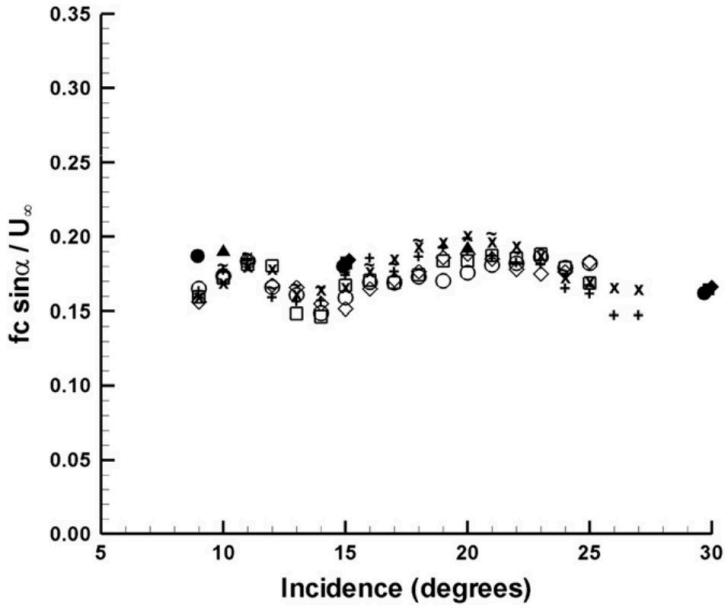

Figure 2-2: Natural shedding frequency of wings with respect to the Strouhal number based on airfoil frontal area [9].

of the airfoil giving a varying induced angle of attack (α_{pl}) depending on the plunge velocity (V_{pl}), surge is a translation parallel to the free stream velocity (U_s) and the flow field change is a time dependent change of the free stream velocity components. The term effective angle of attack (α_{eff}) will be used throughout this thesis which is defined as $\alpha_0 + \alpha_{pl}$.

In order to determine the degree of unsteadiness, a parameter called the reduced frequency is used:

$$k = \frac{\pi f c}{U_\infty} \tag{2.2}$$

where k is the reduced frequency. Similar to the St_c of the airfoils wake in the previous section, the reduced frequency is the ratio of the vortex shedding frequency and free steam velocity and is useful for grouping the different sources that give rise to this unsteadiness [11]. The distinction between the two lies in their application. St_c was used in section 2.1 to measure the natural frequency of the airfoil's wake, whereas k is used to non-dimensionalise the forcing frequency. St_c and k and differ by the product of π, where $k = \pi St_c$.For $0 \leq k \leq 0.05$ the unsteady effects

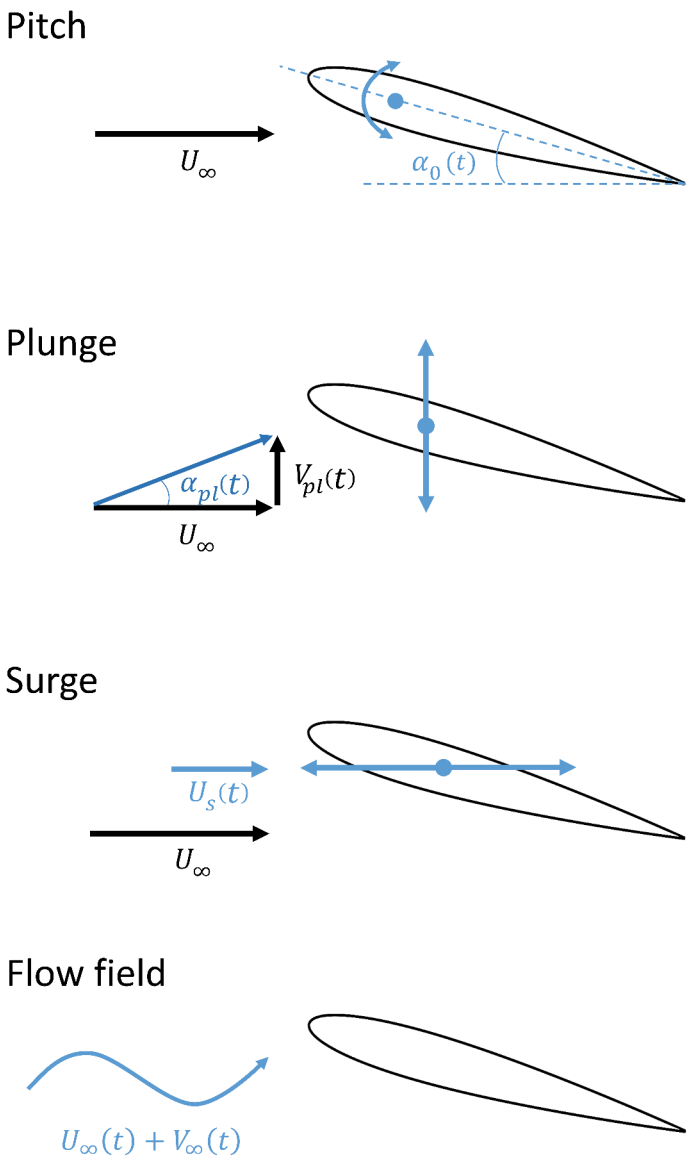

Figure 2-3: Motion types of airfoil unsteadiness.

are small and the flow is often considered to be quasi-steady. For $0.05 < k < 0.2$ the flow is said to be unsteady and the associated effects cannot be ignored. For $k \geq 0.2$ the flow is considered to be highly unsteady and the non-circulatory effects will start to dominate over the circulatory forces [5, 12].

Typically a realistic unsteady aerodynamic scenario will be a combination of pitch, plunge, surge

and flow field change. For research purposes however is it necessary to measure the effects of just one, or in some cases two of these parameters, in order to reduce the complexity. Pitch and plunge have been the main focus of the unsteady airfoil research; the vast majority of which consider only periodic unsteadiness. The following sections will give an overview of the plethora of research on periodically pitching/plunging airfoils as they can provide valuable insight into the bulk flow features that form in an unsteady environment. As mentioned in Chapter 1, recent focus has been to test a range of simple canonical motions to better understand LEV behaviour. These motions are typically transient by definition, i.e. non-repeating, and will be covered in a separate section.

2.4 Wake Structures: Periodic Conditions

The unsteady wake structures presented in this section are generally associated with attached flows. The effective angles of attack induced by the unsteady motion may take the airfoil beyond its static stall angle, leading to flow separation and LEV formation. This will be dealt with in section 2.5 and the focus here is placed on the wake.

2.4.1 Effect on Aerodynamic Forces

Consider an airfoil that experiences an instantaneous step change in α_0. Quasi-steady theory would demonstrate that the corresponding lift change is also instantaneous, however, in reality the lift takes time to respond. The mechanism for this is shown in Figure 2-4a. When α_{eff} is changed, a vortex is formed at the trailing-edge of the airfoil due to the viscosity of the fluid, which changes the circulation bound to the airfoil. As this vortex is shed, the influence of the downwash it induces over the airfoil diminishes and the lift force gradually increases to its quasi-steady value. A good approximation to this behaviour is through Wagner's function, shown in Figure 2-4b, which modifies the quasi-steady lift values in a time-dependant manner. The lift function, $\Phi(\tau)$, starts at 50% of the quasi-steady lift and asymptotically approaches 100% as the vortex travels downstream.

For an oscillating airfoil/free-stream condition, α_{eff} is continually changing and can be con-

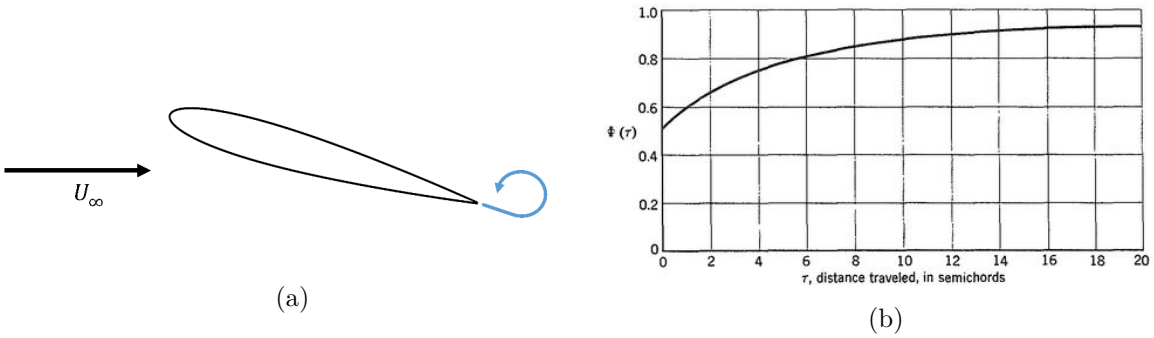

(a) (b)

Figure 2-4: a) Diagram of starting vortex, and b) plot of Wagner's Function, taken from [13].

sidered as a series of infinitesimally small step changes. This results in vorticity of varying strength to be continually shed from the trailing-edge which in turn affects the aerodynamic loads on the airfoil [14], Figure 2-5. The general effect of the shed vorticity in the wake is an attenuation and phase variation of the circulatory lift force with respect to the quasi-steady values [5].

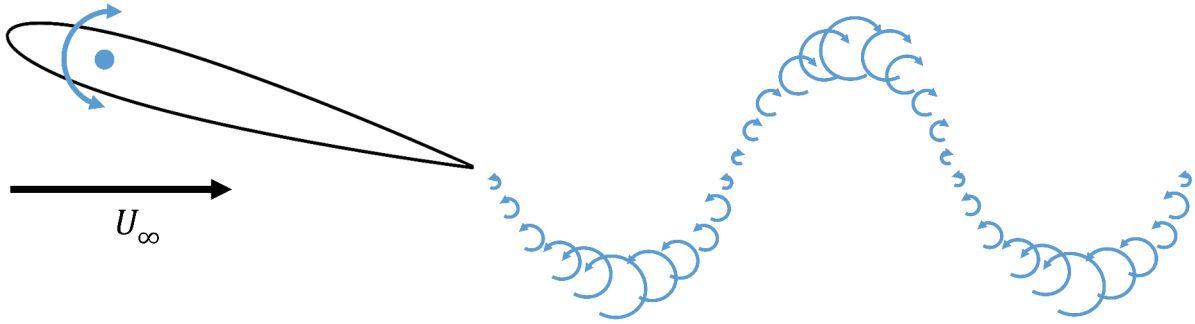

Figure 2-5: Shed vortices from airfoil oscillating in pitch.

The earliest studies of the lift produced by an oscillating airfoil was the theoretical work undertaken by Wagner, Theodorsen, Küssner and von Kármán & Sears who produced exact analytic solutions for the lift and moment based on incompressible 2D thin airfoil theory for various small amplitude, unsteady loading conditions; pitch, plunge and flowfield change [5]. The reader is referred to Bisplinghoff et al. [3] for a full description of these theories. In summary, the models predict the attenuation and phase variation of the circulatory lift force as a complex function of the reduced frequency k. The total unsteady lift force is split into two contributions; the

circulatory component and the added mass component. The circulatory component around an oscillating airfoil is defined by the vorticity in the flow, i.e. what is bound to the airfoil and what is shed into the wake. This effect is modelled through the complex lift function via an imaginary and real component that control the amplitude and phase of the unsteady lift. The added mass component results from the reactive force that is produced when the local fluid around the airfoil is accelerated and increases with k^2 [12]. Corkery *et al.* [15] experimentally revealed the added mass force to arise from a thin vorticity distribution close to the airfoil surface; this will be discussed in more detail in section 2.6.3.

One of the first experimental studies was undertaken by Silverstein & Joyner [16] who measured the phase variation of the circulatory lift force of an airfoil oscillating in pitch and found close agreement with theory up to reduced frequencies of $k < 0.3$. Since then, a plethora of studies have been conducted to corroborate this theory in pure and combined motions. Notable studies include Halfman [17], Reid & Vincenti [18] and Rainey [19] who found close agreement with theory for a range of reduced frequencies of around $k = 0.4$ to 1.0. They found deviations when operating over large α_{eff} excursions, in small α_{eff} excursions close to stall, or operating at low Reynolds numbers. Further breakdown of the theory was documented to occur at higher reduced frequencies, roughly $k > 1$, where the Kutta condition at the trailing-edge was being violated, causing deviations in both lift magnitude and phase values [20]. Chen & Ho [21] later showed that the violation of the Kutta condition was not solely based on k but also on the operating parameters, i.e. airfoil shape, oscillation modes, amplitudes, α_0 and Reynolds number.

2.4.2 Thrust Production

It has been well documented that an airfoil undergoing pure pitch, plunge or free stream oscillations can produce a net thrust force, a historical summary of which is discussed by Platzer et al. [22]. A theoretical study in 1936 by Garrick [23] showed that an airfoil undergoing pure plunge will produce a component of thrust force for any frequency, due to an effective tilt in the lift vector, yet an airfoil undergoing pure pitch will only produce thrust at a certain frequency threshold, as a function of the pivot location. This has been shown experimentally in notable

experiments by Silverstein & Joyner [16] and Koochesfahani [24]. A study by DeLuarier & Harris [25] showed that the production of thrust in the plunging case is not quite as simple as a tilt in the lift vector and was dependant on the suction pressure peak produced by the leading-edge shape of the airfoil.

The most influential parameter for thrust generation of airfoils is the Strouhal number based on amplitude, defined as:

$$St_A = \frac{fA}{U_\infty} \tag{2.3}$$

where A is the peak-to-peak amplitude of the trailing-edge. It is important to note that whilst it is the best variable to predict wake behaviour such as thrust, it is not sufficient on its own. The generation of thrust is attributed to the arrangement of vortices in the wake. At a low St_A the wake of an oscillating airfoil resembles a Kármán vortex street as shown in Figure 2-6. The shed vortices create a time averaged flow opposing the free-stream creating a velocity deficit in the wake, which is indicative of drag production. As St_A is increased the shed vortices gradually invert their position, producing a reverse Kármán vortex street. This wake is considered to be thrust producing as the vortices produce a time-averaged jet in the direction of the free-stream, creating a velocity excess [26–28]. Although this wake switch is a good indicator of thrust production, it has been found by Godoy-Diana et al. [29] and Bohl & Koochesfahani [30] that the switch in wake structures precedes the switch from net drag to thrust and a more complete analysis is required to determine the switching point. The arrangement of shed vortices was also found to be dependant on the profile of oscillation by Koochesfahani [24] where he experimented with non-sinusoidal, periodic pitching waveforms.

A study by Triantafyllou et al. [31] showed the optimal St_A number for thrust efficiency of an airfoil in plunge is between 0.25 - 0.35, corresponding to the St_A range of various swimming fish and also matching the St_A range of flying species documented by Taylor et al. [32]. Godoy-Diana et al. [29] found the thrust producing wakes for pitching foils also occurred within the St_A range

of natural flyers.

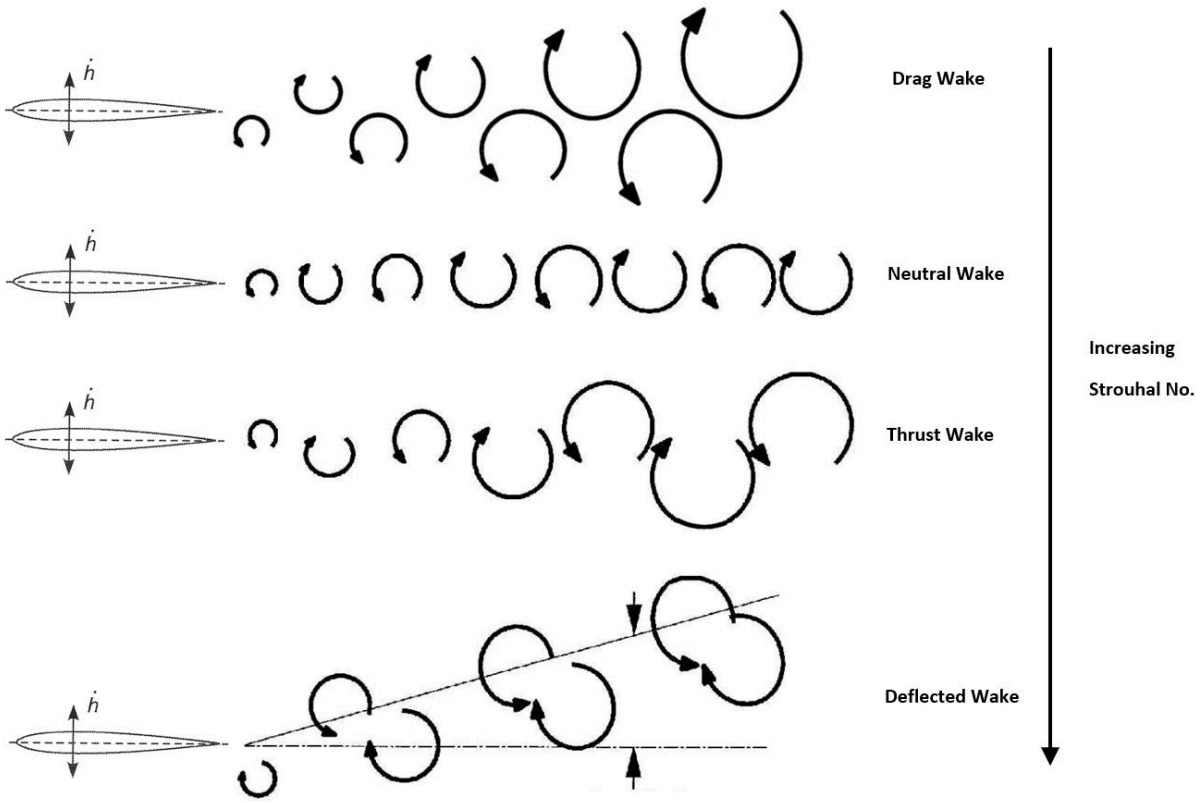

Figure 2-6: Evolution of airfoil wakes with increasing St_A, modified from [5, 26].

2.4.3 Deflected Jets

At very large values of St_A the thrust jets can deflect, Figure 2-6. This asymmetric wake can produce time-averaged lift coefficients, C_L, of up to 3.5 occur even at a zero mean α_0 [27]. Such jets were first studied by Jones et al. [26] who found them to occur at $St_A > 1$ both numerically and experimentally; although more recent studies have shown this to occur around $St_A = 0.32$ to 0.45 in pure pitch and plunge. These deflected jets show significant bifurcation and their direction is highly dependant on the starting conditions, mean α_0 and geometry [27, 29, 33]. Cleaver et al. [27] proposed that the mechanism for deflection is due a difference in strength between the clockwise and counter-clockwise vortex pair that form at the trailing-edge. If the flow is travelling from left to right, a stronger clockwise trailing-edge vortex (TEV) will produce a downwards deflection, whereas a stronger counter-clockwise vortex will cause the jet to deflect

upwards. The direction of jet deflection was found to set the direction of lift enhancement. This explains why, in their findings, the jet direction remained stable at a certain mean α_0 threshold, as the vortex pairs were already significantly asymmetric. The reader is referred to Calderon et al. [34] for a more complete summary of the research on deflected jets.

2.4.4 Finite Wing Effects

One of the fist attempts to analyse a finite oscillating wing was the theoretical study by Reissner and Stevens in 1943 [35]. He modified Theodorsen's complex lift function to account for aspect ratio effects on the circulatory component. As the aspect ratio approaches infinity, the theory approaches Theodorsen's original function. Among many of the underlying assumptions, Reissner and Stevens assumed that there are no three-dimensional effects on the added mass component as this produces no wake. Bisplinghoff et al. [36] reported that the effects of a finite span become less pronounced as the reduced frequency is increased. Deviations from two dimensional theory become significant for aspect ratios of 6 at $k < 0.5$, and aspect ratios of 3 at $k < 1.0$. An experimental study by Widmayer [37] showed excellent agreement with Reissner and Steven's theory for an oscillating wing in pitch with an aspect ratio of 2.

Platzer et al. [22] noted a connected vortex ring pattern that occurs in the wake of a plunging wing, an example of which is shown in Figure 2-7. They note that this example would correspond to a reverse Kármán vortex street in the mid-span plane of the wing. Neef & Hummel [38] found reduced thrust efficiency for a flapping and pitching wing as a result of the tip vortices, which had only weak interaction with the TEV's.

An interesting study by Calderon et al. [34] showed that a finite wing will not produce the deflected jet phenomena, even at St_A numbers that far exceed the threshold for deflected jets in 2D. The presence of the wing tip vortices creates three dimensionality in the wake, where the TEVs do not form in straight tubes but instead split at a spanwise location and link with the tip vortex to produce a connected system, Figure 2-8. This system was found to be symmetrical and hence will not produce a deflected jet. He & Gursul [39] however postulated that the deflected jet could be produced by a finite wing for higher aspect ratios, where the tip vortex has less

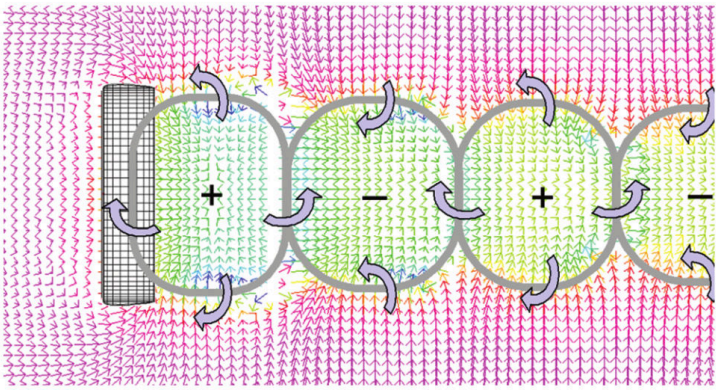

Figure 2-7: Vortex ring structure, taken from [22].

influence on the spanwise shed vorticity.

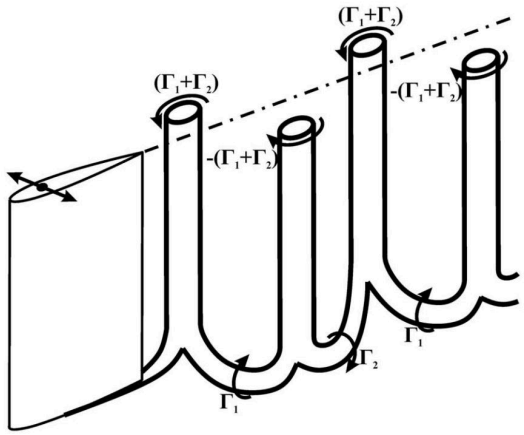

Figure 2-8: Sketch of vortex chain structure that prevents the deflected jet phenomena, taken from [34].

2.5 Leading-Edge Structures: Periodic Conditions

When the unsteady motion involves the airfoil operating at α_{eff} close to or above the static stall angle, the flow will separate from the leading-edge and form coherent vortices that can significantly increase lift, nose-down pitching moment and either enhance or degrade thrust depending on the St_A [8, 11, 40–43].

For plunging motion this is primarily determined by the mean α_0 and the Strouhal number, St_A. It is important to note that St_A is not an absolute indicator for LEV formation and will

be discussed further in section 2.5.2. The Strouhal Number based on amplitude can be linked to the maximum α_{pl} induced by the plunge velocity [27], according to:

$$\alpha_{eff,max} = \alpha_0 + tan^{-1}\frac{V_p l}{U_\infty} = \alpha + tan^{-1}\frac{\pi f A}{U_\infty} = \alpha_0 + tan^{-1}\pi St_A \tag{2.4}$$

where V_{pl} is the maximum plunge velocity in the period. It is clear to see that even for an airfoil at $\alpha_0 = 0°$, a sufficiently high Strouhal number can produce a high $\alpha_{eff,max}$, causing LEVs to form. For pitching motion, the formation of an LEV is primarily determined by α_0, the amplitude of the pitching motion and k. LEV formation is a well known phenomenon in rotor craft that has plagued designers and analysts for over 60 years and as such, there is an abundance of literature on the topic. Because of this the following section is split into the LEVs that form due to the pitching and plunging motions respectively. Unsteady surging [44] and free-stream [45] oscillations can also produce strong LEVs, however for the sake of brevity these have been omitted.

2.5.1 Pitching

Dynamic stall due to pitching is an unsteady phenomenon by which flow separation is delayed and occurs at an angle of attack beyond the static stall angle. This is primarily found to occur on rotorcraft during high speed forward flight or high load manoeuvres where the retreating blade encounters a rapid increase in angle of attack through a combination of free stream changes, cyclic control and blade flapping. Other occurrences can be found on wind turbines and super-manoeuvrable aircraft. It is distinguished from static stall through the presence of an LEV that forms and convects over the suction side of the airfoil, Figure 2-9. This vortex causes a wave of low pressure that significantly enhances lift, up to 100% in some cases [5], whilst the vortex remains over the airfoil. As the vortex convects across the airfoil it causes the centre of pressure to move aft, producing large nose-down pitching moments. The lift enhancement is lost as the vortex is shed into the wake. This is highly problematic because the significant loads variation can excite aeroelastic modes. The onset of dynamic stall usually limits the operational

boundaries of rotor craft [5].

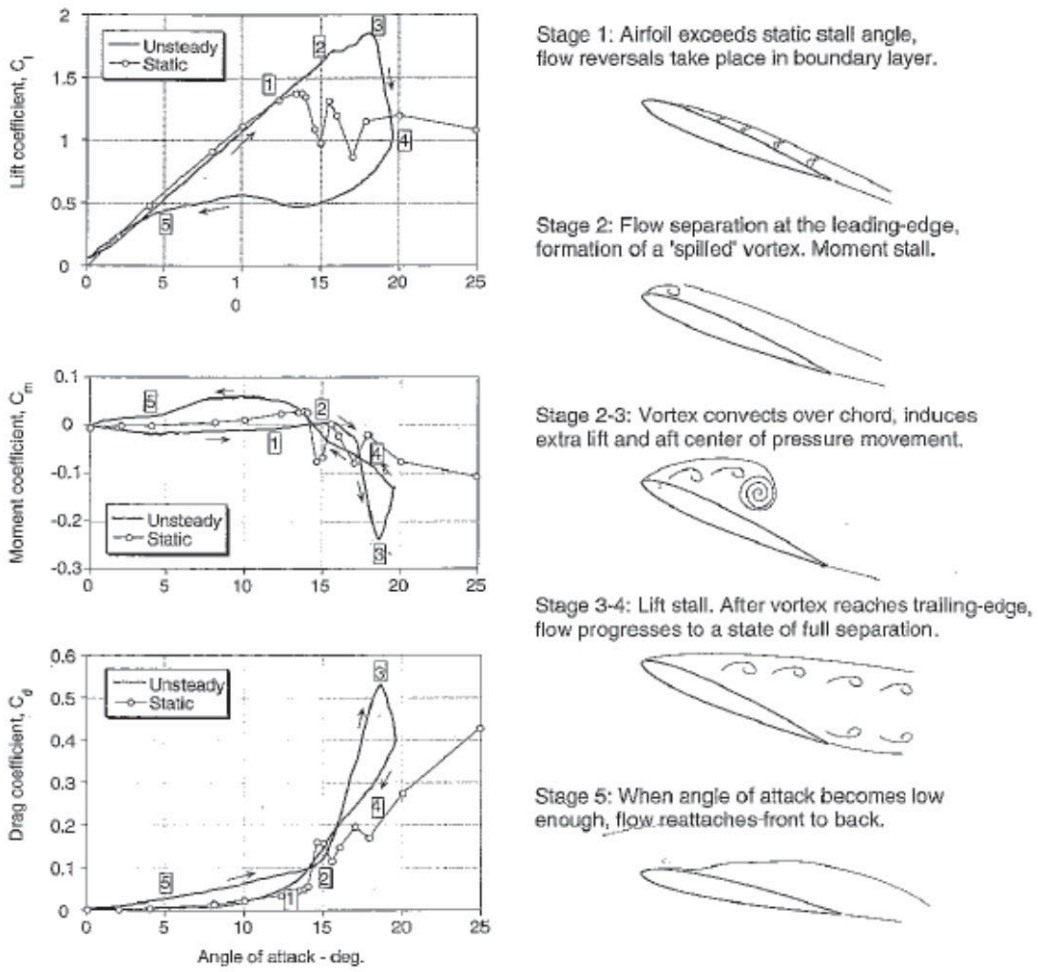

Figure 2-9: Aerodynamic loads and corresponding flow features during a typical dynamic stall event, taken from [5].

Detailed reviews on the field have been conducted by McCroskey [14, 40] and later by Corke & Thomas [46]. The following sections will give a sufficient description of the the main flow features and how they are affected by various parameters.

Flow Morphology

The flow morphology of a typical dynamic stall event can be broken down into the five distinct steps on the oscillation cycle of the airfoil, presented by Leishman [5] in Figure 2-9. Stage 1 occurs when the airfoil is pitched beyond it's static stall angle. Complete flow separation is

delayed due to a reduction in the adverse pressure gradient caused by the motion of the airfoil and the lag in the boundary layer response. During this stage the lift continues to increase. Mulleners and Raffel [47] note a reduction in lift slope from pre- to post-stall angles caused by a thin layer of flow reversal close the airfoil's suction surface due to the increasing adverse pressure gradient. Kelvin-Helmholtz type instabilities occur within this shear layer and small shear layer vortices begin to form. The continued increase in lift during Stage 1 has also been attributed to the formation of a closed separation bubble at the leading-edge [46, 48]. Stage 2 begins when the flow separates from the surface and forms a concentrated vortex that is convected over the chord. The onset and location of Stage 2 is highly sensitive to the Reynolds and Mach numbers, the maximum α_0 and reduced frequency as well as the airfoil geometry [14, 40, 46]. The emergence of the LEV is preceded by the instability of the shear layer vortices, formed in Stage 1, as they begin to interact and coalesce into larger structures. Mulleners and Raffel note that the LEV contains remnants of these strucutres along with the shear layer vorticity emanating from the leading-edge [47]. The LEV continues to grow as vorticity is consumed from a feeding shear layer emanating from the leading-edge. This process continues until opposite signed vorticity generated between the LEV and upper surface is pushed towards the leading-edge, intersecting the feeding shear layer. This is referred to by Mulleners and Raffel as dynamic stall onset [47]. The presence of the shed vortex enhances lift through a low pressure wave, shown in Figure 2-10, as the vortex is convected across the upper surface at approximately 50% of the free stream velocity [40]. The passage of the low pressure vortex core also causes a large negative pitching moment due to the aft movement of the centre of pressure. Stage 3 occurs once the vortex has been shed from the trailing-edge and merges with the wake. Notable studies by Panda & Zaman [11] and Rival & Tropea [42] showed that a counter rotating vortex is triggered at the trailing-edge by the passing of the LEV. These form a pair and are convected downstream in a large mushroom shape. A sudden loss of lift occurs as the flow begins to transition to Stage 4; fully separated flow. In this stage the pitching moment reaches the maximum negative value, which is referred to as *moment stall*. Secondary vortices have been documented to form after the primary LEV due to a closed region of vorticity accumulation which can cause additional, less severe fluctuations in the upper surface pressure [40, 47], see Figure 2-10. Stage 5 is the gradual

reattachment of the flow due to the decrease in angle of attack. It can be seen from Figure 2-9 that reattachment occurs from the leading-edge and progresses aft and takes place at an angle much lower than steady-state stall due to the unfavourable pressure gradient produced by the downwards motion of the airfoil. Reattachment has been reported to be a stochastic process which is extremely difficult to predict [46].

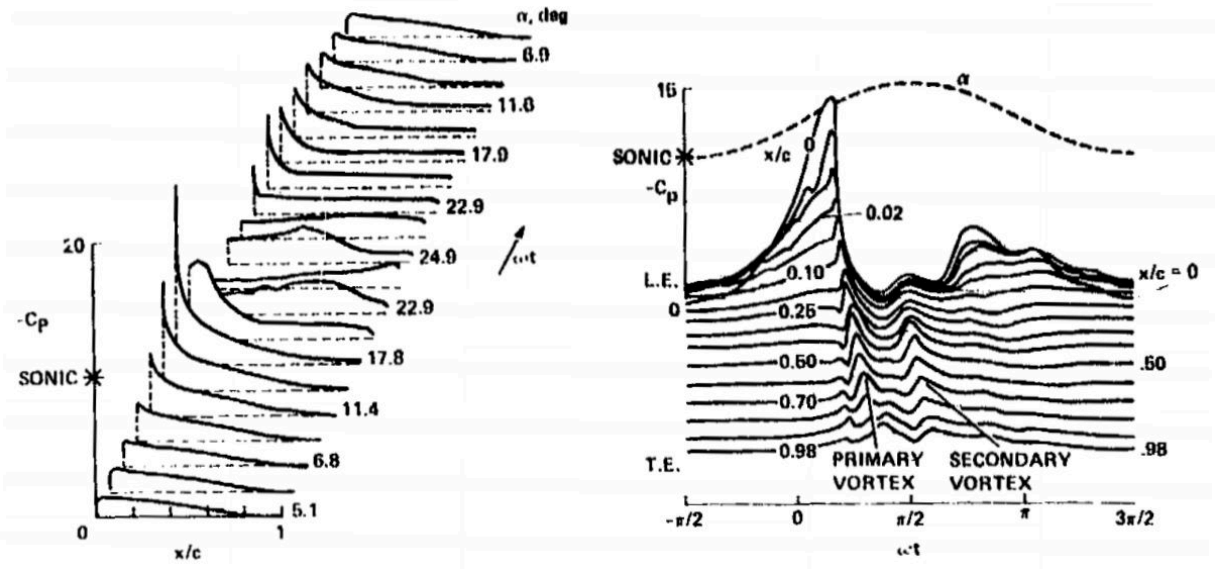

Figure 2-10: Time history of pressures across the airfoil chord during dynamic stall, taken from [40].

Dynamic Stall Regimes

The severity of the dynamic stall process can be categorised into different regimes, put forward by McCroskey [14, 40] in Figure 2-11, which are delineated primarily by the maximum α_0 they achieve in the cycle.

- *No Stall* - The static stall angle is not exceeded and the flow remains attached throughout the cycle. This is predicted well by the analytical theory mentioned in the previous section and a smooth narrow hysteresis loop is present due to the phase lag in the aerodynamic forces.

- *Stall Onset* - This is where the maximum α_0 marginally exceeds the static stall angle so that a small portion of the cycle is spent at a post-stall α_0. Only a small amount of separation

occurs due to the delayed separation effects and this can be seen as a slight distortion in the hysteresis loop. A distinguishing feature of this regime is that it achieves the highest possible lift without significant penalties in drag and pitching moment.

- *Light Stall* - This marks the appearance of the LEV that forms due to sufficient separation, the size of which is in the order of the airfoil thickness. The formation of the LEV is highly dependant on the boundary layer behaviour which is in turn sensitive to the Reynolds number, Mach number, forcing conditions and airfoil geometry. The LEV introduces a significant amount of hysteresis. Figure 2-11 shows the pitching moment in this regime to display a cross over in loop direction, exhibiting a clockwise trajectory which is associated with negative damping and can cause unstable aeroelastic problems such as stall flutter [5, 40]. This regime can also be identified through the onset of moment stall, seen as a sharp drop in pitching moment, Figure 2-11. Mulleners and Raffel showed that light stall occurs when dynamic stall onset occurs after the maximum α_0 has been reached.

- *Deep Stall* - A strong LEV is now present over the upper surface, the thickness of which is in the order of the airfoil chord. It is distinguished from light stall through the significant increase in lift and pitching moment along with a large, sharp drop off in lift after the maximum has been achieved. The largest amount of hysteresis can be seen in this regime, however the amount of clockwise rotation in the pitching moment trajectory is now reduced compared with light stall, and over all tends to be more aerodynamically stable. The aerodynamic loads are relatively insensitive to Reynolds number, Mach number, forcing conditions and airfoil geometry. Mulleners and Raffel showed that deep stall occurs when dynamic stall onset occurs before the maximum α_0 has been reached.

Forcing Effects

The following points will give a short summary of the key effects of each forcing parameter.

- *Reduced Frequency* - This quantifies the degree of unsteadiness and therefore affects the size and shape of the hysteresis loop. An increase in reduced frequency for the same mean α_0

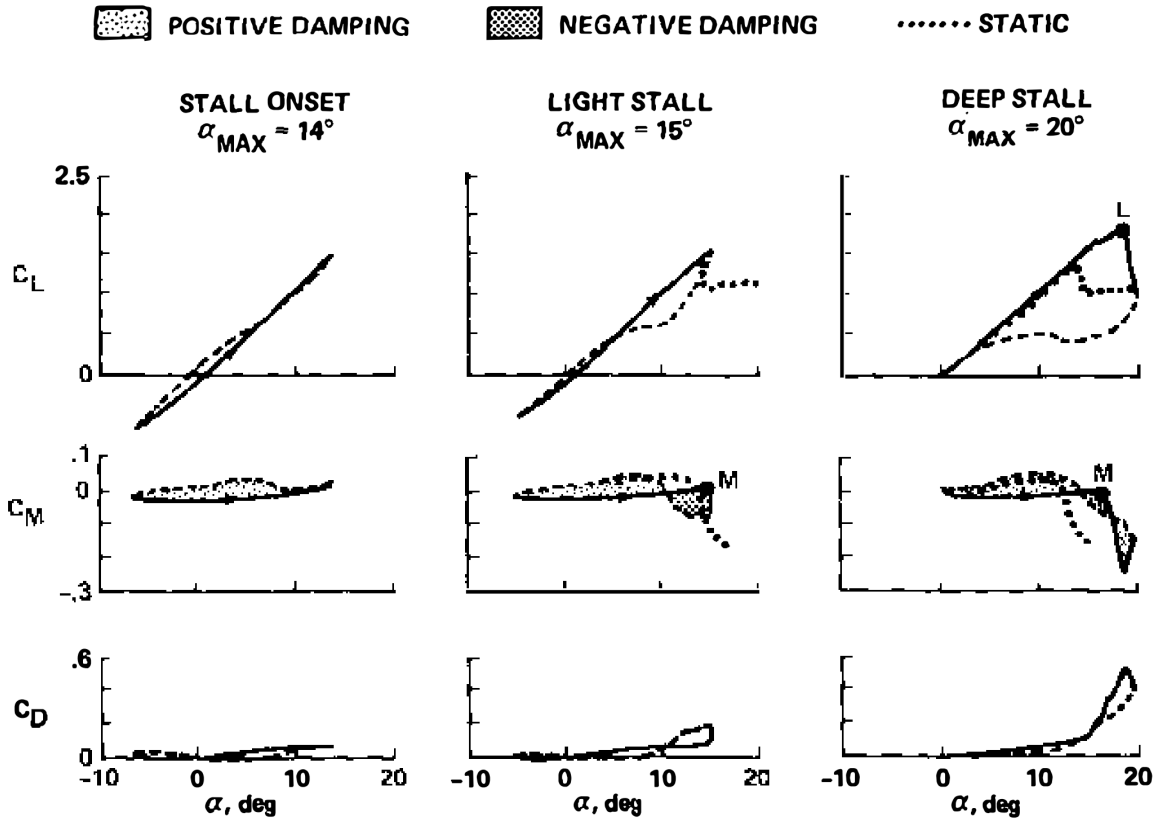

Figure 2-11: Lift, pitching moment and drag plots showing the difference between dynamic stall regimes, taken from McCroskey [14].

and amplitude will delay the onset of dynamic stall, through the alleviation of the adverse pressure gradient, and cause the LEV to form later in the cycle [5, 11, 48]. The phase delay of the LEV was reported to vary linearly with reduced frequency by Panda & Zaman [11]. Leishman [5] notes that for a given mean α_0 and amplitude a high enough reduced frequency can prevent flow separation from happening at any point in the cycle, which can significantly reduced hysteresis. A study by McAlister et al. [48] found that the LEV is stronger and more concentrated as the reduced frequency is increased, indicating that the strength of the vortex corresponds to the circulation around the airfoil at the moment the LEV forms. It has been observed by Ohmi et al. [49] and Kuo & Hsieh [50] that at certain reduced frequencies, synchronised shedding can occur. This is where the LEV reaches the trailing-edge and combines with the co-rotating TEV as it is formed. The phasing of the LEV has also been found by Anderson [41] to be important in thrust production due to its

interaction with the reverse Kármán vortex street.

- *Mean Angle of Attack,* α_0 - This, along with the amplitude of motion, governs the stall regime the airfoil is operating in [14].

- *Amplitude* - Has a very large effect, as described previously. McCroskey [40] measured the effect of increasing the amplitude in the deep stall regime whilst keeping the pitch rate constant and found that, for low amplitudes, the vortex is shed on the downstroke of the motion after the maximum α_0 has been reached. This produces a weaker LEV and more closely resembles the features from the light stall regime in line with the findings of Mulleners and Raffel [47].

- *Airfoil Geometry* - The airfoil geometry has the largest effect in the light stall regime, where the stall characteristics are highly dependent on the separation behaviour of the boundary layer [14]. It can determine whether the separation begins at the leading or trailing-edge, which in turn controls the strength of the LEV and where it forms. McCroskey notes the leading-edge geometry as the principal factor affecting the air loads. A sharp leading-edge will lead to abrupt leading-edge stall and cause rapid changes in the airloads. In contrast, a blunt leading-edge or large leading-edge camber will give rise to trailing-edge stall, which is a much more gradual stall process [40]. McCroskey & Carr [51] provide a detailed comparison of multiple airfoil sections, but note that the forcing conditions are much more dominant in determining the overall dynamic stall characteristics. A comparison study of three airfoil sections is given by Leishman [5]. It was concluded that the airfoils give qualitatively the same behaviour, but display subtle quantitative differences in the air load loops.

- *Reynolds number* - Ohmi et al. [49] found the effect of Re to be much less significant than the other forcing parameters at $Re = 1.5 \cdot 10^2$ to $1 \cdot 10^4$. The most notable difference was a more significant level of turbulence seen in the small scale flow structures. McCroskey [14] also notes that Reynolds number has a weak effect relative to other parameters. In contrast, Oshima & Ramaprian [52] found that dynamic stall can be delayed to a higher

α_0 at critical Reynolds numbers where transition to turbulence plays a role. An earlier transition at higher Reynolds numbers allows the flow to overcome larger adverse pressure gradients; this leads to a more abrupt stall and a more concentrated LEV. The study covered an Re range of $5.4 \cdot 10^4$ to $1.5 \cdot 10^5$.

Finite Wing Effects

The presence of tip vortices can have a significant effect on the flow structures of a three-dimensional wing. Although they introduce a high degree of three-dimensionality into the shape of the LEV as it convects across the chord, the qualitative shape of the air loads do not change as significantly and resemble the trends seen in quasi-steady aerodynamics from the influence of the tip vortices [5, 53, 54]. The results of Lorber et al. (1991) are presented by Leishman in [5] and show the air loads at various spanwise positions of a cantilevered wing. The results display the same qualitative behaviour as a two-dimensional airfoil, displaying a large overshoot in lift and nose-down pitching moment and a wide hysteresis loop. The most notable difference is the reduction of the lift slope along the span of the wing due to the influence of the wing tip vortices, not unlike steady-state aerodynamics. At the outer most portion of the wing, the air loads show no characteristics of dynamic stall and this has been attributed to the dominance of the tip vortices in that location.

The structure and evolution of the LEV that forms during dynamic stall has been investigated in many experimental and numerical studies [53, 55–57]. Schreck & Helint [53] measured the LEV structure of a cantilever wing with an aspect ratio of 2 and found a large degree of deformation in the LEV and a non-uniform lift loading across the wing, Figure 2-12a. This was attributed to the influence of the tip vortex at the outboard section and the splitter plate at the wing root which rapidly deform the LEV as it is convected across the chord. A numerical study by Spentzos et al. [55] showed the same flow structure as Schreck & Helint, in which the influences of the wing tip and wing root quickly deform the LEV into a Ω shape, see Figure 2-12b. The inboard portion of the LEV can be seen to lift off the surface of the airfoil and is shed before the outboard portion. When a symmetry condition was applied at the root of the wing, the vortex

structure exhibited a more symmetrical Ω shape, Figure 2-12c. The study also documented the merging of the LEV and tip vortices and showed the dominance the tip vortex has at the wing tip section. This study was later extended by Spentzos et al. [56] to determine the effect of different plan form shapes and aspect ratios. A remarkably similar flow structure was found for all planforms.

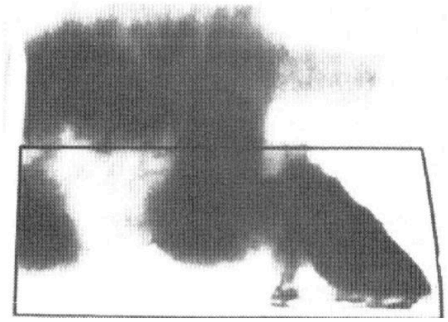

(a) LEV structure of a cantilevered wing

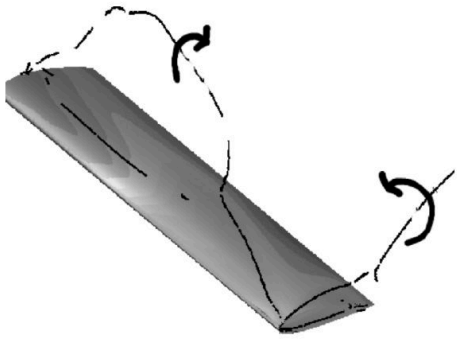

(b) Vortex cores of cantilevered wing

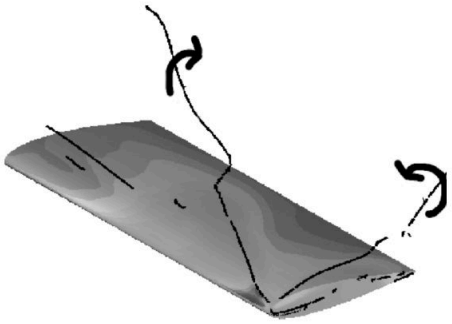

(c) Vortex cores of free finite wing

Figure 2-12: Three dimesnional LEV structures, taken from [53, 55].

2.5.2 Plunging

The vortical structures that form for a plunging airfoil have many similarities with the structures that form during dynamic stall. They both create an overshoot in lift and pithing moment coefficient which causes a large amount of hysteresis in the aerodynamic loads. There are however differences between dynamic stall for pitching and plunging due to the different airfoil kinematics [58, 59]. As previously mentioned, the formation of a LEV for pitching is primarily governed by the maximum α_0 the airfoil experiences, which is a geometric angle and must exceed the

static stall angle by a certain margin, shown by McCroskey in Figure 2-11. Plunging however, experiences an *effective* change in angle of attack due to the superposition of the free-stream and airfoil plunge velocity, Equation 2.4. The formation of a LEV is highly dependent on the α_0, Strouhal number and reduced frequency and does not necessarily delineate with the same criteria as dynamic stall due to pitching.

Comparison to Dynamic Stall

One of the first studies to assess the differences between the two motions was undertaken by Carta in 1979 [58]. The comparison was made through the equivalence of α_0 for pitching and α_{eff} for plunging. Major differences were found between the two motions, especially at a high mean α_0. In some cases, when stall penetration was achieved, the hysteresis loops for pitch were larger than the plunge equivalent, which did not display some of the features associated with dynamic stall described in the previous section e.g. dramatic decrease in lift and moment coefficient. However, the loops more closely matched at higher reduced frequencies. Overall, the normal lift force was shown to be greater for plunging and displayed a higher lift slope, also seen by Chen [59], Rival & Tropea [42] and Lee & Su [60]. This was shown by Carta [58] and Fukushima & Dadone [61], where the peak leading-edge suction is much higher for plunge. The pressure distributions show a less coherent LEV for plunging that is noted to propagate downstream in a less orderly fashion when compared to the equivalent pitching case. This was later confirmed by Chen [59] who found a wider and less pronounced pressure wave. He established the convection speed of the LEV was much less than for pitching, around 20-30% of the free stream velocity. He also showed that the slower propagation speed and elongated shape can sustain lift for a larger portion of the cycle. In the deep stall regime, Rival & Tropea [42] and Lee & Su [60] found that the flow fields of pitch and plunge were in qualitative agreement. Rival & Tropea postulate that the differences in forces are primarily a function of the LEV that is shed and its position. This is reinforced by Maresca et al. [62] and Lee & Su who found good agreement in the aerodynamic loads in deep stall.

Flow Morphology

Despite the differences described above, the core flow morphology of the LEV during plunging is very similar to that of dynamic stall. Visbal [63] numerically investigated the formation of the LEV in deep stall, maximum α_{eff} of 22^o, and provides a detailed description of the flow features and their formation at various phases using instantaneous pressure and vorticity plots, the latter of which can be seen in Figure 2-13. The stall process starts in a similar manner to dynamic stall with flow reversal in the boundary layer, Kelvin-Helmholtz type instabilities and the roll up into shear layer vortices; see Figure 2-13 at $\Phi = 27°$. At $\Phi = 37°$ the shear layer vortices begin to interact and coalesce and by $\Phi = 50°$ the vorticity can clearly be seen accumulating at the leading-edge into an LEV. The LEV emerges at 63^o and at 90^o is the only vortical structure remaining over the airfoil as the shear layer vortex system is either consumed or shed into the wake; roughly corresponding to the maximum lift coefficient shown in Figure 2-14. As the LEV reaches the trailing-edge, $\Phi = 127°$, the low pressure induces a distinct pitching moment stall, see Figure 2-14. A TEV is then triggered at $\Phi = 143°$, also noted by Rival & Tropea [42], where the low pressure causes a second moment stall peak, Figure 2-14. The flow then progressively reattaches from the leading-edge moving aft and becomes fully attached at around $\Phi = 270°$. The same features can be seen in the dye visualisation experiment by Ol et al. [64] and it is noted that the reattachment process is highly three-dimensional. Despite the similarities in flow field to dynamic stall due to pitching, the lift force loop presented by Visbal [63] in Figure 2-14 does not display a similar steep lift drop and subsequently large hysteresis; this was also seen by Ol et al. [64] and in many of the cases presented by Carta [58].

Plunging Regimes

Although the different stall regimes have been applied to the plunging cases discussed in the previous sections, they are not necessarily delineated in the same way as dynamic stall due to pitching and there is currently no consensus on what characterises the different regimes for plunging. Previous researchers [42, 60, 63, 64] have matched the mean α_0 and equivalent amplitude of dynamic stall due to pitching for taxonomy purposes. A rough grouping is given below which is based primarily on the mean α_0 and Strouhal number.

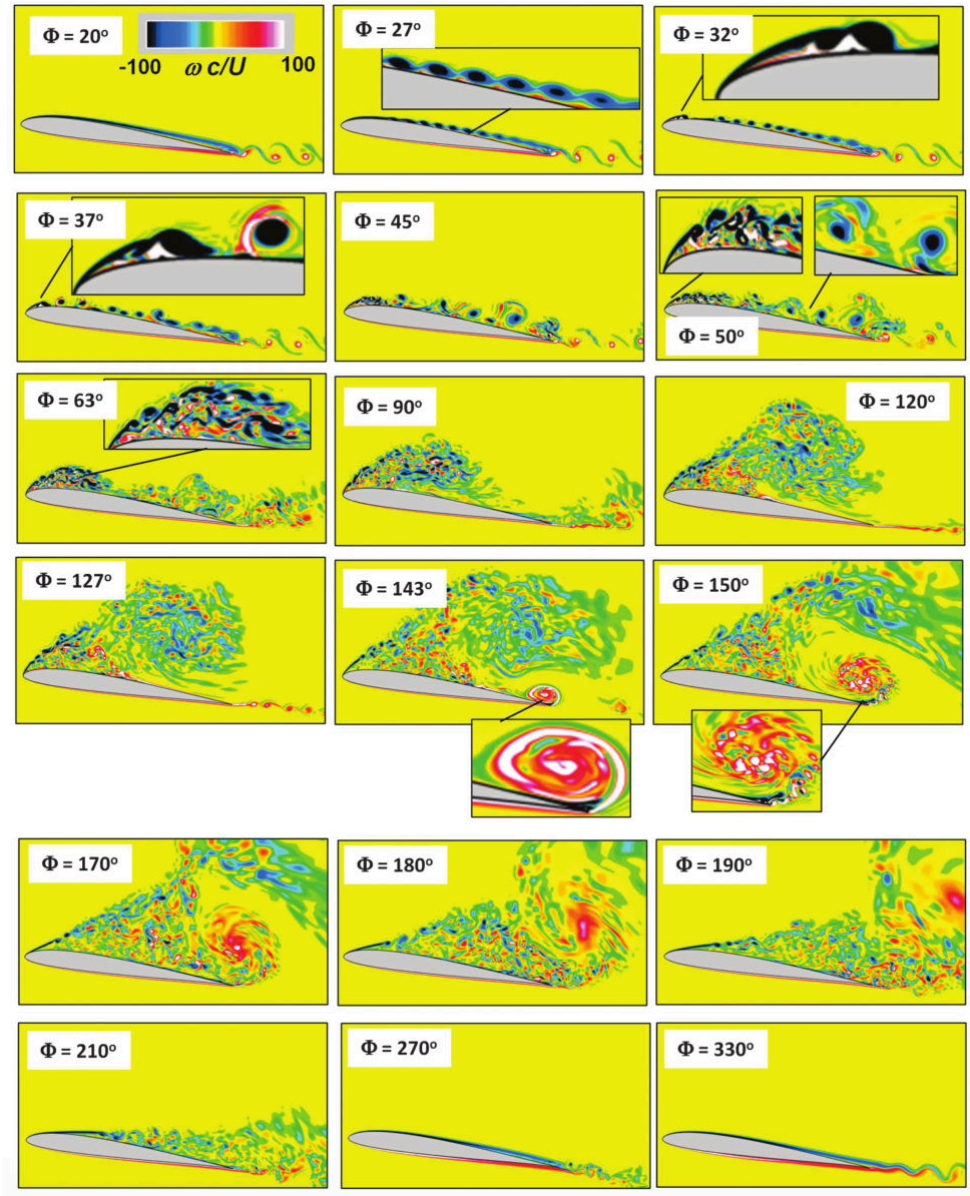

Figure 2-13: Leading-edge vortex formation due to plunge motion, taken from [63].

- *No Stall* - The Strouhal number and α_0 are low enough such that no separation occurs. The aerodynamic forces and wake structures are described in the previous section.

- *Stall Onset* - This is defined as the onset of flow separation from the leading-edge and does not significantly alter the aerodynamic loads from their analytical counterpart. In a computational study by Tuncer & Platzer et al. [65], the boundary for LEV formation on an airfoil at zero α_0 was found to generally occur at a Strouhal number of 0.11 for a

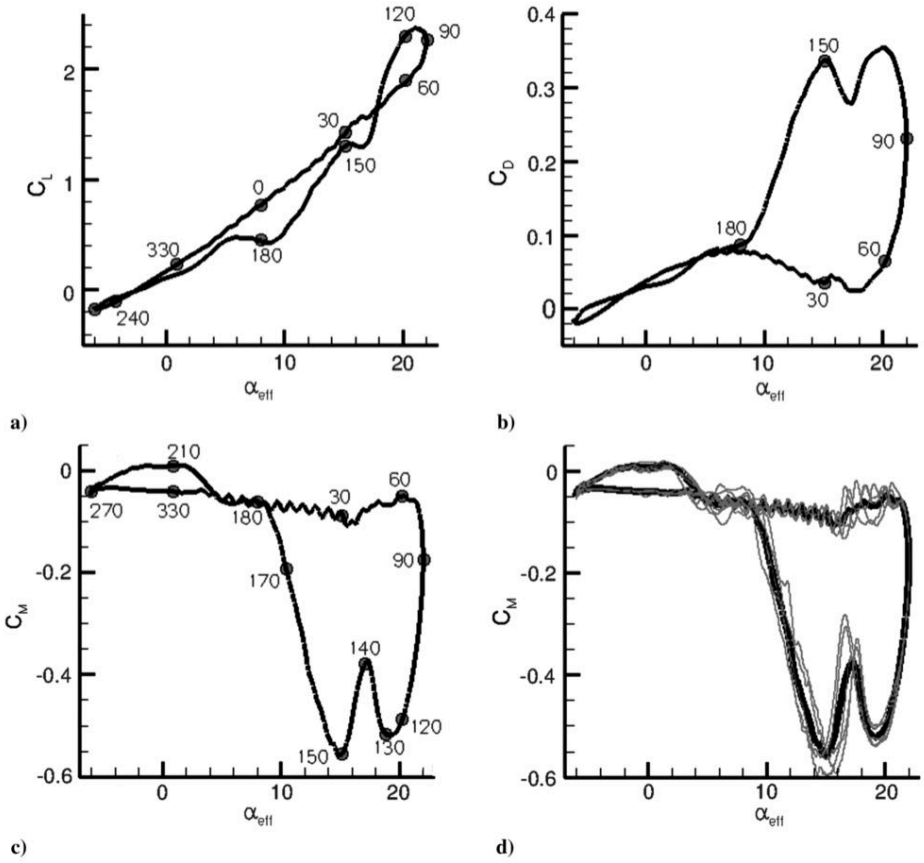

Figure 2-14: Aerodynamic loads induced by leading-edge vortex, taken from [63].

range of frequencies and amplitudes at a Reynolds number of $1 \cdot 10^6$. This corresponds to a maximum α_{eff} of 19° which is well above the static stall angle and is in agreement with LEVs documented in other studies [41, 66–68]. In this regime there is a recirculation region present towards the aft portion of the airfoil that is subsequently shed into the wake. The boundary of LEV formation was found to set the maximum thrust efficiency the airfoil could achieve [65] as the formation of LEVs act to increase drag [43]. A lower LEV formation angle of 17.4° was found by Anderson et al. [41] but only for a certain frequency and amplitude combination. The stall boundary can also be reached through a higher α_0 and lower Strouhal number. An example is given by Chen [59] for $\alpha_0 = 12°$ and $\alpha_{pl} = 2.5°$.

- *Light Stall* - In a similar manner to dynamic stall, this is defined such that the α_{eff} is

sufficient for LEV formation, the presence of which creates more distortion and hysteresis in the aerodynamic forces and further departure from theory. A distinct LEV can be seen in a subsequent study by Tuncer & Platzer et al [69] at $\alpha_0 = 0^\circ$ and a Strouhal number around 0.15; maximum α_{eff} of 25^o. A similar boundary was observed by Chiereghin *et al.* [70]. The aerodynamic loads reported by Carta, Chen, Soltani et al. and Lee & Su [58–60, 71] show light stall occurring at a lower α_{pl} for a higher α_0. An overshoot in lift and decrease in pitching moment are shown along with a loss in lift and negative damping loops in some cases. The α_0 varies from 8-15^o with α_{pl} varying from 4-8^o.

- *Deep Stall* - A strong and more coherent LEV is now present over the airfoil which generally has a greater effect on the aerodynamic loads. In this regime there is a larger overshoot in lift, Cleaver et al. [8] noted an increase in mean lift up to 310% of the maximum static value, and a larger moment stall as seen in the results by Carta [58]. Tuncer et al. [69] and Rival et al. [72] both note the presence of a smaller secondary vortex that forms after the primary LEV. An interesting feature in this region is the absence of a sudden loss in lift in the previously mentioned cases by Visbal [63] and Ol et al. [64]. This phenomenon was was not observed by Maresca et al. [62], Ghoreyshi & Cummings [73] and Lee & Su [60] who tested similar plunge cycles at a lower reduced frequency and found a steep drop in lift after the maximum α_{eff}. The delineation of what differentiates deep stall is evidently not clear and cannot be attributed solely to the Strouhal number or a defined shape in the loops of lift and pitching moment. The order of LEV size is perhaps the feature best to differentiate this regime from light stall, as per dynamic stall due to pitching.

Forcing Effects

The following points will give a short summary of the key effects of each forcing parameter.

- *Reduced Frequency* - It has been documented that the reduced frequency, k, can play a large roll in the formation of the LEV and the arrangement of the flow field. Andro & Jacquin [74] put forward the three main factors that dictate the lift force in a plunging airfoil based on k: i) The LEV suction, ii) the interaction of this LEV with the airfoil surface, termed

"wake capture" and iii) the added mass component, which dominates the aerodynamic forces at high k values but ultimately averages to zero over the cycle. The "wake capture" phenomenon was observed at k=1.26 and found to increase the time averaged lift. This was attributed to two factors: Firstly, the increase in k produced a large acceleration which led to the increase of vortex circulation. Secondly, k is the inverse of the time window for LEVs to form, develop and shed. This allowed the LEV to be formed on the downstroke and captured on the upstroke which increased the time averaged lift. Young & Lai [67] also noted the LEV sensitivity to k, where for a constant St_A, a higher k restricts the time for the vortex to grow resulting in a smaller LEV. Cleaver *et al.* [8] measured the lift of a plunging airfoil at a $\alpha_0 = 15°$ and found the highest time-averaged lift coefficient occurred when the plunging frequency closely matched the natural shedding frequency of $St_c \approx 1$. Two further peaks in lift occurred at its subharmonic, St_c=0.5, and first harmonic frequency, St_c=2, which can be seen on Figure 2-15; similar results were found by Choi et al. [75]. This was termed "vortex lock-in" [76] and defined as a synchronisation between the natural frequency of shedding and the forcing frequency. Choi et al. further defined this as a display of dominate peaks in the lift response that occur only at harmonic frequencies of natural shedding.

Researchers have placed focus on the different vortex arrangements in order to group them into distinct modes [66, 68, 77]. The type of wake structure formed is dependant on the timing of the LEVs arrival with the trailing-edge system, which is primarily governed by k. Lewin & Haj-Hariri [68], Lua et al. [66] and Eslam Panah & Bucholz [77] found that the modes depend on the fate of the LEV; whether it merges with like signed TEVs, forms a dipole with opposite signed TEVs, is shed on its own or is destroyed by its interaction with the airfoil surface.

The reduced frequency can also affect the decline in thrust efficiency when LEVs are formed. A LEV that is shed will produce a thrust force for as long as it remains over the forward-facing front half of the the airfoil. For $\alpha_0 = 0°$, as soon as the LEV crosses the point of maximum thickness it will contribute to drag [67]. At high values of k, the LEV will not

convect as far before another LEV is produced, reducing the impact of the vortex aft of the maximum thickness. This can be seen in the numerical study by Tuncer & Platzer [65] where the thrust degradation is much less severe for higher k values. A plateau in efficiency is observed rather than a sharp drop.

- *Strouhal Number, St_A* - The maximum angle of attack is primarily governed by the Strouhal number, which affects the strength of the LEV. This has been shown by Eslam Panah & Bucholz [77] in Figure 2-16. Note that Figure 2-16 also reinforces the effect of reduced frequency where for the same Strouhal number, the higher amplitude, lower frequency case results in a stronger LEV.

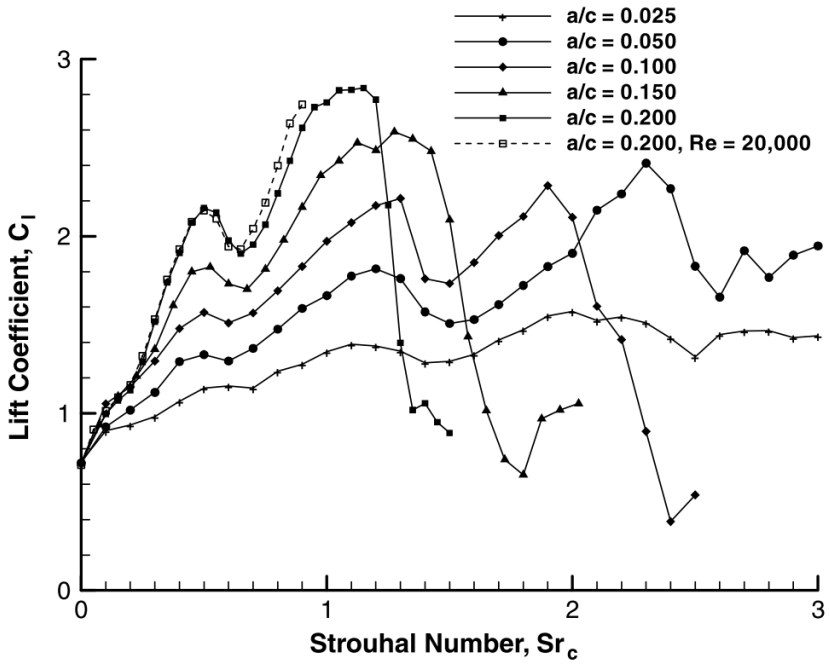

Figure 2-15: Peaks in lift due to vortex lock-in at a post-stall angle, taken from [8].

The Strouhal number also influences the switch from a drag to a thrust producing wake even with the presence of an LEV. Cleaver et al. [8] found two vortex modes within the range of Strouhal numbers considered which had a dramatic effect on the lift and thrust; Figure 2-17a shows the boundary switch between these two modes against plunging amplitude and frequency. Mode-1 occurs when a single LEV convects across the airfoil surface and quickly dissipates through its interaction with the TEV system. This mode

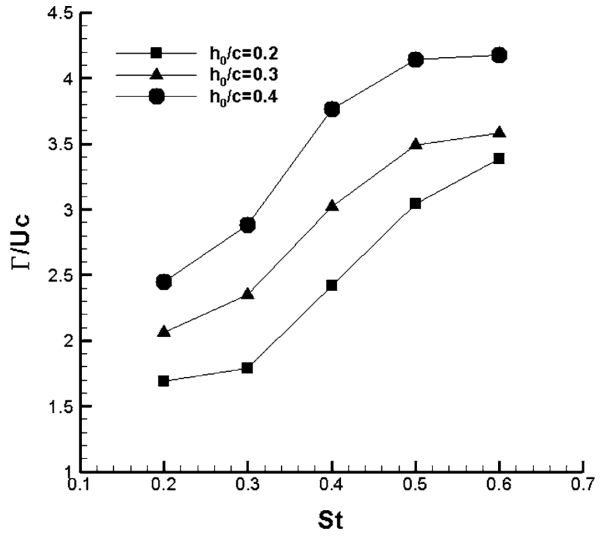

Figure 2-16: Strouhal number effect on LEV circulation, taken from [77].

was associated with large time-average lift coefficients, up to 310%. At a critical Strouhal number range, a Mode-2 flow field occurs where the LEV forms on the downstroke and remains impinged near the leading-edge where its coherence is rapidly reduced. This vortex mode is associated with low lift and high thrust and is primarily due to the formation of a reverse Kármán vortex street that forms at higher Strouhal numbers. The colour plot of the normalised, time-averaged lift coefficient with plunge amplitude and frequency can be seen in Figure 2-17b. High lift zones can be seen to correlate with the natural shedding frequency and its harmonics in the Mode-1 region.

- *Mean Angle of Attack,* α_0 - As stated previously a larger α_0 leads to LEV formation at a lower St_A, and so has a large influence on the severity of the stall [59, 65, 70], i.e light or deep. Chiereghin *et al.* found the time averaged lift increase to correlate with the maximum α_{eff}, which is a function of α_0. A higher α_0 produced a mean lift increase at a lower St_A. The mean angle of attack also has an effect on jet deflection as described earlier.

- *Airfoil Geometry* - Rival et al. [72] conducted a comprehensive study into the effects of airfoil geometry, specifically focusing on the influence of the leading-edge. They found that the sharp leading-edge geometries facilitated faster LEV growth. However the overall topology of the formation and shedding process remained relatively unchanged, which can

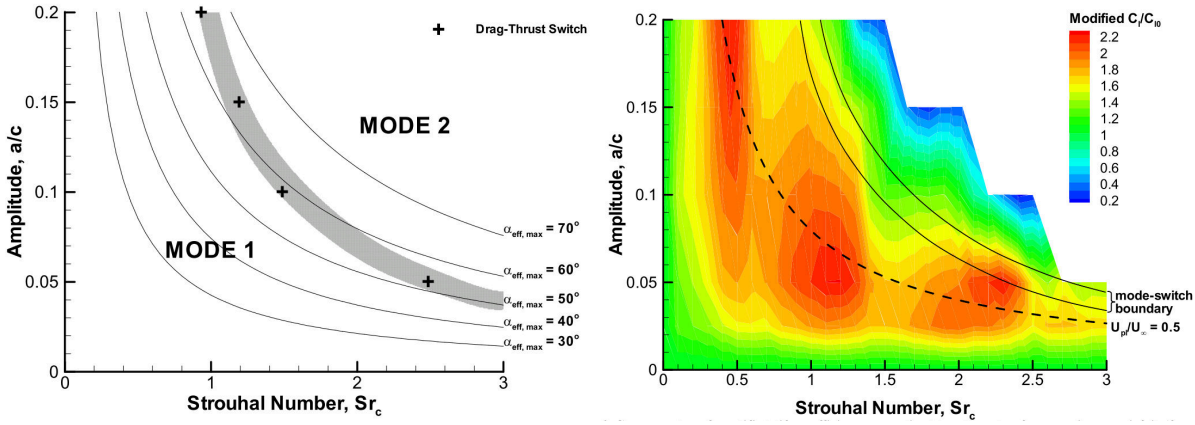

(a) (b)

Figure 2-17: (a Vortex shedding modes shown as a function of plunging amplitude and frequency, b) Colour plot of the normalised lift coefficient against plunging amplitude and frequency, taken from [8].

be seen in the lift coefficient loops. Other studies by Eslam Panah & and Bucholz [77] and Lua et al. [66] show the facilitation of separation for sharper leading-edges. Cleaver et al. [78] compared the LEV formation and jet deflection behaviour of a NACA 0012 and flat plate profile for a mean angle of attack of 0° and 15°. The deflected jet phenomena at 0^o was found the be stable for the NACA 0012 profile, whereas the flat plate displayed an unstable switching between the two jet directions. The effects of camber were investigated by Guerrero [79] who tested a number of different NACA profiles in a Strouhal number range consistent with biological flyers. He found that the camber of the airfoil had a significant effect on lift force but a minimal effect on thrust.

- *Reynolds Number Effects* - Visbal [63] performed numerical simulations and documented the formation and shedding of the LEV as well as the aerodynamic forces for Reynolds numbers in the range of $1 \cdot 10^3$ to $1 \cdot 10^5$. At the lowest Reynolds number he found a single laminar LEV to form. At an intermediate range, multiple LEVs formed and convected across the surface, which caused additional fluctuations in the aerodynamic loads. At the higher Reynolds numbers a single turbulent LEV was found to form and shed later stage in the cycle and can be seen as a phase lag in the lift response. A comparison was made between the lower and upper Reynolds number of the study which found a similar

lift magnitude, although slightly higher for the turbulent case, and a significantly larger moment stall at a high Reynolds number. This is perhaps due to the more pronounced TEV which forms later in the cycle and its interaction with the LEV. Ol et al. [64] assessed the differences in flowfield from $Re = 3 \cdot 10^4$ to $6 \cdot 10^4$ and found very little difference across the range, however no force data was given. In a similar Re range, Kang et al. [80] found at low Reynolds numbers, $Re = 1 \cdot 10^4$ a larger, more diffuse vortex formed compared with $Re = 3 \cdot 10^4$ to $6 \cdot 10^4$ which produced a stronger, more concentrated LEV. In the high Reynolds number range, Tuncer & Platzer [69] observed no significant effect when increasing the Reynolds number from $1 \cdot 10^6$ to $5 \cdot 10^6$.

Finite Wing Effects

The presence of the wing tip has been investigated in a number of experimental and computational studies. Visbal et al. [81] studied the evolution of the LEV on a flat plate at $\alpha_0 = 8°$ which replicated the experimental study by Yilmaz and Rockwell [82]. Figure 2-18a shows the LEV formation and propagation across the cycle. At the start of the plunge, the LEV forms uniformly across the leading-edge. Towards the bottom of the downstroke it becomes pinned to the surface at the wing tips; a significant amount of axial flow towards the centre of the wing is present in the vortex core at this stage. The vortex then detaches from the surface, forming an arch like shape which moves upwards; much like the Ω shape vortex during three-dimensional dynamic stall. During the upstroke the feet of the arch move inwards as the vortex structure is convected across the chord and ultimately connect at the end of the cycle where it is shed into the wake. A large reduction in lift coefficient, lift curve slope and loop distortion was found for the 3D case compared with the 2D counterpart, Figure 2-18b.

A similar arch structure and tip vortex breakdown behaviour was documented by Calderon et al. [83]. Different planforms were tested in high frequency, low amplitude regimes. They found significant distortion in the LEV as it convected across the chord. The amount of undulation was highly sensitive to reduced frequency and was shown to be more pronounced on the higher aspect ratio, elliptical planform; a comparision of the LEV distortion at the end of the downstroke

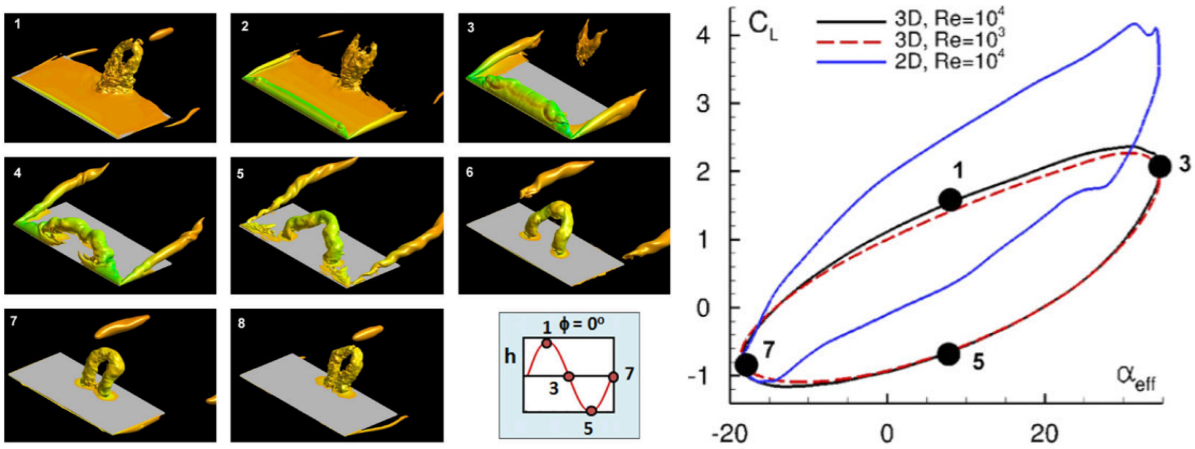

(a) (b)

Figure 2-18: a) Evolution of LEV arch structure on finite plunging wing, (b) associated lift coefficient, taken from [81].

between the planforms can be seen in Figure 2-19. They also confirmed the presence of lift peaks at the natural shedding frequency and its harmonics in three-dimensional flow and noted its attenuation when compared with the two-dimensional results of Cleaver et al. [8].

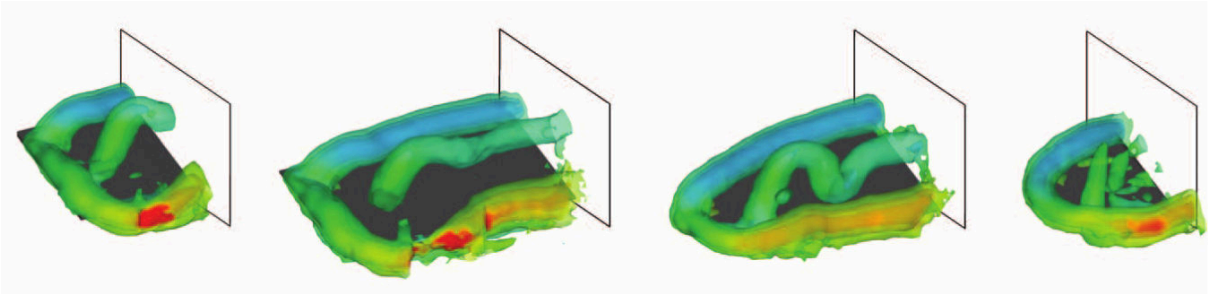

Figure 2-19: LEV distortion at the end of downstroke for various planforms, taken from [83].

Wing tip effects on high aspect wings ($AR = 10$) have been experimentally documented by Chiereghin *et al.* [84], see Figure 2-20. For an unswept wing the LEV leg at the wing tip moves inboard, significantly deforming the LEV. In contrast, the swept wings show wing root LEV leg moving outboard. This served to explain why the swept wing produced larger wing root bending moments. The axial flow along the vortex filament was also extracted and found to increase as the LEV deforms.

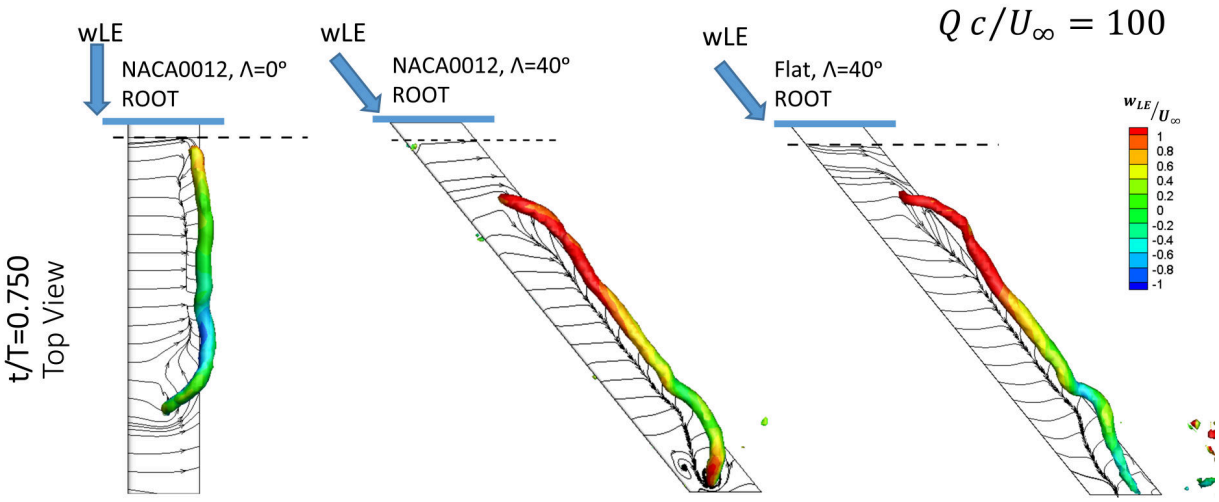

Figure 2-20: LEV distortion on high aspect ratio wings, taken from [84].

2.6 Leading-Edge Structures: Transient Conditions

This section will provide an overview of transient conditions, where there are no repeating motions, and are more analogous to naturally transient scenarios such as manoeuvres and gust encounters.

The earliest and most commonly studied transient motion is the pitch-ramp manoeuvre, where the airfoil is dynamically pitched at a constant angular rate, which was primarily researched to investigate the potential of the dynamic stall effect for super manoeuvrable aircraft [85–87]. Extensive investigations found the non-dimensional pitch rate to be closely linked with the α_0 at which dynamic stall takes place; that is the higher the pitch rate, the higher the α_0 of flow separation [85, 88]. This leads to a more energetic LEV, a greater maximum lift and even the emergence of secondary vortical structures [87, 89]. Pitch-ramp experiments have had a somewhat continued interest for other applications such as wind turbine blades and flow control technologies [90].

The resurgence of transient motion studies came primarily from the discovery by Ellington *et al.*, who showed that the secret to insect flight capabilities was through a stable, attached LEV [91].

The LEV remained close to the leading-edge of a hawkmoth wing throughout the stroke, instead of shedding into the wake (it is now known that the stability of the LEV is due to significant three-dimensional effects and the interested reader is referred to [4] for a full discussion). This kick-started a swathe of research dedicated to understanding the physics that govern LEV growth, strength and stability in both two and three-dimensions. A set of canonical transient wing motions were put forward, based on decomposed wing flapping kinematics, in an attempt to standardise the research effort and better isolate the salient LEV mechanisms [4]. Ol *et al.* argue that such motions are psychically richer than their periodic counterparts [92], allowing researchers to more readily separate acceleration effects from the circulatory response [87]. The following sections are arranged to reflect the shift in focus from specific kinematic conditions to the bulk flow field response to an unsteady input.

2.6.1 LEV Formation and Growth

LEV strength is closely linked with the amount of lift an airfoil or flat plate can produce in extreme conditions; during high α_{eff} motions the influence of airfoil geometry becomes small [40, 93]. Pitt Ford and Babinsky [94] showed that the circulation bound to a flat plate during impulsively started towing is small, i.e. the circulation contained within the boundary layer. Instead, the circulation is primarily contained within the LEV and any additional structures that form at the leading-edge; highlighting the importance of characterising LEV behaviour. For extreme α_{eff} motions, Babinsky and Stevens [95] expressed the basic circulatory force production mechanisms as a function of LEV/TEV strength and position, as follows:

$$C_{L_{circ}} = -\frac{2}{U_\infty^2 c}[(u_{LEV} - u_{TEV})\Gamma_{LEV} + (x_{LEV} - x_{TEV})\dot{\Gamma}_{LEV}] \tag{2.5}$$

Equation 2.5 is derived from the vortex dipole concept, which states that a vortex pair of equal and opposite strength vortices creates a net momentum in the flow directly related to their strength and separation distance [95]. The net momentum acts orthogonal to the line connecting the vortices. Equation 2.5 states that lift is produced through both the growth rate of LEV

circulation ($\dot{\Gamma}_{LEV}$) and the relative velocity between the LEV and TEV ($u_{LEV} - u_{TEV}$). They note that whilst this model is highly simplified, it gives a good foundation of unsteady lift production in extreme conditions [95]. An example of these lift production mechanisms during a typical pitching motion can be seen in Figure 2-21; the added-mass effects will be discussed in a separate section.

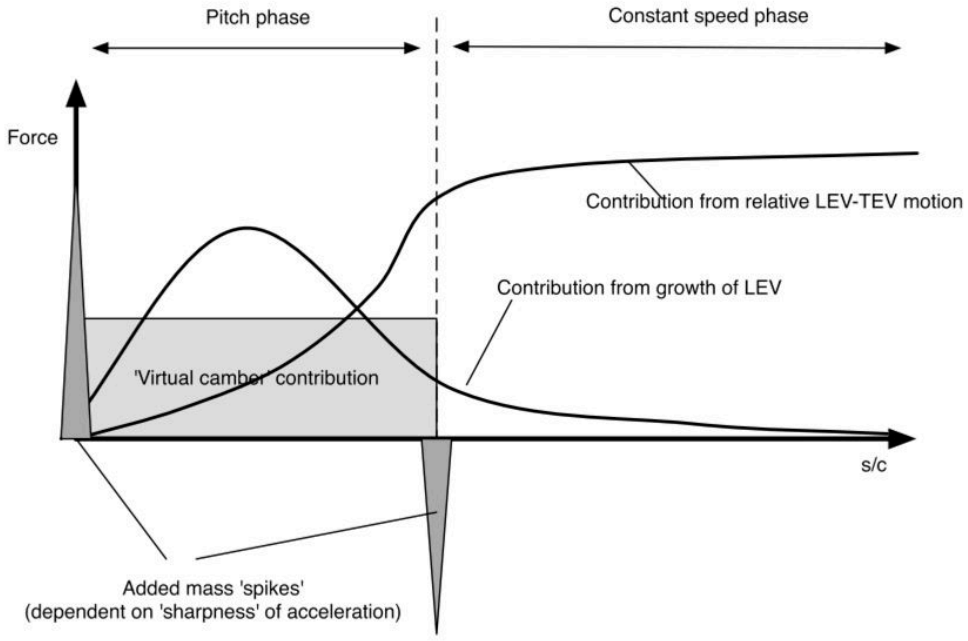

Figure 2-21: Representaion of various force mechanisms for unsteady massively separated flow during pitching motion, taken from [95].

The strength or circulation of the LEV is primarily governed by the convective fluxes entering the vortex as it forms [4], i.e. the amount of vorticity consumed from the feeding shear layer that emanates from the leading-edge. Manar *et al.* [96] showed that vorticity production, and hence LEV circulation, is closely linked to airfoil kinematics. They proposed a new time-scale based on the leading-edge velocity that can be used to normalise LEV circulation measurements. Figure 2-22a displays LEV circulation against time, normalised by the free-stream velocity. When the leading-edge velocity is taken as reference for the time-scale (Figure 2-22b) and the circulation normalisation (Figure 2-22c), excellent collapse can be observed, highlighting a commonality in LEV growth for different motion types (pitch and surge).

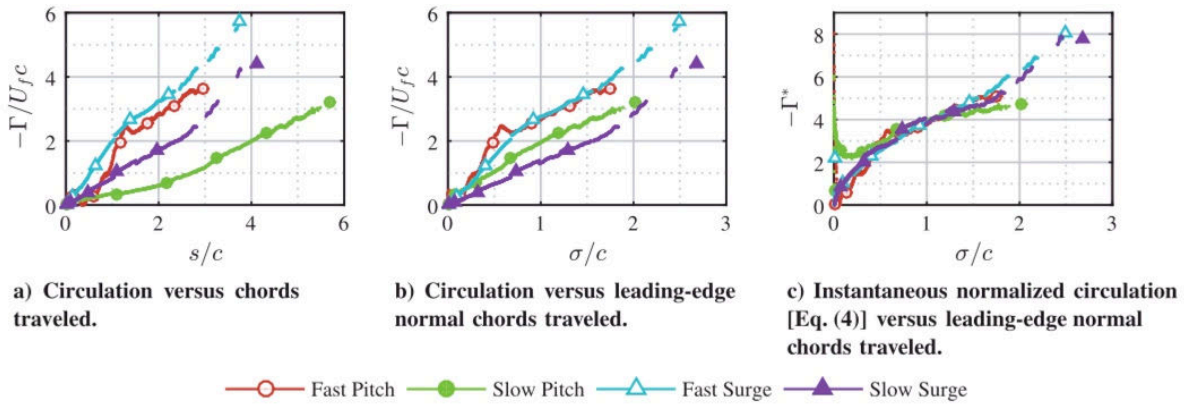

Figure 2-22: LEV circulation on pitching and surging wings, taken from [96].

The lift force was also plotted against the same leading-edge time-scale and a better collapse across the motion types was observed, see Figure 2-23, particularly for the post-motion lift oscillations. This again illustrates the close link of LEV strength and lift production.

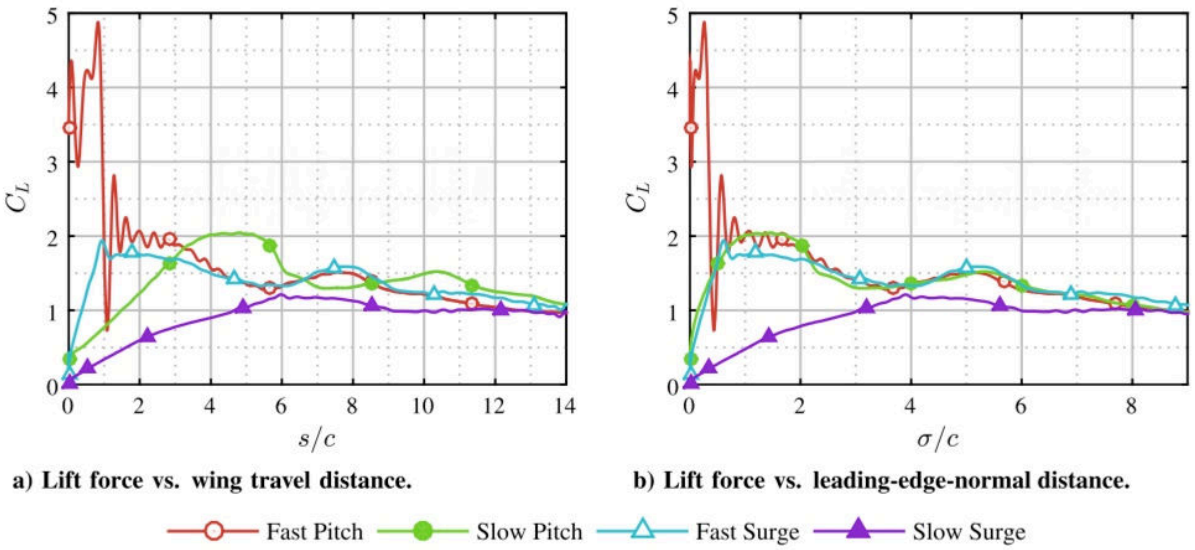

Figure 2-23: Lift of pitching and surging wings plotted on different time-scales, taken from [96].

LEV circulation growth was measured by a joint consortium of researchers in an attempt to elucidate commonality in flat plate lift and LEV responses. Ol and Babinsky [97] present this data, shown in Figure 2-24, and note the striking similarity of LEV circulation histories across various flat plate manoeuvres, geometries and planforms. Two distinct outliers are the "slow" manoeuvres, namely "Surge 6c" and "Pitch 6c" (which occur over 6 chord-lengths of travel).

Eldredge and Jones [4] note the dependency of vorticity generation on acceleration, where slower motions lead to less vorticity production and weaker, more diffuse LEVs. Interestingly, the plot of Wagner's bound circulation function ("Wagner") shows remarkable agreement with the normalised LEV circulations. Using Pitt-Ford and Babinky's observations [94], where the bound circulation can be neglected, Wagner's function can provide a reasonable estimate for the total circulation around a wing i.e. contained within the LEV [97]. A similar observation was made by Perrotta *et al.* [98] who showed attached flow solutions could provide a suitable estimate for circulatory lift during high-amplitude plunging motions, where separation and LEV formation dominate.

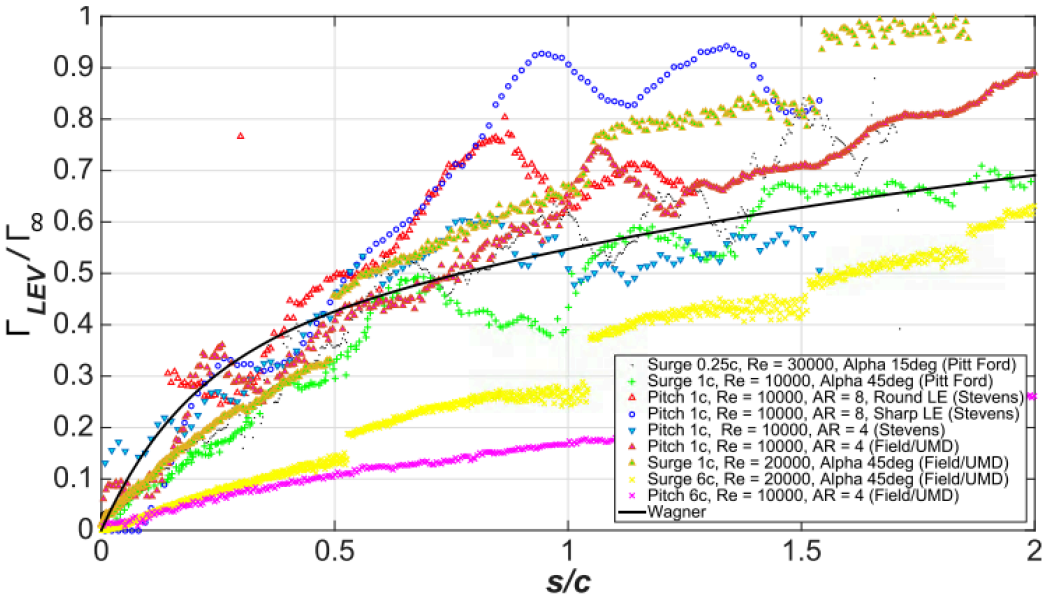

Figure 2-24: Normalised circulation histories of various flat plate geometries and planforms, taken from [97].

As stated in Equation 2.5, the force production is also related to the relative velocities of the LEV and TEV; Babinsky and Stevens [95] estimate these to be approximately 50% and 100% of the free-stream velocity respectively based on representative transient motions. They showed the model in Equation 2.5 is capable of estimating transient lift forces in massively separated flows to a reasonable degree of accuracy - and more importantly, the direct impact of experimental data on the development of reduced-order models.

2.6.2 LEV Shedding

The LEV cannot grow indefinitely. At some point it reaches a maximum size and is shed from the airfoil [4]. Widmann and Rival [99] showed the limiting factor to be the chord length. In their study they tracked topological points in the flow, namely nodes (N), saddles (S) and half-saddles (S'), shown in Figure 2-25. Figure 2-25a illustrates the vortex growth stage; where the LEV is marked with a node and it's boundaries marked by half-saddles. During LEV growth, the feeding shear layer is consumed by the LEV and the downstream half-saddle point moves towards the trailing-edge. Figure 2-25b illustrates the flow topology after the downstream half-saddle moves past the trailing-edge. The half-saddle moves off the surface to form a full saddle point, allowing reversed flow to enter below the LEV, cutting off the feeding shear layer and lifting the LEV away from the surface. The importance of this stage is the dramatic loss in lift that immediately follows [93, 99, 100]. These results have been confirmed in an experimental study by Krishna *et al.* [100], who tracked Lagrangian Coherent Structures to elucidate the topological flow points. It was found that as the half-saddle lifts off the trailing-edge, the reverse flow that enters under the LEV leads to the formation of a secondary, opposite signed vortex that pushes the primary LEV in the chord-normal direction. This mechanism causes the dramatic loss in lift observed, as the LEV is no longer bound the airfoil.

The movement of the half-saddle point has been tracked through surface pressure measurements by Leknys *et al.* [101] during a pitch-ramp motion. They state a reasonable approximation to the half-saddle location occurs where there is a significant pressure gradient at the frontier of the LEV. Through visual inspection of the upper-surface pressure, this approximate method shows validity for half-saddle tracking. Figure 2-26 presents their analysis. The half-saddle location displays a near linear progression across the upper surface in Figure 2-26a, confirmed in the measurements by Krishna *et al.* [100], and a dramatic loss in suction occurs when this reaches the trailing-edge. The diagrams of corresponding flow structure are shown in Figure 2-26b for reference. Alternatively the stagnation streamline [4] or surface velocity [93, 100] can also provide half-saddle location data.

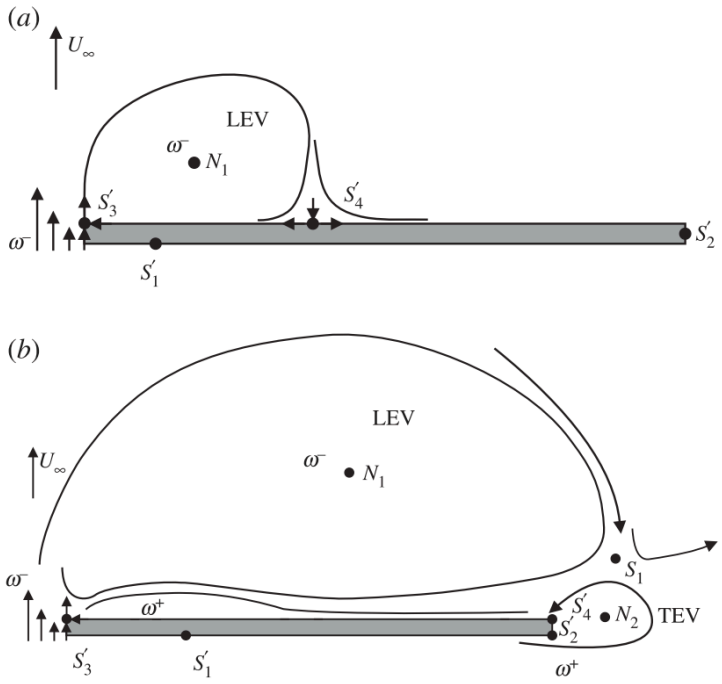

Figure 2-25: Topological flow points during a) LEV growth stage and b) LEV shedding stage, taken from [99].

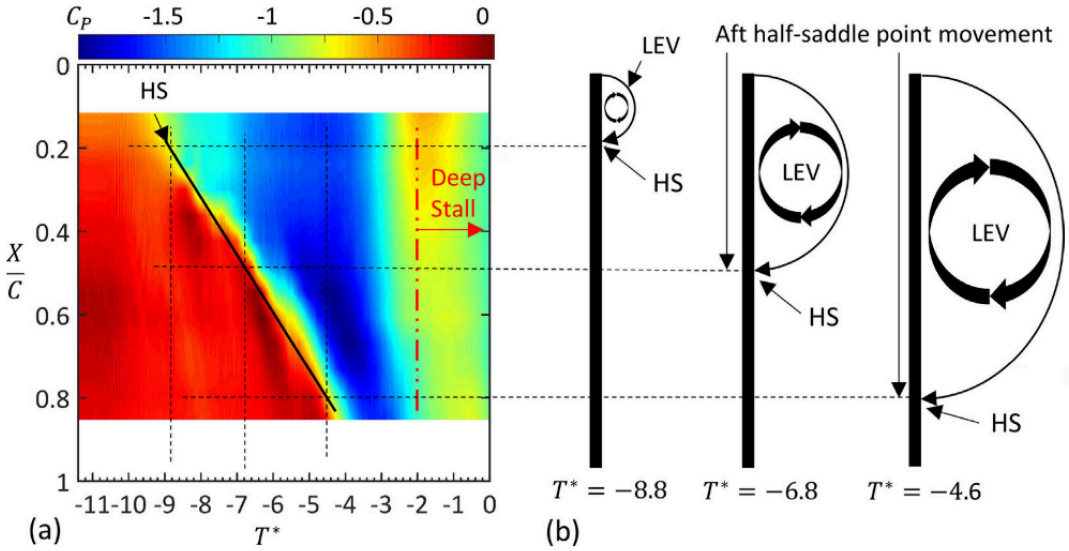

Figure 2-26: Half-saddle tracking from surface pressure, a) half-saddle estimation b) diagrams of corresponding flow topology, taken from [101].

Another mechanism for LEV shedding is through vortex-induced separation, whereby the LEV is prematurely shed across the chord. This can occur when the LEV interacts strongly with the surface flow, leading to the movement of opposite signed vorticity to the leading-edge which intersects the feeding shear layer, cutting off the LEV [47]. Widmann and Rival [99] show that this shedding mechanism is dependent on Reynolds number and will be discussed in section 2.6.4.

2.6.3 Added-Mass Effects

Whilst the strength and dynamics of the LEV largely governs the forces around a wing, the other important lift component is the added-mass force, which can have significant effect for fast motions where large accelerations are incurred [97]. An example of this is shown in Figure 2-23, which highlights the difference between pitch and surge motions. During the acceleration stage (0 to 1 chords of travel), the fast pitch motion reaches a significantly higher C_L and is, in part, due to the large added-mass spikes produced during acceleration and deceleration, as depicted in Figure 2-21. Each type of wing motion produces a different added-mass response, related to the way the airfoil is accelerated in the surrounding fluid.

In an inviscid sense, this added-mass force arises from pressure waves due to the displacement of fluid around a moving body. For example, a plunging airfoil has an added-mass equal to a column of fluid of diameter c (more specifically the projected chord length with respect to the plunging axis, $c \cdot cos\alpha_0$). The added-mass force is then a function of the added-mass and the acceleration profile. Recently, Corkery *et al.* [15] experimentally showed that an accelerating flat plate produces an added-mass vorticity distributed in a thin layer around the plate. Experimental measurements of this region showed excellent agreement with an equivalent vortex sheet representation derived from potential flow theory. A remarkable aspect of the study was that theoretical solution remained valid even in highly separated flows, where large vortical structures reside around the plate. This permits separate treatment of circulatory and added-mass force components. This is a core aspect of the model by Babinsky and Stevens [95], where the added-mass force is linearly superposed onto the circulatory lift response. Experimentally, insight into the weighting of the two lift components can be gained through the total measured lift and the

theoretical added-mass response.

2.6.4 Reynolds Number Effects

There have been a number of studies detailing the minutia of Reynolds number effect, but in general, it has been noted that above a certain threshold, $Re = \mathcal{O}(10^2)$, the effect of Reynolds number has a somewhat benign effect on loads response [4, 96, 97]. Jones and Babinsky [102] studied the effect of Reynolds number on LEV formation around an impulsively started rotating wing. They note that whilst the Reynolds number does not impact the mechanism of lift production, the LEVs at lower Reynolds ($Re = 10K$) numbers tend to grow and shed comparatively quicker than higher Reynolds numbers ($Re = 30, 60K$), which leads to an earlier peak in lift. Insight into this behaviour is given by Widmann *et al.* [99], who studied the impact of Reynolds number on LEV shedding mechanisms. It was found that if the Reynolds number was sufficiently low, the increased viscous interaction between the LEV and boundary layer caused an ejection of opposite signed vorticity that rolls up into a secondary vortex; this is depicted in Figure 2-27. The newly formed secondary vortex intersects the feeding shear layer, causing the LEV to shed before the chord length limit is reached by the downstream half-saddle. Although it appears this would limit the LEV circulation and hence lift magnitude, this is offset by the increased LEV growth rate as found by Jones and Babinsky [102].

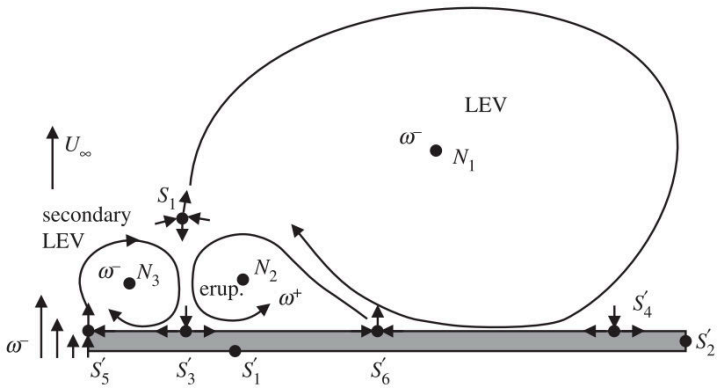

Figure 2-27: Topological flow points during boundary layer eruption mechanism, taken from [99].

Eldredge and Jones [4] put forward a Reynolds number effect based on a leading-edge character-

istic dimension, noting that early LEV growth is not influenced by the chord length limit. This is explored by Rival *et al.* [93] who measured the effect of leading-edge geometries on the LEV detachment process of plunging airfoils. Although the leading-edge geometry had some effect on the lift response, the flow fields were largely similar. A round leading-edge profile exhibited a slight delay in half-saddle detachment, which was linked to LEV growth rate and hence the feeding shear layer characteristics.

2.6.5 Post-stall Vortex Shedding

A great deal of transient motion research has focussed largely on the primary LEV formation and the aerodynamic loads during motion, whilst the loads and flow fields that occur after the motion are somewhat overlooked. Obviously for flight applications this is completely justified, where the critical factor is the primary LEV behaviour, after which the next wing stroke begins. However, for gust load applications the post-motion loads could be critical for control and stability, particularly in the event of multiple gust encounters [103].

In 1988 Lorber and Carta [86] showed that for certain cases, significant lift, drag and moment oscillations could occur after the primary LEV had been shed. They noted similarity to a study by Jumper *et al.* [104] but offered no further insight into the causes. Since then, post-motion oscillations in aerodynamic loads have been well documented to be caused by additional LEVs that form after the primary LEV, not too dissimilar to the secondary LEVs that can form in periodic dynamic stall conditions [47]. This phenomenon is termed *large-scale vortex shedding* and always shows a decay in oscillation amplitude with time. Mulleners *et al.* [103] linked this decay to the location where the LEV/TEV form and interact. Interestingly a remarkably similar post-motion shedding response was obtained for a surging flat plate during two motions; accelerating from rest and accelerating from a steady velocity, i.e. quiescent and fully developed flow conditions. A single exponential fit was shown to describe the temporal decay of lift peaks for the two motions. This has also been shown in a similar study by Henne *et al.* [105]. To highlight the commonality of post-motion vortex shedding, the lift responses of select cases from Rosti *et al.* [106], Mulleners *et al.* [103], Leknys *et al.* [101] and Son *et al.* [107] were extracted

and plotted in Figure 2-28. The responses are presented with the (estimated) static component of lift removed and the non-dimensional time of $\tau = 0$ where significant lift drop off occurs (crudely coinciding with LEV detachment). The oscillations all show strikingly similar levels of decay and oscillation frequency, despite the drastic differences in motion kinematics, airfoil geometry and planform. The lift responses can be seen approaching steady-state in in Figure 2-28 at 14τ. Son *et al.* [107] and Manar *et al.* [96] found that wing aspect ratio can play a significant role in the post-motion shedding, where lower aspect ratios suppress the emergence of additional peaks.

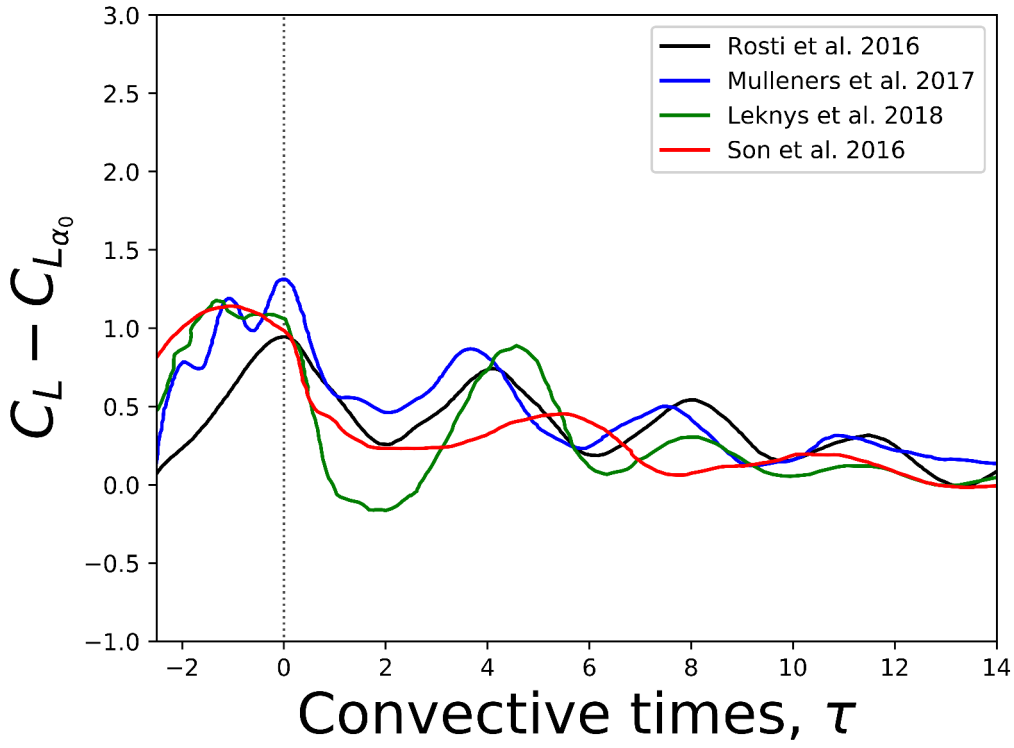

Figure 2-28: Examples of post-motion vortex shedding from literature [101, 103, 106, 107].

2.7 Flow Control Strategies

The control of massively separated flows is put forward as a future issue by Eldredge and Jones [4] in order to better mitigate or enhance LEV influence. There are three main types of flow control devices that can be implemented in steady or unsteady scenarios as documented by Cattafesta III [108]:

- *Fluidic* - These actuators use fluid to influence the flow, through either ejection, ingestion or a combination of both (e.g. Zero-Net Mass-Flux devices).

- *Moving surfaces* - These devices use geometry to influence the flow; such as vortex generators, control surface elements and body motions.

- *Plasma* - These actuators use the effect of discharge-induced electric wind to manipulate the boundary layer [109]. They have gained popularity due to their fast response times and solid-state operation.

There is a vast wealth of research on flow control strategies, however for the sake of brevity the following section will focus specifically on control of massively separated flows, with particular attention to dynamic stall style events. The interested reader is pointed to [108] for a thorough review of flow control technologies.

2.7.1 Passive Control

Passive control refers to a device that influences the flow field using no external energy. Some devices may require an activation energy, e.g. deployable vortex generators, but these are classed as passive if they act passively on the fluid during operation. Such devices have proved attractive due to their simplicity, operation and integration.

Trailing-edge devices are a popular choice for flow control due to their relative simplicity, ease of integration and similarity with existing control surfaces. A primary example of this is the Gurney flap, which modifies the Kutta condition at the trailing-edge to produce a larger suction peak [110]. Zanotti *et al.* [111] tested a deployable Gurney flap in passive operation during deep dynamic stall conditions. No significant benefits were observed in their test case, which highlights the importance of device location, particularly for dynamic stall applications. Choudrhy *et al.* [90] state that for successful disruption and elimination of the LEV, a loads alleviation device needs to be located near the leading-edge of the airfoil. Joo *et al.* [112] combined the Gurney flap concept with a permanent leading-edge droop, as depicted in Figure 2-29. They found that a meaningful reduction in both lift and nose-down pitching moment can be achieved with this

approach.

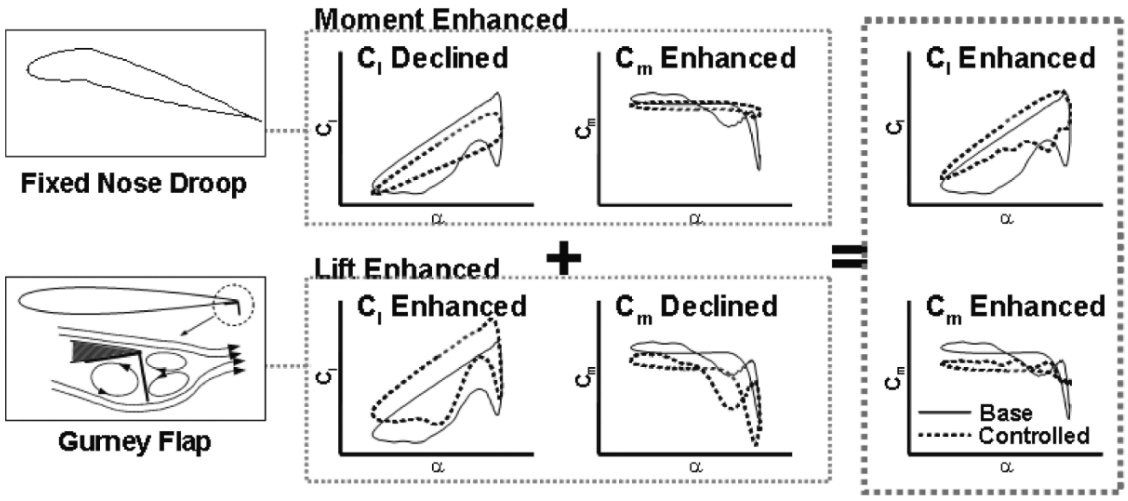

Figure 2-29: Combined benefits of a leading-edge droop and gurney flap configuration, taken from [112].

Gardner *et al.* [113] evaluated the performance of a back flow flap, which consists of a hinged panel that can lift up under low pressure conditions and takes inspiration from the stall control mechanisms on bird wings [114]. They documented a significant disruption of the LEV through reverse flow obstruction over the surface. The efficacy of a leading-edge slat in DSV suppression has been investigated by Carr *et al.* [115]. The slat can delay the onset of separation through reduced loading at the leading-edge and re-energising jet flow through the slot. A critical draw back of this method is the drag penalty incurred. Choudhry *et al.* [90] instigated a number of novel concepts to disrupt the migration of reversed flow towards the leading-edge, a key mechanism in dynamic stall development. Vortex generators were compared against an elevated wire concept at the leading-edge. These devices entrained outer flow through streamwise and spanwise vortices respectively. A second novel concept of an upper surface cavity was tested to act as a reservoir for the reversed flow. Overall, the three devices delayed the onset of dynamic stall and reduced the strength of the DSV, with the elevated wire concept showing the best performance. A similar disturbance generator (DG) concept by Heine *et al.* showed promise in DSV disruption with minimal drag penalties. An array of circular, backwards wedge and forward wedge DG configurations were situated around the stagnation region for moderate angles of attack, which become exposed during dynamic stall excursions. The DGs facilitated

the convection of vorticity from the leading-edge region, resulting in a weaker DSV through the generation of streamwise vortices, see Figure 2-30. The orientation of the streamwise vortices produced by the DGs was found to have a significant impact.

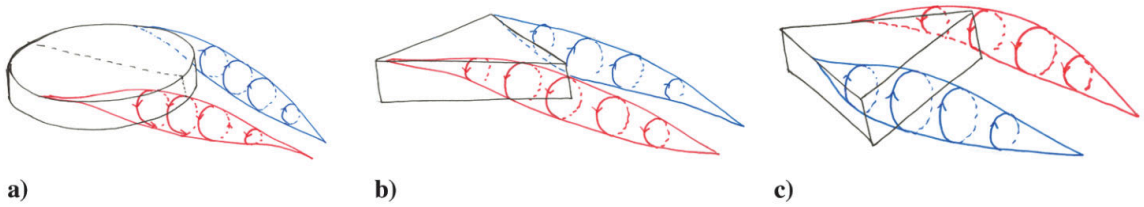

Figure 2-30: Passive disturbance generators, a) circular, b) reverse wedge, c) forward wedge, taken from [116].

Previous examples have focussed on the suppression or disruption of LEVs. In contrast, the influence of passive wing flexibility for lift enhancement has been assessed by Cleaver *et al.* [117] for low aspect ratio plunging wings. Wing flexibility was found to enhance time-averaged lift through a more stable LEV that convects closer to the wing surface, see Figure 2-31. This is made possible through sufficient lag and amplitude increase of the wing tip compared with the root. A detailed review of the role of flexibility on lift enhancement mechanisms is given by Gursul *et al.* [118].

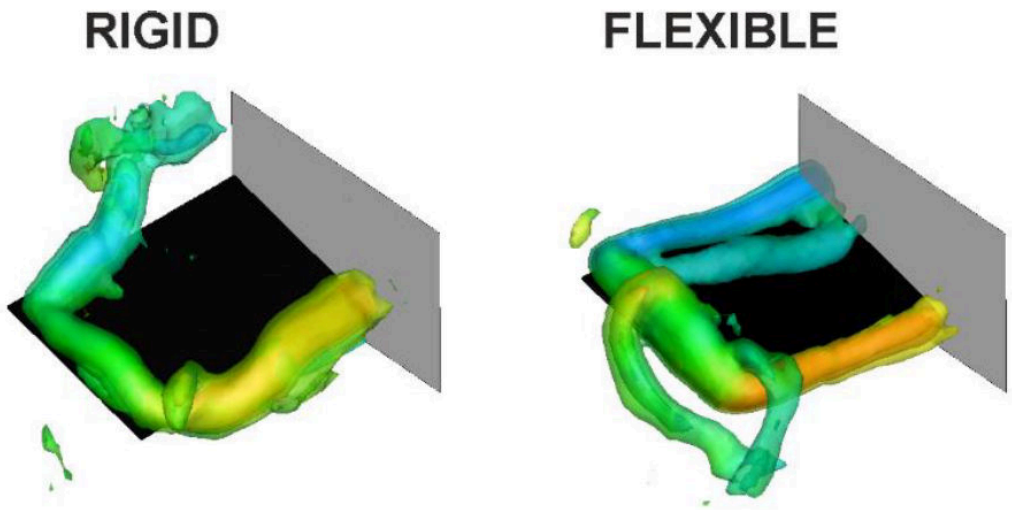

Figure 2-31: Comparison of rigid and passively flexible plunging wings, taken from [117].

2.7.2 Active Control

Active control refers to devices that require external energy to influence the flow. These can have significant performance benefits in terms of the desired control aim, but usually require complex sensing, control and mechanical aspects. In addition, active flow control strategies are prone to instability and often cannot be realistically implemented in their intended application due to a myriad of constraints [90]. Nevertheless the potential benefits of active flow control cannot be ignored and has received significant attention in the past few decades [119].

Trailing-edge flaps have been actively deployed at various forcing combinations in an attempt to reduce the severity of pitching moment stall [120–122]. The mechanism for this was attributed by Green et al. [121] to the suction peak on the lower surface at the hinge location of the trailing-edge flap. Although the strength of the LEV can be marginally reduced by these flaps, Lee & Su [120] documented no significant effect on LEV formation and shedding.

Gardner et al. [113] showed an actively controlled back flow flap can further reduce moment stall. Freymuth *et al.* [123] implemented a rotating leading-edge cylinder to curtail the production of vorticity, see Figure 2-32a, and found dynamic trailing-edge separation could be achieved without DSV formation, see Figure 2-32b. Geissler *et al.* computationally assessed the dynamic leading-edge droop concept during plunging motion. Dynamic stall could be avoided through appropriately phased, small amplitude (10°) droop angles; although the mechanical complexity of such a device in reality was not addressed. The efficacy of deployable vortex generators was assessed by Pape *et al.* [124], who demonstrated a 55% reduction in maximum pitching moment through a 15% duty cycle in order to minimize the drag penalty. They note however the convective time response of the generated vortices, stating that this effect will come into play at higher pitch frequencies.

Blowing from the leading-edge has also been shown to be a successful suppression method. Gardner *et al.* [125] found a reduction in moment stall and peak drag through steady blowing from 10% chord, whilst Müller-Vahl et al. [126] documented a complete elimination of the LEV in deep stall conditions through high momentum blowing. Karim and Acharya [127] sought

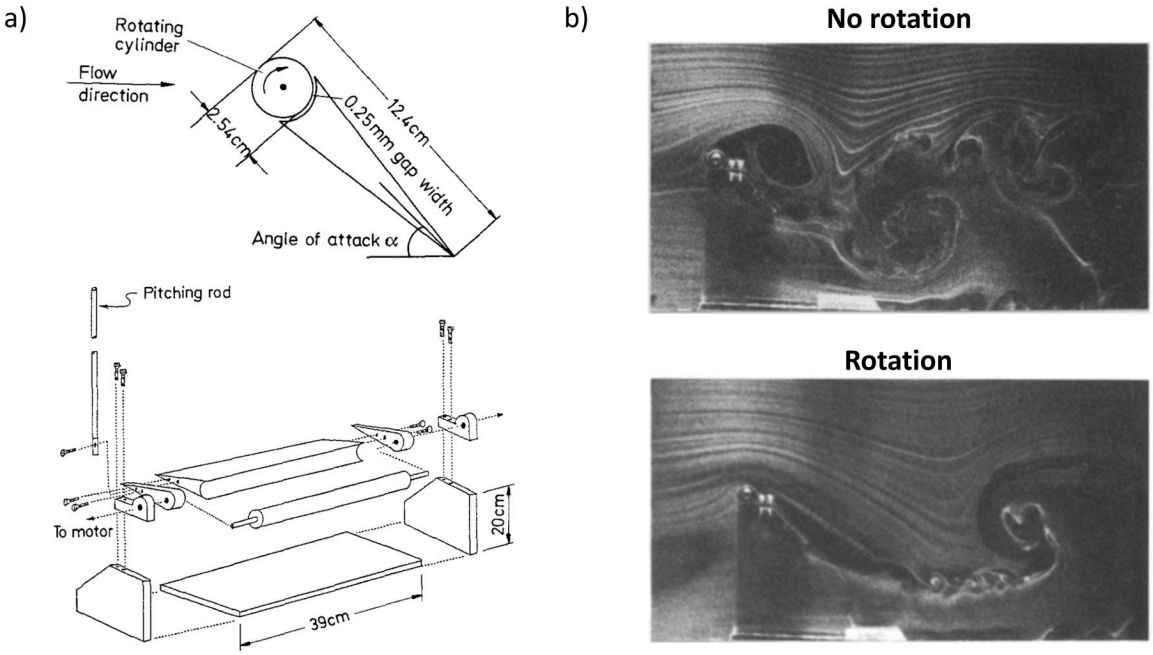

Figure 2-32: a) Diagram of rotating leading-edge cylinder, b) Comparison between off and on condition for rotating cylinder, taken from [123].

to halt reverse flow accumulation through leading-edge suction. This method could eliminate the DSV but the level of suction required was proportional to the pitch rate, Reynolds number, suction size and location. Periodic blowing/suction through Zero-Net Mass-Flux (ZNMF) devices has shown significant benefits in both performance and efficiency over their brute force, steady counterparts, and aim to exploit natural flow instabilities. An example of a ZNMF device is shown in Figure 2-33. These are especially desirable as they eliminate the need for pumps and plumbing to supply flow. Such a device was investigated by Greenblatt and Wygnanski [128]. Oscillatory excitation was found to be superior to steady blowing in light and deep dynamic stall conditions and was dependent on excitation frequency and amplitude. Similar conclusions have been found by Ekaterinaris [129], although they concluded the optimal chord-wise device location was at $x/c = 0.7$ rather than the leading-edge region. Corke *et al.* [130] used plasma actuator with a downstream pressure sensor as feedback control to actively detect and mitigate boundary layer separation. This method proved effective in suppressing the DSV and is an example of a realisable closed-loop control method. They note an optimal excitation frequency of $St_c = 1$, which lines up with the optimal frequencies reported for ZNMF devices [128, 129].

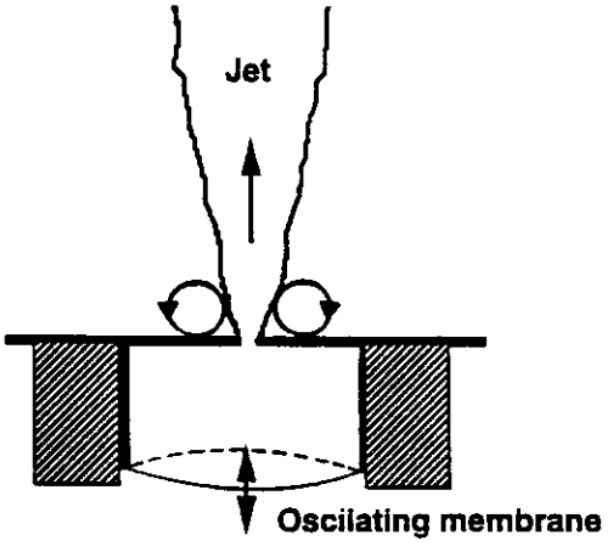

Figure 2-33: a) Diagram of Zero-Net Mass Flux device (synthetic jet), taken from [131].

2.8 Literature Review Conclusions

A significant number of studies have been conducted on the wake structures and LEV formation of periodically pitching/plunging airfoils. These cover a wide range of St_A and k and the aerodynamic loads show a great deal of dependency on both. The presence of an LEV is the primary flow feature that creates an increase in lift, nose-down pitching moment and airload hysteresis. Recently, researchers have looked to non-repeating, transient motions to better understand LEV behaviour, through a more distinct separation of the acceleration and circulatory components. Although significant progress has been made documenting and characterizing LEV growth, shedding and induced loads, there are still a number of novel avenues to explore.

- A commonality of vortex shedding characteristics has been shown across different transient motions and airfoil geometries, a detailed characterisation of which is still lacking. Past studies have been rather limited in scope and present only a handful of cases. A more in depth investigation of this behaviour, and how this might link to periodic motions, would be highly beneficial to the field.

- Ultimately the canonical airfoil motions will have to be combined. This has been outlined as a future issue by Eldredge and Jones [4], as the bulk flow field response to such conditions

is currently unknown. To the authors knowledge, multiple transient motions in quick succession have not been tested for massively separated, vortex dominated flows.

- A general Reynolds number insensitivity has been shown for Reynolds numbers from $\mathcal{O}(10^2)$ to $\mathcal{O}(10^4)$ [4] during transient motions. Further development of experimental rig capabilities is needed to push this boundary to $\mathcal{O}(10^5)$, particularly for plunging motion.

- Flow control strategies have taken on many forms in both passive and active forms to suppress LEV formation. Choudhry *et al.* note that for the successful disruption and elimination of dynamic stall style events, the loads alleviation device needs to be placed in the leading-edge region and deployed before LEV formation takes place. Passive devices still show promise in LEV suppression and continue to attract attention due to their simplicity and ease of integration. Active devices can show superior performance, but are often marred by complex mechanisms and control strategies. The majority of the literature aim to suppress dynamic stall through maintenance of attached flow, but the avenue of prematurely detaching the flow remains relatively unexplored. Simple spoiler devices have been tested by Heathcote *et al.* [110, 132] and Al-Battal *et al.* [133, 134] and show promising lift reduction capabilities for stationary wings. The performance of such a device is yet to be tested during extreme unsteady conditions.

Chapter 3

Experimental Methods

3.1 Introduction

Plunging airfoil experiments were conducted in the University of Bath's water tunnel and large wind tunnel facilities. These consisted of different plunging motions, methods of actuation, sensor measurements and post-processing procedures and as a result, the water tunnel and wind tunnel experiments will be described separately.

3.2 Water Tunnel

Experiments conducted in the water tunnel are presented in all the results chapters, namely 4, 5, 6 and 7.

3.2.1 Experimental Set-up

The water tunnel experiments were performed in the close-loop water tunnel facility at The University of Bath. This facility can provide a free-stream velocity ranging from 0 to $0.5m/s$ to a working section of 381 x 508 x $1530mm$ with a free-stream turbulence intensity less than 0.5% [135]. Figure 3-1 gives a basic overview of the experimental set-up; the specifics and uncertainties of which will be discussed later in this section. The plunging rig is situated on top of the water

tunnel, see Figure 3-1a, which positions a wing vertically in the test section. To enforce quasi-2D conditions a pair of splitter plates were used at the wing root and tip, see Figure 3-1b, which prevent the formation of tip vortices and suppresses the span-wise component of flow. To cover the hole required in the root stationary plate for wing motion, a third moving splitter plate was fixed to the wing root that sits $0.02c$ under the stationary root plate in order to minimize free-surface effects. For the tip splitter plate there is also a clearance of $0.02c$. All wings tested consist of chord length $62.71mm$ and aspect ratio of 5. A rotation stage is situated at the top of wing assembly and can set the geometric angle of attack with an accuracy of $\pm 0.2^o$. This is then connected to a moving carriage through the torque sensor. The moving carriage sits on two $13mm$ diameter shafts that each glide through a pair of pressurised air bushings, providing virtually frictionless motion. This constrains the carriage motion to a single axis, which is perpendicular to the incoming free stream flow, Figure 3-1a. A tension/compression load cell acts as a link between the moving carriage and linear actuator. Since all bending moment and torque loads are absorbed by the air bushings, the load cell can be fairly sensitive to allow greater precision of cross-flow force measurement. Plunging motion is supplied by a Zaber LSQ150B-T3 translation stage powered by a stepper motion with an Zaber X-MCB1 controller.

The water temperature was measured before each experiment to calculate the water density, ρ, and viscosity, μ, in order to provide the free-stream velocity for the desired Reynolds number. Temperature fluctuations were at most $\pm 0.5^\circ$ during tests. All experiments were conducted at a free-stream Reynolds number of $20,000$, with an uncertainty of ± 500.

3.2.2 Airfoil Geometry

For Chapters 4, 5 and 6 the NACA 0012 airfoil profile was used, see Figure 3-2a. This was manufactured using selective laser sintering, sanded smooth and painted matt-black to reduce reflectivity. To provide a high spanwise stiffness, a 25 by $5mm$ carbon fibre insert was slotted along the span at $x/c = 0.25$. In Chapter 7 the effect of placing a mini-tab (or flow fence) on the airfoil's upper surface was investigated, see Figure 3-2b. To produce this geometry, a new wing was printed with a small slot of $1.75mm$ at the mini-tab location to accommodate the mini-tab

geometry. This mini-tab was made from a $1.75mm$ thick carbon fibre sheet that was machined to size and held in position through a friction fit with the wing slot. A single mini-tab height, thickness and position was considered for the experiment, the values of which are shown in Table 3.1. In Chapter 4 an additional flat plate geometry was used, see Figure 3-2c. This consisted of a plate of $2.5mm$ thick carbon fibre machined to size. To ensure flow separation occurred at a fixed point, the edges were machined with a chamfer of length $2.5mm$. Although this produces a small asymmetry in the profile, the effect should be minimal under extreme unsteady conditions.

Table 3.1: Airfoil geometry parameters and associated uncertainties.

Parameter	**Value Considered**	**Estimated Uncertainty**
Airfoil chord length (c), mm	62.71	$\pm 0.01c$
Mini-tab position (x/c)	0.08	± 0.005
Mini-tab height (h/c)	0.04	± 0.005
Mini-tab thickness (x/c)	0.028	± 0.0015
Flat plate chord length (c)	62.71	± 0.001
Flat plate thickness (t/c)	0.04	$\pm$ 0.0015

3.2.3 Airfoil Motions

A variety of plunging motion profiles and test parameters were used for the water tunnel experiments; the following will detail their definition. Figure 3-3a presents a schematic for the NACA 0012 airfoil plunging normal to the free-stream velocity vector, U_∞. Any time-varying plunging motion will induce a vertical component of velocity, $V_{pl}(t)$, with respect to the laboratory frame of reference (y direction). The resultant velocity vector will act at an angle to the x-axis, denoted α_{pl}. The total effective angle of attack, α_{eff}, is then defined as the sum of the induced angle of attack due to plunging motion, α_{pl}, and the geometric angle of attack, α_0.

Figure 3-3b presents the parameters and definition of what is referred to as *transient motion* throughout this thesis and pertains to Chapters 4, 5, and 6. This particular profile was chosen as it is a canonical transient motion profile put forward by Ol *et al.* [92]. The induced angle of attack, α_{pl}, is increased linearly for the duration ΔT_p, held constant at a maximum, $\alpha_{pl,max}$, for the interval ΔT_h and linearly returned to zero for the duration ΔT_p. The motion period $T = 2\Delta T_p + \Delta T_h$ can be varied by altering ΔT_p (as per Ol *et al.* [92] ΔT_h is held constant at 0.05τ) and the amplitude of the motion, $\alpha_{pl,max}$, is considered as the second variable. For every case, motion cessation is defined as $\tau = 0$ and the airfoil is held static for at least 30τ to allow the flow to achieve steady-state conditions. The airfoil is then returned to its initial position by an equal and opposite transient motion, inducing a negative α_{pl}. Once again the airfoil is held static for at least 30τ.

Figure 3-3c details the parameters associated with periodic sinusoidal motion, pertaining to Chapters 5 and 7. The airfoil plunge position, $h(t)$, follows the sinusoidal function:

$$h(t) = \frac{A}{2} cos(2\pi f t) \tag{3.1}$$

with peak-to-peak amplitude, A, and frequency, f. The amplitudes are expressed in their non-dimensional form as A/c, where c is the chord length. Likewise, the frequencies are also expressed in a non-dimensional form as the reduced frequency, $k = \pi f c/U_\infty$. In addition, Chapter 5 considers multiple transient motions as shown in Figure 3-4. This is termed *compound transient motion*. A single transient motion is shown for reference in Figure 3-4a and is equivalent to Figure 3-3b. Where compound transient motions are considered the individual motions are separated by a convective time delay $\Delta\tau$, see Figure 3-4b. Figure 3-4c illustrates the induced angle of attack change for a single cycle sinusoid. This is defined by the parameters in Equation 3.1 and begins at $\tau = 0$. Finally, impulsively started sinusoidal motion is shown in Figure 3-4d and once again is defined to start at $\tau = 0$.

In order to assess the accuracy of achieving the various plunging motions, the position of the

rig was tracked using a Reinishaw RELM20 high accuracy linear encoder. For transient motion, this required custom software demands that were defined through acceleration inputs which were internally controlled by the X-MCB1 controller. Figure 3-5a presents the position accuracy of a typical transient motion and shows reasonable agreement between the demand and actual position with a typical maximum error of 5% of the position amplitude. As the motion is acceleration controlled, relatively large errors in position are expected. The critical factor is the induced angle of attack change, i.e. the velocity profile of the motion. The differentiated position signal is presented in Figure 3-5b and shows the desired $\alpha_{pl,max}$ can be achieved within $0.03\alpha_{pl,max}$. Additionally there is an error in the motion time which is estimated to be $< \pm 0.1\tau$. For sinusoidal motion the X-MCB1 controller has an in-built harmonic function generator and control strategy which is capable of much higher precision. Figure 3-5c and Figure 3-5d shows excellent agreement in position and velocity demands with an estimated error of less than 1% of the amplitude.

Table 3.2 presents the test matrix parameters for transient motion cases and their associated uncertainties. The uncertainty for the geometric angle of attack takes into account the rotation stage accuracy and the error associated with aligning the rig with the free-stream flow. The uncertainties are estimated using the methods of Moffat [136]. Table 3.3 and Table 3.4 present the same for compound transient motion and sinusoidal motion case respectively.

Table 3.2: Parameters for transient motion and their associated uncertainties.

Parameter	**Range Considered**	**Estimated Uncertainty**
Geometric angle of attack (α_0), $^\circ$	0 to 35	$\pm$ 0.28
Amplitude of motion ($\alpha_{pl,max}$), $^\circ$	-30 to $+30$	$\pm$ $0.03\alpha_{pl,max}$
Motion period (T), τ	1.67 to 20.0	$\pm$ 0.1

Table 3.3: Parameters for multiple transient motions and their associated uncertainties.

Parameter	Range Considered	Estimated Uncertainty
Geometric angle of attack, (α_0), $^\circ$	0, 5, 15, 25°	± 0.28
Amplitude of motion ($\alpha_{pl,max}$), $^\circ$	5 to 25	± 0.03$\alpha_{pl,max}$
Motion period (T), τ	1.67 to 2.86	± 0.10
Convective time delay ($d\tau$), τ	0.0 to 6.6τ	± 0.10

Table 3.4: Parameters for sinusoidal motions and their associated uncertainties.

Parameter	Range Considered	Estimated Uncertainty
Geometric angle of attack (α_0), $^\circ$	0 to 15	± 0.28
Amplitude of motion (A/c)	0.05 to 0.50	± 0.01
Motion frequency (k)	0.05 to 0.30	± 0.001

3.2.4 Loads Measurements

Static Loads

A Futek S-beam tension/compression load cell (FSH00103) was used to measure force in the plunging axis only, i.e. the lift component. For pitching moment measurements, a Futek reaction torque sensor (FSH03990) was aligned with the wings quarter-chord axis. To determine the conversion constant between voltage and load, a 5 point calibration was conducted for both sensors using weights of known values. This calibration was repeated three times yielding negligible difference in conversion constant. An example calibration of the lift sensor can be seen in Figure 3-6. Drift was measured throughout the rig commissioning stage and was determined to

be negligible. All static measurements were acquired at 1 kHz for 40 seconds and averaged to yield a single value. The loads were non-dimensionalised through the following:

$$C_L = \frac{\bar{L}}{0.5\rho b c U_\infty^2} \tag{3.2}$$

$$C_M = \frac{\bar{M}}{0.5\rho b c^2 U_\infty^2} \tag{3.3}$$

where ρ is the fluid density and b is the wing span. The uncertainty associated with these coefficients were calculated based on the methods of Moffat [136] and presented in Table 3.5. This process takes a systematic approach to break down quantities of interest, namely Equation 3.2 and 3.3, into it's constituent components, taking account all quantifiable sources of error for each variable. For more information see Appendix B.

Table 3.5: Static load uncertainties.

Parameter	**Estimated Uncertainty**
C_L	± 0.04
C_M	± 0.005

Figure 3-7 presents the static measurements for the lift and quarter-chord pitching moment coefficient from -20 to $+20°$. The static lift coefficient shows excellent agreement with measurements previously conducted at the University of Bath by Chiereghin *et al.* [70], using the current lift measurement system, and Cleaver *et al.* [137], who measured lift via a binocular strain gauge force balance. A significant degree of non-linearity can be seen in the lift curve slope. A plateau is observed at low angles of attack, 0 to $+2°$, before increasing significantly in gradient from 2 to 4° and is in line with previous low Reynolds number studies [138, 139], see Figure 3a. Kim

et al. [138] attributed this region of non-linearity to laminar separation of the boundary layer from 0 to 2° followed by an abrupt reattachment at 3°, corresponding to the significant increase in lift curve slope. The lift curve then shows a decreasing gradient up to 9° before exhibiting an abrupt stall. Wang *et al.* [139] showed the formation of a laminar separation bubble in this region which introduces non-linearity. Good agreement can be observed between the measured lift and literature [114, 138, 139] for low angles of attack, however the stall region shows significant discrepancies. The static lift curve at low Reynolds numbers, $\mathcal{O}(10^4)$, is highly sensitive to both turbulence intensity [139] and Reynolds number [114, 139]. In Figure 3-7b the static pitching moment coefficient measurements are compared with Ohtake *et al.* [140] and show good agreement for a similar Reynolds number. It is unclear as to the cause of the undulations seen in Figure 3-7b, however they are most likely related to the laminar boundary layer behaviour at these low Reynolds numbers.

Dynamic Loads

With the experimental set-up described in 3.2.1, the raw load and torque signals will consist of multiple components, according to:

$$F_{total} = F_{aero} + F_{inertial} + F_{wires} \tag{3.4}$$

which states that for the lift sensor the total force (F_{total}) is a combination of the aerodynamic (F_{aero}), inertial ($F_{inertial}$) and wire force (F_{wires}) contribution. The inertial component is due to the moving mass connected to the end of the load cell; the force of which will scale with acceleration. In order to quantify the inertial component, a StrainSense 4807A accelerometer was mounted to the moving carriage. The acceleration signal was then multiplied by the moving mass and subtracted from the raw load cell signal. The moving mass was determined by applying a sinusoidal motion to the rig in a fully drained water tunnel and dividing the first harmonic of the load cell signal by the first harmonic of the accelerometer signal. The inertial force contribution varies from around 5 to 85% of the total force signal depending on the acceleration. The wire

force component refers to to the elastic stiffness of the wires attached to the sensors on the moving carriage. As the wires are connected to the carriage with an appropriate level of slack to accommodate motion, the force they exert on the carriage changes with displacement. This force was quantified by performing a series of static force measurements in a fully drained water tunnel at incremental displacements. The data was interpolated with a 4^{th} order polynomial fit and used as a quasi-static correction based on carriage displacement. An example of this is presented in Figure 3-8a, which shows a typical example of the force magnitude that can be exerted by the wires. Figure 3-8b plots the comparison of an uncorrected and corrected lift time history. In terms of the torque signal, the total torque is defined as:

$$T_{total} = T_{aero} + T_{inertial} \tag{3.5}$$

where the total torque (T_{total}) is simply the sum of the aerodynamic (T_{aero}) and inertial ($T_{inertial}$) components. No wire force is exerted on the torque sensor. The moving mass associated with the torque was determined through the same method as the load sensor. All dynamic loads were logged at a rate of 2000 samples per motion period.

Figure 3-9a presents the lift and pitching moment for a typical transient motion case with the non-aerodynamic components removed as per Equations 3.4 and 3.5. The raw response in pink displays the raw lift and pitching moment overlay of 30 motion repeats. The ensemble average of this signal is shown in red. Significant undulations can be seen between $\tau = -2$ and 0 and was identified as wing vibration. A series of tap tests were performed to determine the dominant wing ($8.1Hz$) and rig vibration frequencies (32, $40Hz$) which were used as input frequencies for three 3^{rd} order Butterworth Bandstop filters with boundaries of $\pm 2Hz$ around the input vibration frequencies. A moving average was then applied over the filtered signal at 50Hz to remove the remaining high frequency noise, the result of which is shown in blue.

Figure 3-9b presents the overlay of the 30 repeats for the final filtered signal and demonstrates excellent repeatability of the force tests. Greater variation can be seen between $\tau = 0$ and 8

which, as will be shown later, is associated with large-scale vortex shedding phenomenon.

The typical uncertainty bounds of the lift and pitching moment are presented in Figure 3-9c around the ensemble-average, filtered signal. These were quantified using the methods of Moffat [136] where appropriate, full details of which can be found in Appendix B. Figure 3-9d plots the uncertainty bounds independently. The static uncertainties for both sensors are reflected at $\tau < -2.2$, where the wing is held static, and so the uncertainty depends solely on the aerodynamic component in Equations 3.4 and 3.5. The uncertainty increases considerably during the motion period, $\tau = -2.2$ to 0.0, due to the errors in the additional terms present in Equations 3.4 and 3.5. Table 3.6 presents the typical average error for dynamic lift and pitching moment signals.

Table 3.6: Dynamic load uncertainties.

Parameter	**Estimated Uncertainty**
C_L	± 0.15
C_M	± 0.015

3.2.5 Particle Image Velocimetry (PIV) Measurements

Particle Image Velocimetry (PIV) measurements are used throughout this thesis to elucidate the flow field mechanisms responsible for artefacts in the aerodynamic loads. PIV is a technique whereby the flow of interest is seeded with particles and illuminated with a laser sheet. Cameras capture two frames of the illuminated flow in rapid succession (in the order of micro- to milliseconds) and use cross-correlation to determine the motion of the particles, and therefore the flow velocities, in a spatially discretised domain. This results in a 2D grid of velocity vectors over the region of interest. The PIV presented in this thesis is used in a qualitative sense only, however it is still necessary to discuss and, where possible, quantify the errors associated with PIV measurements.

The flow was seeded with 8 to 12μm hollow glass spheres. According to Prasad [141] a simple measure to determine seeding suitability is through the settling velocity based on the Stokes drag:

$$U_s = \frac{g d_p^2 (\rho_p - \rho_f)}{18\mu} \tag{3.6}$$

where g is the gravitational constant, d_p is the particle diameter, ρ_p is the particle density, μ and the ρ_f are the fluid viscosity and density respectively. The estimated settling velocity based on the particle properties is around $6^*10^{-6} m/s$; negligible compared with a typical free-stream velocity of 0.3 m/s.

Measurements were taken at the mid-span plane and focussed on the upper surface of the airfoil; an example of which is shown in Figure 3-10a. The hollow glass spheres were illuminated with a New Wave Solo Nd:YAG 50mJ laser and captured with either a 4 mega-pixel or 8 mega-pixel charged-coupled-device camera. The laser sheet had a thickness of approximately 1mm and was levelled using a spirit gauge to within 0.5°. The image pairs were processed with INSIGHT 4G yielding a resolution from 0.010c to 0.015c depending on the set-up. Post-processing was then applied to replace erroneous vectors with the median of it's neighbouring vectors.

PIV Uncertainty

PIV uncertainty is an accumulation of individual system errors. Calibration, levelling, systems and processing choices all contribute to the overall uncertainty of a velocity vector measurement. A way to estimate this is through the method of Charonko & Vlachos [142], who state that the uncertainty is closely linked with the quality of the image. Errors can be quantified through the cross-correlation peak ratio between the primary and secondary correlation peaks. Figure 3-10c presents the expanded uncertainty (95% confidence level) for the ensemble average of 30 and 100 image pairs. This analysis was conducted in Insight 4G using their inbuilt, validated algorithm [143] and the average error was calculated based on the method of Moffat [136]. Uncertainties up to 1.4% of the free-stream velocity are present in both images, however Figure 3-10d reveals

the vast majority to be $< 0.5\%$. The calibration procedure will introduce a systematic error on the magnitude of the velocity vectors. This was estimated to be small ($< 0.5\%$)

3.3 Wind Tunnel

3.3.1 Experimental Set-Up

The wind tunnel experiments required the full design, manufacture and commissioning of a plunging rig using a similar design to the water tunnel rig described in section 3.2.1 but at a much larger scale. Figure 3-11a shows the basic design concept for the wind tunnel plunging rig. A moving carriage sits on two $40mm$ diameter shafts that each glide through a pair of air bushings that absorb any bending moment and torque loads. The wing mounts vertically to the moving carriage and consists of a NACA 0012 airfoil of chord length $0.23m$ and aspect ratio 5. A root splitter plate connects separately to the moving carriage and forms a moving ceiling element when mounted in the wind tunnel. This can be seen in Figure 3-11b, where the plunging rig is mounted above the wind tunnel test section. The root splitter plate sits above the wind tunnel ceiling with a gap of $0.04c$. The same gap is maintained at the tip splitter plate which enforces quasi-2D conditions. To provide linear motion, a bespoke MOOG, equal-sided hydraulic actuator was mounted above the test section and connected to the rig using a pin-rod linkage arm. The actuator is driven by a MOOG G761 servo-valve and supplied with a variable displacement hydraulic pump built by Universal Hydraulics Ltd. This system can provide up to $3.5kN$ of dynamic force at a maximum measured linear speed of $1.65m/s$ for a stroke of $500mm$. Figure 3-12 presents the tunnel view of the fully assembled rig. The moving ceiling panel can be seen which allows up to $\pm$ $230mm$ of motion from the central position. In order to allow optical access for the PIV cameras, a window was incorporated into the tip splitter plate.

Rig control was implemented through a National Instruments CompactRIO controller with custom software using the Field Programmable Gate Array (FPGA) functionality. This permitted loop rates up to $12.5kHz$ for the particular software version. A Proportional-Integral (PI) control block, based on actuator position feedback from a Linear Variable Differential Transformer (LVDT), ran at a rate of 1000 times per motion period during wing motion, and $2kHz$ when

the wing is held static. Figure 3-13a presents the demand and actual position for a typical transient motion request (defined in 3-3b). Despite the distinct lag, the actuator position follows the demand with reasonable accuracy. A slight asymmetry is present towards the end of the motion and this is an artefact of using PI control with position feedback. The accuracy of the velocity demand is shown in Figure 3-13b and displays reasonable agreement with the shape of the demand. Note, the noise in the velocity profile is an artefact of differentiating the position signal and is not real. Table 3.7 presents the test conditions for transient motions in the wind tunnel and their associated uncertainties.

Table 3.7: Parameters for transient motion and their associated uncertainties.

Parameter	**Range Considered**	**Estimated Uncertainty**
Reynold number	100, 150, 200K	$\pm$ 1786
Geometric angle of attack (α_0), $^\circ$	0 to 30	$\pm$ 0.5
Amplitude of motion ($\alpha_{pl,max}$), $^\circ$	-10 to $+10$	$\pm$ 0.08$\alpha_{pl,max}$
Motion period (T), τ	5.0	$\pm$ 0.4

Along with the position signal, embedded wing root and wing tip accelerometers were also logged to measure wing deflection. The α_{pl} profile is similar when taken from the acceleration signals, however this is not presented as the signals are marred by cumulative error through integration. Aerodynamic data was acquired using an array of pressure transducers, the details of which are discussed in the next section.

The turbulence intensity of the wind tunnel at various tunnel speeds has previously been measured by Heathcote [144], the results of which are presented in Figure 3-14. The turbulence intensity is 1.5, 1.1 and 0.9% for a Reynolds number of 100, 150 and 200K respectively. These values are relatively high due the wind tunnel design velocity of $>20\ m/s$; however the maximum

linear speed of the actuator restricted the wind tunnel speed with regards to the desired $\alpha_{pl,max}$. Turbulence intensity will have an effect on the dynamic stall characteristics [145], however this is expected to be secondary to geometric and motion kinematics parameters.

3.3.2 Wing Design

Due to the large wing aspect ratio required to match the water tunnel conditions, the wing needed to be built with stiffness in mind; however a number of conflicting factors existed. Firstly the wing needs to support not only a large aerodynamic force, but also the inertial loading when subjected to plunging motion. Secondly, the wing needed to remain hollow for the internal mounting of the unsteady pressure transducer array. A trade off study was conducted to assess the wing tip deflection for a given wing skin thickness when subject to an extreme acceleration of $13g$. The NACA 0012 profile was divided into discrete rectangular strips and numerically integrated to find the second moment of area and mass per unit span for a each skin thickness (assuming an isotropic material based on a typical carbon fibre layup). The tip deflection was calculated using the one-dimensional cantilever beam equation that is subject to the inertial and assumed aerodynamic loading. Figure 3-15a presents the results of this analysis for increasing values of wing lift coefficient from 0 to 5. Although highly simplified, it gives useful insight into a usable skin thickness. When $C_L = 0$ the wing is only subject to inertial loading; the greater the skin thickness, the greater the inertial load and wing deflection. When $C_L > 0$ the results show a changing minima depending on aerodynamic loading. A skin thickness of $2mm$ was chosen from this analysis which is the middle ground between $C_L = 1$ and 3.

The final wing section design can be seen in Figure 3-15b and includes necessary modifications for accommodating the unsteady pressure sensors. Firstly to provide access to the sensors, the bottom skin was made detachable. This required the insertion of two spar structures that provide a base for tapped aluminium inserts to allow the bottom skin to be bolted in place. The spar structures and wing skin define a box region that is large enough for the pressure transducer array. Additional skin thickness was added in this region as it is further from the bending axis, an aspect the previous analysis did not take into account.

Unsteady Pressure Measurement System

The force, moment and surface pressure was measured with an unsteady pressure measurements system. A requirement for unsteady pressure measurements is that the transducers are as close to the point of measurement as possible so as to minimise attenuation. In ideal circumstances the two points would coincide; however in practice this is often impossible due to geometrical constraints. The box cavity in the wing permitted the use of individual PCB mounted pressure transducers. However this still imposed a significant constraint on the proximity of the sensors to the measurement points.

Figure 3-16a shows a plan-view schematic of the pressure measurement system layout inside the wing box cavity. The system was designed in-house and made on a principle of modularity. A single system branch consists of four pressure transducers mounted to a PCB board (shown in green) which can be situated near the point of measurement (indicated by the yellow strip); each PCB board then connects with an Arduino mini that logs the data to an internal memory chip. The pressure sensors used were the Honeywell TruStability HSC series with an I^2C digital interface and a range of $\pm$ 2.5kPa. Keeping the system digital reduced the influence of electrical noise leading to higher quality pressure signals. Each system branch sits in idle and waits for a command signal to request a measurement from each sensor. This command signal was provided by the CompactRIO, allowing syncing with the position and acceleration measurements. A small latency of 50ns per transducer is present between the measurement request and storage, however this is orders of magnitude lower than the typical sample rate of the system and will have negligible effect. Only single transient motion was considered for the wind tunnel experiments. Pressure data was logged at a rate of 125 samples during motion (1250Hz) and 1000HZ when the wing was held stationary. Figure 3-17a shows the pressure sensors in situ, with each PCB board connected to an Arduino component via a 10 piece ribbon cable. The transducers are oriented such that the internal diaphragm is aligned with the plunging motion to reduce any acceleration effects. This was quantified and determined to be negligible, for more information see Appendix B. Pressure taps at the leading- and trailing-edge regions were connected to the main box cavity via hollow stainless steel needles, as seen in at the mid-span of the wing. Flexible

tubing connected the pressure transducers to the hollow needle taps, see Figure 3-17b. These were organised such that the length between transducer and measurement point was no greater than the chord length, $0.23m$. The effects of the tube length are quantified in section 3.3.3.

32 pressure transducers were used to measure pressure around a single chordal plane at the mid-span of the wing. To determine the conversion factor between bit count and pressure a 10 point calibration was conducted for each transducer using a Druck portable calibrator; the difference in conversion constant was minimal, never-the-less each transducer was assigned it's own constant. The pressures were non-dimensionalised through the following:

$$C_P = \frac{P - P_\infty}{0.5\rho c U_\infty^2} \tag{3.7}$$

where P is the static pressure at the wing surface and P_∞ is the static pressure of the free-stream velocity. The average static uncertainty of the pressure coefficient was calculated based on the methods of Moffat [136] and presented in Table 3.8.

The pressure distributions for $Re = 100, 150$ and $200K$ at various selected angles of attack are compared against literature in Figure 3-19. At $\alpha_0 = 5°$ the pressure distributions all show good agreement with the computational study by Tang and Dowell [146]. A slight plateau on the upper surface can be observed in their data at $x/c \approx 0.3$ suggesting the presence of a laminar separation bubble. Such feature is not evident in the present study, possibly due to lack of spatial resolution and/or a higher free-stream turbulence intensity. At the stall angle, $\alpha_0 = 10°$, the results on average show good agreement with Rinoie & Takemura [147]. All measurements exhibit a plateau region on the upper surface at $x/c = 0.05$ due to a laminar separation bubble, however there are slight discrepancies between the measurements. This is to be expected, as the stall angle is highly sensitive to free-stream conditions and experimental set-up. The post-stall angle of $\alpha_0 = 12°$ shows good agreement. There is a slight rise in suction at the leading-edge, which Rinoie & Takemura [147] attribute to the averaging of unsteady effects.

The uncertainty in the half-saddle convection speed estimation, pertaining to Chapter 6, is shown

in Figure 3-18. Figure 3-18a presents a pressure map with convective time across the airfoil's upper surface. A low pressure wave can be seen convecting across the chord between $\tau = -2.5$ and -1.0. The frontier of this wave (highlighted in Figure 3-18a) has been linked to the movement of a half-saddle point, a topological flow point on the airfoil surface that separates upstream and downstream flow, by Leknys *et al.* [101]. In this thesis the half-saddle point is estimated through visual inspection and the convective rate is calculated from the gradient, see Figure 3-18b. Such a crude method of estimation is subject to large uncertainty, and this is highlighted in Figure 3-18b as $\pm 0.03 U_\infty$. Nevertheless this analysis can provide useful information on the approximate convection rate of the half-saddle point to compare with literature.

3.3.3 Loads Measurements

Static Measurements

Lift and pitching moment are calculated via numerical integration of the pressure distribution, assuming a linear variation of pressure between each sensor. Figure 3-20 presents the static lift (3-20a) and quarter-chord pitching moment (3-20b) curves for $Re = 100, 150, 200K$ alongside relevant literature. The static loads from the water tunnel rig at $Re = 20K$ are also plotted for reference. At $\alpha_0 = 0°$ the lift at $Re = 100K$ displays a negative C_L. The wind tunnel rig design gives a highly repeatable α_0 setting, therefore this is most likely due to the removable wing panel on the lower surface creating a slight asymmetry which is exacerbated at this particular Reynolds number. At low α_0 ($< 5°$) the lift shows a more linear variation to $Re = 20K$, which is expected for transitional Reynolds numbers. Little variation between the present study is seen for $Re = 100, 150, 200K$ and shows good agreement with literature. More deviation in reported lift coefficients are seen between $\alpha_0 = 5°$ and $10°$, but the present study lies between the spread. In general the stall angle of $\alpha_0 = 10°$ agrees well with literature, however the post-stall regime shows a drastic spread, as this region is highly sensitive to the experimental set-up. The pitching moment in 3-20b is in overall agreement with the spread of values reported in literature. In the transitional Reynolds number regime the pitching moment curve does not show the distinct undulations seen at $Re = 20K$, and instead shows a more monotonic variation, disrupted by a distinct drop at the stall angle $\alpha_0 = 10°$. Interestingly the curves for the present study

at $Re = 100, 150, 200K$ show remarkable agreement across most of the range. The estimated uncertainty for the lift and pitching moment measurements are shown in Table 3.8.

Table 3.8: Static uncertainties.

Parameter	**Estimated Uncertainty**
C_P	± 0.08
C_L	± 0.04
C_M	± 0.01

Dynamic Measurements

The set-up has been validated for static measurements, however the effect of the long tube lengths will have a drastic effect on the frequency response of the unsteady pressure measurements [148]. In order to quantify these effects, the frequency response to an unsteady pressure source was measured for a pressure transducer with and without tubing. The unsteady pressure source consisted of a jet of air that is periodically interrupted by a series of holes in a rotating disk connected to a motor; the frequency of disturbance can be controlled by the rotational speed of the motor. Figure 3-21 presents this set-up. When a hole in the disk is aligned with the air jet, a pressure is transmitted down the tube, see Figure 3-21a. When the disc hole is no longer aligned with the air jet, the flow is completely blocked, see Figure 3-21b. The reference pressure transducer is connected as close as possible to the location of measurement (within $20mm$) and the test transducer is connected via a variable tube length. Tube lengths of 50, 100, 150 and $200mm$ were tested across a range of frequencies.

The results of this experiment are shown in Figure 3-22a, where the amplitude ratio (a1) is defined as the first harmonic of the test transducer signal divided by the first harmonic of the reference transducer signal. These were extracted using Welchs method to obtain the Power

Spectral Density (PSD). Figure 3-22a shows that as the tube length is increased the resonant frequency of the tube decreases drastically. To put this frequency range into perspective, the frequency content of a typical motion occurs within the grey region between 0 and $5Hz$, where the amplitude ratios remain at unity. This is shown in more detail in Figure 3-22b where the PSD of every pressure transducers for a typical unsteady motion are plotted against the Strouhal Number based on chord length for a $Re = 150K$. The majority of the information is contained within $St_c < 0.5$.

In order to give an approximate quantification of the error associated with tube resonance, the amplitude ratio response can be applied as a corrective measure to the PSD of a pressure transducer. The difference between the corrected and uncorrected PSD can give a rough idea of the level of error associated with the tubing. A tube length of $200mm$ was selected as a conservative length estimate and interpolated using a 12^{th} order polynomial fit. The PSD's for all the transducers in Figure 3-22b were averaged to give a single representative PSD. A *very* approximate correction for the tubes would then be the average PSD divided by the amplitude ratio; this is plotted in Figure 3-23a. The cumulative integral with respect to frequency of the corrected and uncorrected PSD is plotted in Figure 3-23b. This shows that the deviation in area under the two PSD's becomes greater the higher the frequency limit of the integration (as expected). Figure 3-23c expresses this as a percentage error. This equates to an approximate pressure amplitude error with respect to frequency that can be effectively suppressed through a low-pass filter. A low-pass filter applied to a pressure signal at $250Hz$ would equate to an approximate error in pressure of 1.5%. As this error is small, no corrective method has been applied to the pressure signals to account for tube length. This has instead been incorporated into the uncertainty analysis.

Figure 3-24a presents the raw, ensemble-average and filtered ensemble-average pressure signals during a typical transient motion for two pressure sensors; the leading-edge ($x/c = 0.00$) and the upper surface, quarter chord ($x/c = 0.25$). The raw signal (pink) demonstrates a reasonably high signal-to-noise ratio and is comprised of the overlay of 30 repeats. Very little difference can be seen between the ensemble-average (red) and the filtered ensemble average (blue). A Butterworth

6th order low-pass filter was applied at $250Hz$ to the ensemble-average response. Figure 3-24b shows the overlay of the filtered raw signals and demonstrates excellent repeatability. The typical uncertainty bounds are shown around the filtered ensemble-average signals in Figure 3-24c. These were quantified using the methods of Moffat [136] where appropriate, more information can be found in Appendix B. These uncertainty bounds are plotted independently in Figure 3-24d. The typical average uncertainty for the coefficient of pressure is displayed in Table 3.9.

The same format of repeats and uncertainties are shown for the lift and pitching moment in Figure 3-25. The raw signals for 30 repeats (pink) show a greater variation for each run than the individual pressure transducers in Figure 3-24. The effect of filtering the pressure signals can be seen at $\tau = -5$ and $\tau = -2$ where a small region of high frequency noise (red) is removed (blue). Figure 3-25b shows the overlay of the individual filtered responses. Overall, an acceptable amount of variation exists between the 30 repeats. A reduction in signal variance can be seen between $\tau = -2$ and 2 which will be shown later in this thesis to be due to a change from separated to attached flow. Typical uncertainty bounds for this motion are plotted around the filtered ensemble-average responses, see Figure 3-25c. These were produced through a stochastic analysis whereby each pressure transducer was assigned a random error within it's own uncertainty bounds during C_P integration. The analysis was repeated 1000 times per time step and the 95% confidence level for the lift and pitching moment were extracted. In addition this, the uncertainty from the repeatability and free-stream variance was also taken into account using the methods of Moffat [136]. More information can be found in Appendix B. The uncertainty variation in Figure 3-25d illustrates the insensitivity of C_L to the stochastic uncertainty method, as most of the random errors cancel each other out. The pitching moment on the other hand displays greater variation. The typical average uncertainty for C_L and C_M are displayed in Table 3.9.

Table 3.9: Typical uncertainties for dynamic motion.

Parameter	**Estimated Uncertainty**
C_P	$\pm$ 0.20
C_L	$\pm$ 0.05
C_M	$\pm$ 0.015

3.4 Rig Comparison

An illustrative comparison of the water tunnel and wing tunnel rig capabilities are shown in Figure 3-26. These are plotted in terms of the maximum induced angle of attack they can produce, $\alpha_{pl,max}$, against a periodic reduced frequency. Limiting factors for the wind tunnel rig are the maximum linear velocity of the actuator and the natural bending frequency of the wing. For the water tunnel the bounds are defined by the maximum linear velocity of the translation stage and the maximum force this can supply.

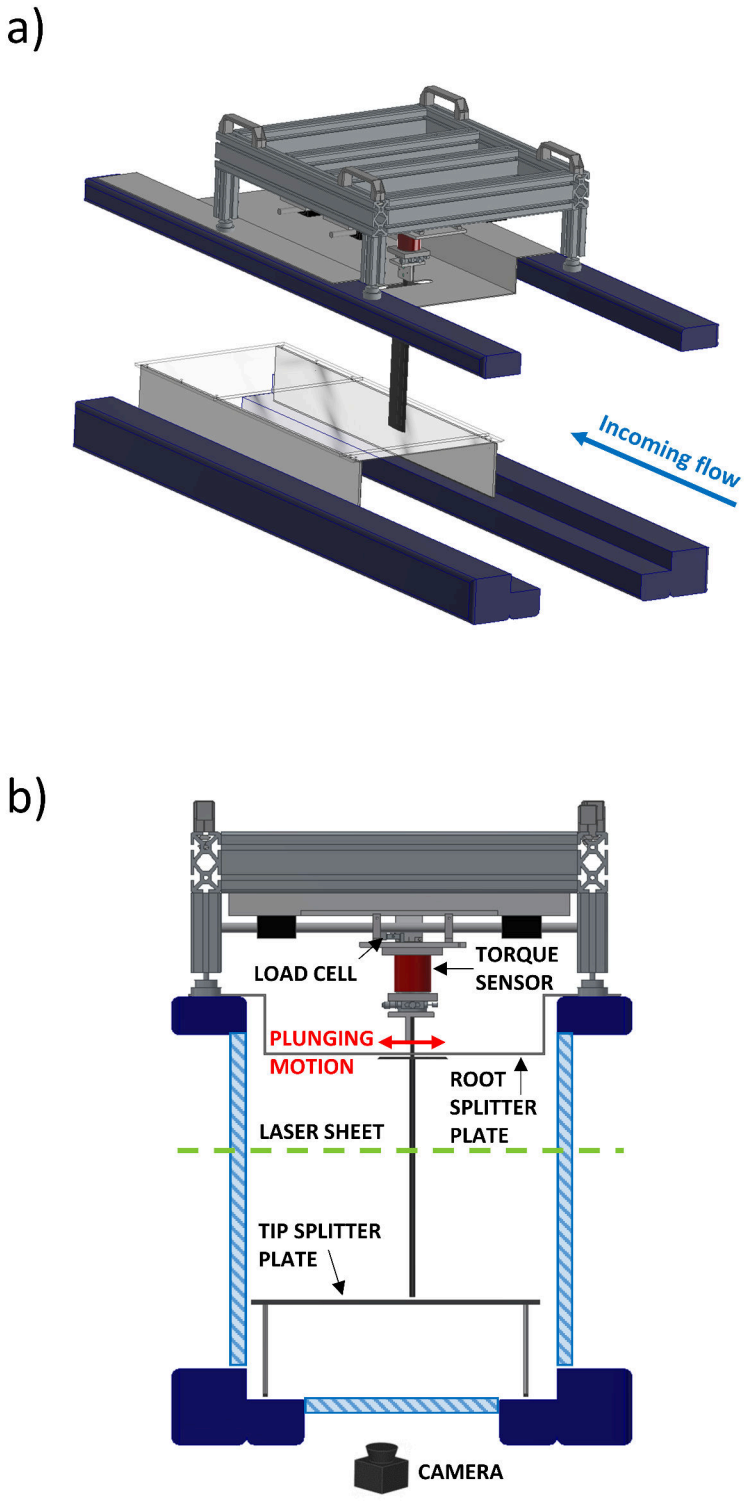

Figure 3-1: Water tunnel test rig, a) isometric view, b) front view.

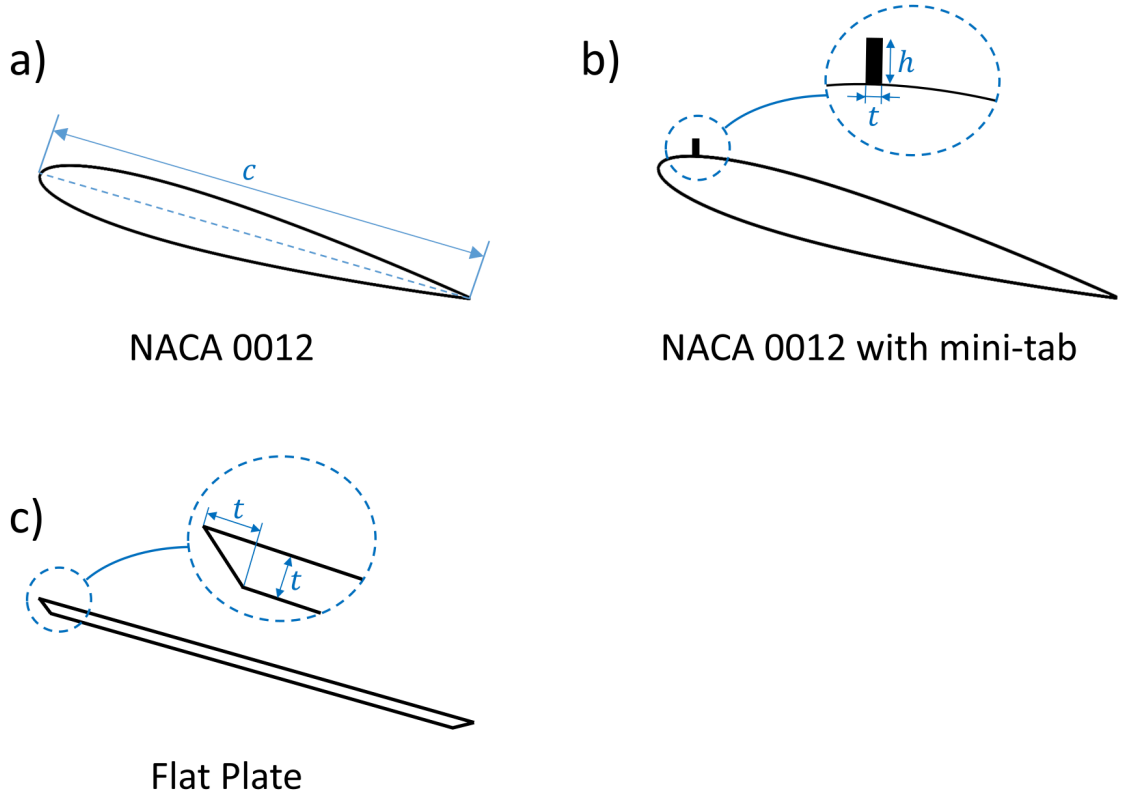

Figure 3-2: Airfoil geometry, a) NACA 0012, b) NACA0012 with mini-tab, c) Flat plate with lower surface chamfer.

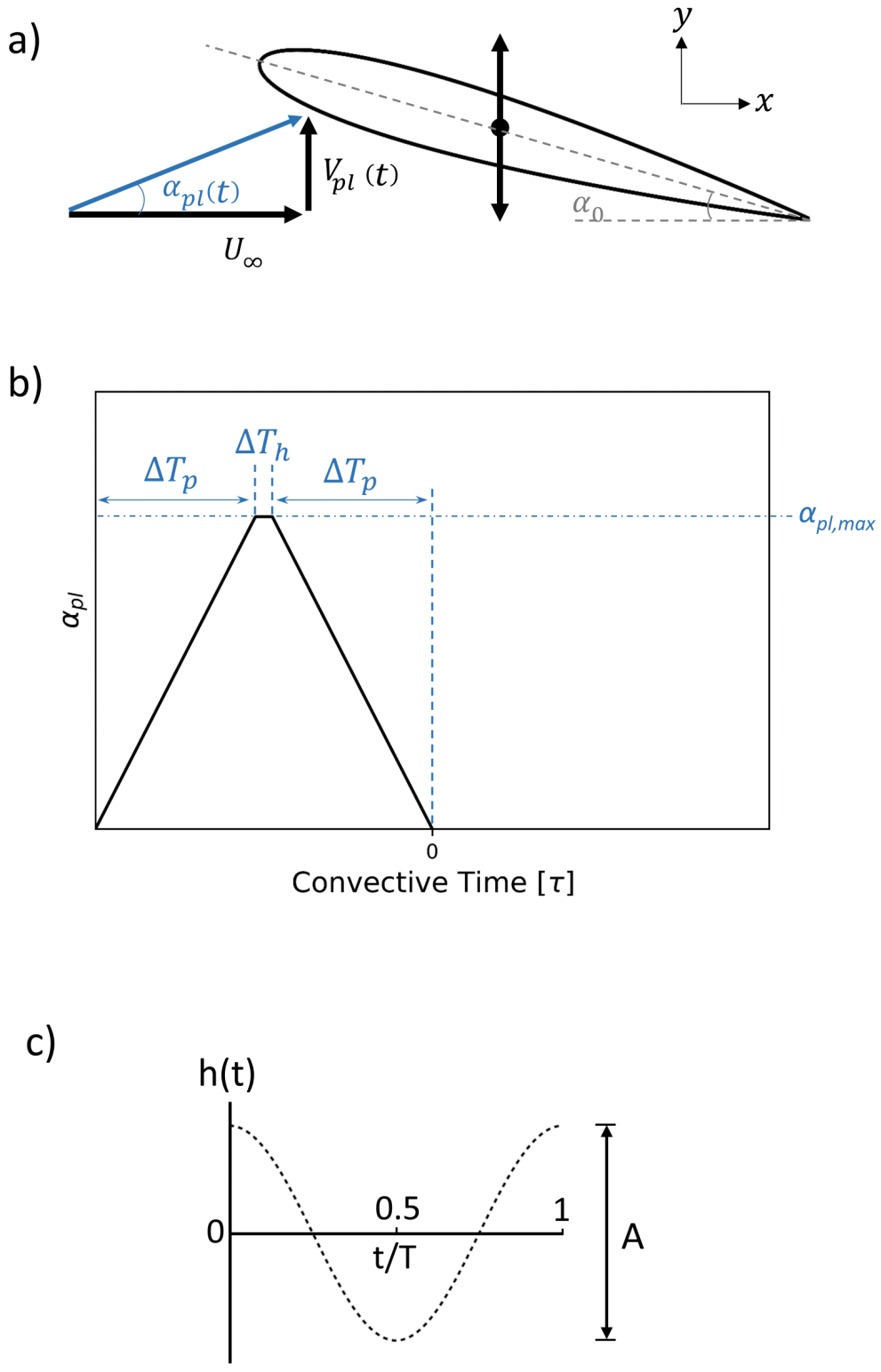

Figure 3-3: a) Airfoil plunging motion parameters, b) profile of effective angle of attack for transient plunging motion, c) profile of effective angle of attack for sinusoidal plunging motion.

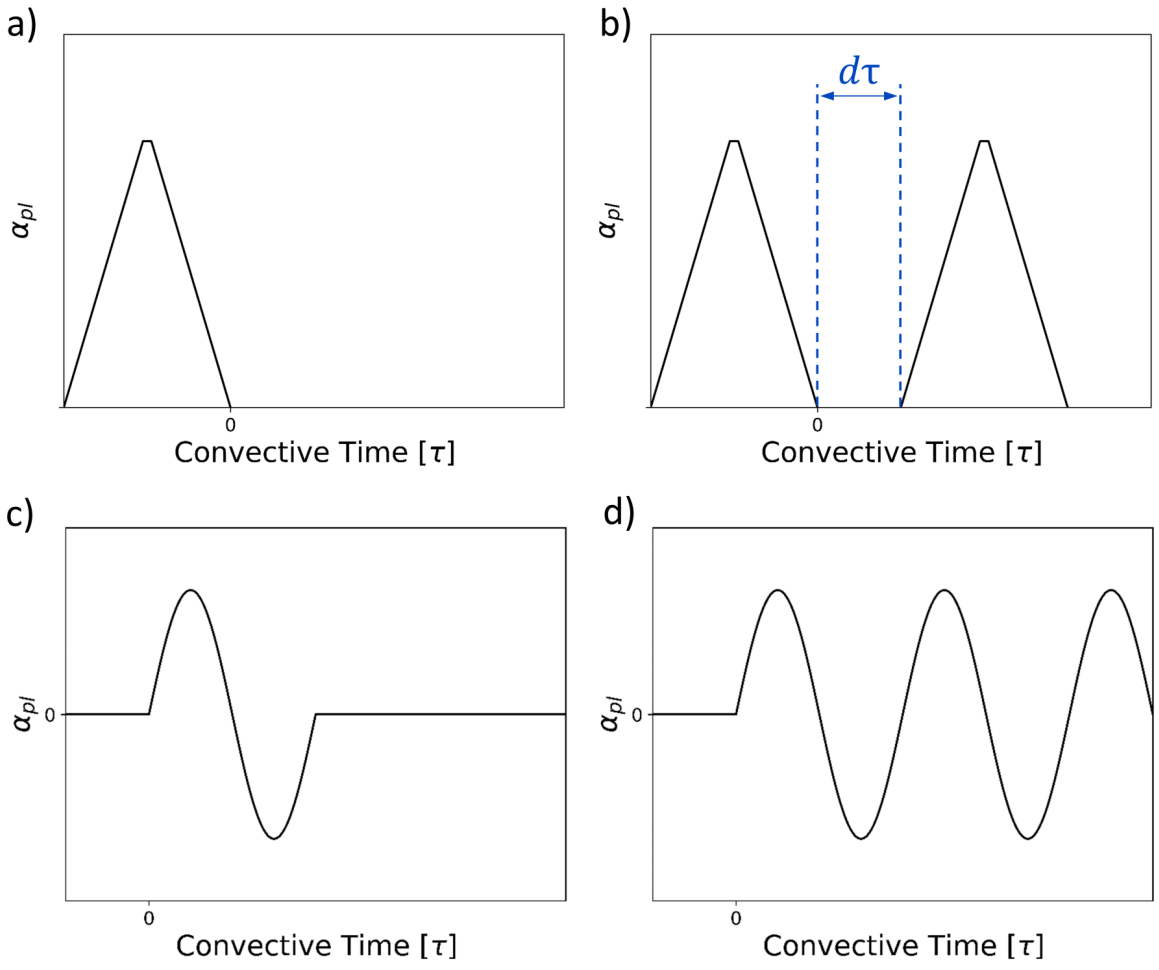

Figure 3-4: Profile of effective angle of attack for, a) single transient motion, b) compound transient motion, c) single sinusoidal motion, d) periodic sinusoidal motion.

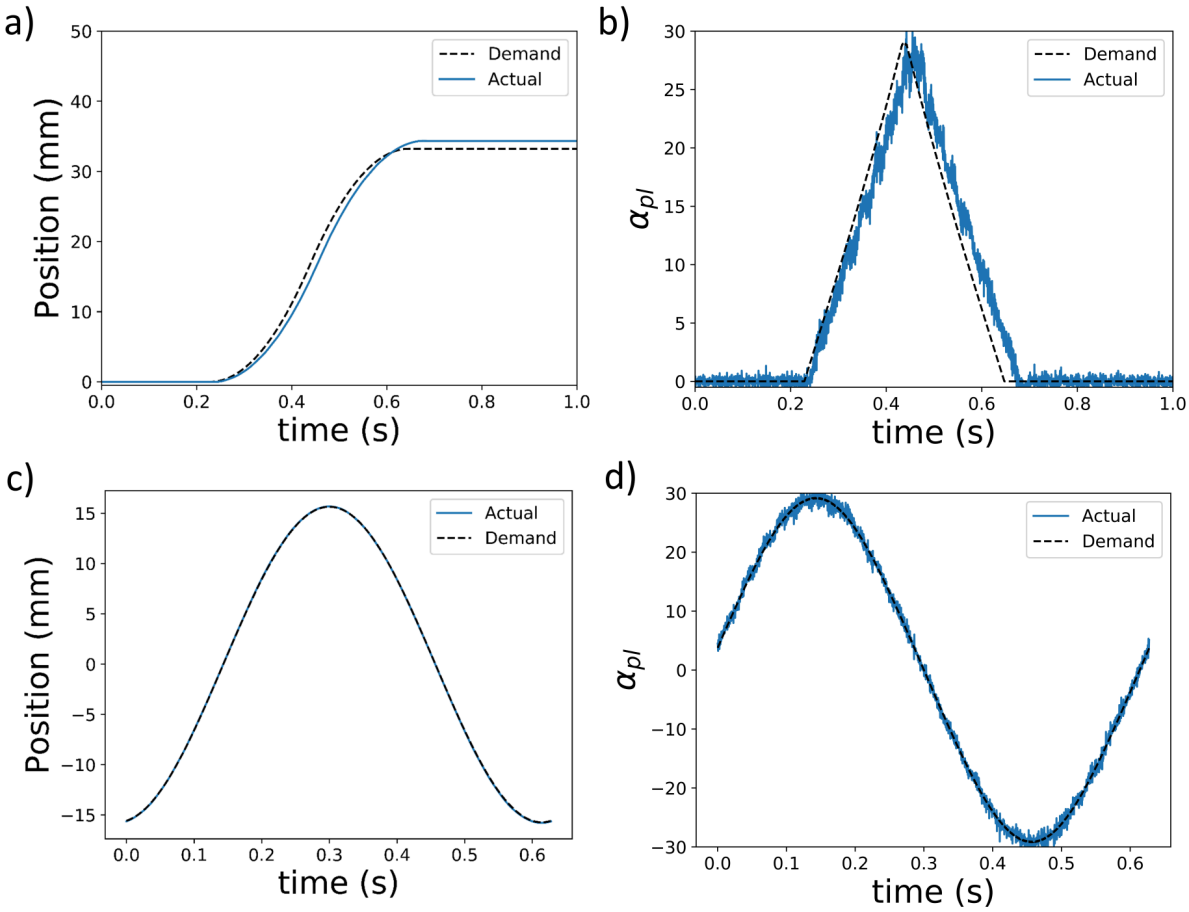

Figure 3-5: a) Position accuracy of transient motion, b) induced plunge angle accuracy for transient motion, c) position accuracy for sinusoidal motion, d) induced plunge angle accuracy for sinusoidal motion.

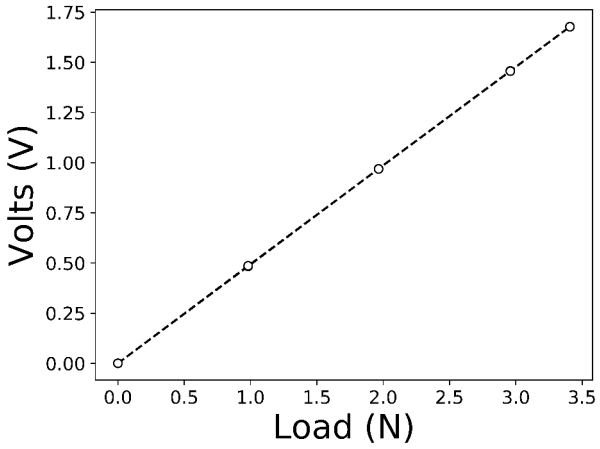

Figure 3-6: Calibration curve for lift sensor.

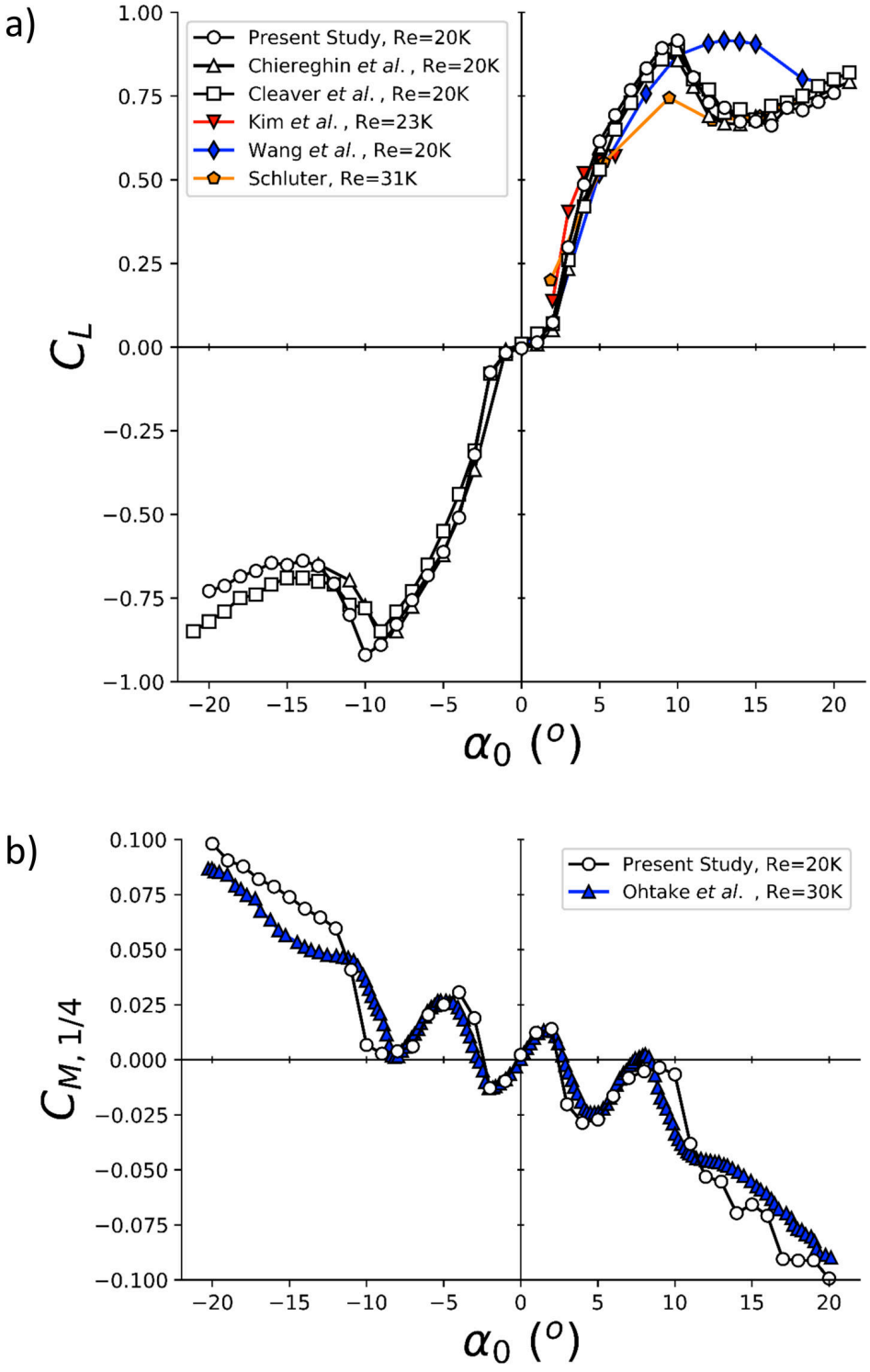

Figure 3-7: a) Static lift coefficient, b) static pitching moment coefficient.

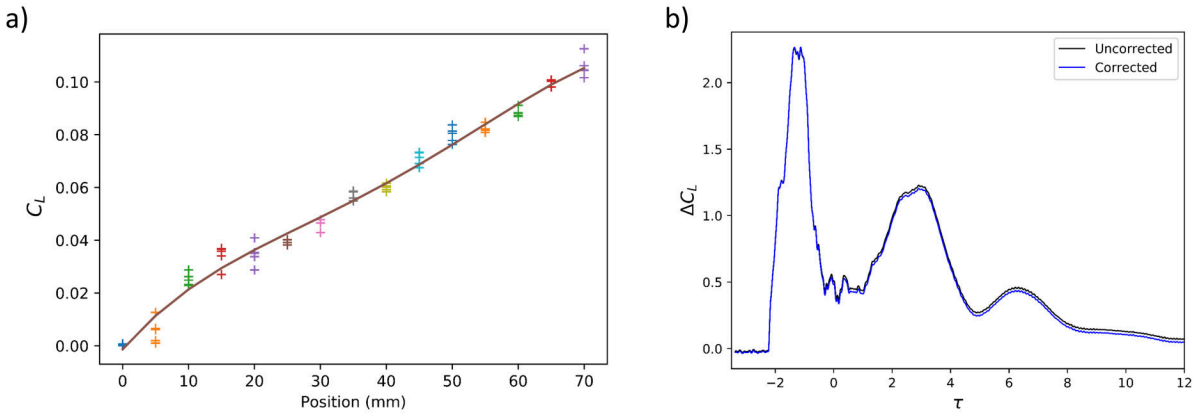

Figure 3-8: a) Typical magnitude of force exerted by wire, b) uncorrected and corrected lift time history.

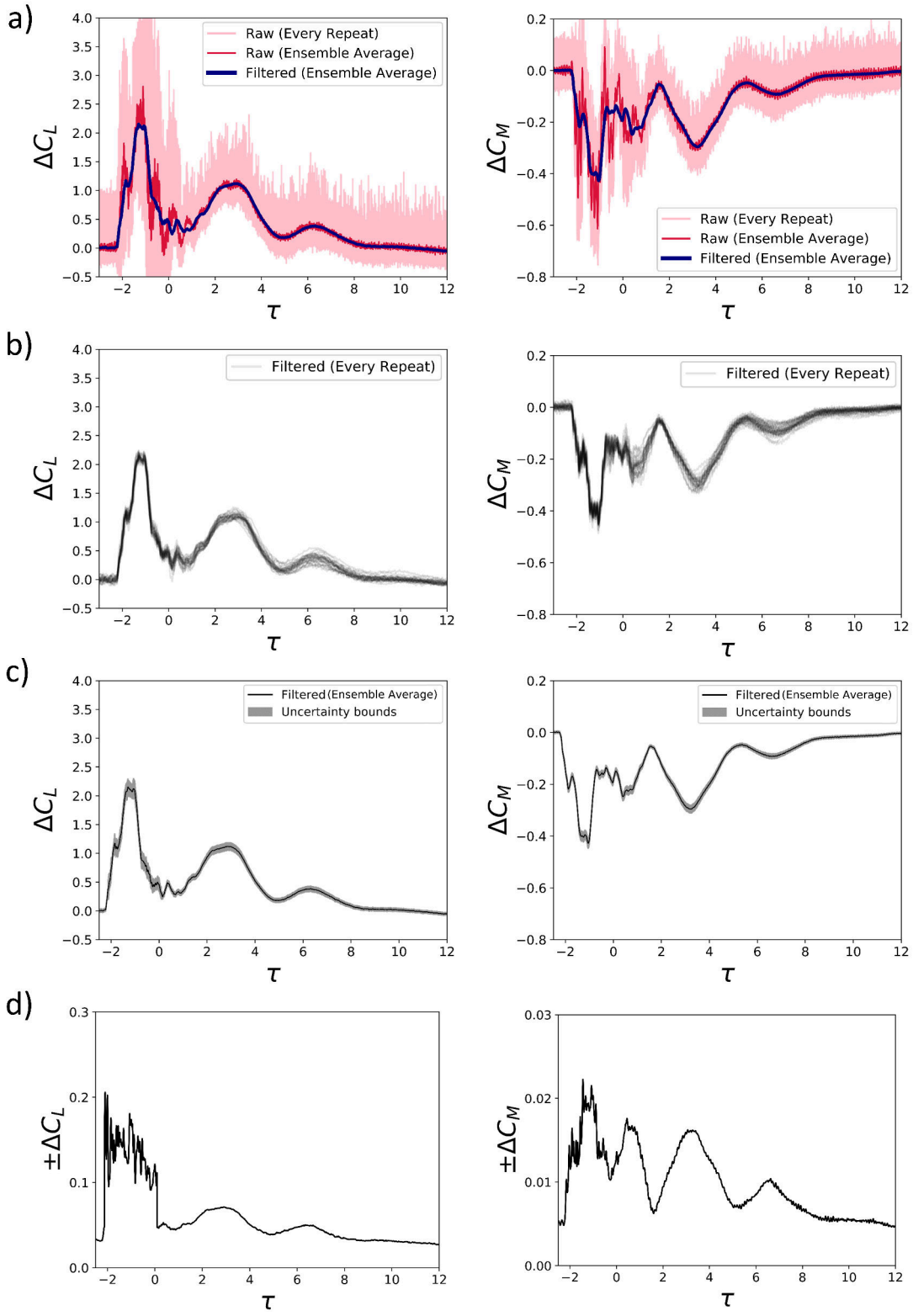

Figure 3-9: a) Raw signal to filtered average signal, b) repeat variation, c) estimated uncertainty with average signal, d) estimated uncertainty.

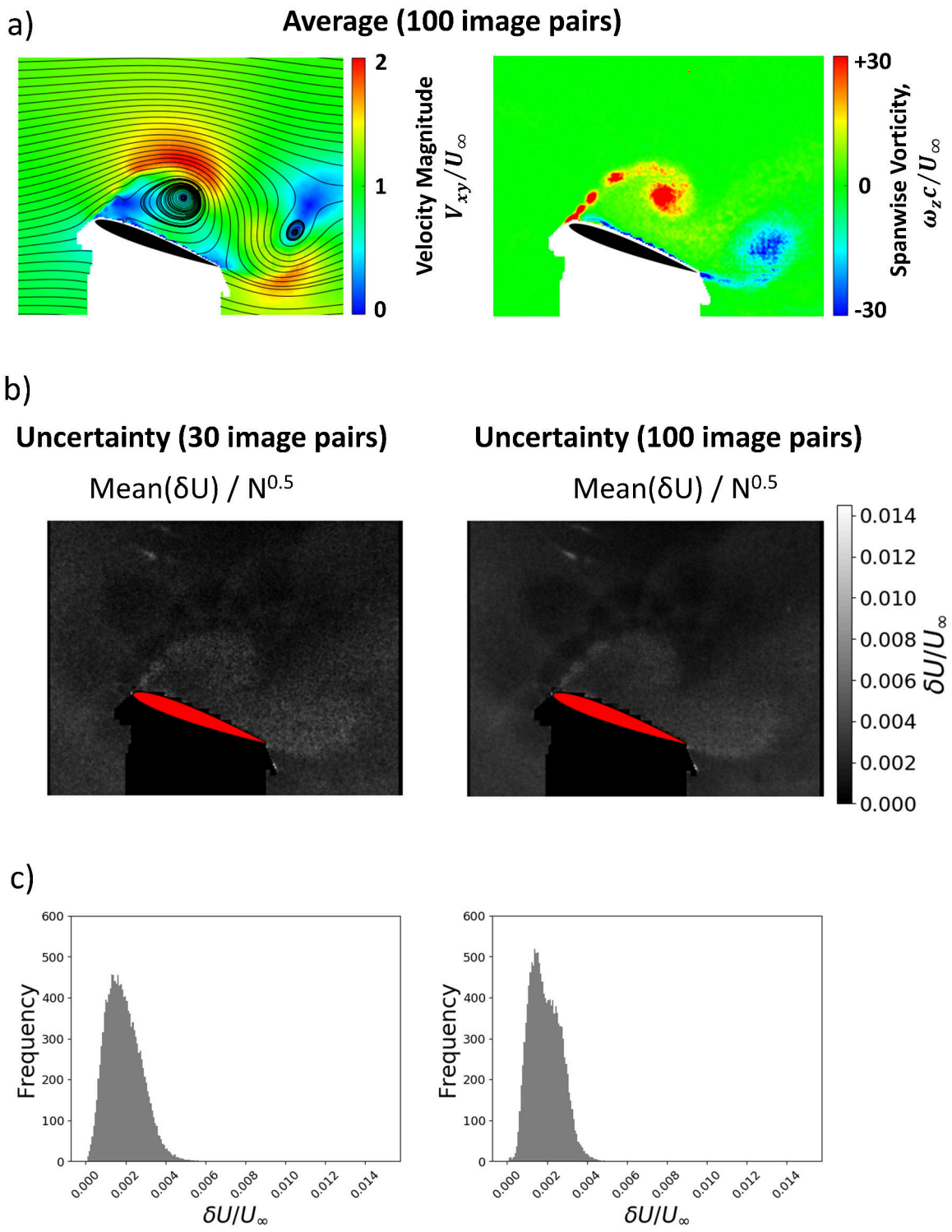

Figure 3-10: a) Normalised velocity and spanwise vorticity plots, b) estimated expanded uncertainty, c) uncertainty distribution.

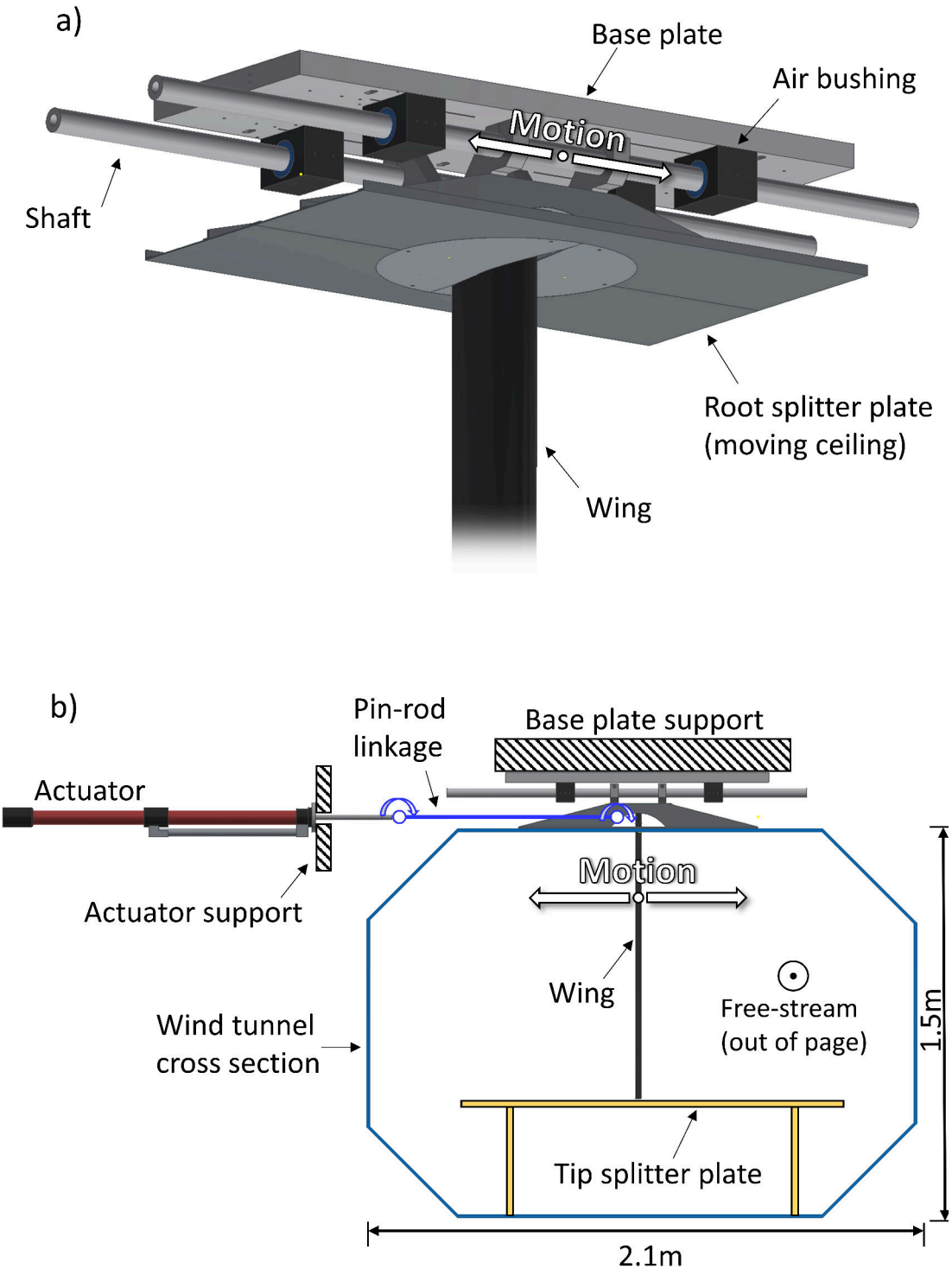

Figure 3-11: a) Plunging assembly with wing, b) Full rig diagram.

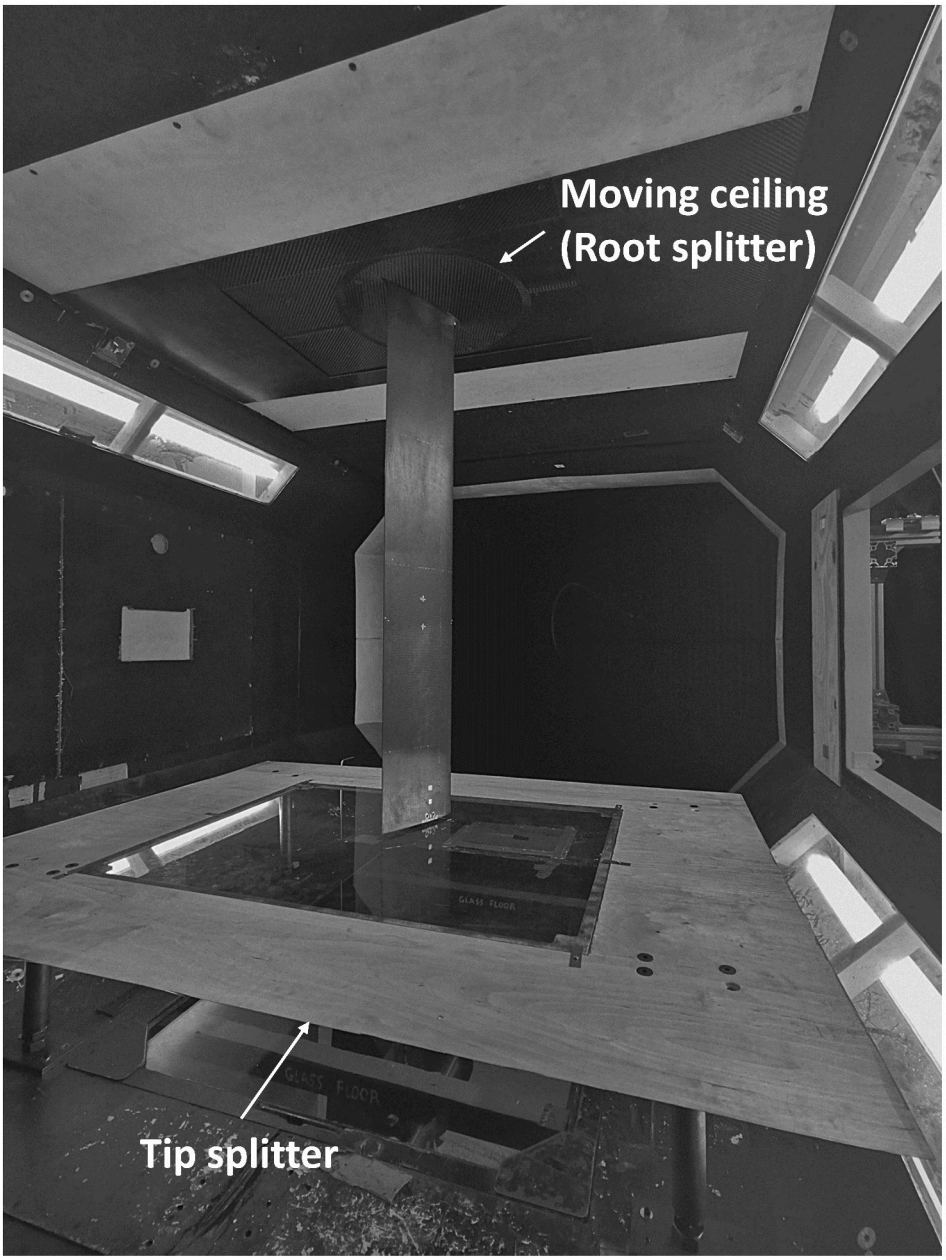

Figure 3-12: Tunnel view of full set-up.

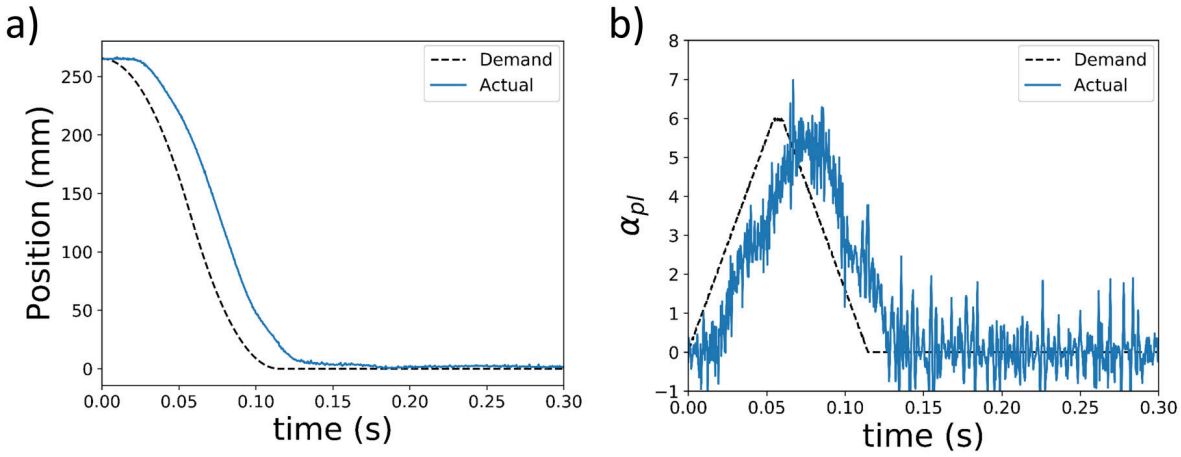

Figure 3-13: a) Position accuracy of transient motion, b) induced plunge angle accuracy of transient motion.

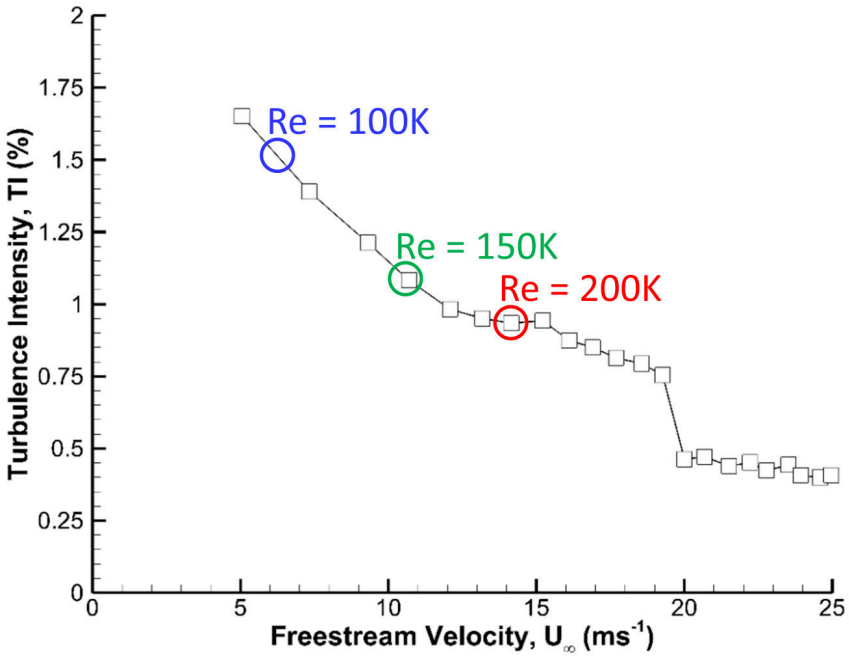

Figure 3-14: Turbulence intensity vs. tunnel speed.

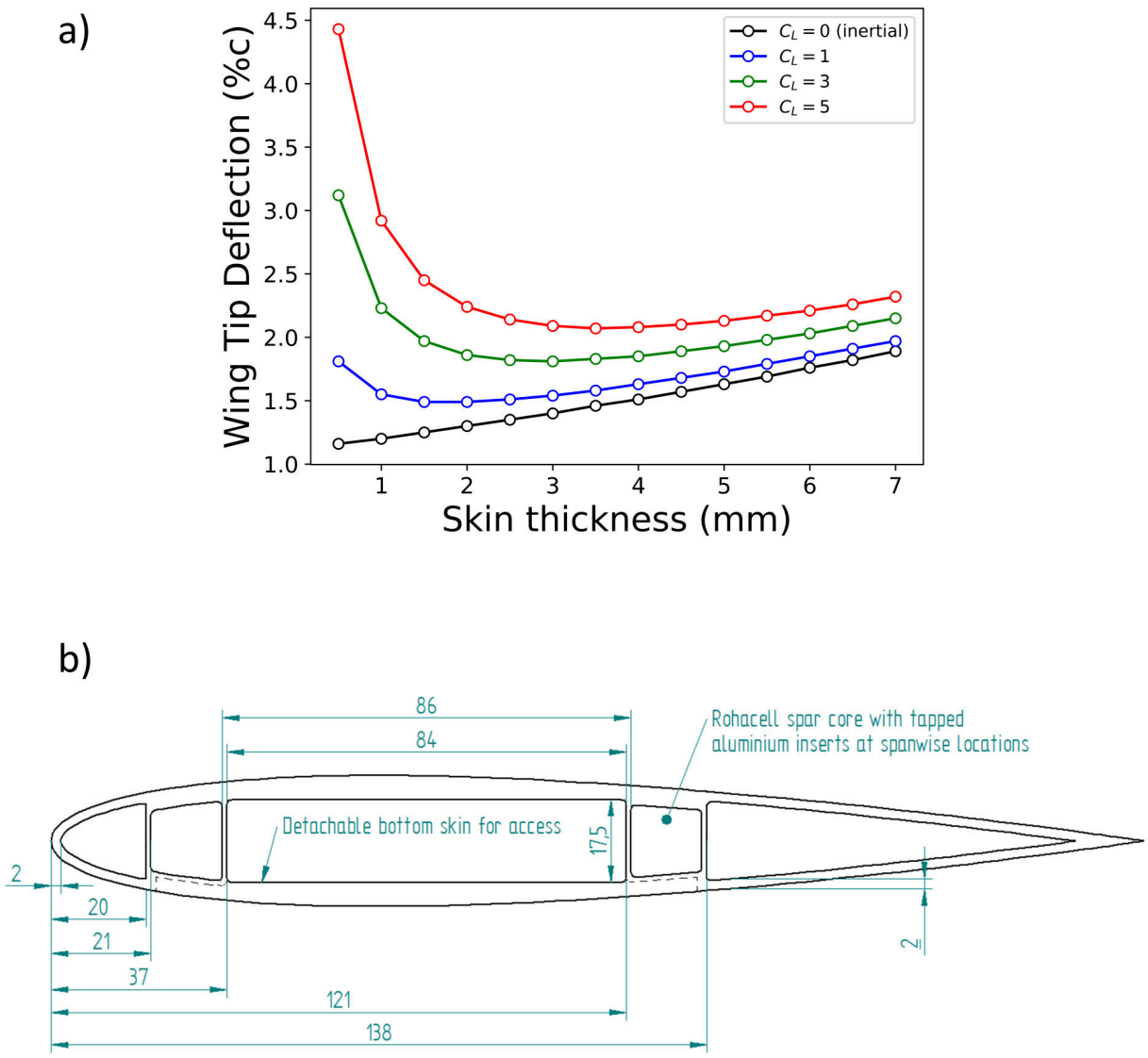

Figure 3-15: a) Wing cross-section, b) wing skin thickness trade-off, c) final wing cross-section design.

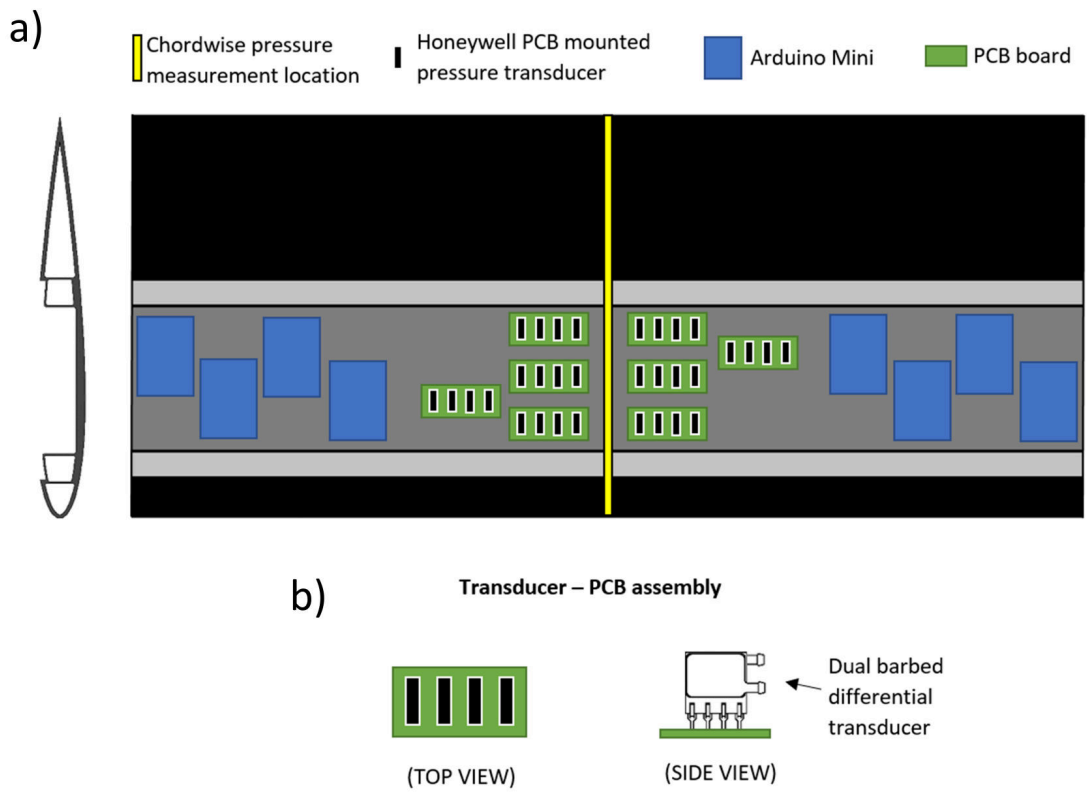

Figure 3-16: a) Top view diagram of in-situ pressure measurement system, b) transducer - PCB assembly.

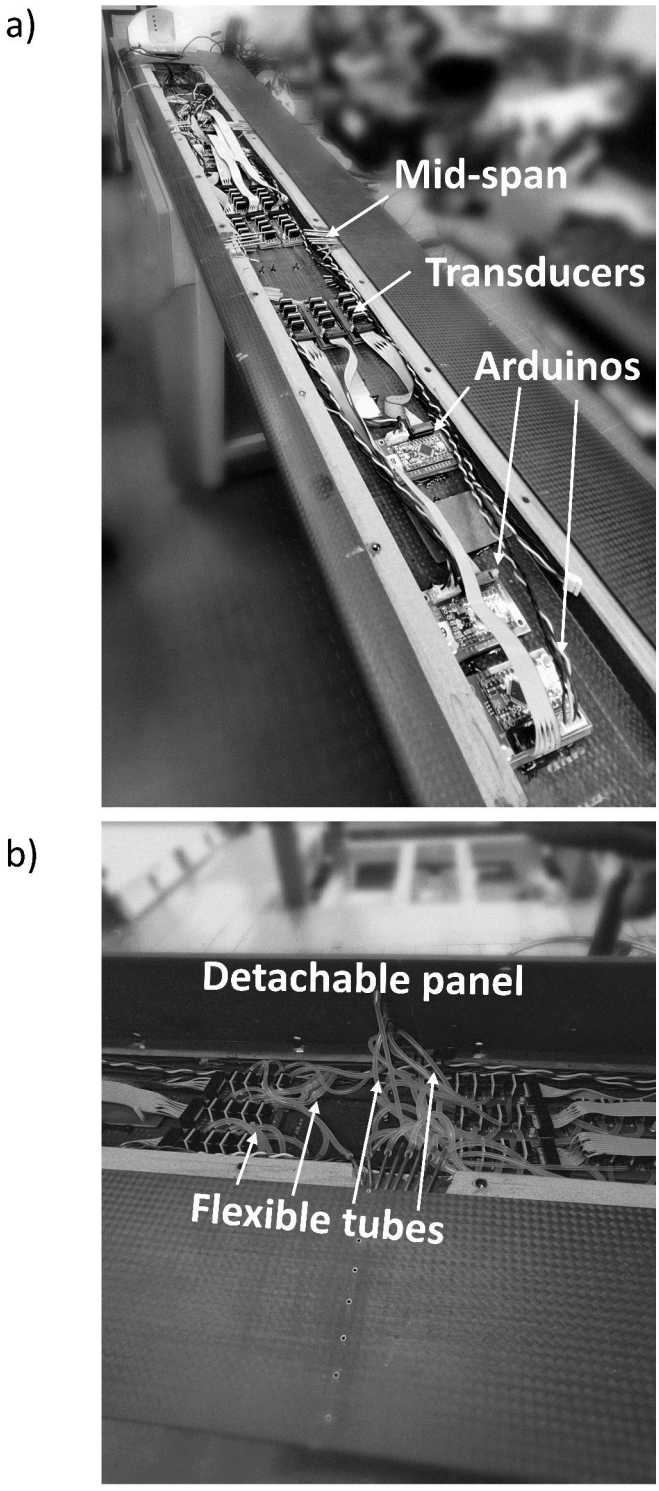

Figure 3-17: a) Photo of in-situ pressure measurement system, b) photo of tubing.

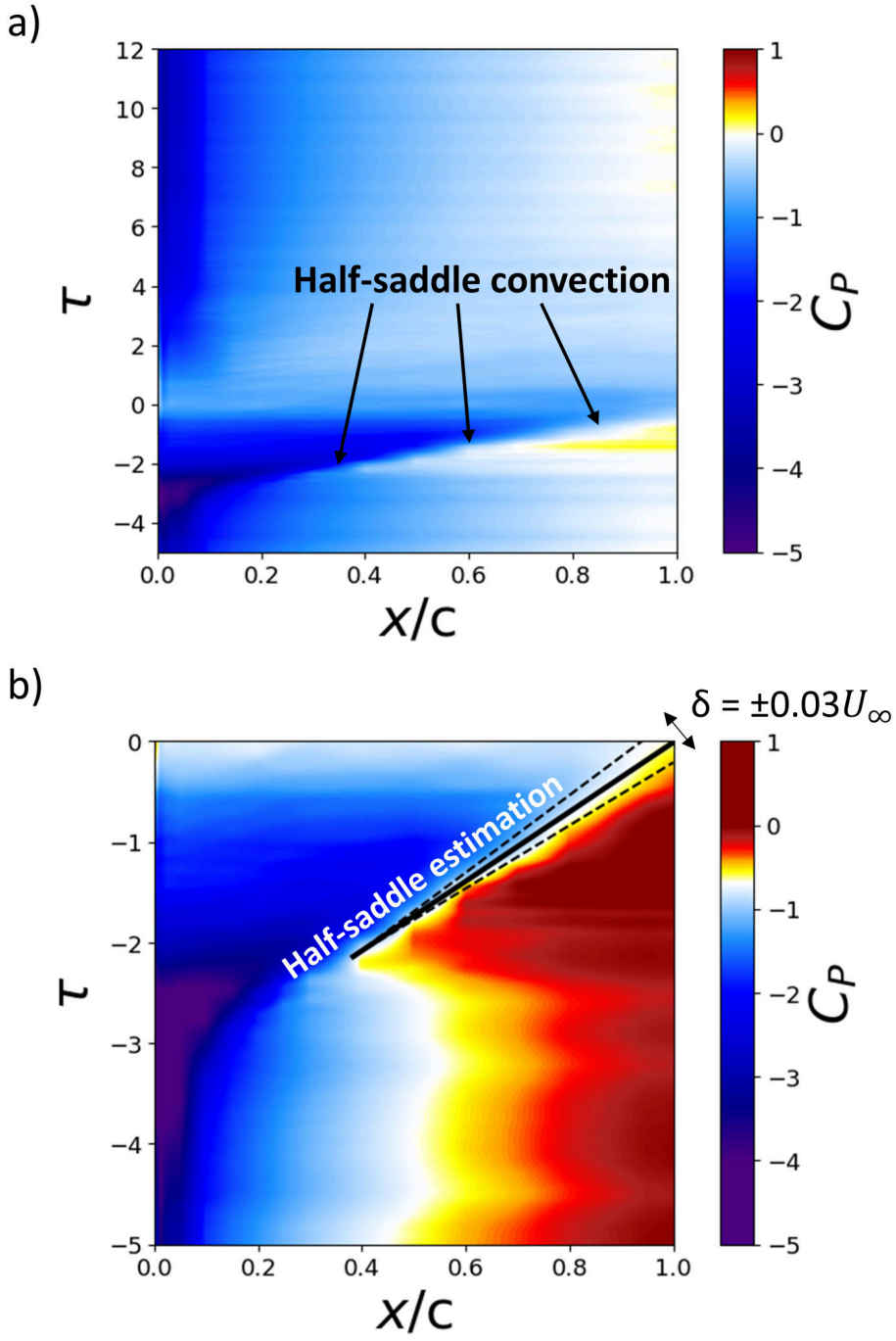

Figure 3-18: a) Pressure map of upper surface displaying half-saddle convection, b) half-saddle convection speed estimation with uncertainty bounds.

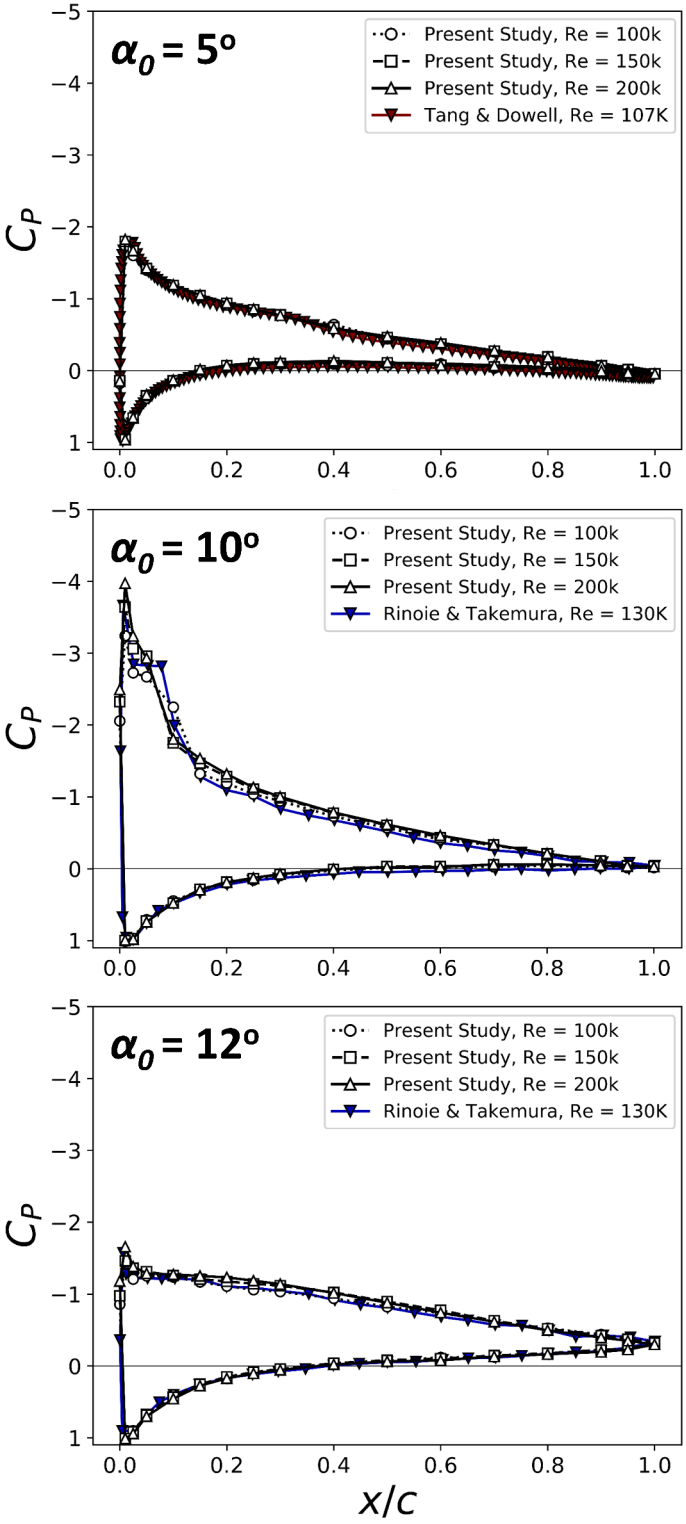

Figure 3-19: Static pressure distributions.

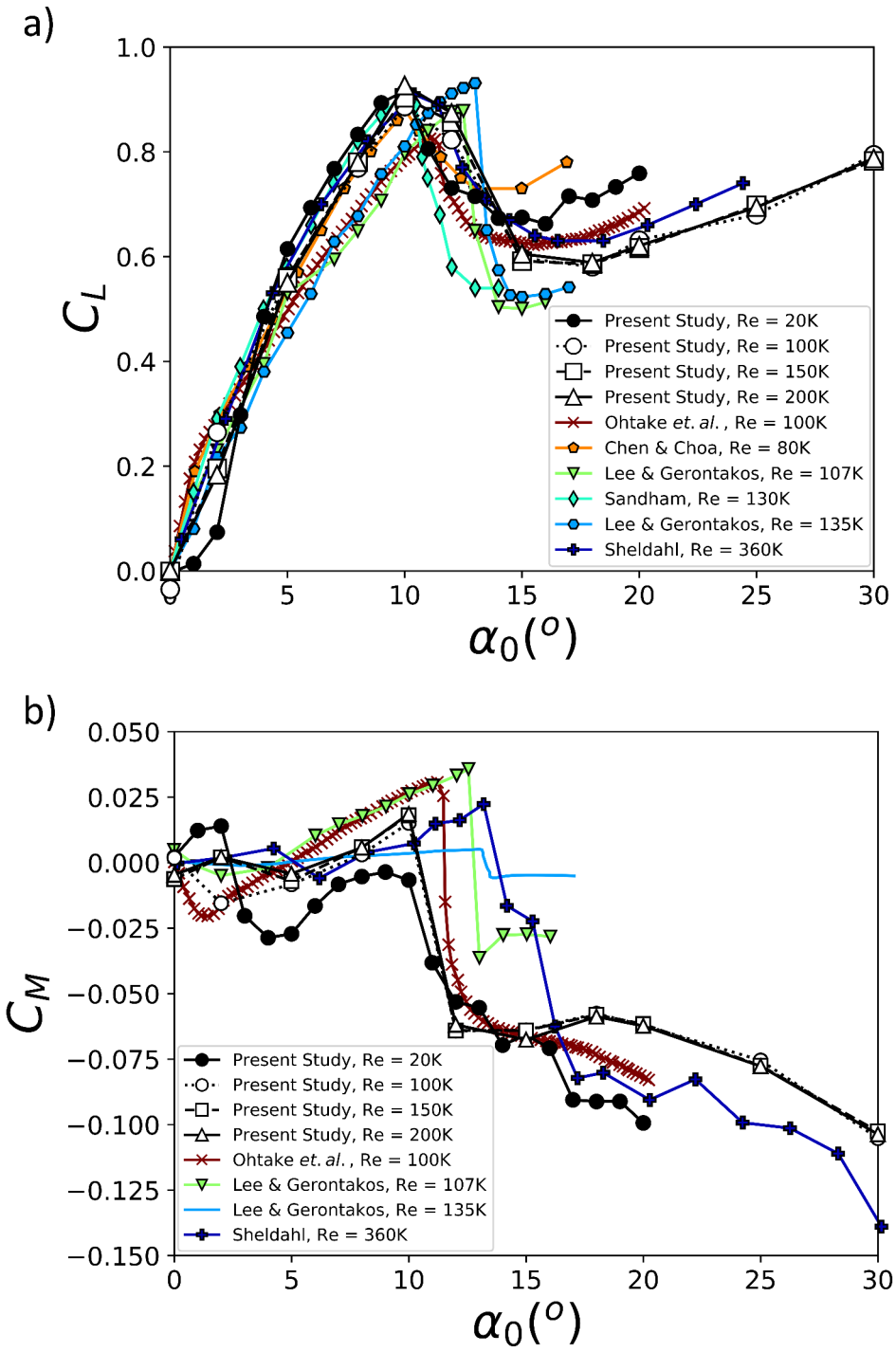

Figure 3-20: a) Static lift coefficient, b) static pitching moment coefficient.

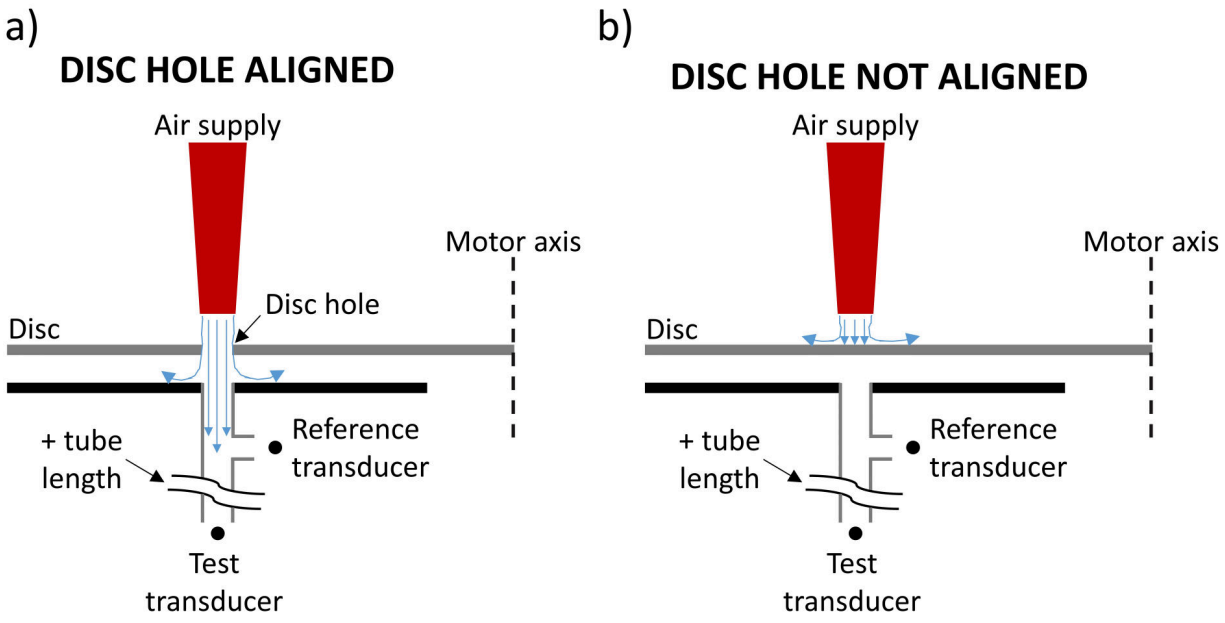

Figure 3-21: a) Unsteady air jet experiment: ON condition, b) Unsteady air jet experiment: OFF condition.

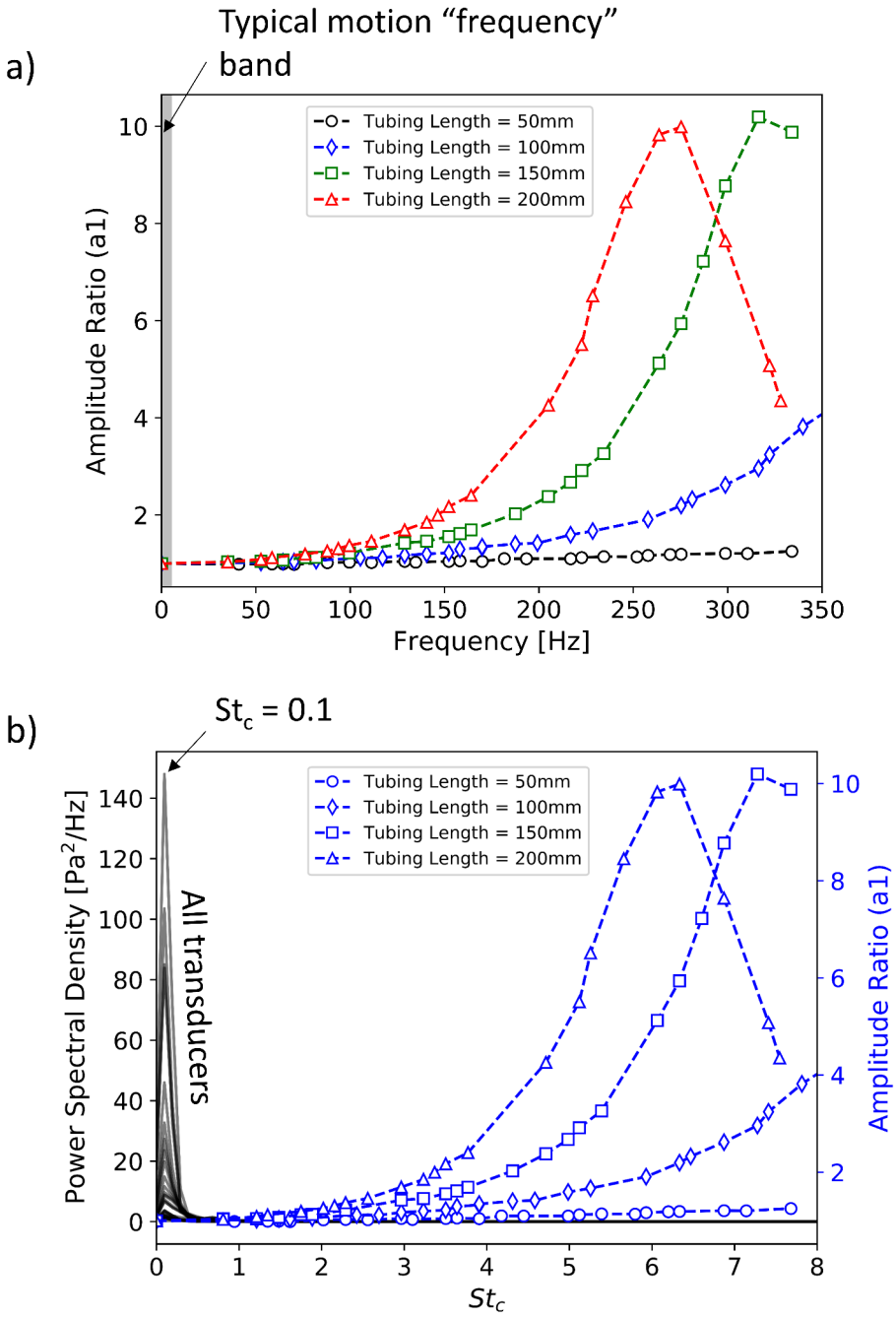

Figure 3-22: a) Resonance effect of tubing, b) Power Spectral Density of pressure transducers.

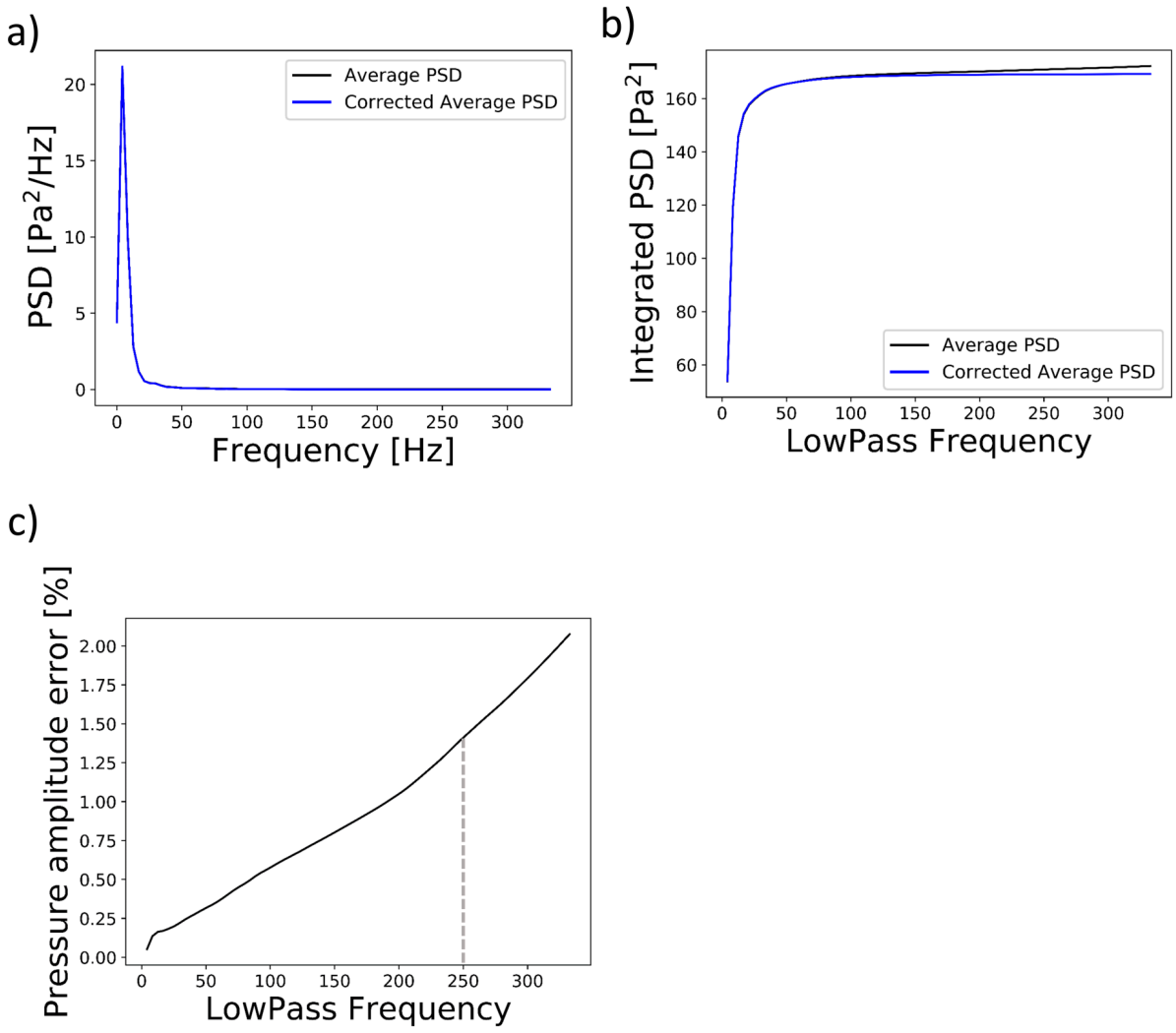

Figure 3-23: a) Average Power Spectral Density (PSD) with corrected average PSD, b) integrated PSD for corrected and uncorrected PSD, c) pressure amplitude error.

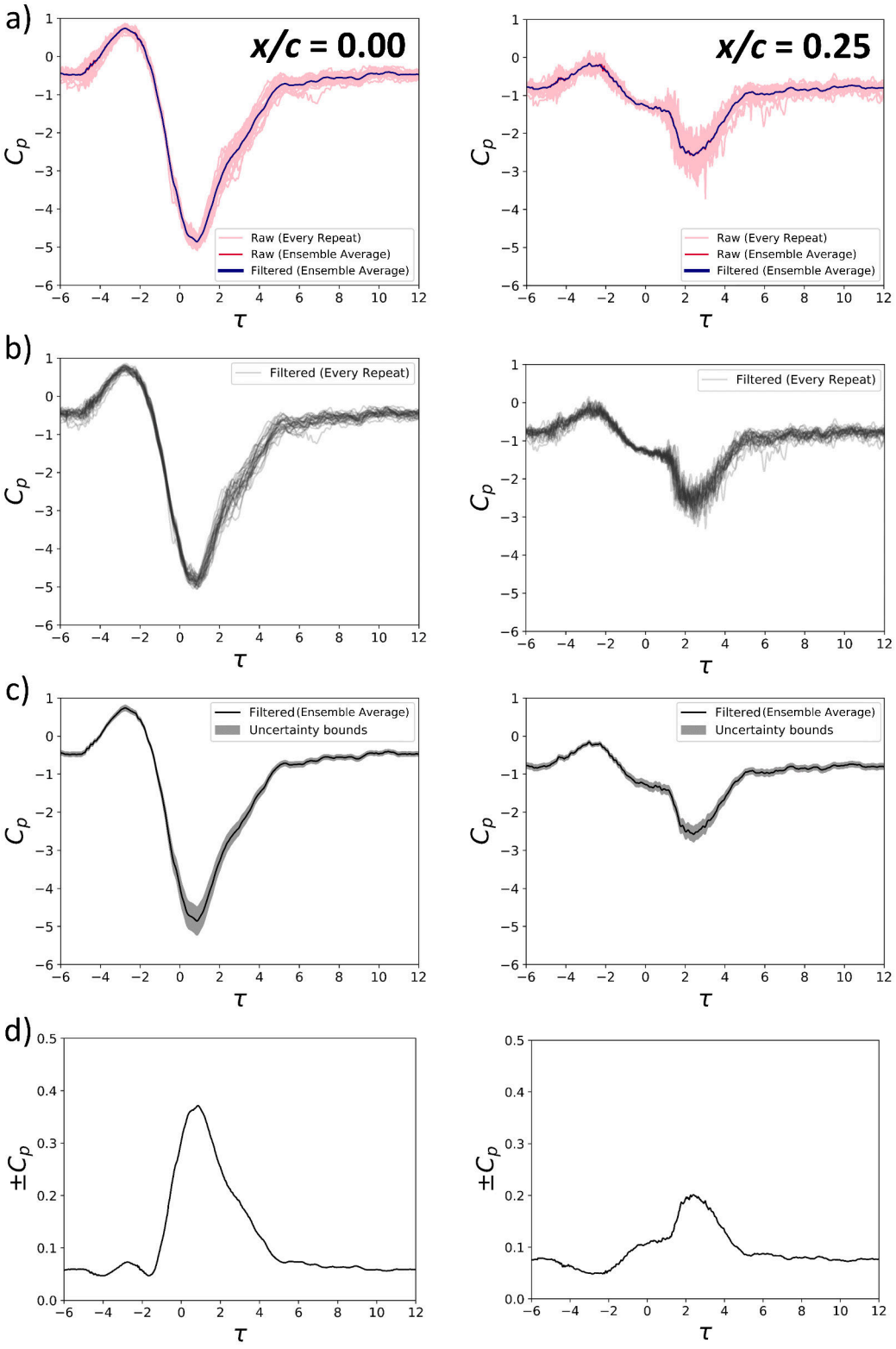

Figure 3-24: a) Raw signal to filtered average signal, b) repeat variation, c) estimated uncertainty with average signal, d) estimated uncertainty.

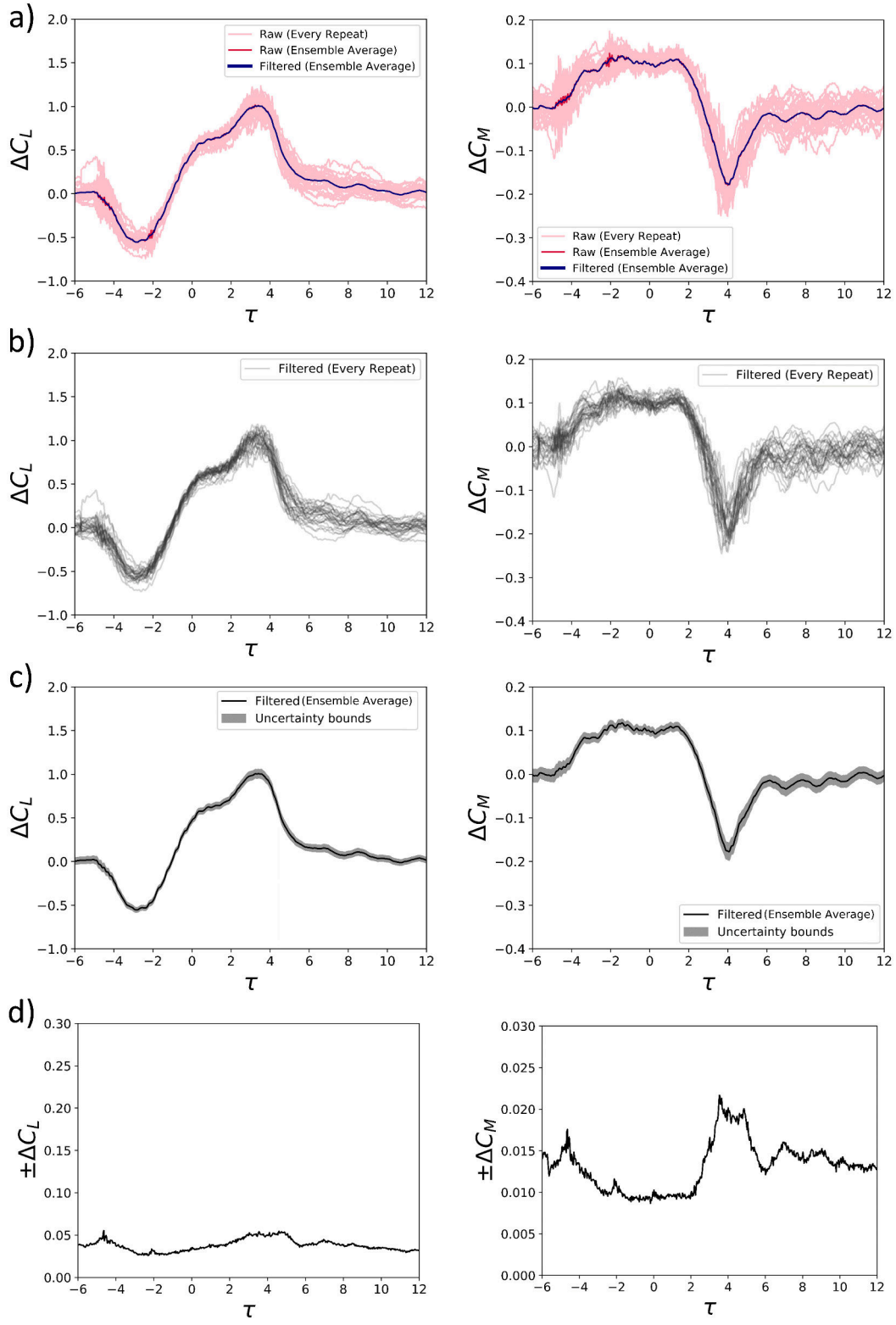

Figure 3-25: a) Raw signal to filtered average signal, b) repeat variation, c) estimated uncertainty with average signal, d) estimated uncertainty.

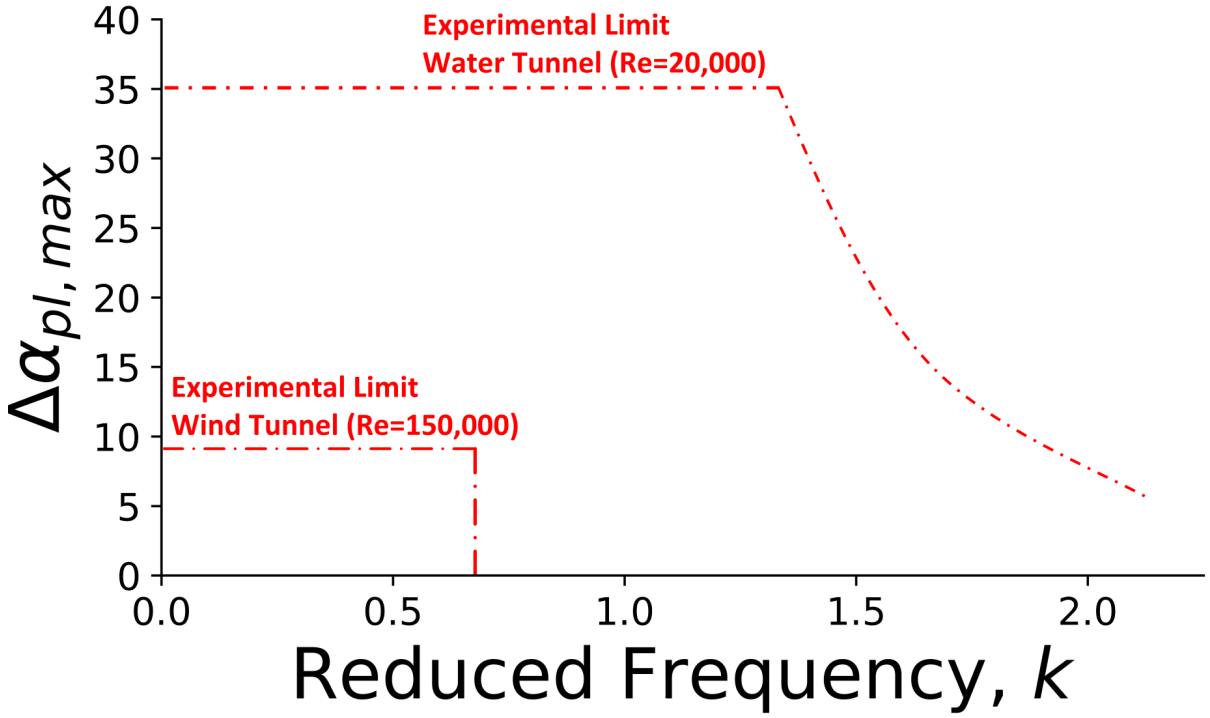

Figure 3-26: Water tunnel and wind tunnel rig capabilities.

Chapter 4

Unsteady Aerodynamics of a Transient Plunging Airfoil

4.1 Summary

This chapter will investigate the unsteady aerodynamic response of airfoils to transient plunging motions. Transient plunging motions have received comparatively little attention to their pitch and surge counterparts and are highly relevant to gust encounters [70, 98, 149, 150] and manoeuvres [92]. Gursul and Cleaver [151] state that unsteady effects are more easily discernible on plunging airfoils as the geometric angle of attack, hence quasi-steady forces and circulation, remains constant. This fundamental study considers the effect of motion amplitude, motion period, geometric angle of attack and airfoil geometry. The measurements include lift, pitching moment and particle image velocity to elucidate the salient features of the aerodynamic response. The largest peak in both lift and pitching moment was observed during the motion for all cases. The peak lift during motion was primarily due to the circulatory component whereas the peak pitching moment was primarily due to the added-mass. These loads increased with effective angle of attack amplitude, yet remained relatively insensitive to motion period. Substantial peaks in the lift and pitching moment were observed at post-stall angles of attack after the end of motion.

This was shown be due to large-scale vortex shedding which appears to be governed by strong interactions between the leading and trailing-edge vortices, leading to a decay in magnitude with time. Both motion amplitude and period showed minimal effect on the frequency of the first vortex shedding cycle, which occurs around the sub-harmonic of the airfoils static shedding frequency. A change in airfoil geometry showed very little change with respect to the aerodynamic loads and the trends in load peak magnitudes/timings were qualitatively similar. Interestingly both airfoils showed a distinct change in vortex shedding frequency, which initiated around the sub-harmonic of the static shedding frequency and gradually increased up to the static value. In terms of the peak magnitudes a fitted exponential curve was shown to best describe the decay. Finally, a potential relationship between the peak magnitude and subsequent cycle frequency was found to follow a linear trend to a reasonable level of correlation, $R^2 = 0.70$.

4.2 Effect of Geometric Angle of Attack

In this Chapter the effect of a single transient motion, as described in Figure 3-3b, on aerodynamic forces and flow fields will be investigated. Cases with a positive $\alpha_{pl,max}$ will be referred to as positive motion whereas cases with a negative $\alpha_{pl,max}$ will be referred to as negative motion, see Figure 4-1.

4.2.1 Force Measurements

The time-histories of ΔC_L and ΔC_M for a positive transient motion, with a typical amplitude ($\alpha_{pl,max} = +25°$) and period ($T = 2.22\tau$), are shown in Figure 4-2a and 4-2b respectively. The x-axis is non-dimensional time, $\tau = U_\infty t/c$, which represents chord lengths travelled. The Δ symbol indicates measurements relative to the static component. Vertical dotted lines are also plotted to indicate the start and end of the motion, with the latter defined as $\tau = 0$. The case presented here is for a NACA 0012 airfoil across a range of geometric angles of attack, α_0. This is a typical case, the main features are generally consistent across the T range but become more pronounced with $\alpha_{pl,max}$, as will be shown in part 4.3.

Consider first the variation of ΔC_L during positive motion in Figure 4-2a. At the onset of motion

all α_0 exhibit a steep gradient reaching a maximum around mid-motion, where a short plateau in the lift response is observed, see region A in Figure 4-2a. The peak lift values initially increase, $\Delta C_{L,Pk} = 2.1, 2.3, 2.3$ for $\alpha_0 = 0, 9, 15°$ respectively before decreasing monotonically, $\Delta C_{L,Pk} = 2.1, 2.0, 1.8, 1.7$ for $\alpha_0 = 20, 25, 30, 35°$ respectively. More significant differences are observed after the peak ($\tau = -1$ to 0), see region B. For $\alpha_0 > 20°$ the relative lift response displays a more rapid decline, even becoming negative for $\alpha_0 = 30, 35°$. Perhaps the most interesting feature during the motion stage is the agreement in lift response across the α_0 range, particularly for $\alpha_0 = 0$ to 20°, despite the drastically different pre-motion flow field conditions, i.e. attached to fully separated flows. It was shown by Chiereghin *et al.* [70] that the flow around a sinusoidally plunging NACA 0012 airfoil at $\alpha_0 = 0°$ will experience separation onset at an effective angle of attack of 25°. For stall and post-stall angles of attack this separation results in a coherent LEV which significantly increases time-averaged lift. A similar effect would be expected here due to the similarities in forcing conditions, transient vs. sinusoidal plunging motion, yet the responses remain remarkably similar. On the other hand, Perrotta & Jones [98] showed excellent agreement in the chord-normal force response, C_N, for a transient plunge manoeuvre across a range of geometric angles of attack, $\alpha_0 = 0°$ to 45°; C_N being the more appropriate force component due to the flat plate geometry tested.

In the post-motion stage, $\tau > 0$, the response of ΔC_L shows distinct differences with α_0, see region C in Figure 4-2a. For $\alpha_0 = 0$ and 9° the lift exhibits a gradual decay to steady-state at $\tau \approx 6$. Minor oscillations can be seen for $\alpha_0 = 0°$ between $\tau = 0$ and 2 which is most likely unaccounted rig/wing vibrations. Interestingly, $\alpha_0 = 9°$ shows a slight negative relative lift between $\tau = 1$ and 4. For the majority of the post-stall cases, $\alpha_0 = 15, 20, 25$ and 30°, the lift response displays significant undulations taking up to 10-12 convective times to approach the steady-state value. At $\alpha_0 = 15°$ the lift response begins to increase at $\tau \approx 1$ to a maximum at $\tau \approx 4$ followed by a gradual decrease approaching steady-state at $\tau \approx 10$. At $\alpha_0 = 20$ and 25° the post-motion lift response shows multiple maxima which is indicative of large-scale vortex shedding. Similar behaviour has been observed by Mulleners *et al.* [103]. The first post-motion peak is larger than for $\alpha_0 = 15°$ and occurs about 1τ prior. The subsequent peak occurs at

$\tau \approx 6$ after a delay of approximately 3.5τ. As a first comparison, the convective time between the two-post motion peaks is in line with transient studies by Mulleners *et al.* [103], Leknys *et al.* [101] and Lorber & Carta [86] who show a similar time delay of 3.5 to 4.5 between lift peaks. For $\alpha_0 = 30°$ the magnitude of post-motion lift peaks is significantly reduced, however the convective time between the two is similar to $\alpha_0 = 20, 25°$. With a further increase to $\alpha_0 = 35°$, the lift response no longer displays the distinct maxima associated with large-scale vortex shedding and rapidly converges to bluff body type oscillations from $\tau > 4$ [101].

Figure 4-2b shows the relative pitching moment response for the same cases as Figure 4-2a. The peak nose-down pitching moment in region D shows a strong dependence on α_0, increasing monotonically from $\Delta C_M = -0.17$ at $\alpha_0 = 0°$ to $\Delta C_M = -0.54$ at $\alpha_0 = 35°$. Similar to the lift response, significant differences are also seen in the aft portion of the motion in region E. At $\alpha_0 = 0°$ the pitching moment displays an equal and opposite nose-up peak. This indicates an attached flow condition, where C_M is independent of the circulatory component and solely dependent on the added-mass [2]. For the transient motion profile in Figure 3-3b, the added-mass component mirrors the acceleration profile, which in this case is a square wave. An increase in α_0 causes a initial suppression of the nose-up peak, where it is completely eliminated for $\alpha_0 = 15$ and 20°. The nose-up peak then gradually returns with further increase in α_0. Shortly after motion cessation, the pitching moment displays another nose-down peak at around $\tau = 0.5$ to 1 for $\alpha_0 = 9$-30°. Figure 4-2b also highlights the large-scale vortex shedding behaviour at post-stall α_0, see region F. The post-motion nose-down peak locations approximately coincide with the corresponding ΔC_L peaks in Figure 4-2a but with a slight delay in τ.

Figure 4-3a and Figure 4-3b present ΔC_L and ΔC_M for the equivalent negative motion case, $T = 2.22\tau$ and $\alpha_{pl,max} = -25°$. Considering first the lift response during motion in Figure 4-3a, similar but inverse behaviour is observed across the range of α_0. A steep drop in relative lift results in a minimum around mid-motion, see region A. The relative lift then sharply increases before exhibiting a more gradual increase to motion cessation at region B. After motion cessation the pre-stall angles of attack $\alpha_0 = 0$ and 9° again show a gradual decay to steady-state by $\tau \approx 6$, whereas all post-stall angles of attack considered display distinct vortex shedding behaviour, see

region C. This vortex shedding results in positive relative lift similar to the positive motion case. Similar to the positive motion case, $\alpha_0 = 15°$ exhibits only a single post-motion peak, albeit more delayed at $\tau \approx 4.5$. As α_0 is increased the first post-motion peak occurs earlier along with the emergence of more vortex shedding cycles that show a reduced magnitude decay with τ. These shedding cycles will be analysed in more detail in 4.2.2 and 4.4.

The pitching moment response for the negative motion case is shown in Figure 4-3b. Less variation over the α_0 range is seen here compared with the positive motion case. In the initial stages of the motion (region D) ΔC_M is in reasonable agreement across all α_0 curves, whereas during the aft portion of the motion (region E) the nose-down peak is suppressed as α_0 is increased. The post-motion stage (region F) shows interesting features in the pitching-moment response, particularly for $\alpha_0 > 20$. The nose-down ΔC_M peaks do not correlate as strongly with the peaks in ΔC_L and instead display two distinct nose-down peaks in quick succession between $\tau \approx 2$ to 6.

4.2.2 Flow Field Measurements

To elucidate the underlying flow structures behind the features presented in Figure 4-2 and Figure 4-3, flow field measurements are presented for positive cases with $T = 2.22\tau$, $\alpha_{pl,max} = +25°$ and $\alpha_0 = 9, 15°$ and $20°$, as well as a negative case for $T = 2.22\tau$, $\alpha_{pl,max} = -25°$ and $\alpha_0 = 15$. The corresponding time-histories of relative lift and pitching moment coefficient are also presented at the top of each figure. On these time-histories the various peaks are highlighted along with the start/end of motion. Also shown is an estimation of the added-mass component using the well-established Theodorsen model [2], which states that the added-mass force is proportional to the product of the plunging acceleration, taken from the rig accelerometer signal, and the mass of a local fluid column with a diameter of one chord length.

The stall case of $\alpha_0 = 9°$ is shown in Figure 4-4. Figure 4-4a presents ΔC_L, Figure 4-4b presents ΔC_M, and Figure 4-4c shows the vorticity flow field with streamlines superposed at different values of τ. The flow fields display clockwise/positive vorticity in red and counter clock-wise/negative vorticity in blue. For this case the motion starts at $\tau = -2.22$. During the

initial acceleration it is clear that the lift and pitching moment increase is dominated by the added-mass component, shown in Figure 4-4a and Figure 4-4b. As the effective angle of attack increases between $\tau = -1.7$ and -1.4, the upper surface shear layer begins to roll-up into small coherent structures. At this point a maximum nose-down pitching moment is observed, denoted as M1 in Figure 4-4b. By $\tau = -1.1$ a coherent LEV has formed whilst the small structures from the initial shear layer are shed into the wake. At this point in the motion the airfoil is producing the maximum ΔC_L, denoted as L1 on Figure 4-4a. The relative lift time-history shows that the circulatory lift is the most dominant component of ΔC_L at L1, with the added-mass contributing a relatively small amount. Once the maximum ΔC_L has been reached the lift drops rapidly due to both the sign change in added-mass and the decreasing α_{pl} induced by the motion. At $\tau = -0.8$ a region of counter-clockwise vorticity between the vortex and airfoil is generated which accumulates beneath the feeding shear layer. The counter-clockwise vorticity appears to intersect and cut off the feeding shear layer [47, 72] prior to shedding at $\tau = -0.3$. At this instant of τ the circulatory force is directly counteracted by the large negative added-mass component resulting in a small positive ΔC_L. This lift is sustained for a short period after $\tau = 0$, presumably due to the influence of the LEV still convecting over the airfoil. Between $\tau = 1$ and 5 the relative lift exhibits a slight negative value, which coincides with the partially separated shear layer reattaching to the upper surface.

The impact of the LEV is also apparent in the pitching moment measurements. The added-mass prediction shows an approximately constant value of $\Delta C_M \approx -0.4$ during the acceleration phase; followed by an approximately constant value of $\Delta C_M \approx 0.4$ during the deceleration phase. During the acceleration phase from $\tau = -2.2$ to -1.1, ΔC_M demonstrates similar trends to the added-mass. However during the deceleration phase from $\tau = -1.1$ to 0.0, there is a significant difference, with the experiment consistently exhibiting a lower pitching moment. Once the motion is complete at $\tau = 0$, ΔC_M demonstrates a distinct nose-down spike. These artefacts correlate with the inception of the LEV at $\tau \approx -1.7$, its growth from $\tau \approx -1.7$ to -0.5, and subsequent detachment and convection from $\tau > -0.5$. As the LEV convects over the upper surface, it moves further from the quarter-chord point producing a larger nose-down ΔC_M which can be

seen in Figure 4-4b. When the LEV moves over the trailing-edge it triggers the formation of a TEV which coincides with the distinct nose-down ΔC_M peak between $\tau = 0.0$ and 1.0. The LEV/TEV pair then shed into the free-stream as the well documented "mushroom" shape dipole [72, 152] visible at $\tau = 1.0$. Past this point the streamlines indicate some separation on the upper surface which corresponds with the reduced lift between $\tau = 1.0$ and 6.

Figure 4-5 presents the same T and $\alpha_{pl,max}$ but with α_0 increased to 15°. Before the motion starts at $\tau = -2.2$ the flow is in a fully separated state, indicated by the separated shear layers from the leading and trailing-edge. At motion inception the lift and pitching moment response is once again dominated by the added-mass component. By $\tau = -1.7$ the leading and trailing-edge shear layers have started to roll-up into distinct vortices and the remaining shear layer aft of the vortices begins to shed into the wake. L1 once again occurs at $\tau = -1.1$ where there is a strong LEV at the leading-edge. A striking difference between this case and $\alpha_0 = 9°$ is the LEV position, which is further above the upper surface and further downstream. As the motion progresses the gap between the vortex and the upper surface increases considerably compared with $\alpha_0 = 9°$ and the feeding shear layer is dragged upwards. Due to the increased vertical distance of the LEV, less counter-clockwise vorticity is generated at the airfoil surface. Despite this, the feeding shear layer is still cut off by $\tau = -0.5$. At $\tau = 0.0$ the LEV has reached the trailing-edge and promotes the roll-up of the trailing-edge shear layer into a new TEV [63]. A reduced nose-down pitching moment is observed compared with $\alpha_0 = 9°$ at $\tau = 0.5$, the cause of which is unclear. By $\tau = 0.5$ the LEV has been completely shed and the TEV is fully formed. At this point the lift and nose-down pitching moment begin to steadily increase, resulting in a maximum ΔC_L at $\tau = 4.0$ (L2) and ΔC_M at $\tau = 4.2$ (M2). The flow field indicates that this is due to a secondary, less coherent LEV that forms over the entire airfoil upper surface. The inception of this vortex can be traced back to $\tau = 0.0$ where the feeding shear layer interacts with the counter-clockwise vorticity kicked up by the primary LEV. The shear layer propagation is momentarily retarded by this flow which results in the accumulation of clockwise vorticity [47]. The streamline reattachment in the leading-edge region gradually spreads across the upper surface, marking the inception and growth of the secondary LEV. It is believed that streamline

reattachment is also promoted by the induced downwash from the coherent TEV at $\tau = 1.0$. The secondary LEV is then shed around $\tau \approx 5.0$ inducing a much weaker tertiary TEV which appears to have no further distinguishable effect on the upstream leading-edge shear layer.

Figure 4-6 shows the same forcing parameters as Figure 4-4 and Figure 4-5 but with α_0 increased to 20°. The vorticity distribution for the first portion of the motion is very similar to that of $\alpha_0 = 15°$, see Figure 4-5c, however at $\tau = -1.1$ the LEV is lifted further from the upper surface, suggesting that LEV vertical position is a function of α_0. Despite the increased distance L1 is similar to $\alpha_0 = 9, 15°$. In the aft portion of the motion the LEV position remains marginally higher than for $\alpha_0 = 15°$, see Figure 4-5c and Figure 4-6c. As the LEV passes the trailing-edge a strong nose-down pitching moment peak occurs in Figure 4-6b at $\tau \approx 0.5$. The LEV triggers the formation of a secondary TEV which appears somewhat stronger when compared with $\alpha_0 = 15°$. The inception and growth of the secondary LEV is similar to Figure 4-5c between $\tau = 0.0$ and 1.0, however its propagation occurs at a greater rate. By $\tau = 3.0$ the secondary LEV has fully formed, corresponding to the peak in both lift (L2) and nose-down pitching moment (M2). The vorticity distribution shows a more coherent vortical structure, giving rise to a larger peak in lift and nose-down pitching moment. A tertiary TEV is then formed as the secondary LEV passes over the trailing-edge, which in turn influences the leading-edge shear layer, promoting further roll-up. A weaker third peak in relative lift (L3) and nose-down pitching moment (M3) can be seen at $\tau \approx 6$, corresponding to the formation of a weaker tertiary LEV. This vortex shedding process is damped out at around 12 convective times where the lift and pitching moment approach steady-state. This damping behaviour is not a result of the ensemble averaging process and shows the same behaviour in the instantaneous results, matching similar studies [101, 103].

It is evident from the flow field measurements that the distinct fluctuations in aerodynamic loads at post-stall angles of attack are caused by large-scale vortex shedding which is triggered by the LEV formed during motion. Through comparison of the positive motion flow fields for $\alpha_0 = 15°$ and $\alpha_0 = 20°$, Figures 4-6c and 4-5c, it can be seen that the post-motion increase in lift is caused by the same mechanism, yet $\alpha_0 = 15°$ only shows a single shedding cycle whereas $\alpha_0 = 20°$ displays two shedding cycles. The reason for this remains unclear, however Manar *et*

al. [96] postulate that this is likely due to a lack of vortex circulation necessary for strong vortex shedding.

A negative motion case equivalent to Figure 4-5 is presented in Figure 4-7 to elucidate the mechanism for the post-motion peaks. During the acceleration phase the leading-edge shear layer is pushed back onto the airfoil surface resulting in flow reattachment. The reattachment point propagates downstream towards the trailing-edge from $\tau = -1.7$ to -0.5. At this point a small trailing-edge vortex has formed, presumably due to the proximity of the deflected leading-edge shear layer. At motion cessation, the flow appears to be fully attached across most of the chord and the lift begins to increase almost linearly. During this time the clockwise positive vorticity on the upper surface begins to roll-up into small coherent structures, as seen at $\tau = 1.0$. At $\tau = 2.0$ these are shed into the wake as indicated by a small roll-up in the trailing-edge shear layer, and the upper surface vorticity begins to accumulate just aft of the leading-edge. From $\tau = 2.0$ to 3.0 this region of vorticity propagates downstream and begins to lift off, forming a distinct vortex over the upper surface. This bears strong resemblance to $\tau = 4.0$ for the positive case in Figure 4-5 and produces a similar magnitude peak in both lift (L2) and nose-down pitching moment (M2). A TEV is induced as the LEV passes the trailing-edge between $\tau = 5.0$ and 6.0 but, like the positive case, this has no further discernible impact on the loads.

From this example it is evident that vortex shedding for negative motion is triggered by flow reattachment as the airfoil is translated upwards into its separated wake, followed by dynamic flow separation. The flow field development is reminiscent of a typical dynamic stall event; attached flow beyond its static stall angle, shear layer roll-up and the emergence of a coherent vortical structure. Unlike the positive motion case, the vortex shedding cycles are not dependent on the LEV formed during the motion, but on the degree of flow reattachment; this helps explain why strong vortex shedding is still observed for $\alpha_0 = 35°$. The first post-motion peak seen in Figure 4-3 begins to decrease beyond $\alpha_0 = 25°$ which suggests the flow is only partially reattaching prior to vortex formation. The results indicate an $\alpha_{eff,min} <= 0$ is required for full flow reattachment, however this will most likely be highly dependent on motion period, T.

4.3 Motion Period and Amplitude Effects

This section will explore the effects of plunging kinematics on the aerodynamic loads response; namely the motion period, T, and amplitude, $\alpha_{pl,max}$. The results focus on α_0 between 0° and 20° and the data has been reduced to the peak relative lift and pitching moment values, denoted $\Delta C_{L,Pk}$ and $\Delta C_{M,Pk}$ respectively. Once again, L1/M1 refers to the peak load during motion, L2/M2 is the first post-motion peak associated with the vortex shedding cycle and L3/M3 is the subsequent vortex shedding peak. The test matrix consists of motion period, T, from 1.67τ to 20τ and amplitude, $\alpha_{pl,max}$, from $-30°$ to 30°. Values of large T and $\alpha_{pl,max}$ could not be tested due to the constraint in displacement amplitude, i.e., proximity of the water tunnel walls.

Figure 4-8 presents the relative lift and pitching moment coefficients for L1/M1, L2/M2 and L3/M3 plotted against $\alpha_{pl,max}$ for each T across the α_0 range. Consider first the distribution of $\Delta C_{L,Pk}$, for L1 at each α_0. The lift is relatively insensitive to T at every α_0 for both positive and negative motions and shows a monotonic variation with $\alpha_{pl,max}$. An insight into this insensitivity can be gained by considering the total lift force as the sum of its circulatory and added-mass components. In 4.2.2 it was shown that the more dominant component of lift at L1 was circulatory through comparison of the relative lift response with the estimated added-mass contribution. This was only marginally affected by separation and the onset of LEV formation as shown by the similar lift response across α_0 during the motion. As a result, the lift variation up to L1 can be considered as a build up of circulation with the added-mass force superposed [94]. As the motion period decreases, the growth of the circulatory component begins to lag whilst the added-mass component increases due to higher accelerations, resulting in a similar net lift force.

In terms of pitching moment, Figure 4-8 shows a distinct difference of M1 between geometric angles of attack. For $\alpha_0 = 0°$, $\Delta C_{M,Pk}$ monotonically decreases with $\alpha_{pl,max}$. As α_0 is increased to stall and post-stall angles the negative motion peaks follow a similar monotonic trend, whilst the positive motion peaks decrease further, particularly at high T. The cause of this inversion with respect to T is not currently clear, but is most likely due to the influence of the LEV. From Figures 4-4, 4-5 and 4-6 it is observed that M1 coincides with the formation of the initial TEV,

which has been documented to induce a low pressure at the trailing-edge [63]. In contrast to the lift at L1, the pitching moment does not collapse as well with T, see Figure 4-8.

The results for L2/M2 are plotted for post-stall angles of attack and are indicated by a dashed line, see Figure 4-8. Note that a second peak was not observed for pre-stall and stall α_0. For both lift and pitching moment the curves show insensitivity to T, particularly at the higher amplitudes. Interestingly L2 and M2 both show distinctly different trends for positive and negative motions. This reflects the findings of 4.2.2 for which different flow field mechanisms were responsible for the upper surface vortex at L2/M2. For positive motion a monotonic increase can be seen, similar to L1/M1 albeit with a lower gradient. It was shown in Figures 4-5 and 4-6 that the secondary vortex formed due to leading-edge shear layer interaction with the primary LEV, and subsequently triggered TEV, suggesting that the secondary vortex strength at L2/M2 is dependent on the strength of the primary LEV. Figure 4-8 maintains this suggestion as the trend of L2/M2 closely resembles that of L1/M1. On the other hand, L2/M2 for the negative motion cases quickly saturate to a near constant value. The point of lift and moment saturation changes with α_0; $\alpha_{pl,max} \approx -10^\circ$ for $\alpha_0 = 15^\circ$ and $\alpha_{pl,max} \approx -15^\circ$ for $\alpha_0 = 20^\circ$. Figure 4-7 showed that the post-motion peak was a result of flow reattachment followed by the emergence of an upper surface vortex. The results in Figure 4-8 suggest that, in a quasi-steady sense, as long as the total effective angle of attack is sufficient to fully reattach the flow, no additional increase in L2/M2 can be achieved with increasing amplitude.

For L3/M3, Figure 4-8, the same trends as L2/M2 are observed at $\alpha_0 = 20^\circ$ across all motion periods and amplitudes. The similarities of the peak magnitude trends highlight the dependence of L3/M3 on L2/M2. A stronger vortex over the upper surface of the airfoil at L2/M2 will induce stronger subsequent vortex shedding cycles.

One of the most striking features of Figure 4-8 is the similarity in L1 across all α_0, despite the drastically changing flow fields from pre- to post-stall conditions. Figure 4-9a compares L1 for $\alpha_0 = 0, 5, 9, 15$ and 20° where a remarkable collapse can be seen, particularly for the positive motion cases; the negative cases show a slight gradient change as α_0 is increased. A theoretical lift

prediction is also shown in Figure 4-9a which is defined by $2\pi\alpha_{pl,max}$; this provides a reasonable prediction of maximum possible lift during motion, in line with the findings of Chiereghin *et al.* [70]. Of course, the lift at L1 is normalised only by the free-stream velocity and does not take into account the additional dynamic pressure produced by the velocity of the motion. Figure 4-9b shows the re-normalised lift peak with the maximum plunge velocity during motion, defined as:

$$C_{L_{,L1,mod}} = \frac{L}{\frac{1}{2}\rho\sqrt{U_\infty^2 + V_{pl,max}^2}S} \tag{4.1}$$

where $V_{pl,max}$ is the maximum plunge velocity. As expected the gradient of L1 is reduced by the re-normalisation. At $\alpha_{pl,max} = 30°$ the L1 magnitude has dropped from $\Delta C_{L_{,L1}} \approx 3$ to ≈ 2. The theoretical $2\pi\alpha_{pl,max}$ curve now over predicts the lift response considerably.

Figures 4-10 look at the peak timings across the parameter space for pre- and post-stall α_0 respectively. These are denoted by $\tau_{\Delta C_{L,Pk}}$ and $\tau_{\Delta C_{M,Pk}}$, where $\tau = 0$ is the end of the motion. The timing information for the peak magnitudes can be very sensitive to signal noise, particularly at low peak magnitudes. Where no meaningful peak timing could be detected, the data point was omitted. Consider first the timing for L1/M1 at $\alpha_0 = 0, 9, 15, 20°$ in Figure 4-10. All measurements show L1 and M1 is dictated by the motion for both lift and pitching moment. The spread of L1/M1 with T is a manifestation of the motion being defined so that it ends at $\tau = 0$. L1 occurs approximately around mid-motion with some deviation at higher T, which is most likely due to measurement noise. For the pitching moment M1 occurs marginally sooner, with the exception of $\alpha_0 = 9°$ at higher values of T.

The timings of L2 and M2 are shown in Figure 4-10 for $\alpha_0 = 15, 20°$. For positive and negative motion the times of L2/M2 are on average later for a decreased T and show more variation at lower values of $\alpha_{pl,max}$. Consider first the positive motion. From the discussion in section 4.2.2, L2/M2 was shown to occur once the initial LEV had reached the trailing-edge, triggering a secondary TEV. As a first approximation, the convection speed of the LEV can be assumed

constant. A lower T would therefore mean the LEV would be at a greater distance from the trailing-edge at $\tau = 0$, taking a longer time to reach the trailing-edge and trigger the secondary TEV. This behaviour is more or less reflected in Figure 4-10 and is once again an artefact of the $\tau = 0$ definition. Deviation from this trend occurs at higher $\alpha_{pl,max}$ magnitudes, particularly for L2. For $\alpha_0 = 15°$ a lower T produces a slightly later peak in lift and pitching moment for positive motion. The cause of this is unclear at this time, but could be linked to the influence of initial LEV strength on the vortex convection speed [77]. For the negative motion cases this dependency on T is most likely due to the finite response time of the flow. A lower T means the flow will have had less time to respond to the changing α_{pl} and so would take a relatively longer time to develop into a post-motion LEV, as seen in Figure 4-10. The peak locations for negative motion also tend to converge at high $\alpha_{pl,max}$ values. For $\alpha_0 = 20°$ the peak locations for lift and pitching moment display the same relation with T and $\alpha_{pl,max}$, with the peaks occurring approximately one convective time prior to that of $\alpha_0 = 15°$. The influence of α_0 on the timing of L2/M2 has been shown in Figure 4-6 to be due to an earlier roll-up of the leading-edge shear layer and occurs across the whole parameter range. Another interesting feature of the peak timings is the effect of amplitude. For the negative cases, L2 and M2 occur significantly earlier for lower amplitudes, mirroring the trend seen in L2/M2 magnitude shown in Figure 4-8 and is likely due to only partial flow reattachment. The positive motion cases on the other hand display a much lower sensitivity to $\alpha_{pl,max}$.

The timing of L3 closely follows the trend of L2, reflecting the large-scale vortex shedding behaviour. Figure 4-10 displays a near constant gap between L2 and L3 at around 3 to 3.5τ which indicates a roughly constant shedding frequency. This represents a fundamental frequency of large-scale vortex shedding and can be linked to the optimal time for vortex formation, as reported in [153]. As an example case, the shedding frequency for $\alpha_0 = 20°$, $T = 2.22\tau$ and $\alpha_{pl,max} = +25°$ is $St_c = 0.32$; which is taken as inverse of the convective time between the two peaks. Converting this to a modified Strouhal number based on the projected area of the airfoil, defined as:

$$St_{c,mod} = \frac{f \cdot c \cdot sin(\alpha_0)}{U_{\text{inf}}} \tag{4.2}$$

yields a value of 0.11; suggesting that this is a sub-harmonic of the static, bluff-body shedding frequency, $St_{c,mod,\alpha_0} \approx 0.17$ to 0.20 [9]. This is plotted in Figure 4-11 as the modified Strouhal number, $St_{c,mod}$, against plunge amplitude, $\alpha_{pl,max}$. It is important to note that some results were omitted from this Figure where a definitive peak location could not be accurately determined. The results show shedding to occur at $St_{c,mod} \approx 0.11$ for the majority of the test cases. This corresponds to the sub-harmonic of the static shedding frequency which was measured to be $St_{c,mod,\alpha_0} = 0.20$.

4.4 Effect of Airfoil Geometry

To further investigate the vortex shedding behaviour, this section will compare the aerodynamic loads of a NACA 0012 airfoil to a flat plate geometry, see Figure 3-2, for the same forcing conditions as 4.2. The flat plate geometry has a sharp leading-edge to deliberately enforce flow separation. In particular this section will provide a more detailed investigation of the trends through data reduction. As shown in Figure 4-12, the typical flat plate aerodynamic response shares the same key features as the NACA0012 in terms of load peaks.

Figure 4-13 presents the results of both the NACA 0012 and flat plate geometry for the positive and negative motion cases presented in the previous section; $T = 2.22$ and $\alpha_{pl,max} = -25, +25°$ for $\alpha_0 = 0, 5, 9, 15, 20, 25, 30, 35°$. Figure 4-13a shows $\Delta C_{L,Pk}$ for the NACA 0012 and flat plate airfoil for positive motion. Qualitatively $\Delta C_{L,Pk}$ shows reasonable agreement between the two geometries; the magnitude of L1 marginally decreases for both as α_0 is increased and L2/L3 show a strong dependency on α_0. A few minor discrepancies however can be seen. For positive motion at low α_0, the NACA 0012 exhibits a small increase in $\Delta C_{L,Pk}$ from $\alpha_0 = 0°$ to 9° before gradually decreasing up to $\alpha_0 = 35°$. The flat plate shows a greater $\Delta C_{L,Pk}$ at $\alpha_0 = 0°$ which continually decreases with α_0. For L2 the NACA 0012 displays an increase in $\Delta C_{L,Pk}$ before dropping significantly at $\alpha_0 = 30°$, as discussed previously. The flat plate however shows a more

gradual decrease in $\Delta C_{L,Pk}$ from $\alpha_0 = 15°$ and in general shows a lower magnitude, particularly at $\alpha_0 = 20°$. Interestingly the flat plate also displays a second peak in lift at $\alpha_0 = 9°$. From the data presented in 4.2.2, this is presumably due to flow separation present over the flat plate in its steady-state condition due to the sharp leading-edge. For the negative motion case in Figure 4-13b, the two airfoil geometries show better agreement, particularly for L2.

The equivalent pitching moment peaks are presented in Figure 4-13b and 4-13d. Again, the two geometries show reasonable agreement in M1, M2 and M3. The most striking difference for M1 is at low values of α_0 where the flat plate consistently shows a larger nose-up pitching moment during the negative motion. The trends for M2 and M3 bear a strong resemblance to their L2 and L3 counterparts but inverted, indicating that both are determined by the same phenomenon, i.e., the strength of the LEV.

The timings of the load peaks presented in Figure 4-13 are shown in Figure 4-14. These are denoted by $\tau_{\Delta C_{L,Pk}}$ and $\tau_{\Delta C_{M,Pk}}$, where $\tau = 0$ is the end of the motion. Where no meaningful peak timing could be detected, the data point was omitted. Overall the two geometries show similar trends and peak timing values. For both $\tau_{\Delta C_{L,Pk}}$ and $\tau_{\Delta C_{M,Pk}}$, L1 and M1 remain roughly constant with α_0. This peak occurs around mid-motion for L1 and marginally earlier for M1. The timings for L2/M2 and L3/M3 also show very similar trends. The most distinct difference between the geometries can be seen in the pitching moment for negative motion, see Figure 4-14d, where the flat plate displays a much earlier occurrence of M2 and M3. Between $\alpha_0 = 20°$ and 30° the timing gap remains roughly constant as a result of the vortex shedding phenomenon; the vortices form and shed on their convective time-scale, independent of the motion.

Up to this point only the magnitudes and timings of the first three peaks have been considered. It has been shown previously in Figures 4-2 and 4-3 that additional shedding peaks can emerge, particularly at high α_0. The timing between L2 and L3 in Figure 4-14 exhibits a roughly constant value of 3.5 to 4 convective times, and once again, represents the fundamental frequency of large-scale vortex shedding. This result is interesting, as logically the frequency must change with time to eventually match the bluff-body shedding frequency. This behaviour has been qualitatively

shown in the study by Leknys *et al.* [101], who observed the change from large-scale to bluff-body vortex shedding on a flat plate. To demonstrate this behaviour, Figure 4-15 shows the shedding frequency of each cycle measured using a peak magnitude detection. The timing of each shedding cycle is taken as the central τ between shedding peaks. Also indicated on the graphs are the static shedding frequency bands defined by the maximum and minimum shedding frequency measured in the lift signal for static post-stall angles of attack. This frequency was obtained through Fast Fourier Transform (FFT) and are in agreement with the measurements of Rojratsirikul *et al.* [9].

Figure 4-15 presents the shedding frequency change for the NACA 0012 airfoil. At $\alpha_0 = 20°$ and 25° the shedding frequency is very similar for both positive and negative motions and sits between $St_{c,mod} = 0.11$ to 0.12. A slightly higher shedding frequency can be seen for $\alpha_0 = 30°$ and 35° for the negative motion cases. For positive motion at $\alpha_0 = 30°$ the shedding frequency is much higher and close to the static shedding frequency. From the lift time-history of this case in Figure 4-2a it was seen that the shedding peaks were much lower in magnitude and not necessarily considered *strong* vortex shedding. Beyond the first shedding cycle the frequency asymptotically approaches the static frequency band by around 15 to 20 convective times. Due to the increased decay rate for $\alpha_0 = 20, 25°$ a limited number of cycles were available.

The results of the flat plate airfoil are presented in Figure 4-15b where similar features can be seen. More data points were available for the flat plate as its sharp leading-edge facilitates additional shedding cycles. The shedding frequency still shows an increase with convective time up to the static frequency band, however the trend is more linear. By the end of the data presented the frequency is marginally under the static band.

Through comparison with similar transient studies it can be seen that remarkably similar vortex shedding phenomena can occur for different transient motions, such as plunge, pitch and surge. In general the post-motion peaks caused by vortex shedding show both a sub-static shedding frequency and a magnitude decay. With this in mind, Figure 4-16 directly compares the experimental data with relevant transient studies [86, 101, 103, 106, 107] to highlight the generalities

of vortex shedding behaviour. The studies cover a range of transient motions, airfoil geometries, wing aspect ratios and angles of attack, see table 4.1. The data was extracted through plot digitisation where the peak values were selected. It is also important to note that for some cases the static lift and static shedding frequency had to be estimated based on typical values to use for normalisation. However, despite these large uncertainties Figure 4-16 still serves to highlight commonality between different vortex shedding studies.

Table 4.1: Transient studies used for data extraction.

Study	**Airfoil geometry**	**Aspect Ratio**	**Motion**	α_0	**Reynolds number**
Rosti *et al.* [106]	NACA 0020	2D (Numerical)	Plunge Ramp	20°	20,000
Mulleners *et al.* [103]	Flat Plate	6	Surge Acceleration	30°	22,500
Lorber & Carta [86]	SSC-A09	2D	Pitch Ramp	30°	2,000,000
Leknys *et al.* [101]	Flat Plate	2D	Pitch Ramp	$20, 25, 30, 40°$	20,000
Son *et al.* [107]	Flat Plate	6,8	Pitch Ramp	45°	10,000

Figure 4-16a presents a comparison of the normalised peak magnitude decay with τ. The y-axis is defined as the relative peak lift normalised by the relative peak lift of the first and largest shedding peak. Reasonable collapse can be seen across the studies and a distinct trend in peak magnitude decay is evident. Mulleners *et al.* [103] quantified this decay by using a fitted exponential decay and showed excellent agreement with experimental results. They observed a delay of $\tau \approx 20$ after motion cessation for the forces to relax to 10% of the maximum lift peak. The fitted exponential curve in Figure 4-16a takes into account the entire data set and shows a relaxation time of $\tau \approx 15$; this difference is to be expected due the variety of testing conditions, particularly α_0. To highlight this effect the same data is plotted in Figure 4-16b but coloured by α_0. Separate exponential decays are also plotted for each α_0. On average a higher rate of decay can be seen for $\alpha_0 = 20, 25°$, which corresponds to the current study and the results of Leknys *et al.* [101]. The computational study by Rosti *et al.* [106] shows one of the lowest decay rates

despite occurring at $\alpha_0 = 20°$. This is possibly due to the spanwise periodic boundary conditions used in the simulation leading to more spanwise coherent structures [154] that are able to induce stronger subsequent vortices. As a result, this was omitted from the exponential decay fit. It is evident that the decay rate is not attributable to a single parameter. The shedding process is due to a strong interaction between the leading and trailing-edge vortices which depend on wing kinematics, Reynolds number and geometry. The exact mechanism for the decay is not clear from the data presented here. Mulleners *et al.* [103] attribute the decay to the movement of the formation and interaction region between the LEV and TEV, however there is insufficient temporal resolution in the PIV images to corroborate this.

Figure 4-16c presents a comparison of the normalised shedding frequency. The y-axis is defined as the local shedding frequency normalised by the static shedding frequency. A distinct change in frequency can be seen for the majority of the cases, starting from $St_{c,mod}/St_{c,mod,\alpha_0} \approx 0.55$ to 0.75 and gradually increasing to the static shedding frequency by $\tau \approx 15$ to 20. The study by Rosti *et al.* [106] displays very little change in frequency and remains around the sub-harmonic for the data presented. Once again this is possibly due to the use of spanwise periodic boundary conditions in the simulation. The reason for spread in frequency for the first shedding cycle is interesting but not currently clear. Figure 4-16d plots the same data coloured by α_0, however no clear trends can be distinguished.

The results shown in Figure 4-16 suggest a possible correlation between peak magnitude and shedding frequency; that is the higher the shedding peak magnitude, the lower the subsequent shedding frequency. This idea is explored in Figure 4-17a where the normalised peak magnitude is plotted against the normalised shedding frequency. The frequency here is taken as the forward difference from the local peak, the idea being that the local peak magnitude influences the frequency of the next shedding cycle. Figure 4-17a shows marginal collapse, but is marred by the choice of peak normalisation, which does not represent an absolute magnitude to compared with other cases. In Figure 4-17b the relative lift peaks, $\Delta C_{L,Pk,n}$, are normalised by the difference between $2\pi\alpha_0 \cdot cos(\alpha_0)$ and the corresponding static lift coefficient, C_{L,α_0}. By normalising in this way an assumption is made which effectively states that the theoretical maximum circulatory

lift is equal to $2\pi\alpha_0 \cdot cos(\alpha_0)$, whether the circulation is contained within the boundary layer or an upper surface vortex [94]. $2\pi\alpha_0$ is multiplied by the cosine of α_0 to reflect the fact that vortex lift acts primarily in the chord normal direction [95]. Although this is a somewhat crude normalisation it serves to scale the lift peaks to enable an initial comparison. Figure 4-17a shows there is a moderate correlation between the normalised peak magnitude and shedding frequency, with $R^2 = 0.70$. The linear fit suggests a sub-harmonic shedding frequency when the peak magnitude is close to the assumed theoretical maximum. This indicates that the shedding immediately after the initial disturbance starts at the sub-harmonic, quickly increasing to the static shedding frequency as the peak magnitudes decay.

4.4.1 Conclusions

Lift, pitching moment and flow field measurements have been conducted for a NACA 0012 and flat plate airfoil undergoing transient plunging motions across a large parameter space. The key findings are summarized as follows:

- During motion the peak lift was found to be primarily due a build up of the circulatory component. Conversely the peak pitching moment magnitude was found to be primarily dependent on the added-mass force. The peak loads showed an increase with effective angle of attack amplitude, yet remained relatively insensitive to motion period.

- For post-stall angles of attack significant undulations in the post-motion load time-histories were observed for both positive and negative motions. Flow field measurements revealed this to be caused by large-scale vortex shedding, in which the shedding of a leading-edge vortex triggers the formation of a trailing-edge vortex which in turn triggers the formation of a new leading-edge vortex. This process is repeated until there is sufficient decay where no new vortex is formed.

- The frequency of the first post-motion, large-scale vortex shedding cycle was found to correspond to the sub-harmonic of the static shedding frequency. This holds relatively constant for all motion periods and amplitudes tested.

- A distinct change in frequency occurs during large-scale vortex shedding. It was shown that subsequent shedding cycles increase in frequency from the sub-harmonic to the static shedding frequency within 10 to 20τ. This phenomenon was also shown to occur for similar transient studies in literature.

- The vortex shedding lift peaks were shown to follow an exponential decay and agreed well with other examples in literature. A possible link between peak magnitude and subsequent cycle frequency was explored and showed a reasonable correlation with a linear fit, with $R^2 = 0.70$.

- There was minimal difference between the NACA 0012 and flat plate airfoil geometry. Both showed similar qualitative trends in peak loads and timings.

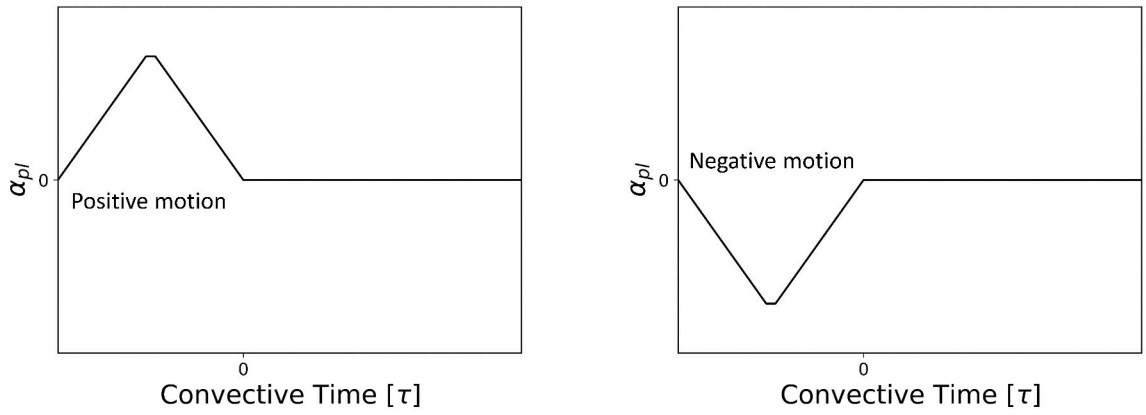

Figure 4-1: Profile of motion induce angle of attack, α_{pl}, for positive and negative motions with convective time $\tau = tU_\infty/c$.

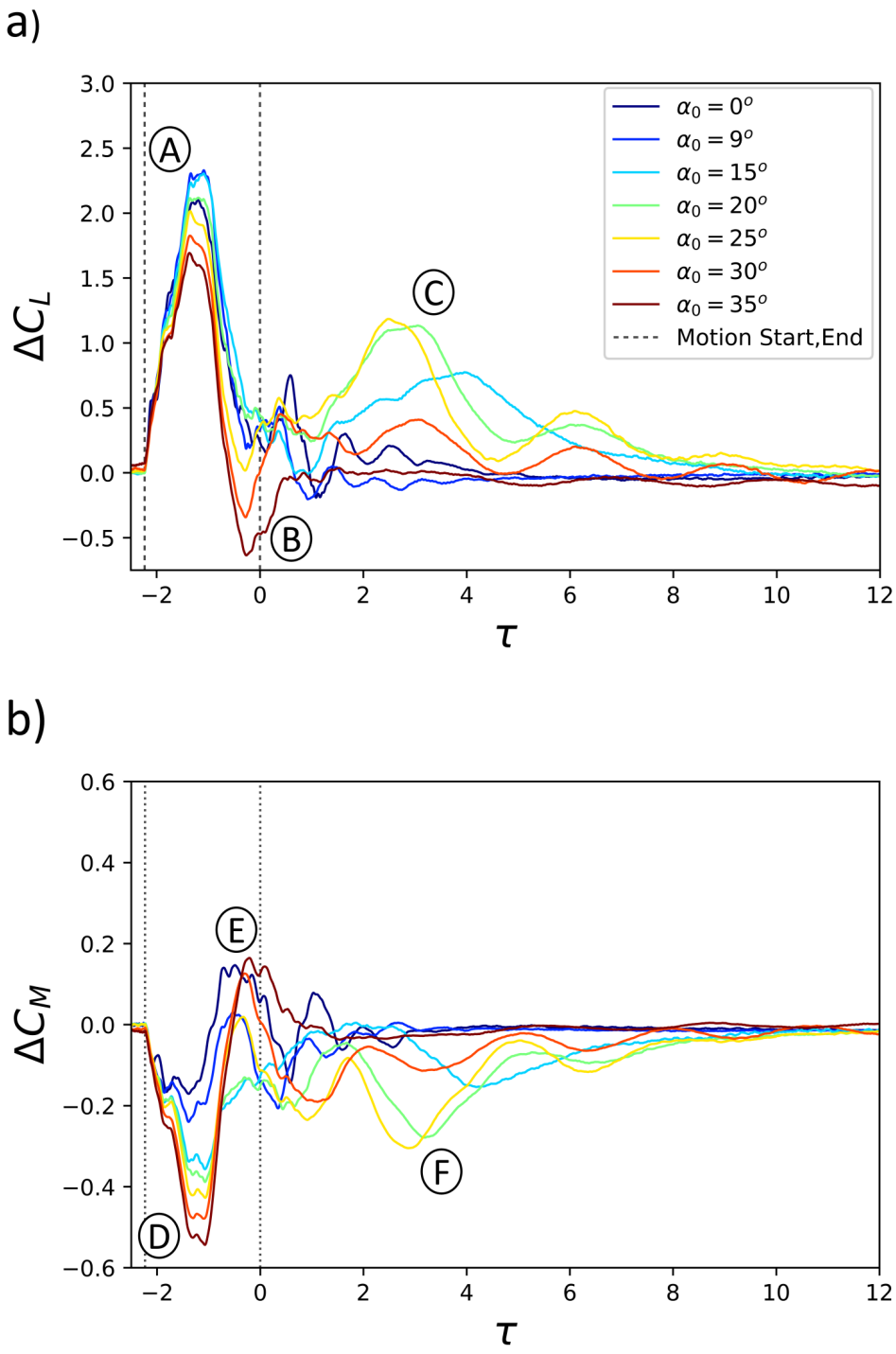

Figure 4-2: NACA 0012 positive motion: a) Relative lift and b) relative moment coefficient time histories. $\alpha_0 = 0, 9, 15, 20, 25, 30°$, for $T = 2.22$, $\alpha_{pl,max} = +25°$.

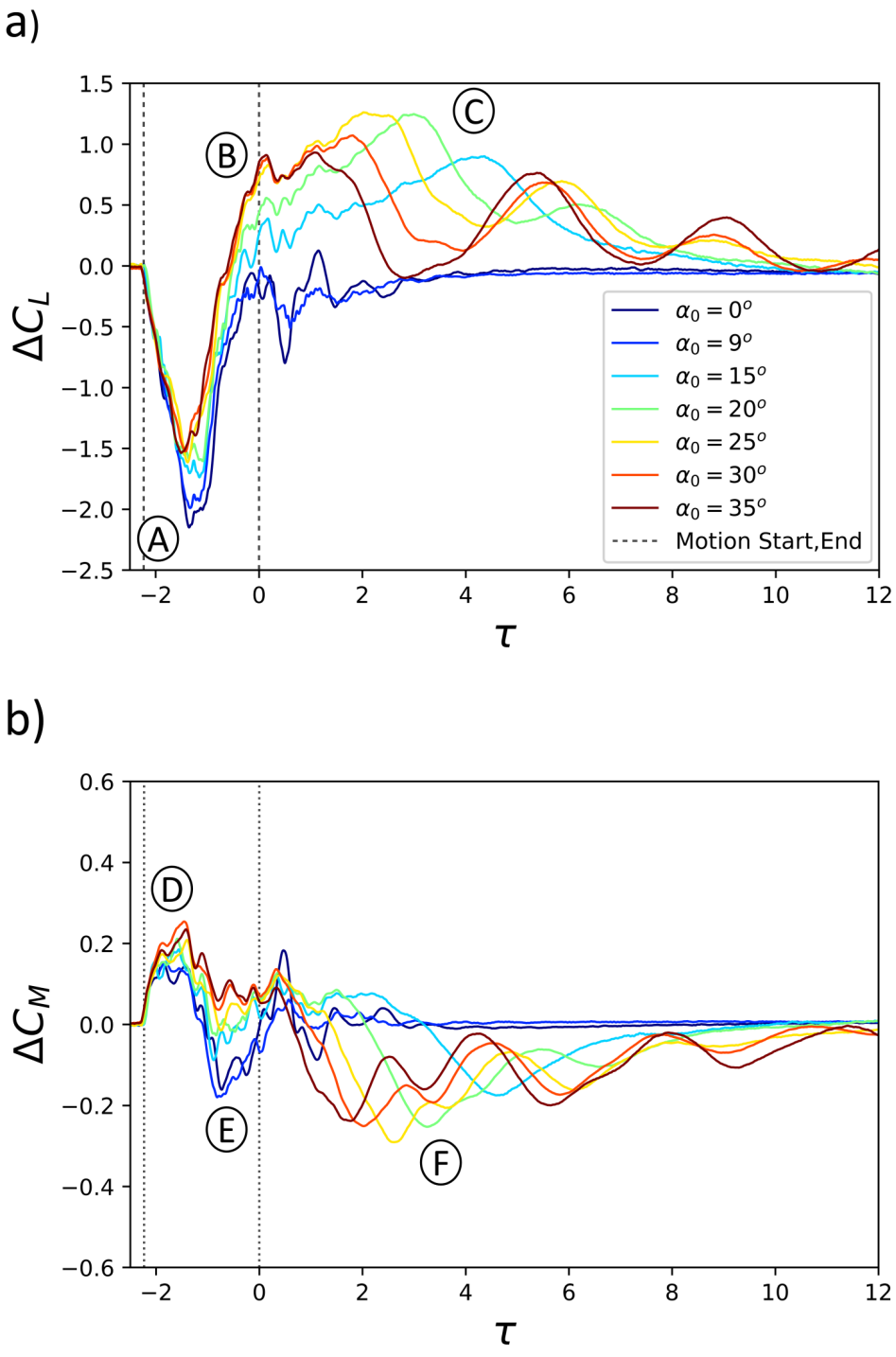

Figure 4-3: NACA 0012 negative motion: a) Relative lift and b) relative moment coefficient time histories. $\alpha_0 = 0, 9, 15, 20, 25, 30°$, for $T = 2.22$, $\alpha_{pl,max} = -25°$.

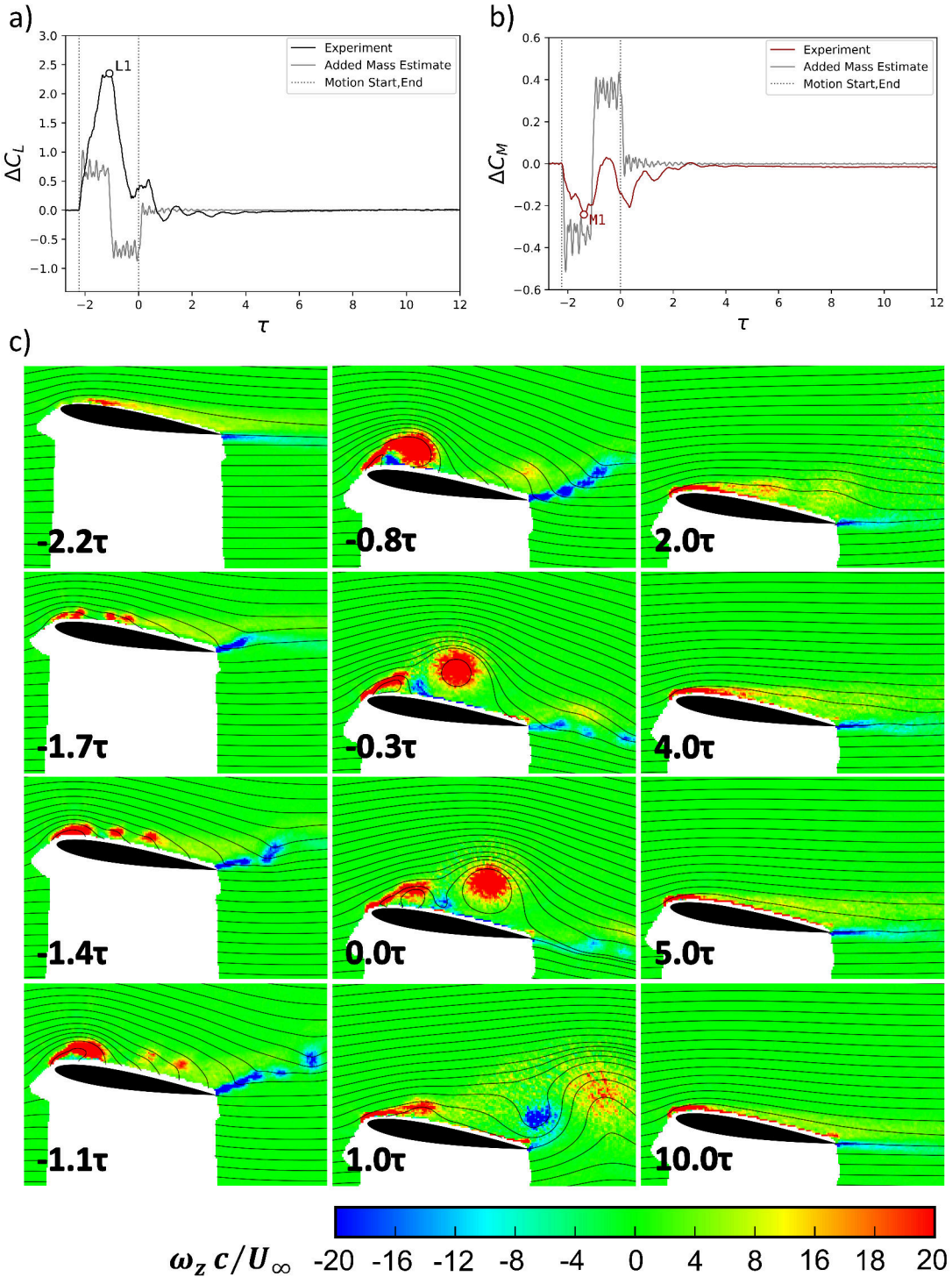

Figure 4-4: $\alpha_0 = 9°$ for $T = 2.22$, $\alpha_{pl,max} = +25°$: a) relative lift, b) relative pitching moment with the added-mass estimation, c) phase-averaged normalized spanwise vorticity with streamlines.

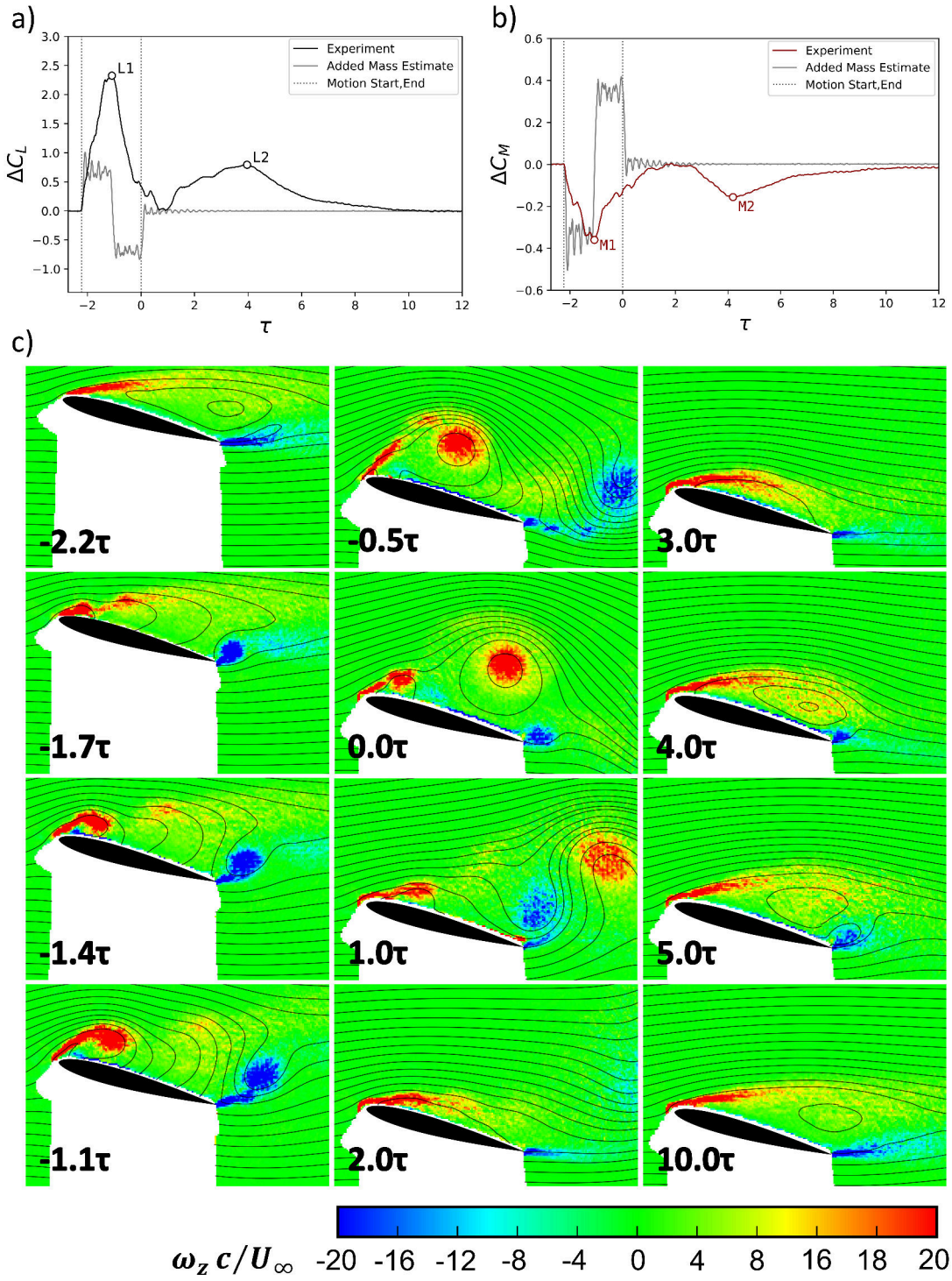

Figure 4-5: $\alpha_0 = 15°$ for $T = 2.22$, $\alpha_{pl,max} = +25°$: a) relative lift, b) relative pitching moment with the added-mass estimation, c) phase-averaged normalized spanwise vorticity with streamlines.

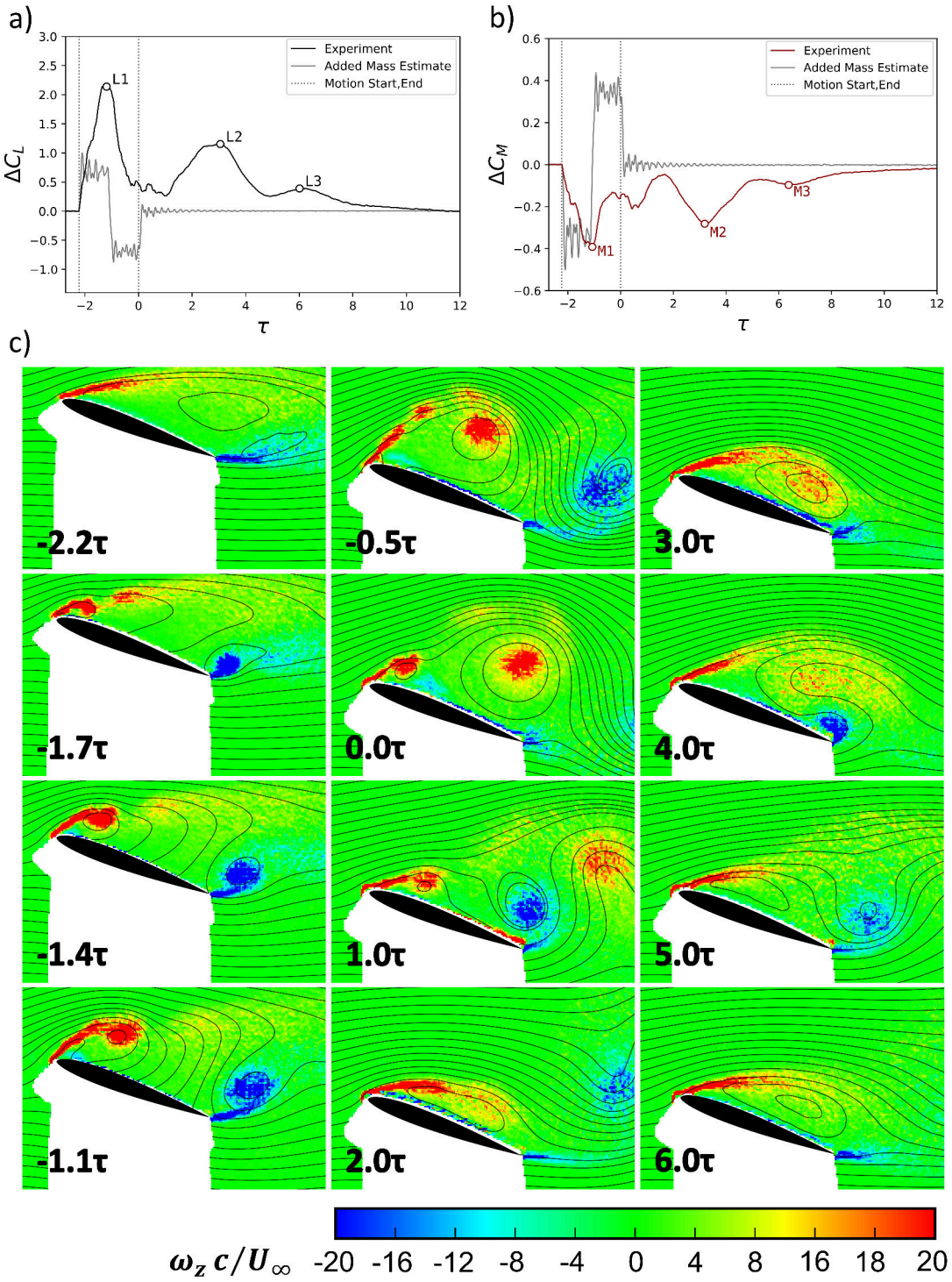

Figure 4-6: $\alpha_0 = 20°$ for $T = 2.22$, $\alpha_{pl,max} = +25°$: a) relative lift, b) relative pitching moment with the added-mass estimation, c) phase-averaged normalized spanwise vorticity with streamlines.

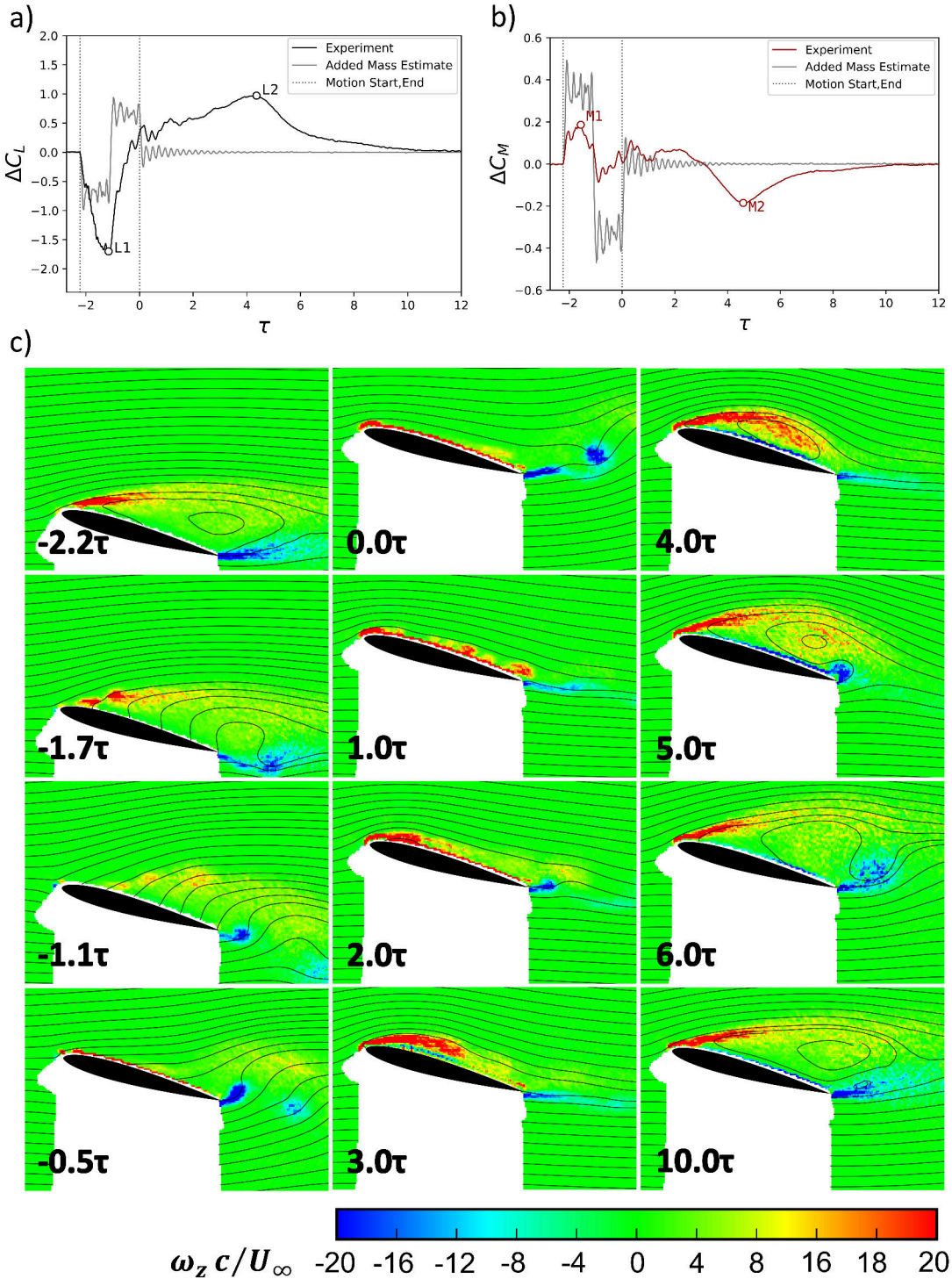

Figure 4-7: $\alpha_0 = 15°$ for $T = 2.22$, $\alpha_{pl,max} = -25°$: a) relative lift, b) relative pitching moment with the added-mass estimation, c) phase-averaged normalized spanwise vorticity with streamlines.

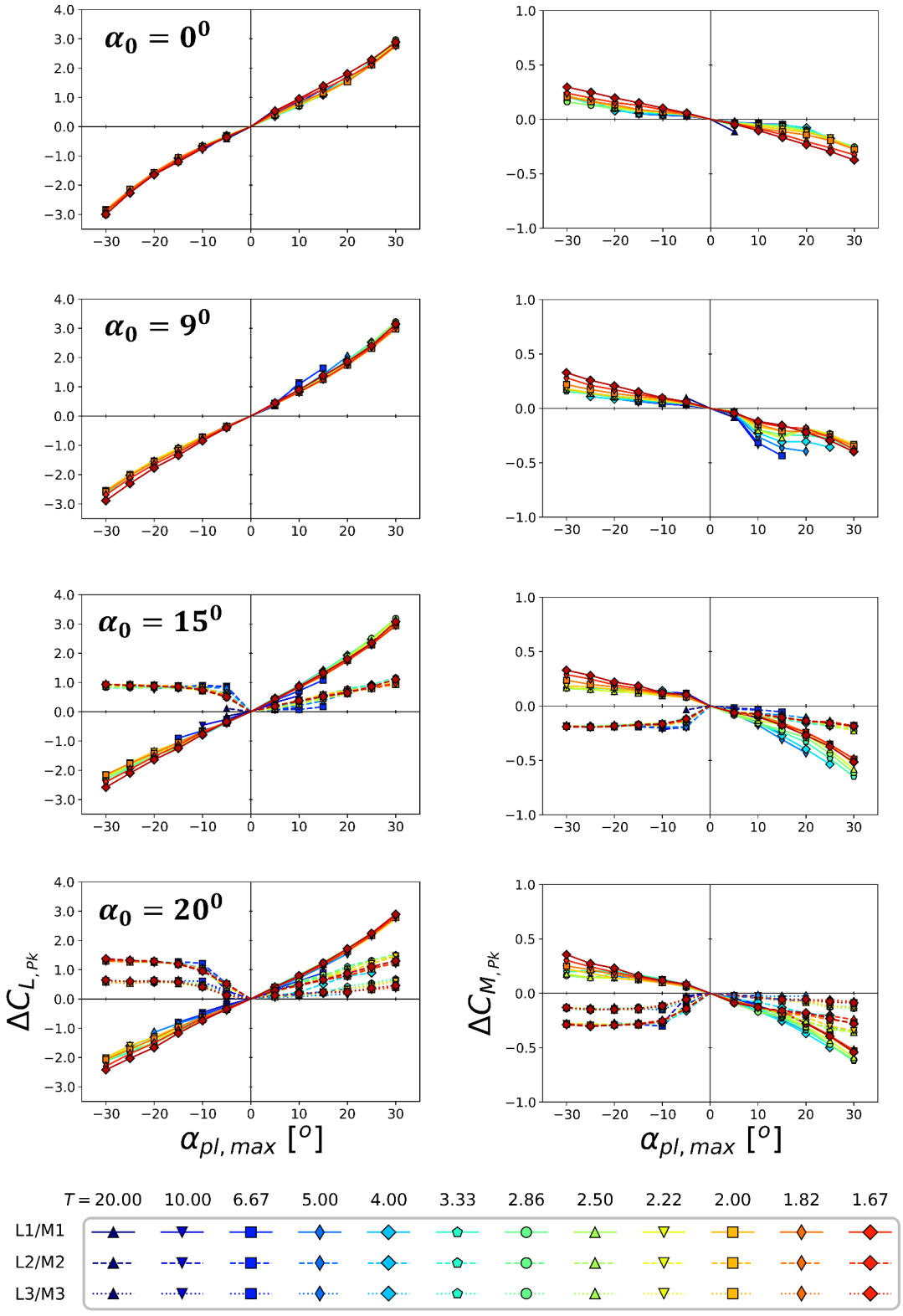

Figure 4-8: Relative lift and pitching moment coefficient for L1/L2/L3 and M1/M2/M3 respectively with $\alpha_{pl,max}$

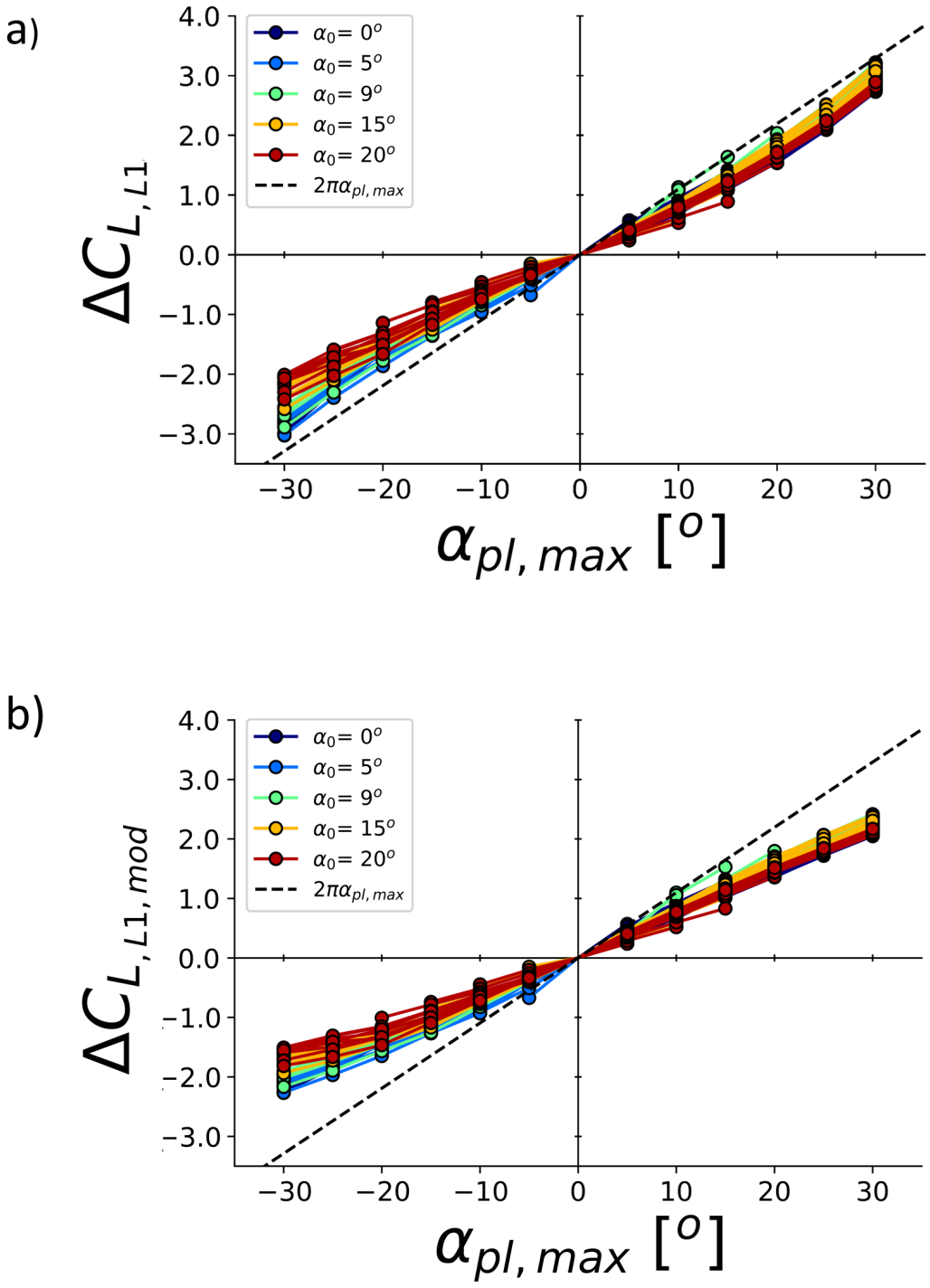

Figure 4-9: a) Relative lift coefficient for L1, b) modified relative lift coefficient for M1 with $\alpha_{pl,max}$ across the α_0 range.

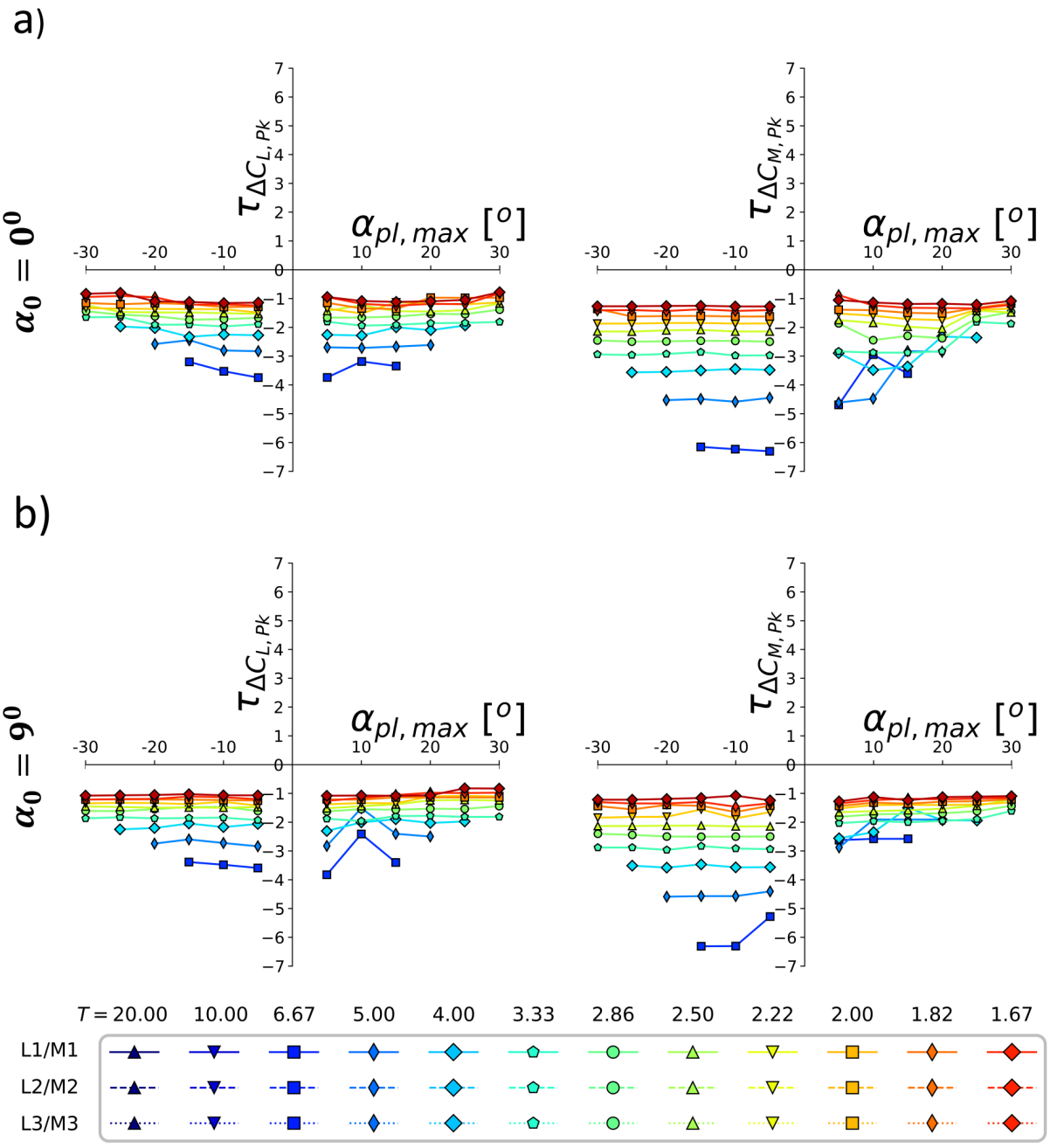

Figure 4-10: Timing information of L1/L2/L3 and M1/M2/M3 - a) $\alpha_o = 0°$, b) $\alpha_o = 9°$.

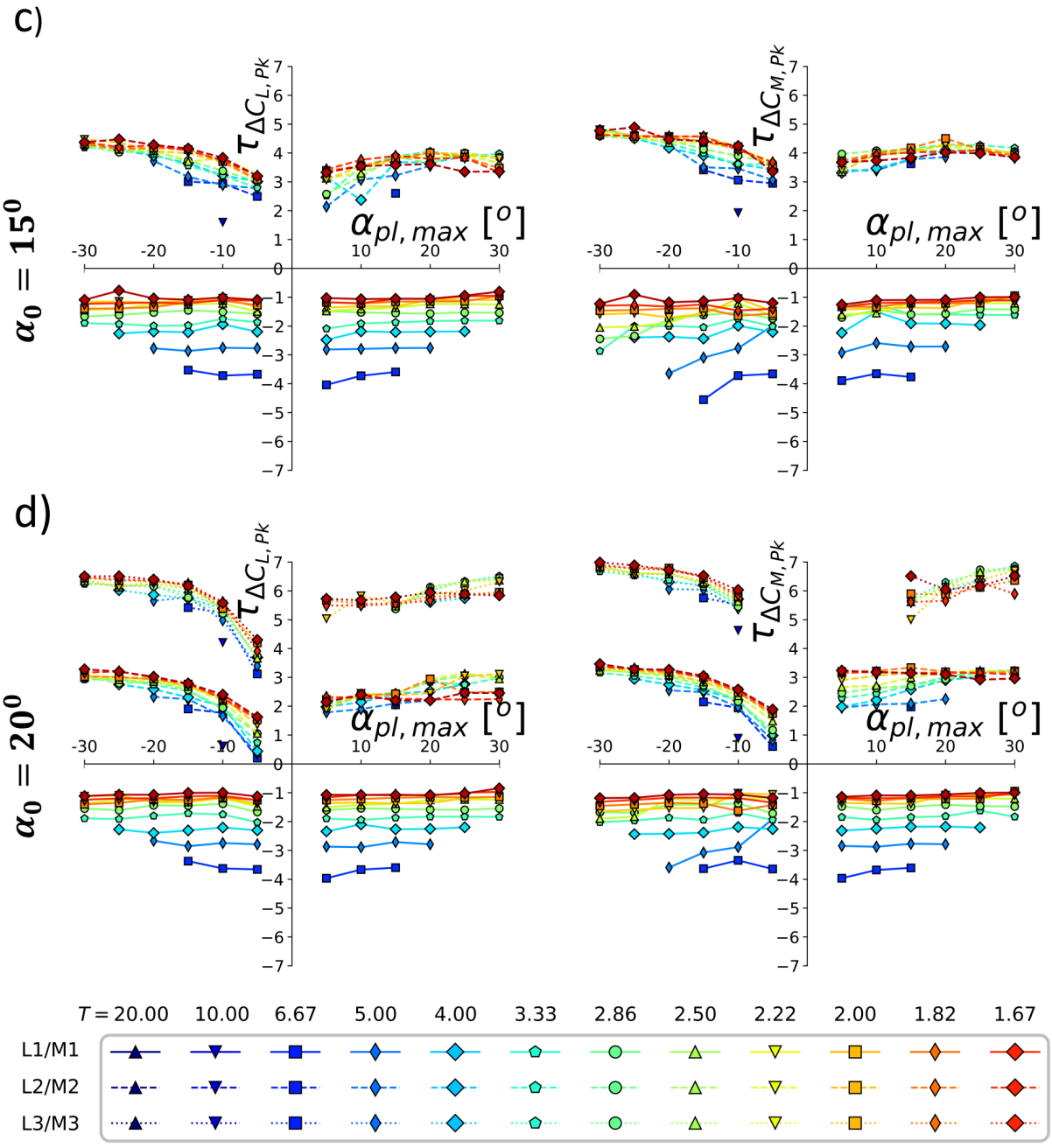

Figure 4-10: (Continued) Timing information of L1/L2/L3 and M1/M2/M3 - c) $\alpha_o = 15°$, d) $\alpha_o = 20°$.

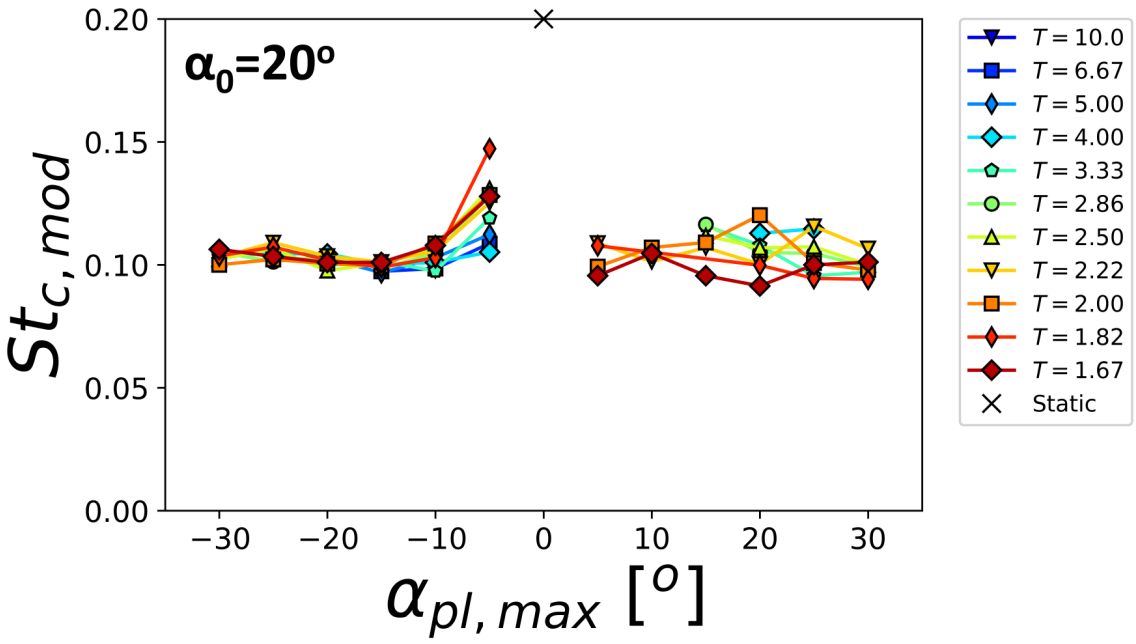

Figure 4-11: Modified Strouhal number from τ_{L3}-τ_{L2} for $\alpha_0 = 20°$

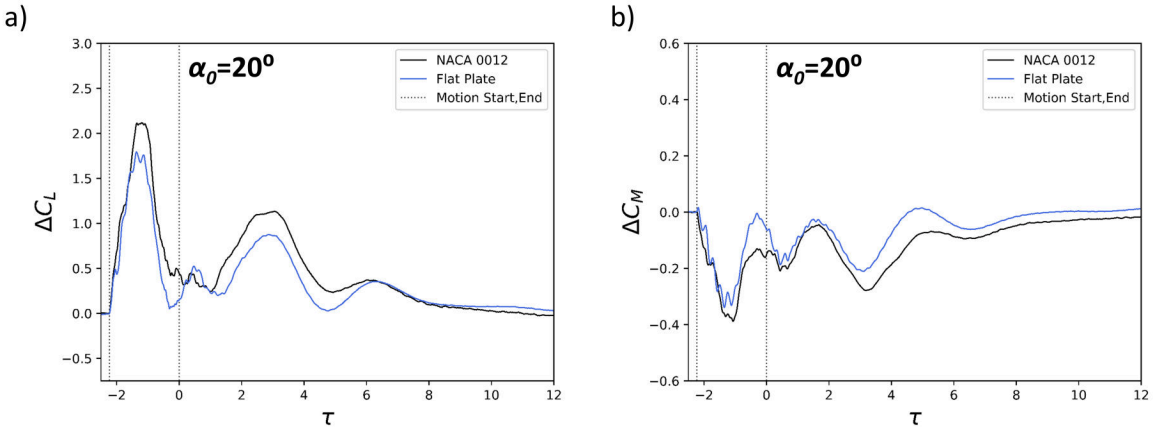

Figure 4-12: a) Relative lift and b) Relative pitching moment of NACA 0012 and flat plate at $\alpha_0 = 20°$ for $T = 2.22\tau$ and $\alpha_{pl,max} = +25°$.

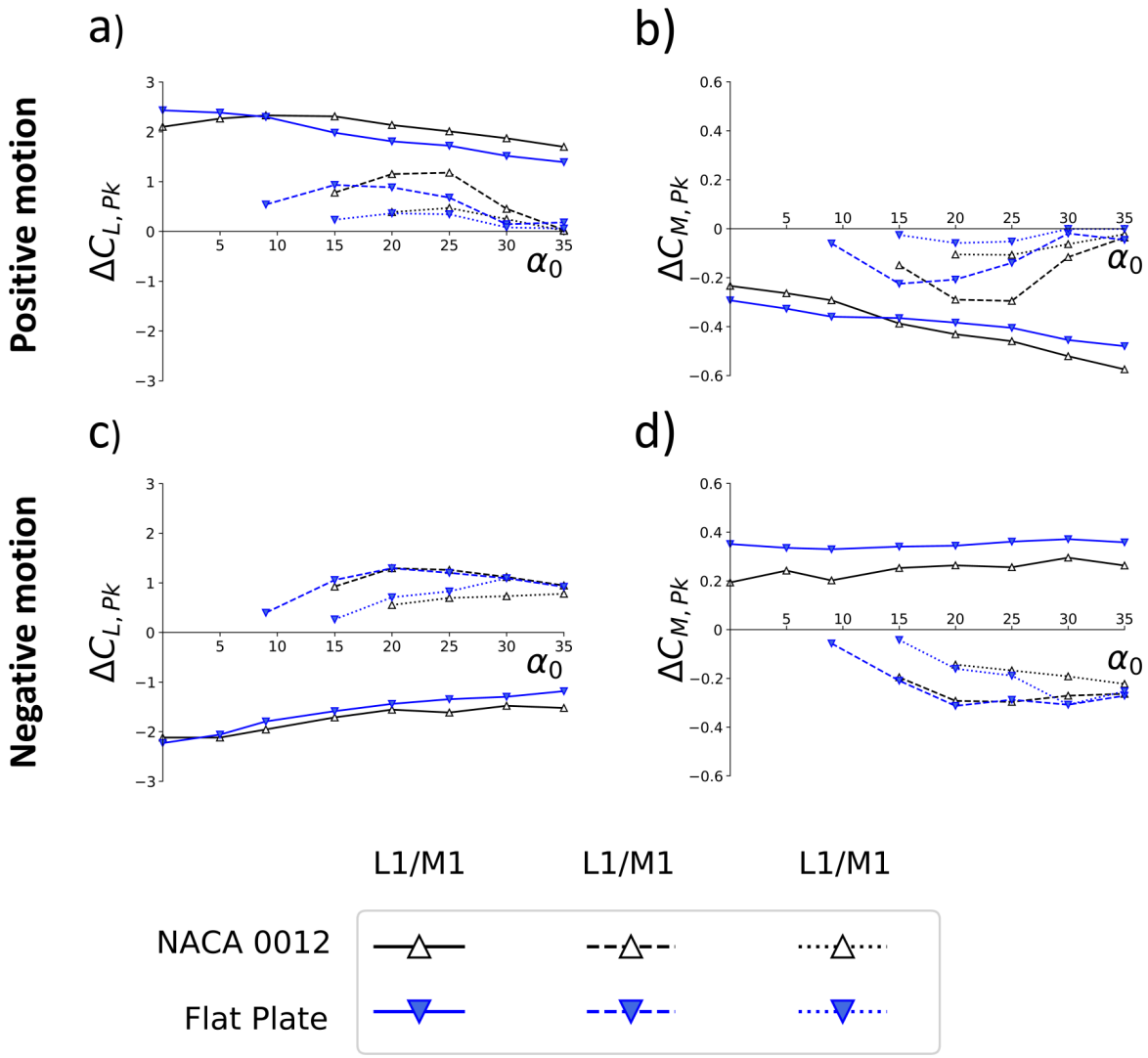

Figure 4-13: a,b) Positive motion, c,d) negative motion: Relative lift and pitching moment coefficient of NACA 0012 and flat plate for L1/L2/L3 and M1/M2/M3 with α_0 for $T = 2.22\tau$, $\alpha_{pl,max} = \pm 25°$

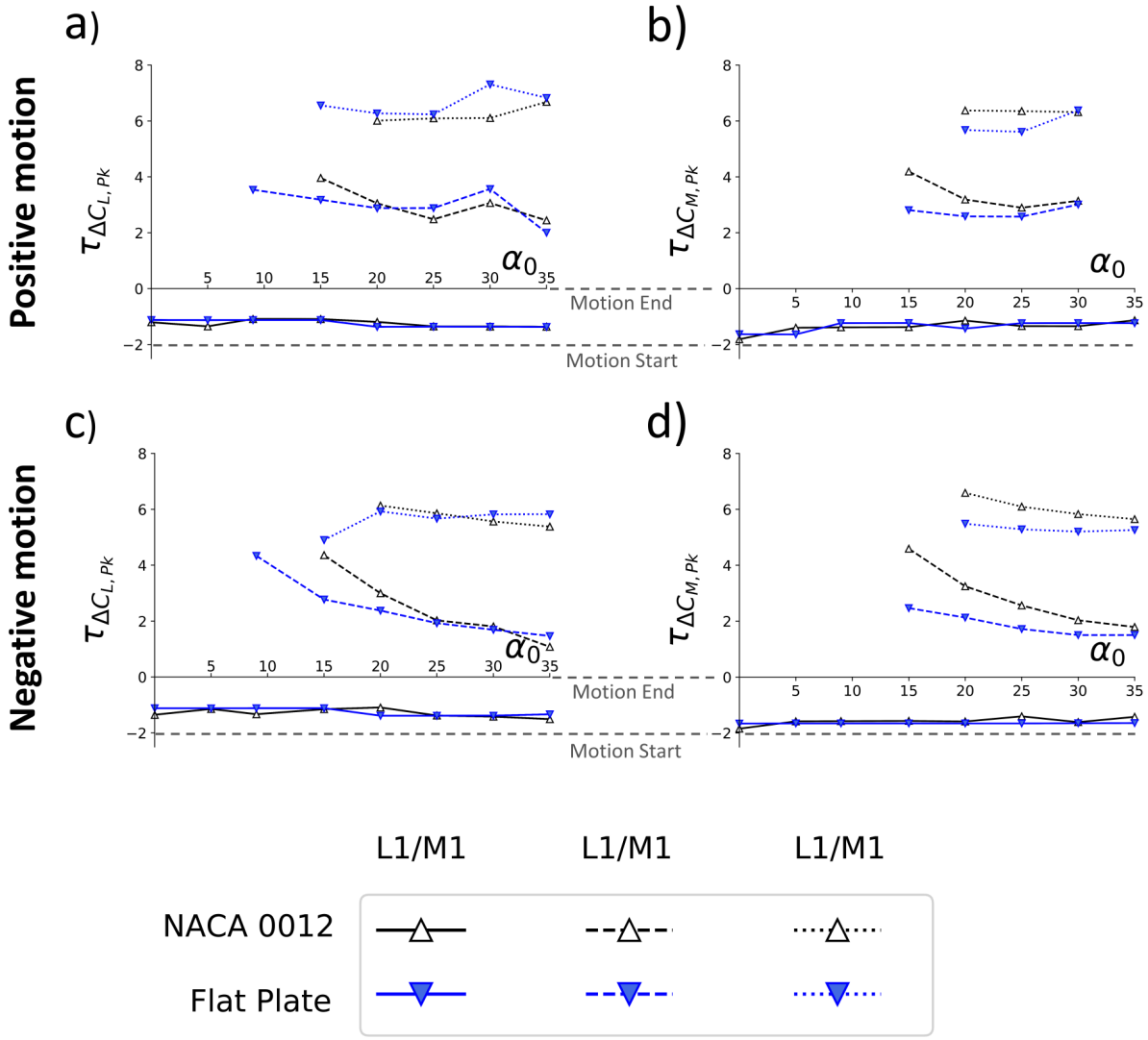

Figure 4-14: a,b) Positive motion, c,d) negative motion: Timing information of NACA 0012 and flat plate for L1/L2/L3 and M1/M2/M3 with α_0 for $T = 2.22\tau$, $\alpha_{pl,max} = \pm 25°$

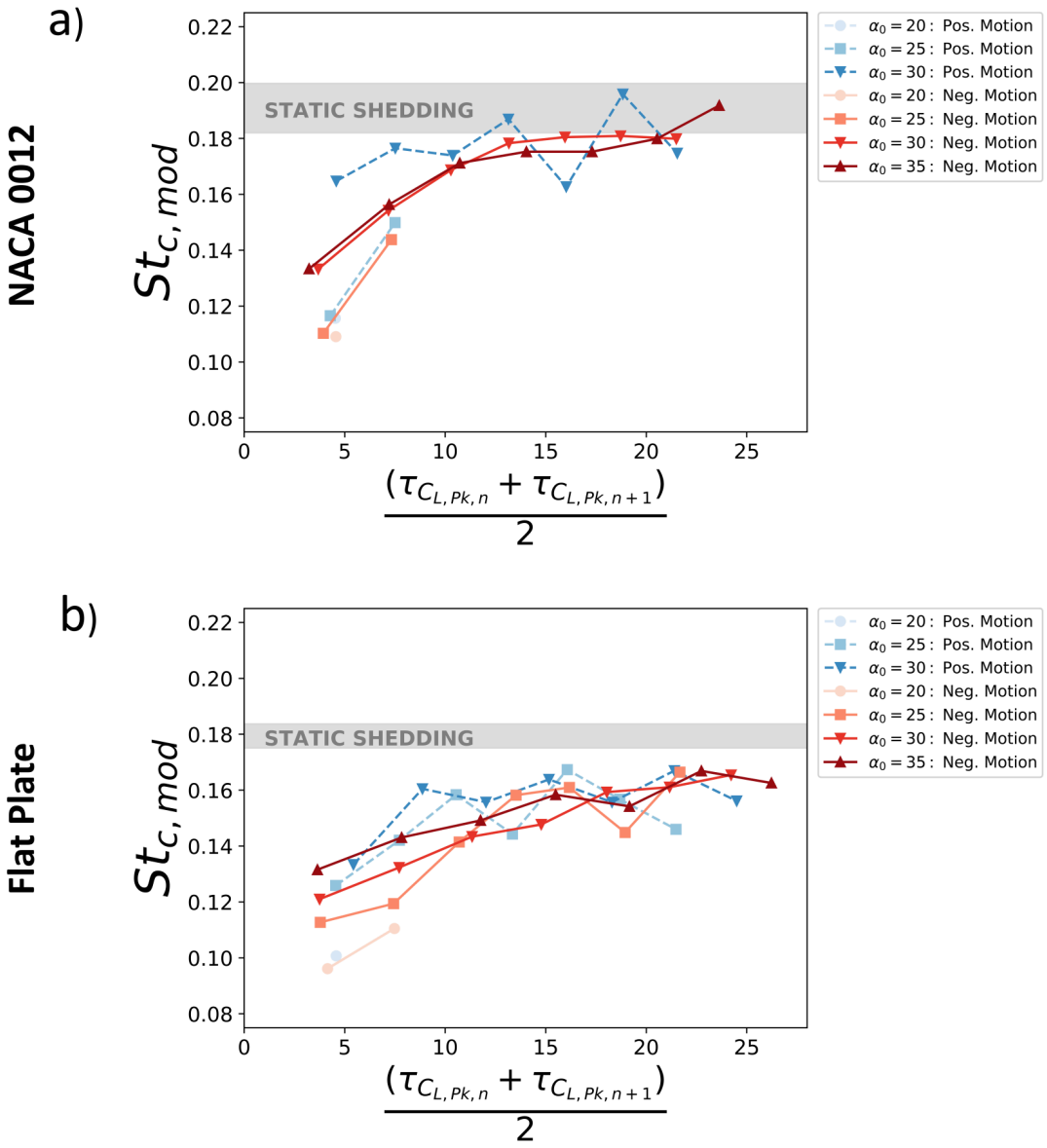

Figure 4-15: Modified Strouhal number based on chord, $fcsin(\alpha_0)/U_\infty$, between successive post-motion lift peak timings for a) NACA0012 airfoil and b) flat plate.

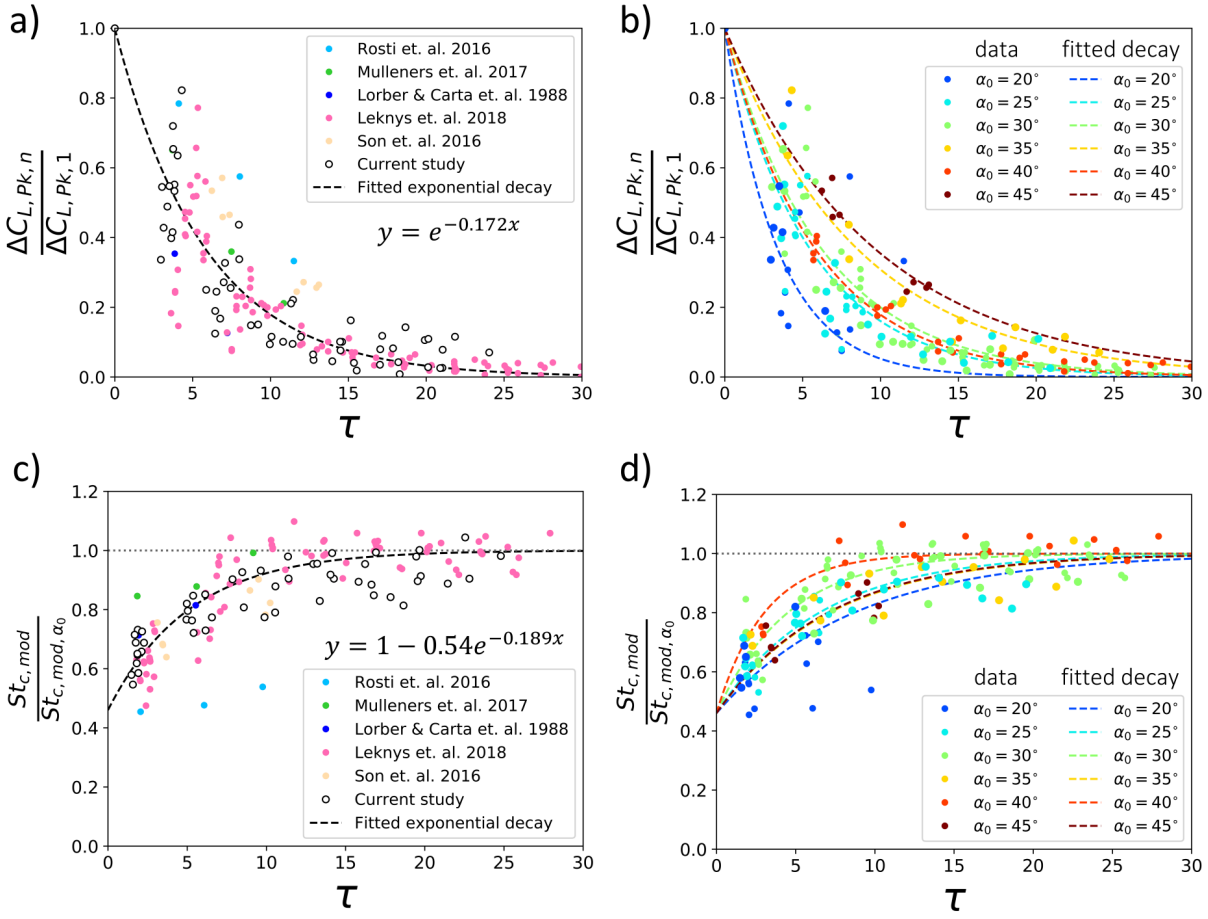

Figure 4-16: Vortex shedding magnitude and frequency vs. τ : a) lift peak normalised by first lift peak, b) normalised peak lift coloured by α_0, c) frequency of shedding event normalised by static shedding frequency, b) normalised shedding frequency coloured by α_0.

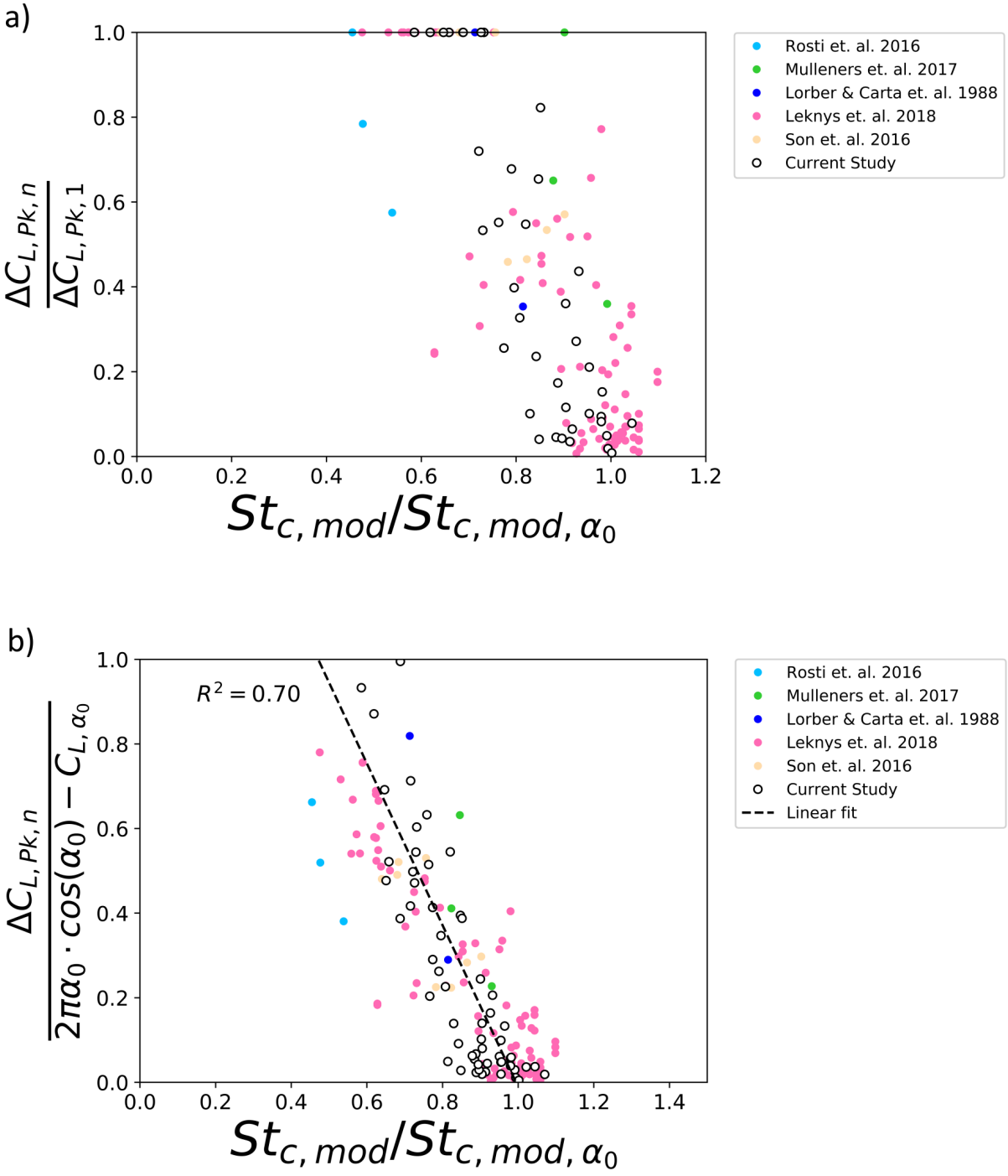

Figure 4-17: a) Normalised peak lift against normalised shedding frequency, b) peak lift normalised by $2\pi\alpha_0 \cdot cos(\alpha_0) - C_{L,\alpha_0}$ against normalised shedding frequency.

Chapter 5

Compound Transient Airfoil Motions and the Principle of Linear Superposition

5.1 Summary

This Chapter explores the aerodynamic response of an airfoil to multiple transient motions; more specifically, additional motions that occur well within the window of large-scale vortex shedding exhibited by post-stall airfoils. As outlined by Eldredge and Jones [4], canonical transient motion combinations need to be examined in order to determine the bulk flow field response, with particular attention to LEV behaviour. This can inform reduced-order models that could ultimately be used to predict multiple gust encounters and optimal agile manoeuvres. However by introducing additional and potentially different transient events the parameter space increases considerably, producing an implausible number of cases to test experimentally [103]. This leads into the second aspect of this study, which aims to probe the applicability of the linear superposition principle for vortex dominated flows; that is, can the response to multiple transient events be estimated through the sum of the individual responses? The word *estimated* is appropriate because it is

obvious that with such complex flows, linear superposition will always be an approximation. This is put rather succinctly by Eldredge and Jones:

> *"...it is abundantly clear that no such principle can exist in these large-amplitude motions with highly nonlinear fluid dynamics."*
>
> — Eldredge & Jones [4].

With that said, the concept of using the linear superposition principle in such flows is not new. A recent study by Mulleners *et al.* [103] found the lift response of a transient surging flat plate to be largely independent of the initial flow conditions, i.e. vorticity distribution, leading them to postulate the following:

> *"If the response to a single gust is mostly independent of the initial state of the flow, the response to a succession of gusts with different strengths in irregular succession should be the result of the linear superposition of the individual responses, even though each encounter may be characterized by nonlinear effects."*
>
> — Mulleners *et al.* [103].

The two distinctive quotes shown above are in direct contrast, yet both contain their own merit. The results in the following section are intended to investigate the effect of multiple transient motions and where, if at all, the linear superposition principle can be applied.

The aerodynamic response to multiple transient motions was explored through load and flow field measurements, with a particular focus on post-stall behaviour. It was found that the introduction of a second transient motion in the post-motion large-scale vortex shedding window produced a significant increase in peak lift and pitching moment. Remarkably, the increase in loads response could be described through the linear superposition of the single case responses with an excellent degree of accuracy; a normalised correlation value of > 0.95. This somewhat linear behaviour was found to coincide with the merging of the distinct vortical structures over the airfoil upper surface. Breakdown of the vortex merging behaviour, and subsequently the linear superposition prediction, occurred when the upper surface vortices reached a critical separation

distance of one chord length, resulting in a destructive interaction. For up to four transient motions, the effect of timing was found to become increasingly significant on the applicability of the linear superposition principle. The limits of the principle were then examined for periodic motion, where the linear superposition of a single sinusoidal cycle was compared against the true periodic experiment. It was found to predict the mean lift increase well for frequencies of $k < 0.47$; lift amplitudes were in reasonable agreement for all frequencies and amplitudes tested. It is recommended that other canonical motions are studied to test for commonality in vortex merging behaviour. Although the linear superposition principle remained valid across many of the cases presented in this chapter, it will not necessarily hold true for all airfoil kinematics.

5.2 Canonical Case

The lift and pitching moment response to a single transient plunging motion case are shown in Figure 5-1a and 5-1b for comparison. This is the typical case used in 4.2, with $T = 2.22$ and $\alpha_{pl,max} = 25°$. The motion period is indicated by the shaded grey region. Considering first the lift in Figure 5-1a, ΔC_L displays an almost identical response during the motion stage for $\alpha_0 = 5°$ and $20°$ despite the significant differences in initial flow state, i.e. attached and fully separated flow respectively. The pitching moment on the other hand shows distinct differences in the motion phase, see Figure 5-1b. In the post-motion stage the significant lift and pitching moment undulations for $\alpha_0 = 20°$ are caused by large-scale vortex shedding, as described in Chapter 4, which were shown to occur for post-stall angles of attack. The key stages of this shedding process are shown in Figure 5-1c, where alternate LEV/TEV shedding creates the fluctuations in aerodynamic loads. The different vortices have been assigned a subscript based on their order of formation.

Figure 5-2a and 5-2b show the lift and pitching moment response for two equal transient motions with the same forcing conditions as Figure 5-1a and 5-1b; all compound transient motions will consist of the same T and $\alpha_{pl,max}$ unless otherwise stated. The second motion period is again indicated by a shaded grey region and occurs at a convective time delay, $\Delta\tau$, from the end of the first motion, as described in Chapter 3 (see Figure 3-4b). In this particular case $\Delta\tau = 2.2$ was

chosen so the second motion would initiate when LEV_2 from the single case if forming, see Figure 5-1c. Solid lines indicate experimental measurement; dashed lines indicate linear superposition prediction. For the sake of clarity, the peak loads and vortices have been assigned a subscript based on the motion they form under. First motion is assigned a subscript "A" and the second motion is assigned a subscript "B". For example, the first peak in lift during the first motion is denoted $L1_A$, and the first vortex that forms during this motion is denoted LEV_{1A}.

Consider first the response of ΔC_L in Figure 5-2a for $\alpha_0 = 5°$. The response of the second motion is almost identical to the first albeit with a slight reduction in the peak, L1_B. After the first motion is complete at $\tau = 0.0$, the lift response sits around $\Delta C_L \approx -0.2$ before the second motion is introduced. From this it can be observed that the amplitude of L1_B is almost identical to the first and its overall maximum appears to depend on the state of the flow prior to the motion. It is then of no surprise that the linear superposition estimate, shown by the dashed line, agrees well with the experiment. A slight phase discrepancy exists between experiment and linear superposition which initiates at the start of the motion, $\tau = 2.2$, possibly due to the flow field responsible for the slight negative lift from $\tau = 0.0$ to 2.2. The maximum effective angle of attack for this case is 30°, which is sufficient for LEV formation. It is likely that the shedding of this LEV between $\tau = 0.0$ to 2.2 leaves behind some degree of shear layer separation on the upper surface, which could be the source of the phase discrepancy. At $\alpha_0 = 20°$ the peak lift response for the second motion shows a drastic increase from $\text{L1}_A \approx 2.1$ to $\text{L1}_B \approx 3.2$, yet curiously displays the same fundamental behaviour as $\alpha_0 = 5°$. This is illustrated by the remarkable agreement of the linear superposition prediction, despite the growing LEV prior to the second motion, see Figure 5-1c at $\tau = 2.2$. Although surprising, this behaviour is hinted at by the single motion lift response in Figure 5-1a, where ΔC_L shows little sensitivity to the initial conditions; i.e. attached or separated flow. Linear superposition then slightly over-predicts the vortex shedding peak at $\tau \approx 7$, due to the addition of the third peak in the single motion case, before falling back into agreement as the shedding process decays. The pitching moment response in Figure 5-2b displays the same behaviour as the lift and even more remarkably displays good agreement with the linear superposition prediction. There is a slight under-prediction of the

nose-down peak at $\tau \approx 4.5$ which corresponds to the shedding of the LEV over the trailing-edge and the subsequent inception of a TEV. Similar to the lift response, the nose-down peak at $\tau \approx 7$ is over-predicted due to the addition of the third shedding peak in the single motion case.

5.3 Effect of Convective Time Delay

In general Figure 5-2 demonstrates a reasonably good performance of linear superposition, regardless of the prior flow field. However it is important not to overstate this result as it shows just one possible timing of the second motion within the vortex shedding window. With that in mind, Figure 5-3 investigates the effect of the second motion delay from $\Delta\tau = 0.00$ to 3.33 with respect to ΔC_L and provides the corresponding flow fields during the motion period. For comparison purposes, the same phases during the single motion case are presented as "*Single*". For the sake of brevity only the lift response cases are shown here. In general the pitching moment was found to closely correspond to the lift in terms of linear behaviour with $\Delta\tau$ and will be shown in section 5.5. The interested reader is referred to Appendix A for an example of the pitching moment responses.

For $\Delta\tau = 0.00$, Figure 5-3, the peak in ΔC_L shows a significant increase during the second motion from $\mathrm{L1}_A \approx 2.1$ to $\mathrm{L1}_B \approx 2.7$ followed by a comparatively steeper drop in the aft portion of the motion when compared with the first. As the motion ends, ΔC_L displays a short lived increase before exhibiting the first large-scale vortex shedding peak at $\tau \approx 5$. Linear superposition predicts the lift response reasonably well in the first potion of the motion but consistently over-predicts the response from $\tau \approx 1$ before falling back into agreement at $\tau \approx 7$. From the flow field images it can be seen that the second motion initiates at $\tau = 0.00$, approximately when the LEV_{1A} is passing over the trailing-edge. As the second motion progresses, LEV_{1B} appears stronger and closer to the airfoil surface, see $\tau = 0.56$ to $\tau = 1.11$, than LEV_{1A} at the corresponding phases in the first motion, see $\tau = -1.67$ to $\tau = -1.11$ for the "*Single*" case. This serves to explain the reason for the increase in $\mathrm{L1}_B$ during the second motion. In addition, TEV_{1B} is comparatively strengthened and forms over the upper surface at the trailing-edge, $\tau = 0.56$, possibly due to the influence of LEV_{1A} as it passes over the trailing-edge. The short lived peak in ΔC_L at $\tau = 2.22$

is likely caused by the presence of LEV_{1B} over the upper surface and the influence decay of the TEV_{1B} as it convects into the wake.

When the convective time delay is increased to $\Delta\tau = 1.11$, there is a further increase of L1_B up to $\Delta C_L \approx 3.2$. The subsequent vortex shedding peaks are comparatively larger than for $\Delta\tau = 0.0$ and marginally exceed that of the single case, see Figure 5-1a. Linear superposition in this case shows excellent agreement, with minor discrepancies in peak lift at $\tau \approx 2$ and ≈ 6. The corresponding flow field images show rather interesting vortex behaviour. At the start of the second motion, $\tau = 1.11$, the early stages of LEV_{2A} formation can be seen along with the TEV_{2A} and LEV_{1A} being shed into the wake. During the acceleration phase, $\tau = 1.67$, LEV_{2A} is cut off from its feeding shear layer as the vorticity emanating from the leading-edge begins to roll up into a new, more coherent vortical structure, LEV_{1B}. At $\tau = 2.2$, LEV_{1B} appears much stronger. The remnants of LEV_{2A}, observed around the mid-chord position at $\tau = 1.67$, can be seen stretching into LEV_{1B} at $\tau = 2.22$. At this point ΔC_L has reached its maximum and it interesting to note the absence of a TEV in close proximity to the airfoil. This could explain why the lift reaches much higher values compared with the $\Delta\tau = 0.0$ case; i.e due to a reduction in induced downwash. By $\tau = 2.78$ the two vortical structures have combined into a single larger structure, LEV_{2A+1B} and begin to approach the trailing-edge at $\tau = 3.33$.

The lift response for $\Delta\tau = 2.22$ has been discussed previously in Figure 5-2a and so the focus here will be on the flow field behaviour. The motion initiates at $\tau = 2.22$, where LEV_{2A} spans the entire upper surface. Once again when the airfoil accelerates downwards, $\tau = 2.78$, LEV_{2A} is pinched off from the leading-edge due a roll up of the feeding shear layer. At L1_B, $\tau = 3.33$, the two vortices display stronger interaction. LEV_{1B} is lifted further from the airfoil surface as LEV_{2A} is stretched and forced underneath. Despite the inhomogeneous structure of the combined vortex (LEV_{2A+1B}), L1_B remains at $\Delta C_L \approx 3.2$, perhaps again owing to the absence of a distinct TEV. The merged vortical structure then begins to rotate as it is convected downstream. A distinct spiral pattern is particularity apparent at $\tau = 4.44$.

The final case in Figure 5-3 is for a convective time delay of $\Delta\tau = 3.33$, where the lift response

shows drastically different behaviour. In the initial motion stage, the lift increases in line with the linear superposition prediction, reaching a peak of around $\Delta C_L \approx 2.5$. After this point the lift drops dramatically, even becoming slightly negative by the end of the motion and is in stark contrast to the linear superposition prediction. This deviation from linear behaviour is elucidated in the corresponding flow field images. At motion inception, the flow field exhibits the fully formed, coherent LEV_{2A}. During the initial stages of the second motion, $\tau = 3.89$, the same qualitative behaviour is seen, where the feeding shear layer begins to roll up into the forming LEV_{1B}. At this point LEV_{2A} has passed the trailing-edge and begins to deform significantly over the induced TEV. At mid motion, $\tau = 4.44$, LEV_{1B} is less coherent and has been lifted a greater distance from the airfoil surface, even when compared to LEV_{1A} in the "*Single*" motion case. This combined with the formation of the coherent TEV_{1B} explains the large drop in $\mathrm{L1}_B$ magnitude when compared with the other cases. LEV_{2A} appears to be almost completely annihilated at this stage and shows no merging behaviour. From $\tau = 5.00$ the weakened LEV_{1B} convects downstream at a greater chord-normal distance which subsequently induces weaker vortex shedding, seen in the lift response from $\tau \approx 8$.

From the data presented in Figure 5-3 it can be seen that the problem of linear behaviour for compound motions depends on the merging process of the co-rotating vortices on the upper surface of the airfoil; namely LEV_{2A} and LEV_{1B}. The data suggests that providing the proximity of the two vortices are below a critical distance they will constructively interact and merge, forming a larger vortex. It appears that this critical distance is roughly on the scale of a chord length, as shown by the destructive interaction of the two structures at $\tau = 3.33$. Linear superposition fails in this regime, as the two-structures no longer constructively combine into a single structure. This regime could be linked to the LEV shedding mechanism as described by Widmann *et al.* [99], where the arrival of the half-saddle point at the trailing-edge marks the onset of shedding, i.e. a chord length limit.

Insight into the interaction of LEV_{2A} and LEV_{1B} can be gained by looking at the canonical problem of the merging of co-rotating vortex pairs, a detailed review of which is given by Leweke *et al.* [155]. For the simplest case, a pair of free, equal strength vortices will begin to rotate around

each other due to their mutual induced velocities before eventually merging; providing they are below a critical core size to separation distance ratio [155]. Figure 5-3 echoes this behaviour, particularity for $d\tau = 2.22$ where the two vortices rotate around each other in a clock-wise sense. The problem of the merging process in the current cases however becomes more complex due to both an unequal strength between the vortex pair and the influence of the airfoil upper surface boundary. A clear pattern in Figure 5-3 is the dominating behaviour of LEV_{1B} over LEV_{2A}. For $\Delta\tau = 1.11$ and 2.22, LEV_{1B} deforms LEV_{2A} leading to a stretched region of vorticity that subsequently wraps around LEV_{1B}; similar to the behaviour of free, unequal strength vortex pairs as documented by Trieling *et al.* [156]. The imposed boundary condition of the airfoil upper surface acts, in a simplified sense, as a reflection plane which produces additional induced velocities on the vortex pair [157]. Wang *et al.* [158] noted an increased rotation rate and merging speed on a vortex pair in close proximity to a ground plane. The case of $\Delta\tau = 3.33$ increases the complexity further due to the apparent chord length limit, where the introduction of the TEV appears to aid the destruction of LEV_{2A}.

5.4 Effect of Second Motion Amplitude

The data presented in Figure 5-3 showed the linear superposition principle holding reasonably well for $\Delta\tau = 2.22$ despite the rather complex vortex merging process. LEV_{1B} was much stronger and exhibited dominant behaviour over LEV_{2A}, which could be a prerequisite for the success of the linear superposition prediction. Figure 5-4 explores the effect of strength ratio between LEV_{2A} and LEV_{1B} which is achieved by altering the second motion amplitude, $\alpha_{pl,max}$. Lift and corresponding flow field images are presented for second motion amplitudes ranging from $\alpha_{pl,max} = 5^\circ$ to 25°. Also shown is the single motion case for comparison purposes, Figure 5-4a. For the second motion amplitude of $\alpha_{pl,max} = 5^\circ$, Figure 5-4b, the effect of the additional vorticity generated at the leading-edge is to slightly delay the shedding process compared with the single motion case. When $\alpha_{pl,max}$ is increased to 10° the effects on the flow field are more discernible, Figure 5-4c. At $\tau = 3.3$ the emergence of two structures starts to become apparent and at $\tau = 3.9$ a faint swirling pattern can be seen. Interestingly these features are common

amongst all the amplitudes tested and predominantly become more pronounced when amplitude of the second motion is increased, see Figure 5-4d to 5-4f. The distinct roll-up of the feeding shear layer at $\tau = 2.8$ becomes apparent from a second motion amplitude of $\alpha_{pl,max} = 15°$ to 25°. As LEV_{1B} becomes stronger the interaction between the vortex pair increases and the resulting bulk vortical structure is at a greater vertical distance from the airfoil surface leading to an increased shear layer angle with respect to the chord ($\tau = 3.9$). All the cases in Figure 5-4 show more or less linear behaviour, highlighted by the agreement of the experiment and linear superposition prediction. This figure maintains the suggestion that the primary factor governing the linear lift response is the distance between LEV_{2A} and LEV_{1B}, rather than the ratio of their strengths.

5.5 Correlation of Linear Superposition

In order to quantify the agreement of the linear superposition prediction with the experiment, a normalised correlation is proposed:

$$\frac{\Delta C_{L,exp.} \cdot \Delta C_{L,lin.sup.}}{\frac{1}{2}(\Delta C_{L,exp.} \cdot \Delta C_{L,exp.} + \Delta C_{L,lin.sup.} \cdot \Delta C_{L,lin.sup.})} \tag{5.1}$$

where $\Delta C_{L,exp.}$ and $\Delta C_{L,lin.sup.}$ are the relative lift for the experiment and linear superposition prediction respectively. Equation 5.1 gives the cross product of the two lift signals divided by the average of the cross products of each signal with itself, resulting in correlation ranging from -1 to +1. It is important to note that all correlation values are based off the same measurement window of 10 convective time units from the start of the second motion. This was chosen to avoid agreement bias once the lift signal approaches steady state.

The results of the normalised correlation analysis are presented in Figure 5-5 and shows a variety of different testing conditions from $\mathrm{d}\tau = 0$ to 7. Note here that the cases consist of equivalent motion periods and amplitudes for both motions. The distinct deviation from agreement at $\tau = 3.33$ shown in Figure 5-3 can be seen in Figure 5-5a as a drop in the normalised correlation,

which is closely related to the time for LEV_{2A} to reach the trailing-edge, see Figure 5-1. Consider first the comparison of the different motion periods; $T = 2.86$, 2.22 and 1.67. At $\Delta\tau = 0$ the correlation exhibits a significant decrease with decreasing period, particularly for $T = 1.67$. This is most likely due to an increased interaction between LEV_{1A} and LEV_{1B}. Evidence for this can be seen in Figure 5-3 for $\Delta\tau = 0.00$ at $\tau = 0.00$, where LEV_{1A} is approaching the trailing-edge. At higher frequencies LEV_{1A} will have had comparatively less time to convect and so will have a greater influence on LEV_{1B} as it forms. It is believed that a similar effect is also occurring in the correlation dip at $\tau = 3.33$. For small motion periods, LEV_{2A} will have had less time to develop and convect before the initiation of the second motion, meaning the vortices will be more likely to constructively interact and merge. The poor correlation regions at $\tau = 0.00$ and 3.33, Figure 5-5a, are short lived and quickly rise to a good level of agreement, > 0.95. Interestingly the correlation remains good between $\tau = 6$ to 7 despite the additional weaker vortex shedding peaks, see Figure 5-4a. A similar result was also found in the reduced amplitude cases for $T = 2.22$ and $\alpha_{pl,max} = 5, 15°$. Figure 5-5a shows no significant drop across the range of $\Delta\tau$ and, from the results shown in Figure 4-8, indicates that linear behaviour persists in weaker vortical flows. This notion is reinforced once more by the results for the $\alpha_0 = 15°$ case, at $T = 2.22$ and $\alpha_{pl,max} = 25°$. It was shown previously in Figure 4-8 that the secondary peaks caused by LEV_{2A} are not as strong and as such, good correlation is exhibited across the $\Delta\tau$ range. Interestingly the normalised correlation for the ΔC_M in Figure 5-5b responses show the same features as ΔC_L Figure 5-5a.

5.6 Additional Transient Motions

It is important to keep in mind that good agreement between linear superposition prediction and experiment has only been demonstrated for two transient motions, meaning that the linear superposition prediction will not necessarily hold for additional motions. Figure 5-6 explores the lift response to four transient motions with a constant convective time delay between each motion from $\Delta\tau = 0.50$ to 2.00. For these cases it was necessary to reduce the amplitude of the motion to $\alpha_{pl,max} = 15°$ due to the constraint of the tunnel wall proximity.

Figure 5-6a shows the lift response to four transient motions separated by a convective time delay of $\Delta\tau = 0.5$. With the introduction of the second motion, the lift peak $L1_B$ increases by ≈ 0.5 and is maintained for the subsequent motions. Overall the linear superposition prediction agrees well with the experimental signal, but shows signs of a potential agreement drift with additional motions. A window of sustained lift can be observed between motions three and four in the experimental signal, something that is not picked up by the linear superposition prediction. For a convective time delay of $\Delta\tau = 1.00$, Figure 5-6b, the linear superposition agreement is very good, particularly after the end of the fourth motion. As the convective time delay is increased further to $\Delta\tau = 1.5$ and 2.0, Figures 5-6c and 5-6d, the linear superposition prediction begins to drift out of agreement. It is surprising to see that the experiment actually exceeds the lift prediction of the linear superposition and by the fourth motion the peak ΔC_L has increased by around 100%. Figure 5-6 shows that the timing becomes even more important for multiple transient motions. The agreement of linear superposition can drift significantly in certain cases. This is most likely related to the vortex positions and the subsequent merging behaviour seen previously.

5.7 Periodic Motion

The results shown in Figure 5-6 point towards the establishment of periodic behaviour, where the response shows no cycle to cycle variation in a phase averaged sense. It is interesting to see that the lift maxima all show an asymptotic increase, which perhaps mirrors the mean lift increase for sinusoidally plunging airfoils [151]. The aim of this section is to investigate the effect of compounding sinusoidal motions, not only to see how the lift and flow field develops, but to also test the limits of the linear superposition principle. An example of this is shown in Figure 5-7a for a single sinusoidal cycle, following the motion profile of Figure 3-4c. The solid black line shows the relative lift response for a single sinusoidal cycle at $\alpha_0 = 15°$. A distinct vortex shedding peak can be seen after the motion at $\tau \approx 7$ which closely resembles Figure 4-2a and 4-3a. Note that for these cases, $\tau = 0$ denotes the **start** of the motion. By summing the individual response cycle by cycle, the periodic linear superposition response can be constructed, shown by

the dashed line in Figure 5-7a, which will be compared against the true experimental periodic case. This asks the question; is the mean lift increase information, as seen in [70], contained within the vortex shedding behaviour of a single cycle? Figure 5-7b shows the mean lift and lift amplitude extraction that will be used later to compare the experimental signal with the linear superposition prediction.

The following periodic cases were selected to mirror the forcing conditions tested by Chiereghin *et al.* [70] and focus on a geometric angle of attack $\alpha_0 = 15°$ for comparison purposes. Figure 5-8 presents the relative lift response and corresponding flow field images for a range of k at $A/c = 0.5$. The flow field images are taken for the first three periods at a normalised period of $t/T = 0.25$, i.e. quarter-cycle, which approximately corresponds to the point of maximum lift for sinusoidal motion [70].

A distinct change in lift response can be seen between the first and second cycle for $k = 0.24$ in Figure 5-8a which is elucidated by the corresponding flow field images. In cycle 1 the leading-edge shear layer exhibits very weak roll up just aft of the trailing-edge, whereas in cycles 2 and 3 a coherent LEV is present over the upper surface. Very good agreement between the experiment and linear superposition prediction is visible; the main discrepancy being the absence of the secondary peak, presumably due to the shedding of an additional vortex. At $k = 0.47$ the difference between the first and second cycle becomes less distinct, see Figure 5-8b. The amplitude displays reduced variation whilst the mean lift shows a large increase with τ. This is shown in the flow field images to be due to an apparent strengthening of the LEV which moves closer to the airfoil surface. Linear superposition provides a reasonable prediction, but tends to slightly over-predict the peaks and troughs. For $k = 0.63$ in Figure 5-8c, a similar trend is displayed. The amplitude remains virtually constant whilst the mean lift increases. Again the flow field images indicate a strengthening of the LEV which moves towards the airfoil surface, but also show a suppression of the TEV from cycle 1 to 2. The linear superposition response shows good agreement with the peak lift, but drastically over-predicts the troughs. Finally, for $St_c = 0.94$ the same trends in lift response are visible, see 5-8d. Flow field images indicate less change in both the LEV strength and position and again show a suppression of the coherent

TEV between cycle 1 and 2. Linear superposition predicts the amplitude reasonably well but shows gross over-prediction of the mean lift component.

To gain a more detailed insight into how the lift response develops, the mean relative lift and cycle amplitudes were calculated and plotted in Figure 5-9a and 5-9b respectively for both the experimental and linear superposition responses. Figure 5-7b shows how these were determined. The mean lift is tracked from a sliding average with a window of one motion period, giving a smooth variation with τ. Cycle amplitudes were based off the difference between the cycle peak and trough, giving singular points that were taken to occur at the mid-cycle. Both mean lift and cycle amplitude were normalised by their final periodic value which was taken as the average of the last 30 cycles from a 50 cycle run. All frequencies in Figure 5-9a show an asymptotic increase in the mean lift component to their final periodic value. Each frequency converges to steady-state within approximately 10τ from their point of initiation; i.e. the mid-point of the first cycle. Linear superposition shows reasonably good prediction of this convergence time but shows discrepancies in the normalised magnitude variation, particularly at high frequencies. In terms of cycle amplitudes, Figure 5-9b, the lower frequencies display a greater variation from the first cycle; the higher amplitudes on the other hand, $k > 0.63$, show very little amplitude variation and is most likely due to the added-mass effect. Linear superposition shows good agreement with this trend but discrepancies in normalised magnitude again start to appear at higher frequencies. The results in Figures 5-9a and 5-9b show that periodic conditions are reached after a critical convective time, rather than a critical number of motion cycles.

Finally, Figures 5-9c and 5-9d show the mean lift and amplitude (a1) once the experimental and linear superposition responses reach a periodic state. The amplitude here is taken as the first harmonic of the signal (a1); calculated via FFT. Both mean lift and amplitude are in line with the data presented by Chiereghin *et al.* [70]. For an amplitude to chord ratio of $A/c = 0.1$, linear superposition shows excellent agreement in terms of the mean lift component up to $k = 0.47$, Figure 5-9c. For higher frequencies the mean lift is progressively over-predicted. At $A/c = 0.3$ and 0.5, there are small differences between experiment and prediction from $k = 0.16$ to 0.47. The under-prediction stems from the secondary LEV present in the experiment which is responsible

for the secondary peak in the lift response at $A/c = 0.5$ and $k = 0.24$, see Figure 5-8a. Beyond $k = 0.47$ linear superposition massively over-predicts the mean lift response. This drastic rise in mean lift is due to the continued summation of the single lift responses, which can take up to 10τ to fully decay after motion cessation. At higher frequencies, $k > 0.31$, the mean lift will begin to increase due to the accumulation of the lift in this decay period. More accurate predictions of the mean lift component have been achieved by superposing an exponential decay on the post motion lift response with a half-life of one period. However these results are omitted due to the arbitrary implementation of the exponential correction. In terms of lift amplitude, a reasonable level of agreement can be seen for all amplitudes, with some discrepancies between $k = 0.47$ and 0.94, the reasons for which are not currently clear.

5.8 Conclusions

The response to compounding transient motions has been investigated through lift, pitching moment and flow field measurements to investigate vortex behaviour and to test the applicability of the linear superposition principle as a predictive tool. The key findings are:

- Significant increases in peak lift occurred for post-stall angles of attack during the second of two transient motions. The lift response could be reasonably estimated through linear superposition of the single motion response with a surprising level of accuracy; quantified through a normalised correlation parameter. Flow field measurements revealed this linear behaviour to coincide with a merging process of two vortices on the airfoil upper surface. Breakdown of the linear superposition principle occurred when the upper surface vortices were at a sufficient separation distance of approximately one chord length, resulting in destructive interference.

- A normalised correlation between the experiment and linear superposition prediction was defined. It was shown that the normalised correlation remained above 0.95 for most of the test cases. T was a significant influencer on the correlation at a convective time delay between the two motions of $\Delta\tau = 0.00$ and 3.33 and was postulated to be again due to

the vortex separation distance. Smaller amplitude cases exhibited good correlation across the entire $\Delta\tau$ range, suggesting that the linear superposition principle performs better in weaker vortical flows.

- The amplitude of the second motion showed very little effect on the accuracy of the linear superposition prediction, reinforcing the notion that the separation distance of the upper surface vortices is the critical factor that governs linear behaviour.

- The effect of $\Delta\tau$ becomes more significant for additional transient motions. Linear superposition was shown to remain valid in a relatively smaller window of $\Delta\tau$ during four successive transient motions. Around this window the prediction showed a significant drift from agreement, which could possibly worsen for additional motions. The maximum peak lift showed an asymptotic increase of around 100% relative to the first motion lift peak.

- An extension to periodic motion was investigated. The linear superposition of a single sinusoidal cycle was compared with experiment. It was found to capture the mean lift increase remarkably well for $k < 0.47$, beyond which it displayed drastic over-prediction. This was postulated to be due to increased LEV strength at higher frequencies. The amplitude however was captured with a reasonable degree of accuracy across the range of frequencies and amplitudes tested. At higher frequencies this is likely due to the dominance of the added-mass component.

This chapter opens an interesting avenue for future research. Compound transient motions will need to be extended to pitching and surging motions to test for any commonality in vortex behaviour. Although linear superposition performed well in this specific plunging motion, it is not reasonable to assume a similar performance for other canonical motions.

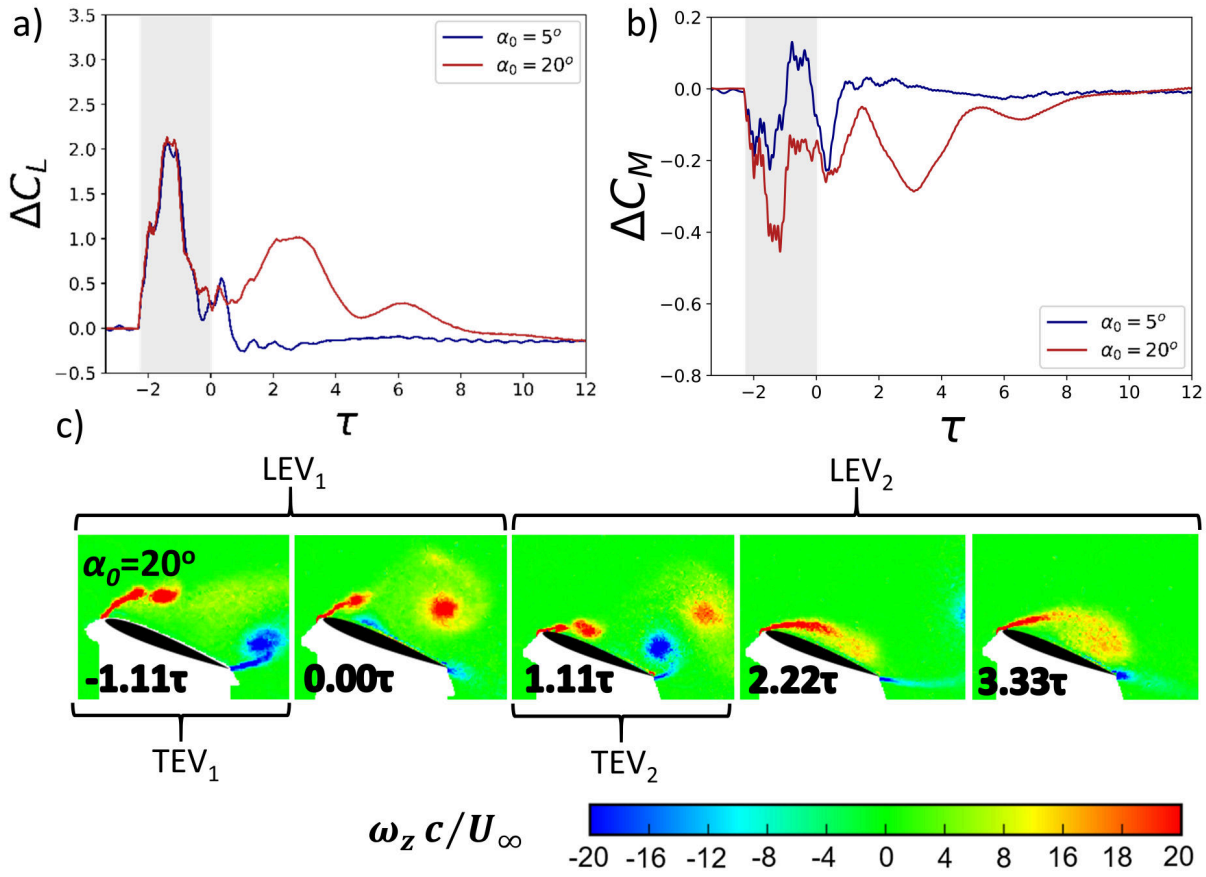

Figure 5-1: Single transient motion, $T = 2.22$ and $\alpha_{pl,max} = 25°$; a) ΔC_L for single transient motion at $\alpha_0 = 5, 20°$, b) ΔC_M, c) key corresponding flow field development stages for $\alpha_0 = 20°$

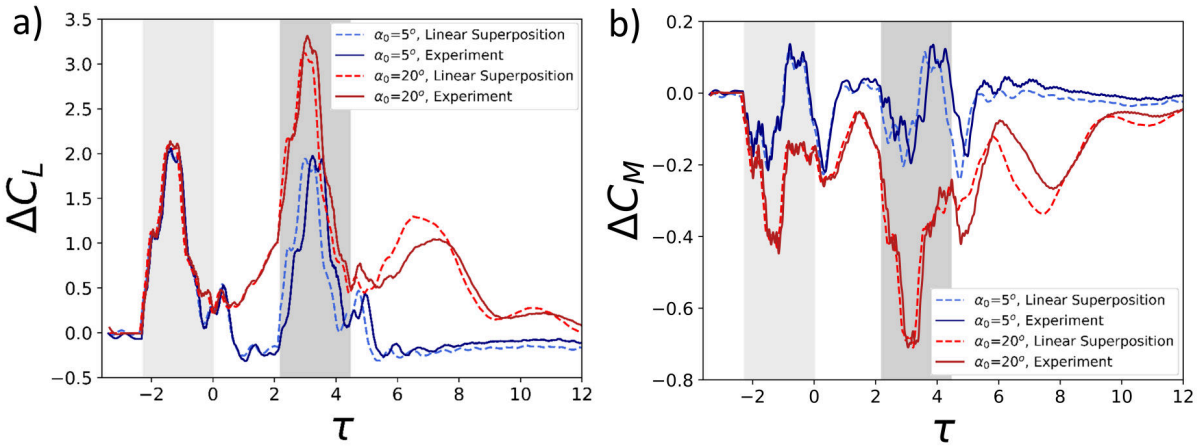

Figure 5-2: Compound transient motion, $T = 2.22$ and $\alpha_{pl,max} = 25°$; a) ΔC_L for compound motion with $\Delta\tau = 2.2$ at $\alpha_0 = 5, 20°$, e) ΔC_M for same compound motion case.

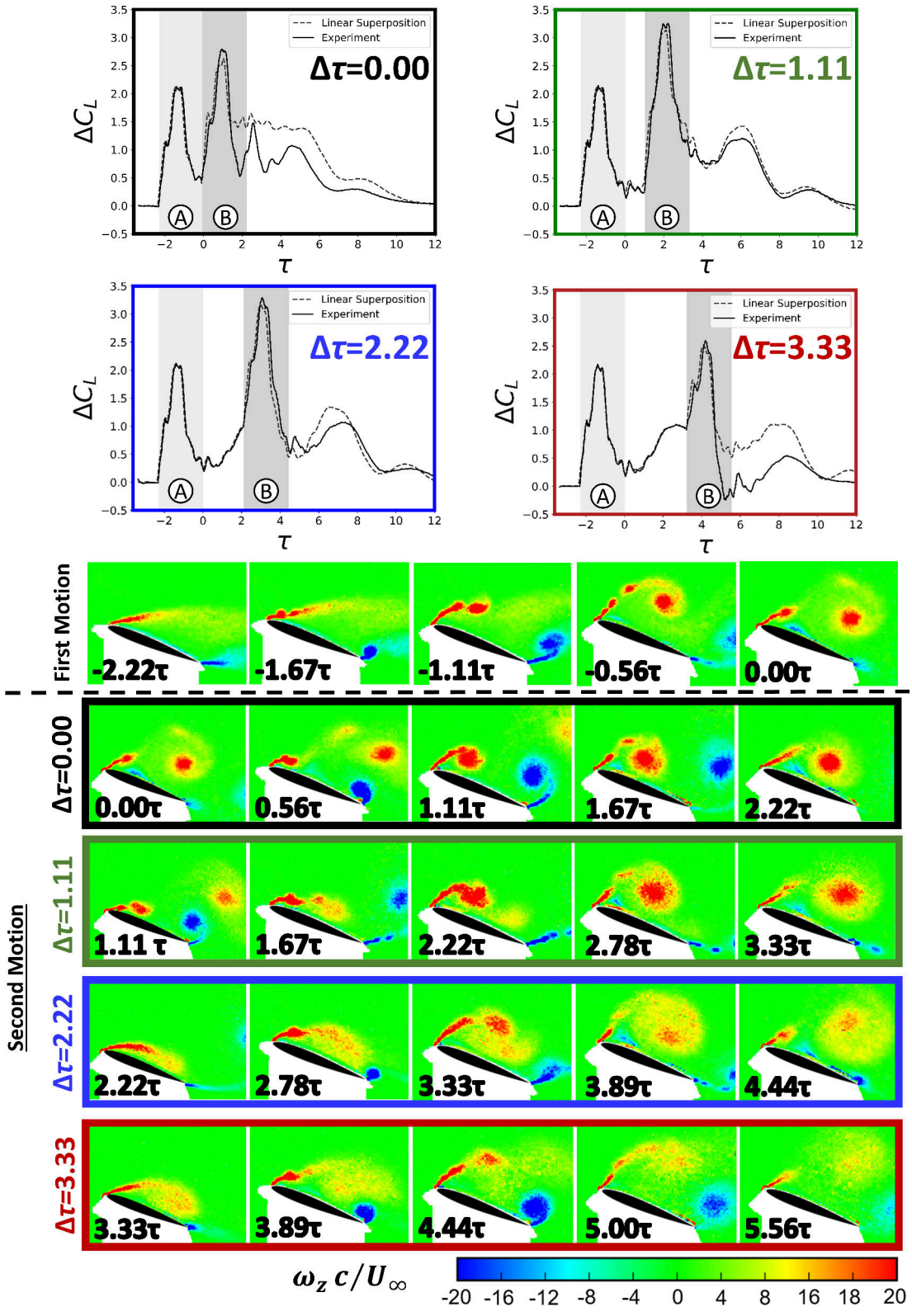

Figure 5-3: Effect of second motion delay, $\Delta\tau$, on ΔC_L with corresponding flow field images.

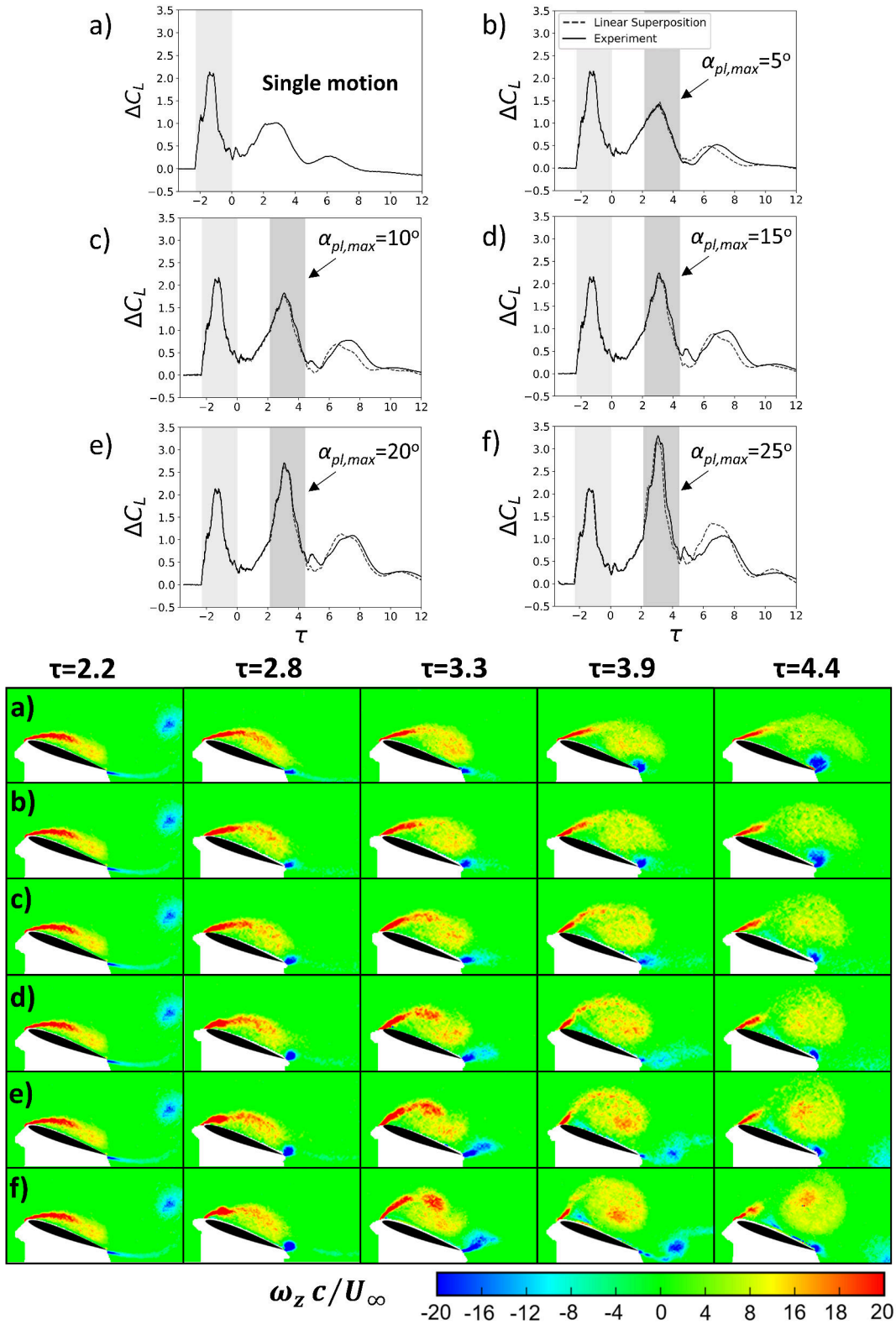

Figure 5-4: Effect of second motion amplitude, $\alpha_{pl,max}$, on ΔC_L with corresponding flow field images for $\Delta\tau = 2.22$; a) Single motion, b) $\alpha_{pl,max} = 5°$, c) $\alpha_{pl,max} = 10°$, d) $\alpha_{pl,max} = 15°$, e) $\alpha_{pl,max} = 20°$, f) $\alpha_{pl,max} = 25°$.

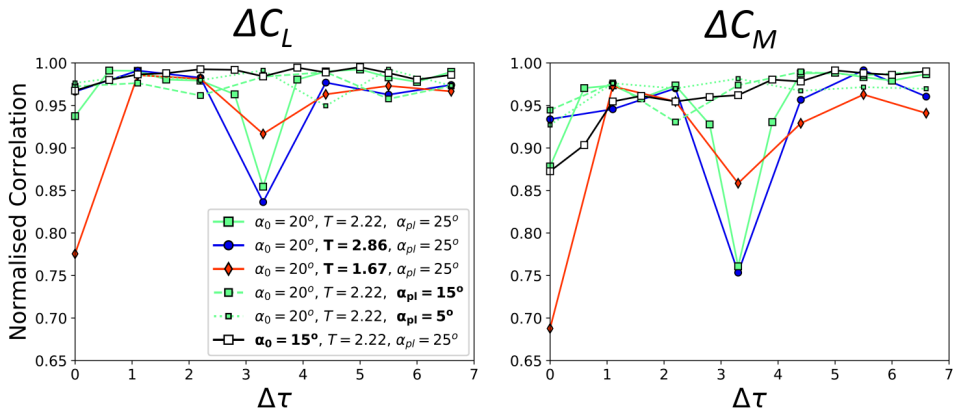

Figure 5-5: Normalised correlation of linear superposition and experiment.

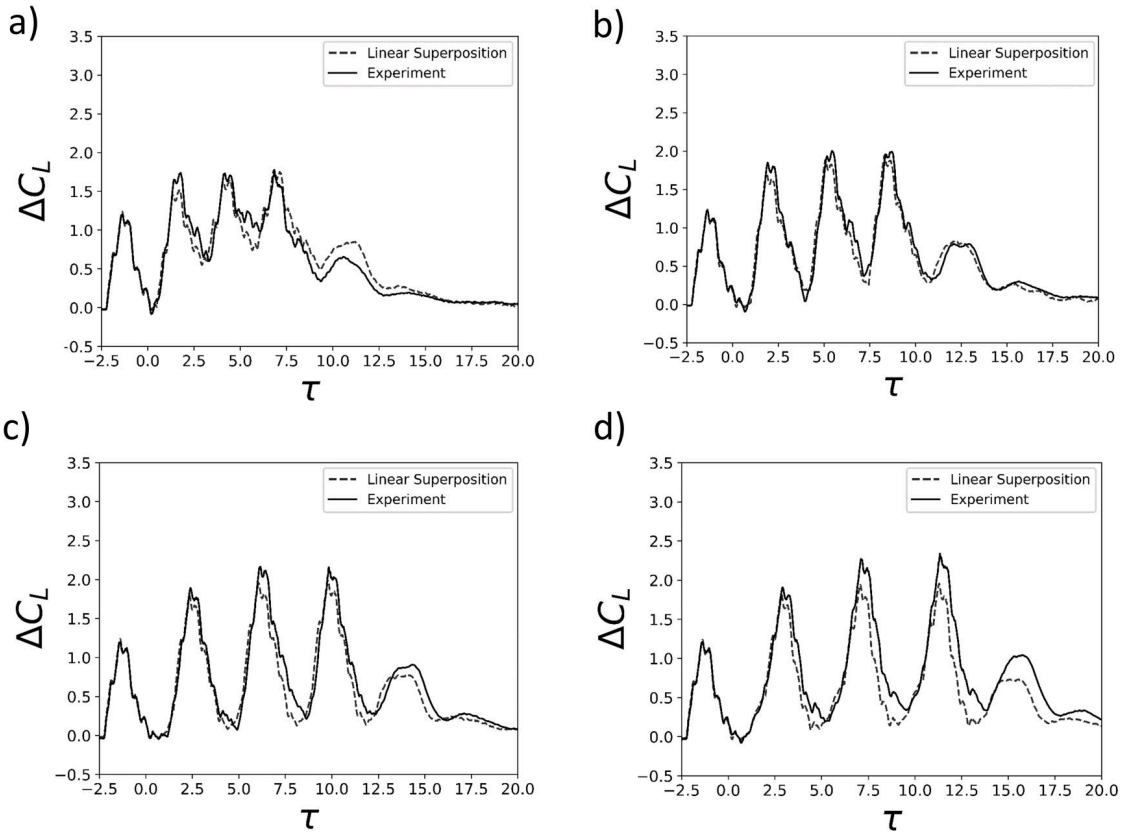

Figure 5-6: Four compound transient motions, a) $\Delta\tau = 0.5$, b) $\Delta\tau = 1.0$, c) $\Delta\tau = 1.5$, d) $\Delta\tau = 2.0$.

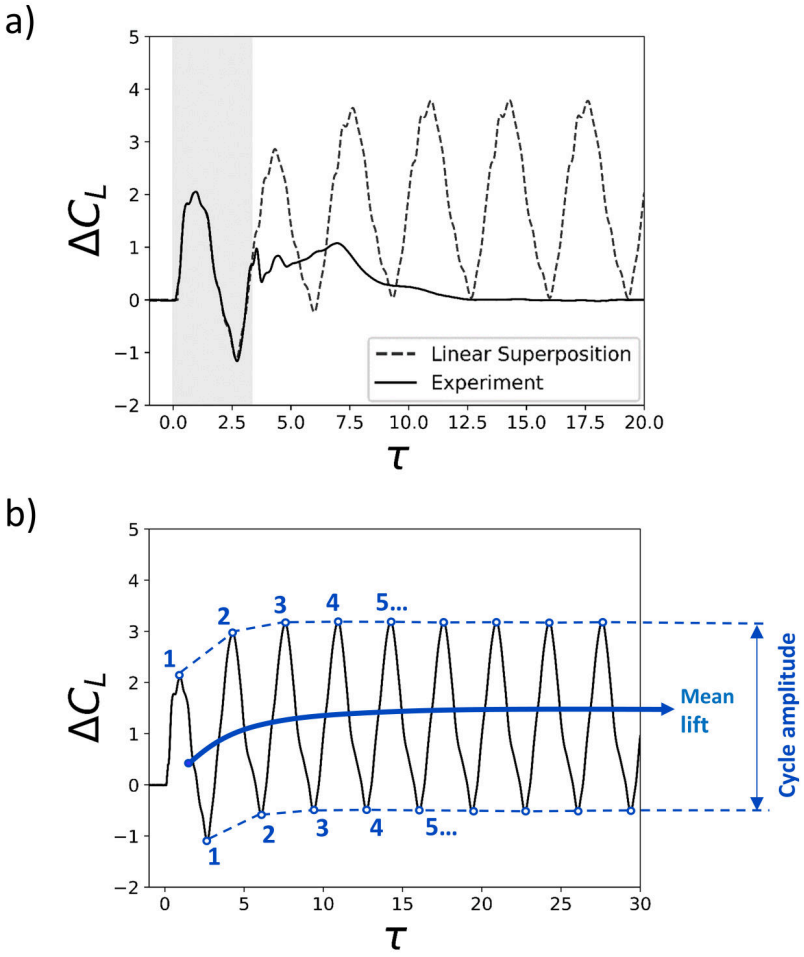

Figure 5-7: Sinusoidal motion, a) example of lift response for single sinusoidal motion with the linear superposition, b) mean lift and cycle amplitude extraction for sinusoidal motion.

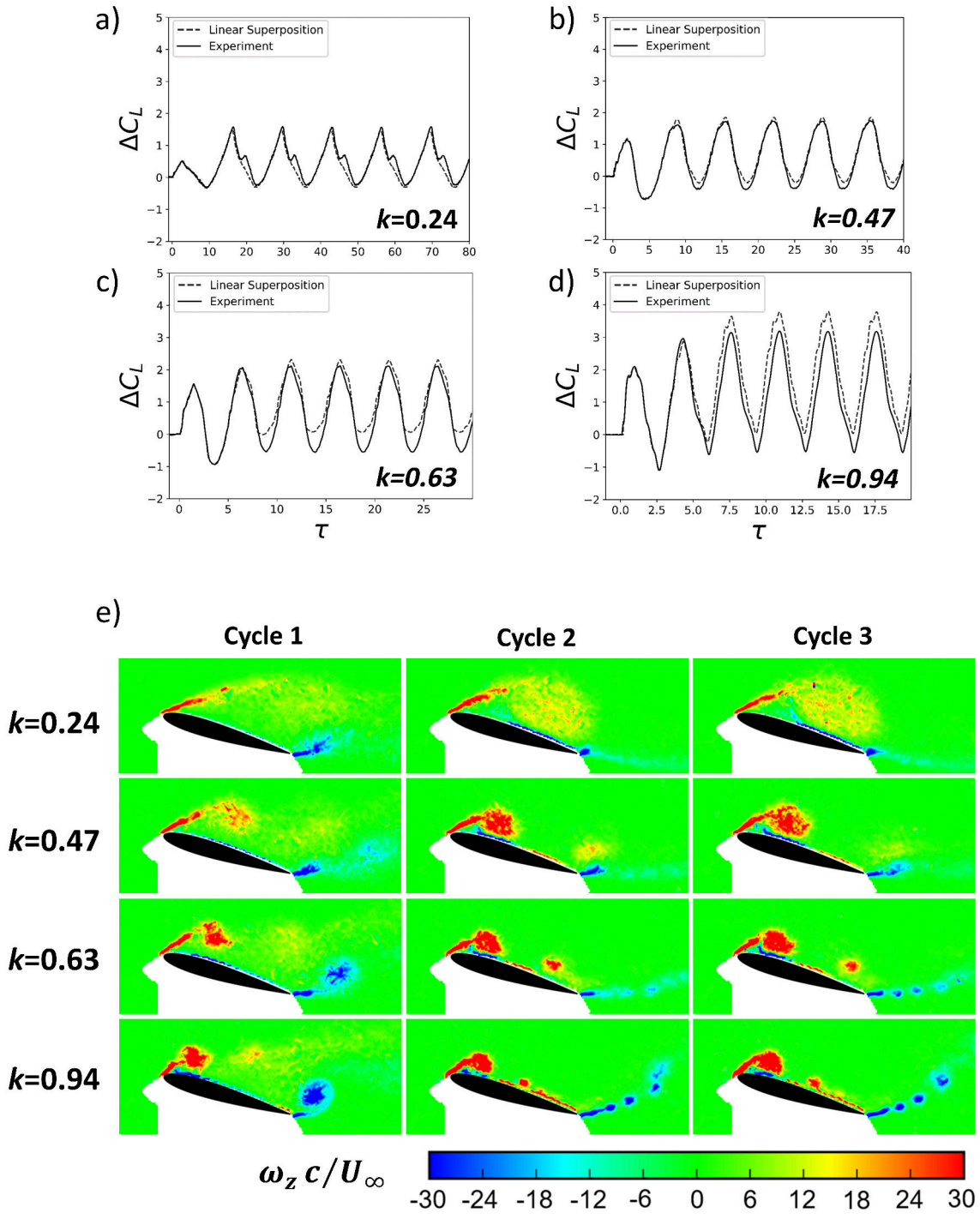

Figure 5-8: Periodic sinusoidal comparison with linear superposition of single sinusoid lift response for, a) $k = 0.24$, b) $k = 0.47$, c) $k = 0.63$, d) $k = 0.94$, e) corresponding flow fields at $t/T = 0.25$ (quarter-cycle) for first 3 motion periods.

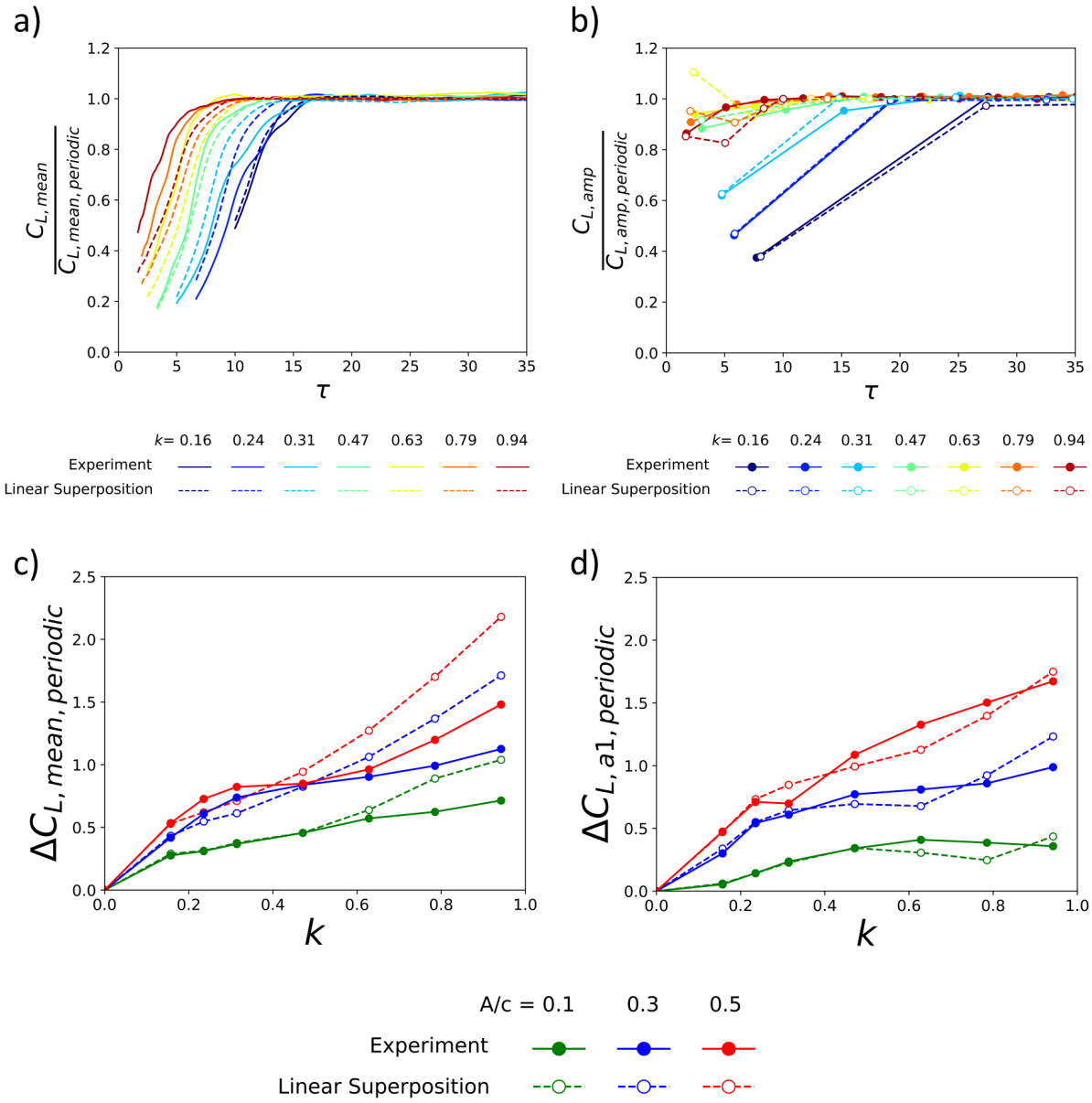

Figure 5-9: Periodic sinusoidal comparison with linear superposition of single sinusoid, a) normalised mean lift variation with τ, b) normalised cycle amplitude with tau, c) mean lift values against k at periodic condition, d) first harmonic of lift signal against k at periodic condition.

Chapter 6

Reynolds number effects

6.1 Summary

Research into massively separated, vortex dominated flows has largely focussed on the low Reynolds (Re) number regime where biological fliers and swimmers operate. It is perhaps fortuitous that the performance requirements on experimental rigs to test in this regime are relatively low, the vast majority of which take place in water tunnels or towing tanks. Reynolds number insensitivity has been demonstrated through a wealth of research for Reynolds numbers from $\mathcal{O}(10^2)$ to $\mathcal{O}(10^4)$ [4], however in order to push this envelope further experiments must migrate to the wind tunnel environment where performance requirements become extreme. If general Reynolds number insensitivity can be demonstrated into the transitional/turbulent regime, as per Eldredge and Jones [4], confidence will be reinforced in the use and extrapolation of low Reynolds number findings to high Reynolds number applications. The following study compares the aerodynamic response of a transient plunging airfoil between an equivalent water tunnel and wind tunnel experiment at $Re = 20K$ and $100, 150K$ respectively. Lift, pitching moment and flow field measurements show only minor differences between $Re = 20K$ and $Re = 150K$ in terms of aerodynamic loads, stemming from the unsteady shear layer behaviour. During large-scale vortex shedding, pressure measurements showed the peak loads to occur when the chord-wise area exposed to the induced low pressure was maximised and revealed the aftward movement

of the lower surface stagnation region to be a significant contributor to the aerodynamic loads. The LEV velocity was estimated from the movement of the low pressure frontier across the chord and shown to vary between 0.21 to $0.29U_\infty$ depending on motion type and α_0. This frontier provides a reasonable approximation of the airfoil half-saddle point [101], a topological flow point on the surface that divides forward and reversed flow. The half-saddle marks the shedding of the LEV and subsequent loss of suction when it reaches the trailing-edge in line with recent studies [93, 99–101]. Finally, the peak loads for $Re = 20, 100, 150K$ displayed good collapse and showed excellent agreement with the data from Chapter 4, adding confidence in the use of low Re measurements for the high Reynolds number applications.

6.2 Aerodynamic Loads

Figure 6-1 presents the time-histories of ΔC_L and ΔC_M for $Re = 20K$ and $150K$. The case selected here is for motion period $T = 5.0$ and amplitude $\alpha_{pl,max} \pm 8°$; the use of a larger motion period and smaller amplitude combination when compared with Chapter 4 is due to the wind tunnel rig limitations as described in Chapter 3. Consider first the positive motion cases shown in Figure 6-1a and 6-1b. For the initial portion of the motion, indicated by the dashed line, the lift response is almost identical between $Re = 20K$ and $150K$ for all α_0 tested. At mid-motion however, $\tau = -2.5$, the differences between different Re and α_0 start to manifest. For $\alpha_0 = 0°$ at $Re = 150K$ the lift shows a marginal yet consistent increase above $Re = 20K$ which extends beyond the end of the motion to around $\tau \approx 10$. Better agreement between Reynolds numbers is seen for $\alpha_0 = 5°$ and $10°$, where the latter displays a distinct sustained lift increase for the aft portion of the motion. At $\alpha_0 = 15°$ the lift drops significantly from $\tau = -2.5$ to a negative value before recovering from $\tau \approx 0$. For this case, $Re = 150K$ displays a number of small post-motion lift peaks rather than the single smooth increase seen at $Re = 20K$; these will be discussed later. With regards to the pitching moment, $Re = 20K$ and $150K$ are in qualitative agreement for all α_0 and both display the distinct peaks in nose-down pitching moment at $\alpha_0 = 10, 15°$. The large nose-down peak at $\alpha_0 = 10°$ is indicative of coherent LEV formation and shedding, which serves to explain the sustained lift increase in Figure 6-1a. A slight delay is present in the timing of

nose-down peaks at $Re = 150K$, which indicates earlier shedding of the LEV at a lower Reynolds number, in line with [102].

Slightly better levels of agreement between $Re = 20K$ and $150K$ are also displayed during the negative motion cases, see Figure 6-1c and 6-1d. All pre-stall α_0 exhibit similar behaviour in both lift and pitching moment response. A more rounded lift response is exhibited during the motion for $Re = 150K$ when compared with the sharper peak seen for $Re = 20K$. It is of the authors belief that this is a rig specific feature, possibly manifesting from the differences in actuation methods, described in Chapter 3. Nevertheless the lift curves are in close agreement, particularly when taking the measurement uncertainties into account, also described in Chapter 3. For the post-stall condition of $\alpha_0 = 15°$ the lift and pitching moment display the characteristic post-motion vortex formation and shedding from $\tau = 0$. This was determined in Chapter 4 to be due to flow reattachment during the motion period followed by separation and roll-up. The results suggest a somewhat stronger vortex that sheds at a slightly later time for $Re = 150K$ which is particularly visible in the pitching moment response, see Figure 6-1d.

Figure 6-2 presents results for the same motion as Figure 6-1 at the additional post-stall conditions of $\alpha_0 = 18, 20, 25$ and $30°$. During positive motion the lift and pitching moment responses show similar behaviour. There is a drop in maximum ΔC_L as α_0 is increased from $18°$ to $30°$, similar to the smaller period, larger amplitude cases shown in Figure 4-2a. In contrast to Figure 4-2b however, the nose-down pitching moment peak also decreases with increasing α_0, possibly due to the lack of a strong vortex present over the airfoil in the present cases. In the post-motion stage, all post-stall α_0 display multiple lift and pitching moment peaks for $Re = 150K$, an artefact that is not observed in pre-stall conditions, see Figure 6-1. The cause of these peaks is elucidated in Figure 6-3a which presents the chord-normal acceleration superposed onto the relative lift response for the $\alpha_0 = 18°$ case. Significant wing oscillations occur from $\tau > 0$ that coincide with the inception of the lift peaks. The acceleration leads the lift maxima which infers that the peaks are caused by a circulatory component rather the added-mass effect. This is verified in Figure 6-3b, where the upper surface pressure coefficients are mapped with τ. Multiple vortical signatures can be observed from $\tau > 0$ as low pressure bands that convect across

the chord, corresponding to the lift peaks in Figure 6-3a. This will be addressed in section 6.5. Additional pressure maps will be discussed in section 6.3.

Considering the negative motion cases in Figure 6-2 at $\alpha_0 = 18°$, the lift and pitching moment once again point towards a slightly stronger vortex that is shed around 1τ later for $Re = 150K$; this case also marks the emergence of an additional peak for $Re = 20K$ and $150K$ at $\tau = 5$ and 6 respectively. Interestingly when α_0 is increased further to 20°, the post-motion lift peak for $Re = 20K$ exceeds the $Re = 150K$ case. This data point was checked for repeatability and was confirmed to be valid. The additional vortex shedding peak observed at $\tau \approx 5$ for $Re = 20K$ in the lift and pitching moment response is no longer present at $Re = 150K$, presumably due to a lack of vortex strength required for additional shedding [96]. When α_0 is increased further to $25, 30°$ the first post-motion lift and pitching moment peaks reduce significantly and additional maxima are displayed at $\tau \approx 3, 6, 9$. Lift and pitching moment signals are consistently larger for $Re = 150K$ which is most likely related to the excitation of the free shear layer through wing vibration as described previously.

6.3 Flow Field and Pressure Distribution Measurements

To better understand the differences in loads response between $Re = 20K$ and $150K$, Figures 6-4, 6-5, 6-6 and 6-7 present the flow fields for select cases. The associated ΔC_L and ΔC_M are shown in part a) and b), and the corresponding pressure distributions for $Re = 150K$ are shown in Figure 6-8. The flow field comparison between $Re = 20K$ and $150K$ for $\alpha_0 = 15°$, $T = 5.0$ and $\alpha_{pl,max} = 8°$ is shown in Figure 6-4c. The motion starts at $\tau = -5.00$ where the flow field begins in a steady-state, stalled condition. Both $Re = 20$ and $150K$ show fully separated flow and the upper surface pressure distribution for $Re = 150K$ is virtually constant, see Figure 6-8a. At mid-motion, $\tau = -2.50$, the lift and nose-down pitching moment are at their maximum. Figure 6-4c indicates for both Re a weak vortex forming above the airfoil associated with higher velocity above the leading-edge shear layer and marginal increase in velocity above the trailing-edge. This is demonstrated in Figure 6-8a through an increase in suction on the upper surface with a broad peak around $x/c = 0.8$. This combined with the lower surface stagnation point moving reward

and spreading causes the increase in lift and nose-down pitching moment observed. Note that the additional dynamic pressure introduced by the motion is around 1% and as such, has not been factored in to the calculation of C_P. At motion cessation the weak vortex is shed and the leading-edge shear layer is deflected upwards, causing the lift to drop below the static value through decreased upper surface suction, see Figure 6-8a. Beyond $\tau = 0.00$ the lift and pitching moment responses of $Re = 20$ and $150K$ begin to differ more significantly as described previously, however no significant difference can be seen in the velocity magnitude plots in Figure 6-4c. A low pressure wave is observed in Figure 6-8 at $\tau = 2.00$ around the mid-chord region and is responsible for the lift peak in the $Re = 150K$ case (which is influenced by wing vibration).

Figure 6-5 presents the lift, pitching moment and flow field measurements for the equivalent negative motion case, $\alpha_0 = 15°$, $T = 5.0$ and $\alpha_{pl,max} = -8°$. The motion starts with the same fully separated flow state, see Figure 6-5c, and at mid-motion the flow begins to reattach from the leading-edge due to the reduced total effective angle of attack. Both $Re = 20$ and $150K$ display minimum relative lift around this time which is produced through an increase in pressure on the upper surface and a decrease in pressure on the lower surface, see Figure 6-8b. At motion cessation, $\tau = 0.00$, the flow is almost fully reattached for $Re = 150K$, indicated by the leading-edge suction peak in Figure 6-8b, whereas a significant band of separated flow is still present over the upper surface for $Re = 20K$, as expected for lower Re flows. As time progresses the flow in both cases begins to separate and roll-up. For $Re = 20K$ the small recirculating region near the leading-edge spreads over the chord at $\tau = 2.00$ and by $\tau = 3.23$ the maximum lift and nose-down pitching moment is achieved, caused by an elongated vortical structure as indicated by the vorticity plot. For $Re = 150K$ the flow detachment process begins from a fully attached flow state which takes comparatively longer to progress. Vortex inception can be seen at $\tau = 2.00$ which progressively grows in size and induces maximum loads at $\tau = 3.65$. The pressure plots in Figure 6-8b show this clearly as a low pressure wave convecting and spreading from the leading-edge region. At $Re = 150K$ the vortex appears stronger and more coherent which is indicated by the increased velocity above the leading-edge shear layer. Similar to the findings from Chapter 4, it appears that the degree of flow reattachment influences the strength

of the subsequent LEV for negative motion cases.

To elucidate the progression in flow field with α_0, Figure 6-6 shows results for $\alpha_0 = 18°$, $T = 5.0$ and $\alpha_{pl,max} = -8°$. At $\tau = 0.00$ the flow is reattached for the majority of the chord for $Re = 150K$, caused by the reduction in effective angle of attack during the motion. The pressure distribution in Figure 6-8c highlights this as a distinct leading-edge suction peak followed by a comparatively reduced suction in the aft portion of the upper surface when compared with the equivalent case for $\alpha_0 = 15°$, see Figure 6-8b. For $Re = 20K$ the flow displays a larger region of separated flow over the airfoil with no signs of significant reattachment. Despite this, shear layer roll-up is still observed and a distinct vortex can be seen convecting across the chord from $\tau = 1.67$ to 2.00. Similar flow features are present for $Re = 150K$, but once again the flow takes a comparatively longer time to develop into a marginally stronger LEV, as indicated by the velocity magnitude at $\tau = 2.53$. This induces peaks in the lift and nose-down pitching moment with a 0.53τ delay compared with $Re = 20K$. The vortex induces a broad low pressure region on the upper surface, see Figure 6-8c, extending from the leading-edge to $x/c \approx 0.8$ and somewhat increases the high pressure region on the lower surface.

When α_0 is increased further to 20° different behaviour is observed and the lower Re case now produces the larger, more delayed peak in lift and pitching moment. Figure 6-7c indicates that the reduction in effective angle of attack is no longer sufficient to reattach the flow for both $Re = 20, 150K$. At $\tau = 0.00$ both cases display significant separation across the entire chord. No suction peak exists in the upper surface pressure distribution for $Re = 150K$, which instead displays a suction wave around $x/c \approx 0.25$ indicating vortex formation. The vortex convects and grows until $\tau = 1.03$ where the peak lift and nose-down pitching moment occur. The vorticity plot at this time instant indicates a more diffuse, less coherent vortex compared to $Re = 20K$. At $Re = 20K$ the vortex takes a longer time to form, produces stronger load peaks and appears to be sufficiently strong to induce an additional shedding event at $\tau \approx 5$.

With regard to the positive motion cases, an interesting feature is the similarity of the peak lift across the α_0 range, despite the drastically different flow-fields, see Figure 6-1a; similar to the

findings in Chapter 4. To explore this further, the relative lift, pitching moment and flow fields at $Re = 150K$ are shown in Figure 6-9 for $\alpha_0 = 5, 10, 15°$. These will be discussed along with the pressure distributions presented in Figure 6-10 to elucidate how the lift changes manifest. The relative pressure coefficient, ΔC_P, is also plotted alongside the plots of C_P to highlight the chord-wise position of the pressure changes and is defined as:

$$\Delta C_P = C_P - C_{P,\alpha_0} \tag{6.1}$$

where C_{P,α_0} is the static pressure distribution. The motion starts at $\tau = -5.00$ where the flow fields are in their steady-state, see Figure 6-9c. The pressure distributions at this time instant in Figure 6-10a show attached flow for $\alpha_0 = 5, 10°$ and complete separation for $\alpha_0 = 15°$. At $\tau = -3.75$ the lift response is almost identical for all α_0. Notable changes in the flow field are the increased velocity in the leading-edge region for $\alpha_0 = 5, 10°$ which is verified by the increase in suction peak in Figure 6-10. The distribution of ΔC_p highlights this suction peak increase along with a slightly increased pressure on the lower surface for the majority of the chord; related to the aft movement of the stagnation point. For $\alpha_0 = 15°$ however the flow remains massively separated and Figure 6-9c shows a change in the streamline recirculation just aft of the quarter-chord. The corresponding pressure distribution displays a near constant increase in upper surface suction across the chord with a slight maxima at $x/c \approx 0.3$, see Figure 6-10b. This is observed in the ΔC_p distribution and suggests the presence of a weak vortical structure. The approximately constant increase in lower surface pressure along with the absence of leading-edge suction causes the pitching moment to decrease, see Figure 6-9b. A similar maximum lift is obtained for all α_0 at $\tau = -2.50$ despite the significant flow field differences. The velocity magnitude plots in Figure 6-9c show attached flow for $\alpha_0 = 5°$, LEV inception for $\alpha_0 = 10°$ and massively separated flow with weak vortex formation for $\alpha_0 = 15°$. These flow field differences yield significant variations in pressure distribution as shown in Figure 6-10c which are more clearly shown in the ΔC_p distribution. For $\alpha_0 = 5°$ the attached flow creates a typical leading-edge suction peak which leads to a slight pitching moment increase. Vortex inception for $\alpha_0 = 10°$ induces a suction

wave centered around $x/c \approx 0.15$ and creates a similar pitching moment increase to $\alpha_0 = 5°$. At $\alpha_0 = 15°$ the entire upper surface experiences a suction increase which is marginally biased towards the trailing-edge at $x/c \approx 0.75$. This corresponds with the weak vortex position in Figure 6-9c and leads to the excursion in nose-down pitching moment. At $\tau = -1.25$ the suction peak for $\alpha_0 = 5°$ begins to decrease as α_{pl} begins to reduce. A distinct vortex is present over the aft portion of the airfoil at $\alpha_0 = 10°$ which leads to a nose-down pitching moment spike and sustained lift increase. The nose-down pitching moment is made more severe by the loss of suction peak at the leading-edge, see ΔC_p in Figure 6-10d. For $\alpha_0 = 15°$ the weak vortex has been shed and a weak TEV has formed which leads to a reduction in lift [159]. Figure 6-9c shows the leading-edge shear layer deflected at a greater angle from the chord line which manifests as a reduction in upper surface suction, see Figure 6-10d. Interestingly, an increase in lower surface suction at the trailing-edge region can be seen, possibly caused by the formation of the TEV. After $\tau = 0$ the lift drops dramatically for $\alpha_0 = 10°$ as the vortex is shed into the wake. The leading-edge shear layer takes time to reattach to the airfoil contour after being lifted from the surface during unsteady separation, thus leading to the reduction in lift observed.

6.4 Surface Pressure Analysis

Surface pressure analysis can reveal the behaviour of vortex formation and convection, giving a detailed view of how the lift and pitching moment features are produced. Figure 6-11 presents the contours of the upper and lower airfoil surface with τ for $\alpha_0 = 10°$ during positive motion, and $\alpha_0 = 15, 18, 20°$ during negative motion, i.e. the cases where strong vortex formation is present. Consider first the case $\alpha_0 = 10°$ for positive motion in Figure 6-11a. Vortex inception can be seen in the leading-edge region at $\tau \approx -3$ which induces significant low pressure in a small closed region. As time progresses the vortex undergoes a process of accelerated growth until $\tau \approx -2.5$ where the low pressure region progresses across the chord linearly with time; the initiation of which is marked by a drop in leading-edge suction. In a similar study by Leknys *et al.* [101], the linear expansion of this low pressure frontier was linked to the movement of a half-saddle point, a topological flow point on the airfoil that represents the boundary between

forward and reversed flow [93], see Figure 2-26. Leknys *et al.* [101] noted a significant collapse in upper surface suction at the point where the half-saddle reached the trailing-edge, in line with the findings of Rival *et al.* [93], Widmann & Tropea [99] and Krishna *et al.* [100]. Figure 6-11a highlights the approximate location of the half-saddle point, where the pressure gradient changes rapidly in the chord-wise direction. The dotted line represents the growth rate and convection of the LEV and is estimated to progress at approximately $0.29U_\infty$ in this linear region. A dramatic loss of suction can be seen at $\tau \approx -0.5$ where the half-saddle point reaches the trailing-edge. which coincides with the drop in lift and nose-down pitching moment spike, see Figure 6-9c. As the half-saddle approaches the trailing-edge a spike can be seen in lower surface high pressure;a feature that is visible in all the cases presented in Figure 6-11. Leading-edge suction then begins to rebuild from $\tau \approx 1$ as the shear layer reattaches to the airfoil upper surface, shown previously in Figure 6-9c, which coincides with the growth of the high pressure region on the lower surface.

Figure 6-11b presents $\alpha_0 = 15°$ for negative motion. A favourable pressure gradient is produced on the upper surface during the motion between $\tau = -5$ and 0 which allows the flow to reattach to the airfoil. From $\tau = -1$ the attached flow begins to produce a leading-edge suction peak on the upper surface which rapidly expands between $\tau \approx 0.5$ to 1 before progressing linearly across the chord, elucidating the vortex emergence, growth and convection similar to the previous case. During this time the lower surface initially shows decreasing pressure from $\tau = -5$ to -2.5 as the stagnation point moves towards the leading-edge during the acceleration phase. In the deceleration phase, $\tau = -2.5$ to $\tau = 0$, this is reversed. After the motion stage, $\tau = 0$ to $\tau = 5$, the lower surface displays a broad high-pressure region which correlates with the growth and formation of the upper surface LEV. As the upper surface half-saddle point approaches the trailing-edge, a distinct high pressure spike is observed in the lower surface pressure around $\tau = 3.5$. As the upper surface vortex grows and convects the lower surface stagnation region is sustained at a more aft location, highlighting the increased circulation produced by the bound vortex [94, 100]. Maximum lift corresponds to the point where the majority of the upper surface is exposed to the low pressure induced by the vortex [101], coinciding with the maximum aftward movement of the stagnation region at $\tau = 3.6$. Once again a rapid drop in lift is observed

approximately where the half-saddle estimation reaches the trailing-edge. At this point the vortex is no longer bound to the airfoil [93, 99, 101] which leads to a drop in upper surface suction and foreward movement of the stagnation region. A growth and convection rate of $0.21U_\infty$ has been estimated here for the linear region, a notable decrease from the previous case.

The same negative case for $\alpha_0 = 18°$ is presented in Figure 6-11c. In general, the same trends as $\alpha_0 = 15°$ can be seen. At motion cessation, $\tau = 0$, the flow was shown to be partially reattached over the front half of the airfoil, see Figure 6-6c, which manifests as a leading-edge suction peak of similar magnitude to $\alpha_0 = 15°$. This suction peak then rapidly expands between $\tau \approx 0$ and 0.5 before exhibiting the same linear growth rate across the chord. During this time the stagnation region has shifted aftwards across the lower surface and it sustained between $\tau \approx 1$ to 3. Complete suction breakdown again occurs approximately where the half-saddle point reaches the trailing-edge, which was estimated to travel at around $0.25U_\infty$.

When α_0 is increased to 20° the motion is no longer sufficient to reattach the flow and as such the upper surface pressure distribution shows a distinctive lack in leading-edge suction peak, Figure 6-11d. The vortex signature is more faint in this case, but nevertheless displays a growth and convection of roughly $0.25U_\infty$.

The half-saddle convection speeds from Figure 6-11 have been estimated to range from 0.21 to $0.29U_\infty$ for different α_0 and motion types. This is somewhat higher than Leknys *et al.* [101] who showed convection speeds varying between 0.16 and $0.22U_\infty$. They found a strong dependence on pitch rate, although only presented the convection data for a small subset of the study. The half-saddle convection speed is evidently a complex phenomena and dependent on a wide range of variables, such as motion kinematics, α_0 and airfoil geometry. It remains an open question and the accurate tracking of which will require the use of recent advances in Lagrangian flow diagnostics as shown by Krishna *et al.* [100]. It is also interesting to note that the estimated half-saddle convection speeds equate to chord length convection times of 3.4 to 4.8τ. This corresponds with the findings of Chapter 5, which showed destructive LEV interaction and a distinct drop in linear superposition correlation at convective time delay of $\Delta\tau = 3.3$, see Figure

5-5, suggesting that the location of the half-saddle point can serve as a reasonable predictor for the linear behaviour of compounding transient motions.

6.5 Additional Cases with Data Reduction

For a more complete picture of the Reynolds number effect and to better isolate any rig specific features, an additional Reynolds number of $100K$ was tested in the wind tunnel. Relative lift and pitching moment for positive and negative motion are presented in Figure 6-12 at $\alpha_0 = 15°$, $T = 5.0$ and $\alpha_{pl,max} \pm 6°$. The corresponding pressure maps for the upper and lower surface are shown in Figure 6-13 at $Re = 100, 150K$. In general, the intermediate Reynolds number of $100K$ shows good agreement with $Re = 20, 150K$ and displays only minor discrepancies in the magnitudes and timings of the lift and pitching moment peaks. The wing vibration still has an effect for $Re = 100K$ which can be seen in the positive motion lift and pitching moment, see Figure 6-12a,b. Figure 6-13a shows this effect in more detail as low pressure vortical signatures convecting across the chord from $\tau = 0$. These bands are more closely spaced for $Re = 100K$ due to the combination of lower free-stream velocity and constant wing vibration frequency. At $Re = 100K$ the motion acceleration is reduced compared with $Re = 150K$, which results in smaller magnitude wing oscillations; yet Figure 6-12 displays a similar lift peak magnitude to $Re = 150K$ around $\tau = 2$. This indicates that the wing vibration may not be as influential as previously suggested. For the negative motion, Figure 6-13b shows a similar low pressure progression on the upper surface, with loss of suction occurring slightly sooner for $Re = 100K$.

To further demonstrate the small effect of Reynolds number, the peak loads were extracted for a range of $\alpha_{pl,max}$ from $-10°$ to $+10°$ for $\alpha_0 = 15°$ and $T = 5.0$. These are plotted in Figure 6-14. Note that due to wind tunnel rig limitations the maximum amplitude that could be reached for $Re = 150K$ was $\alpha_{pl,max} = \pm 8°$. For the first peak, L1/M1, all three Reynolds numbers collapse reasonably well across the amplitude range, see Figure 6-12a. A slight spread between the Reynolds numbers exists, but this does not show a clear trend and is close to the bounds of uncertainty. Similar conclusions are drawn from the trends of L2 and M2 in Figure 6-12b, where all Reynolds numbers display the same fundamental behaviour; although a slightly higher

L2 and M2 are found for $Re = 100,150K$ which is most likely due to wing vibration. Figure 6-12c shows the results of Figure 6-12a,b superposed from the results in Figure 4-8 for $\alpha_0 = 15°$. The results fit very well with the previous data set and it is not unreasonable to assume that a similar level of agreement, if not better, would exist for larger amplitude motions [4, 40, 49, 97].

6.6 Conclusions

The effects of significant Reynolds number change on the aerodynamic response of a transient plunging NACA0012 airfoil has been investigated through lift, pitching moment, unsteady pressure and flow field measurements. The key findings are:

- The lift and pitching moment responses remained relatively unchanged between $Re = 20K$ and $150K$. For negative motion, small differences in vortex strength and timing were attributed to the propensity of the shear layer to reattach during motion at a higher Reynolds number.

- Pressure maps revealed the low pressure signature of the upper surface vortex growth and convection stage. Vortex inception coincides with a small, intense region of low pressure situated at the leading-edge. This region grows rapidly and begins to spread across the chord at near constant speed. The point of maximum lift occurs when the chord-wise area exposed to the low pressure region is maximised, i.e. when the LEV and therefore half-saddle point reach the trailing-edge. During vortex growth and convection the lower surface stagnation region moves aftward as a result of increased circulation provided to the airfoil by the bound vortex and is a significant component to the lift and nose-down pitching moment increase.

- Estimates of the vortex growth and convection speed were between 0.21 to $0.29U_\infty$ depending on the motion type and α_0. These estimates were extracted from the approximate location of a half-saddle point, a topological flow point on the airfoil surface dividing the region of forward and reversed flow, which approximately coincides with the strong adverse pressure gradient that precedes the upper surface vortex [101]. In line with current liter-

ature [72, 93, 101] a drastic loss of suction on the upper surface coincided with the arrival of the half-saddle point at the trailing-edge. This also marks the forward movement of the stagnation region, indicating the shedding of the circulation contained in the bound vortex.

- Peak lift and pitching moment values collapsed well for $Re = 20,100,150K$ across a range of motion amplitudes at $\alpha_0 = 15^\circ$ and $T = 5.0$. Despite a small amount of spread, the results showed excellent agreement with the large parameter sweep from Chapter 4.

This study reinforces the notion that Reynolds number has a minimal effect on massively separated and vortex dominated flows [4, 40, 49, 97], adding confidence in the applicability of low Re measurements to high Re applications.

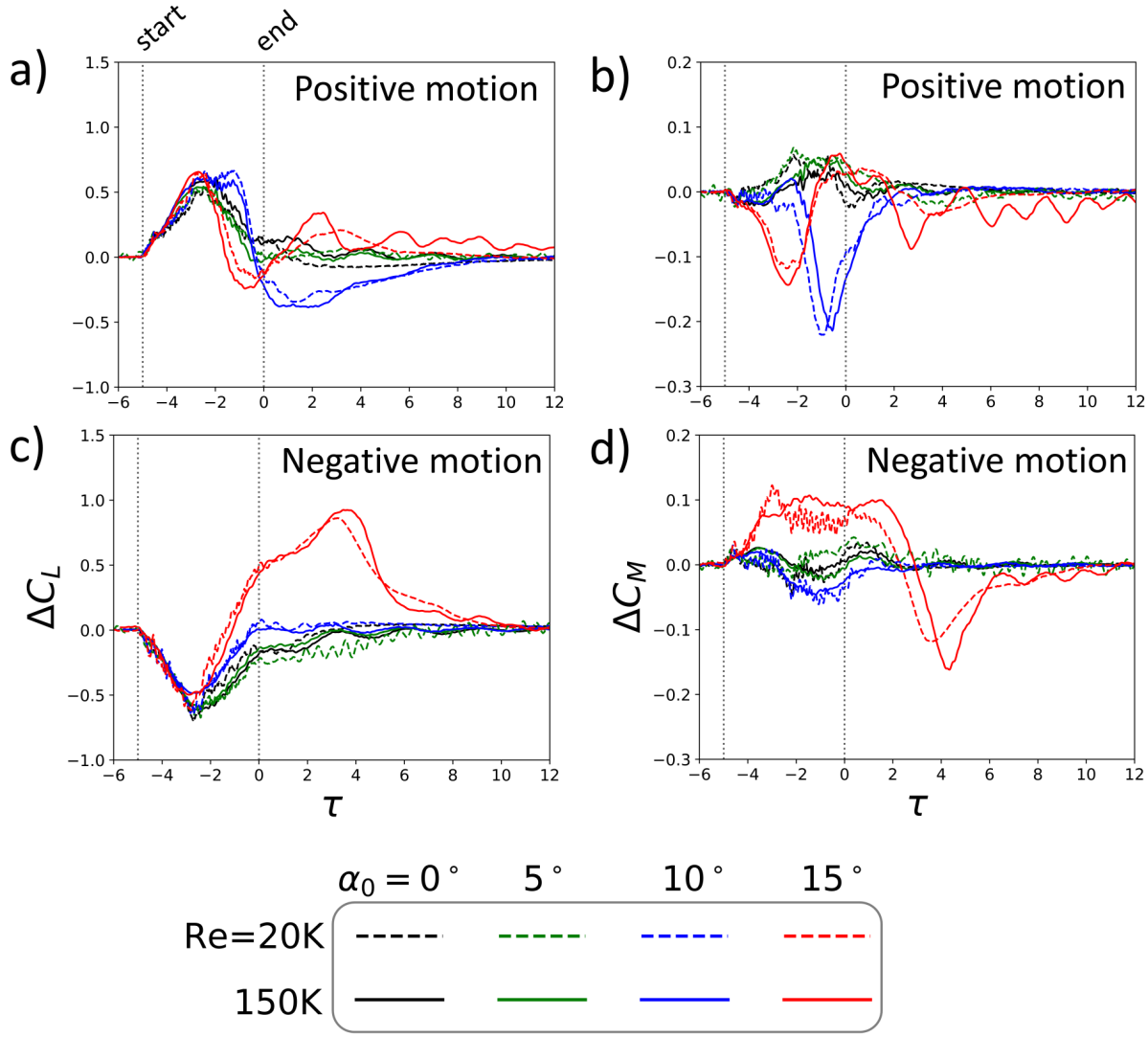

Figure 6-1: Comparison between $Re = 20K$ and $150K$ for a single plunging motion at $T = 5.0$ and $\alpha_{pl,max} = \pm 8°$ with $\alpha_0 = 0, 5, 10, 15°$. a) relative lift for positive motion, b) relative pitching moment for positive motion, c) relative lift for negative motion, d) relative pitching moment for negative motion.

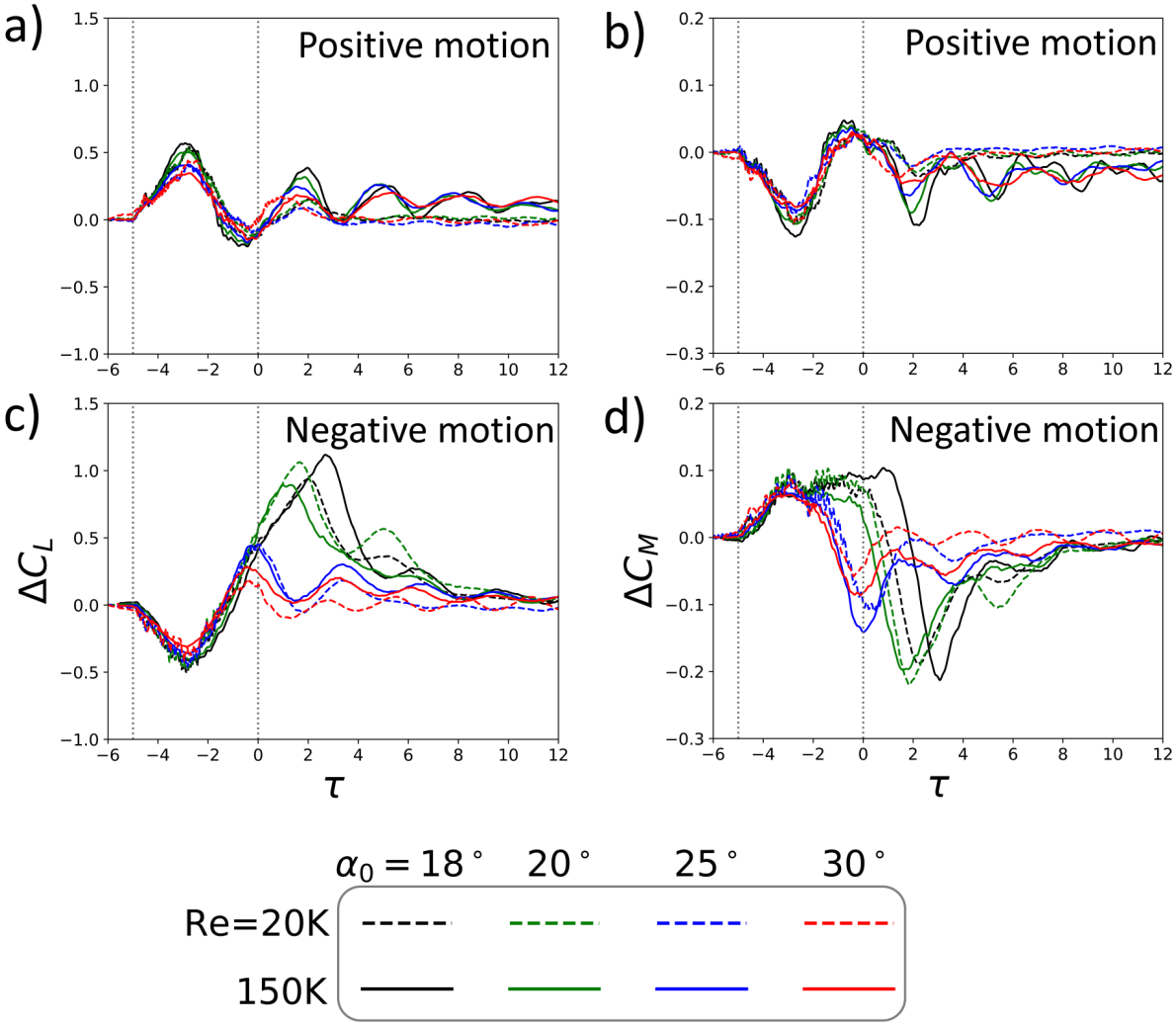

Figure 6-2: Comparison between $Re = 20K$ and $150K$ for a single plunging motion at $T = 5.0$ and $\alpha_{pl,max} = \pm 8°$ with $\alpha_0 = 18, 20, 25, 30°$. a) relative lift for positive motion, b) relative pitching moment for positive motion, c) relative lift for negative motion, d) relative pitching moment for negative motion.

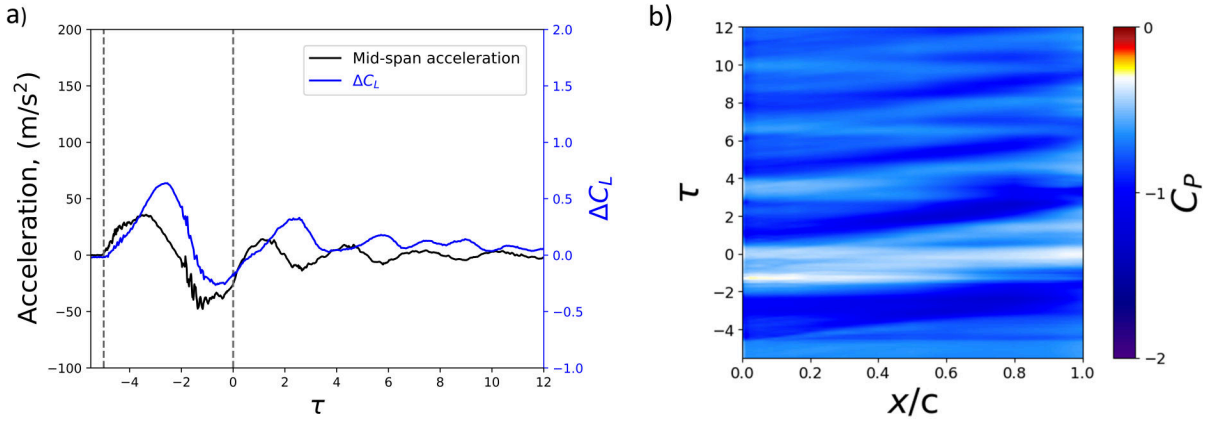

Figure 6-3: a) Chord-normal acceleration with relative lift coefficient, b) coefficient of pressure with τ for $\alpha_0 = 18°$, $T = 5.0$, $\alpha_{pl,max} = 8°$ - positive motion.

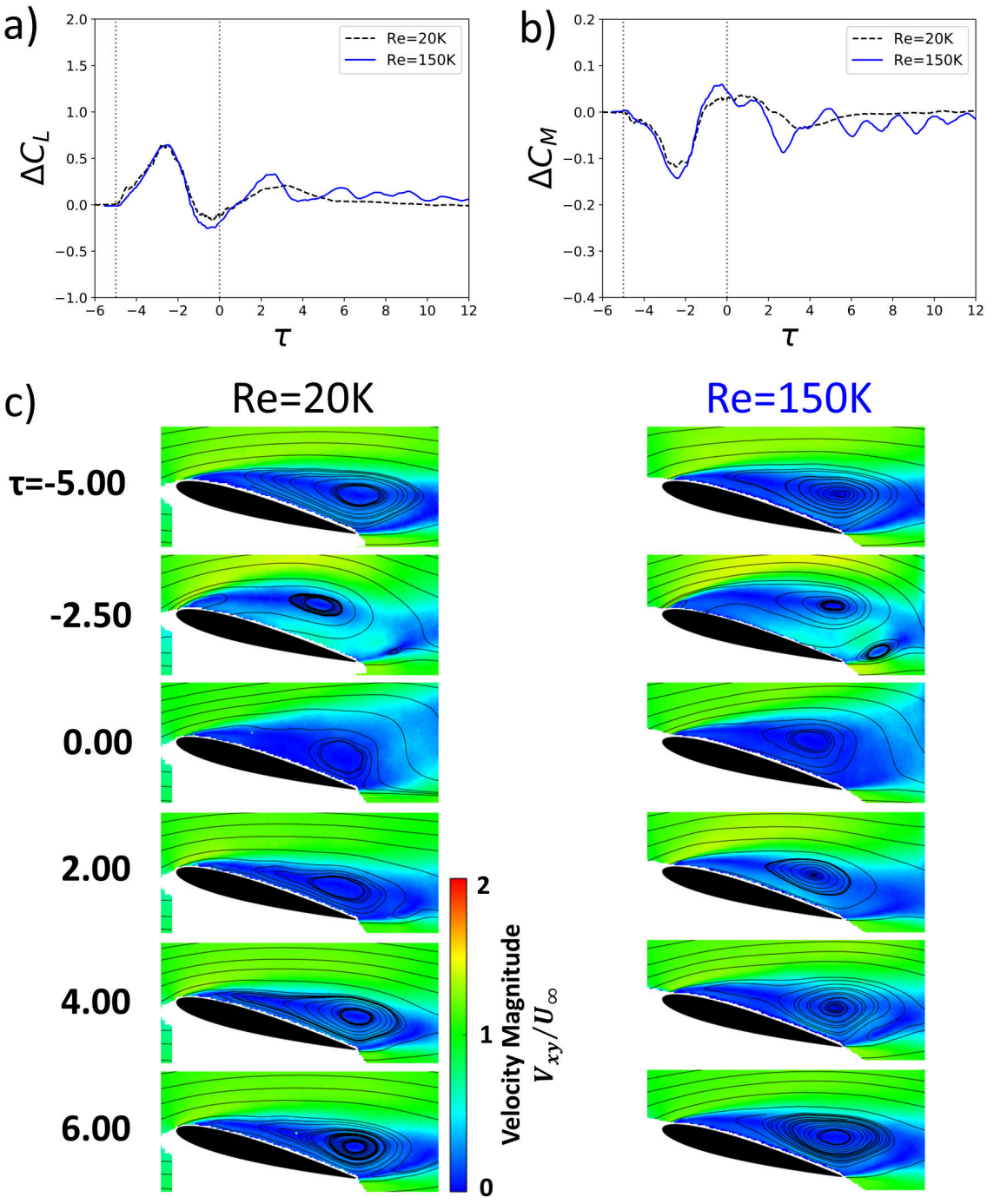

Figure 6-4: Comparison between $Re = 20K$ and $150K$; $\alpha_0 = 15°$, $T = 5.0$, $\alpha_{pl,max} = 8°$; a) relative lift coefficient, b) relative Pitching moment, c) velocity magnitude at select times.

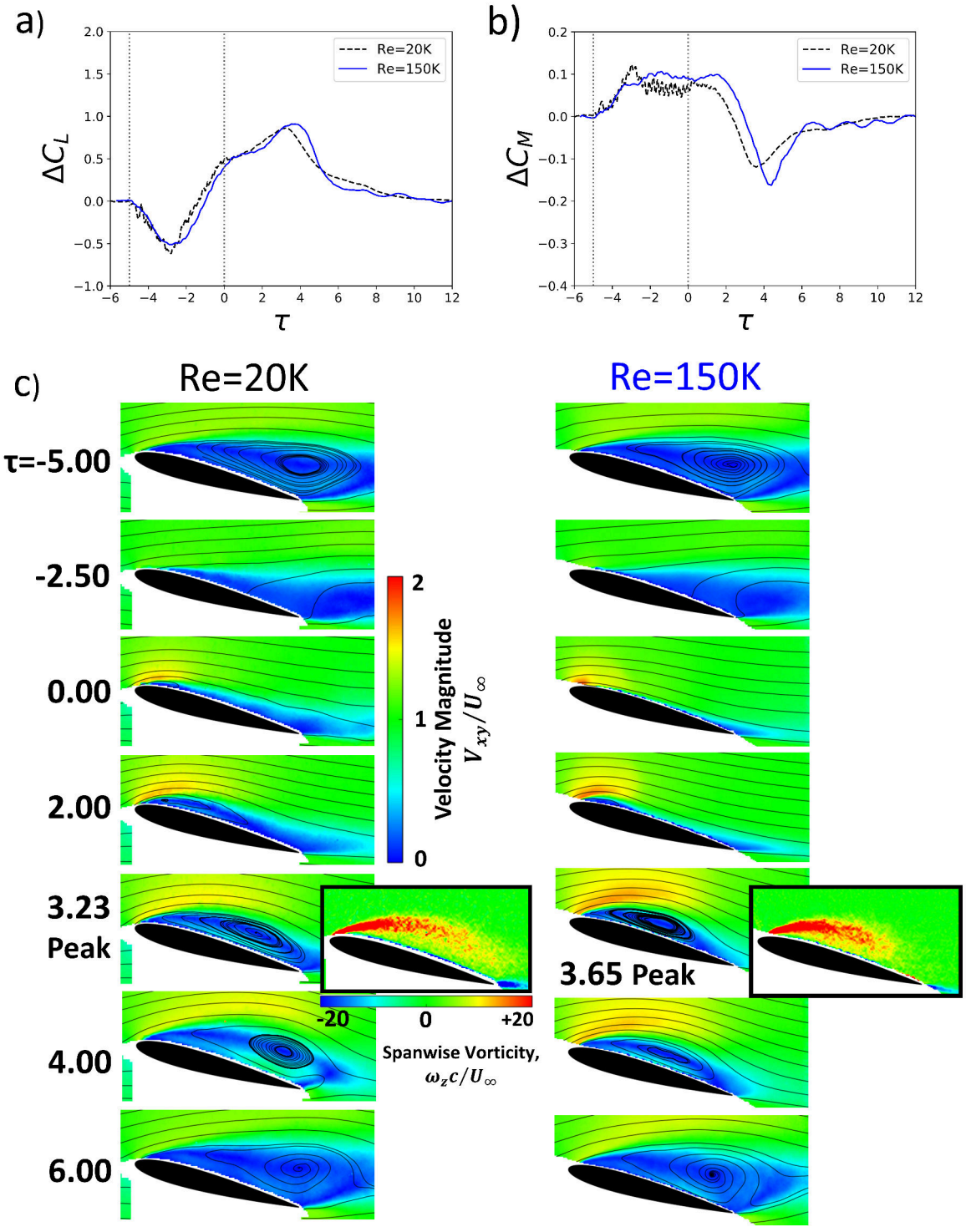

Figure 6-5: Comparison between $Re = 20K$ and $150K$; $\alpha_0 = 15°$, $T = 5.0$, $\alpha_{pl,max} = -8°$; a) relative lift coefficient, b) relative Pitching moment, c) velocity magnitude at select times with select spanwise vorticity plots.

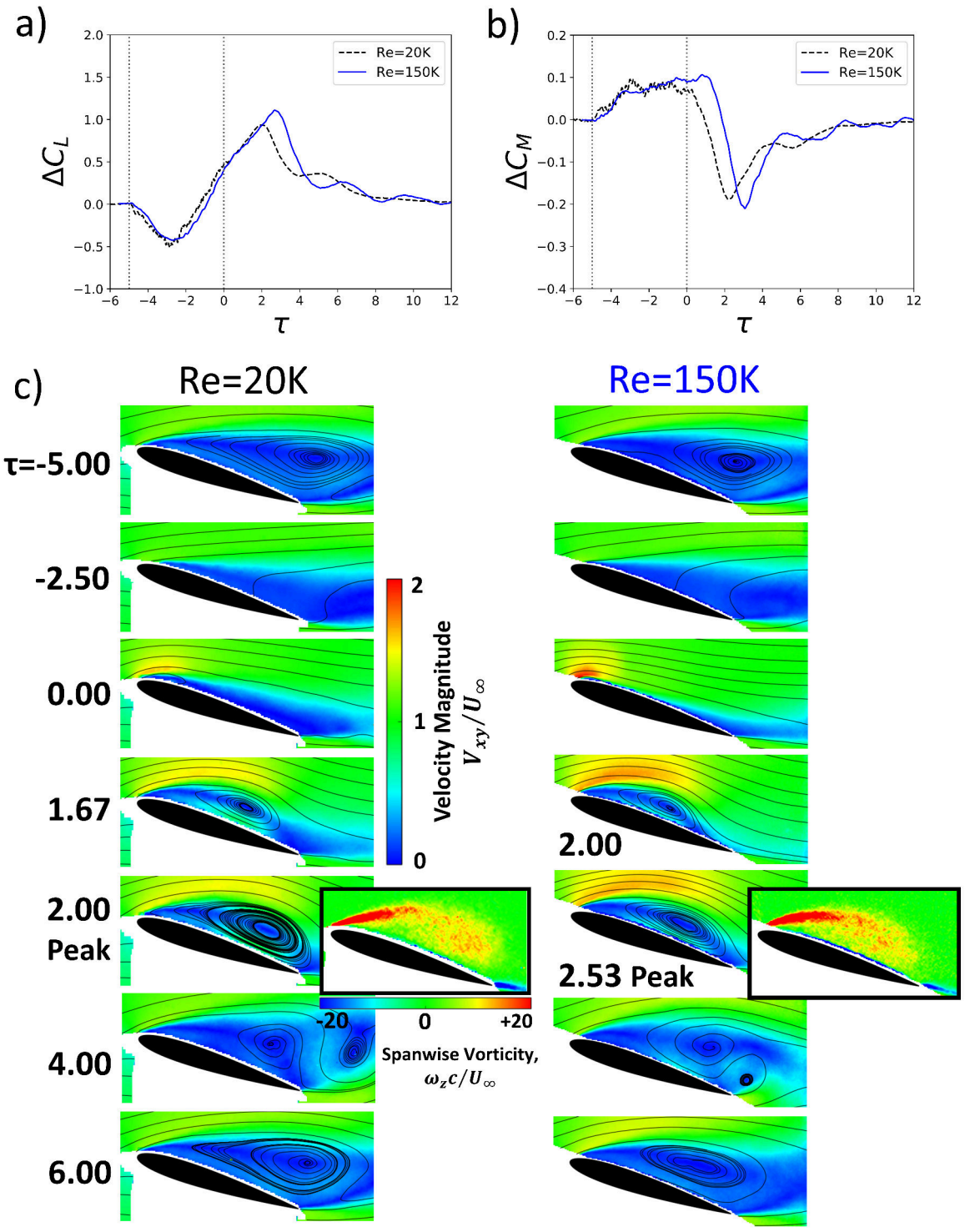

Figure 6-6: Comparison between $Re = 20K$ and $150K$; $\alpha_0 = 18°$, $T = 5.0$, $\alpha_{pl,max} = -8°$; a) relative lift coefficient, b) relative Pitching moment, c) velocity magnitude at select times with select spanwise vorticity plots.

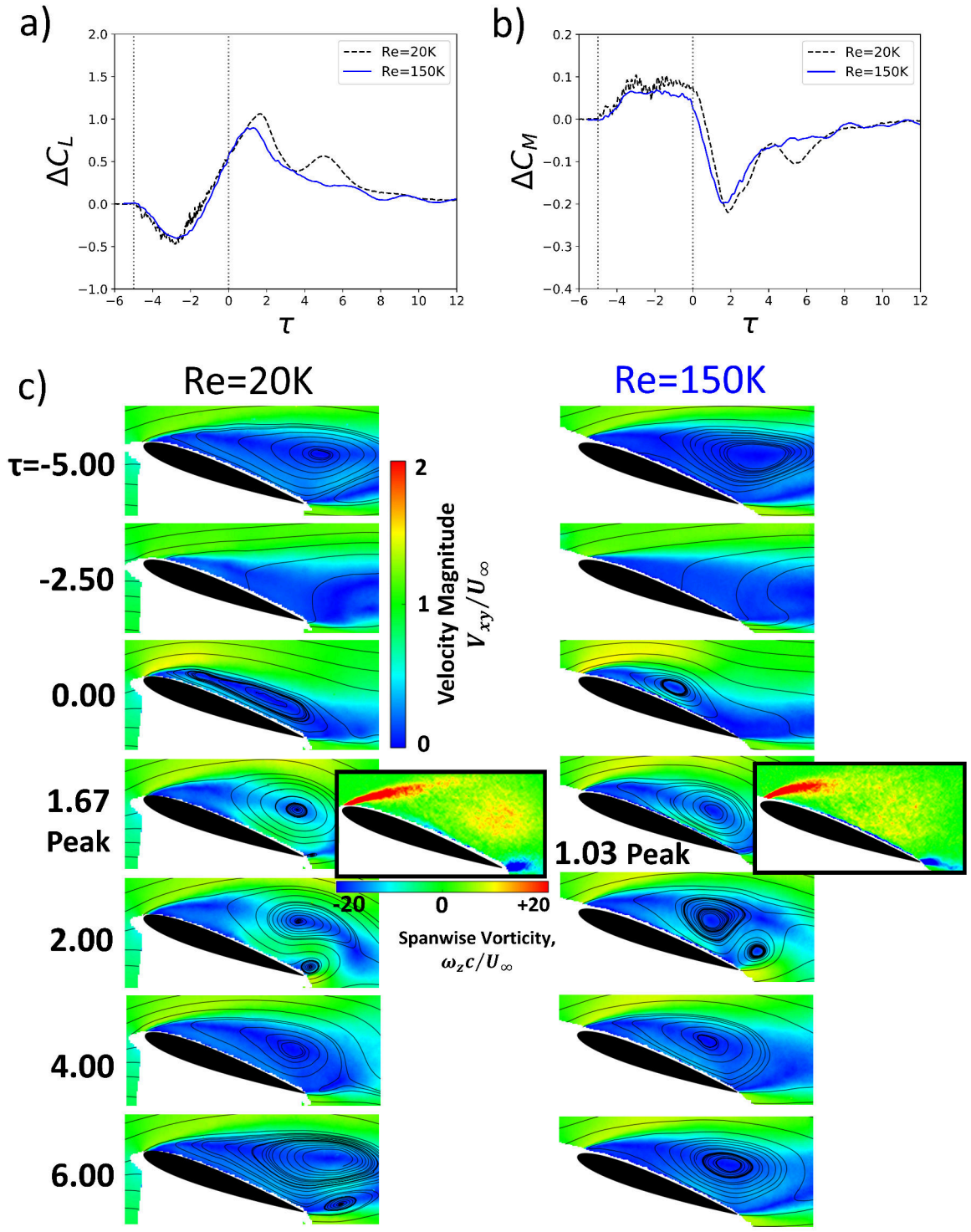

Figure 6-7: Comparison between $Re = 20K$ and $150K$; $\alpha_0 = 20°$, $T = 5.0$, $\alpha_{pl,max} = -8°$; a) relative lift coefficient, b) relative Pitching moment, c) velocity magnitude at select times with select spanwise vorticity plots.

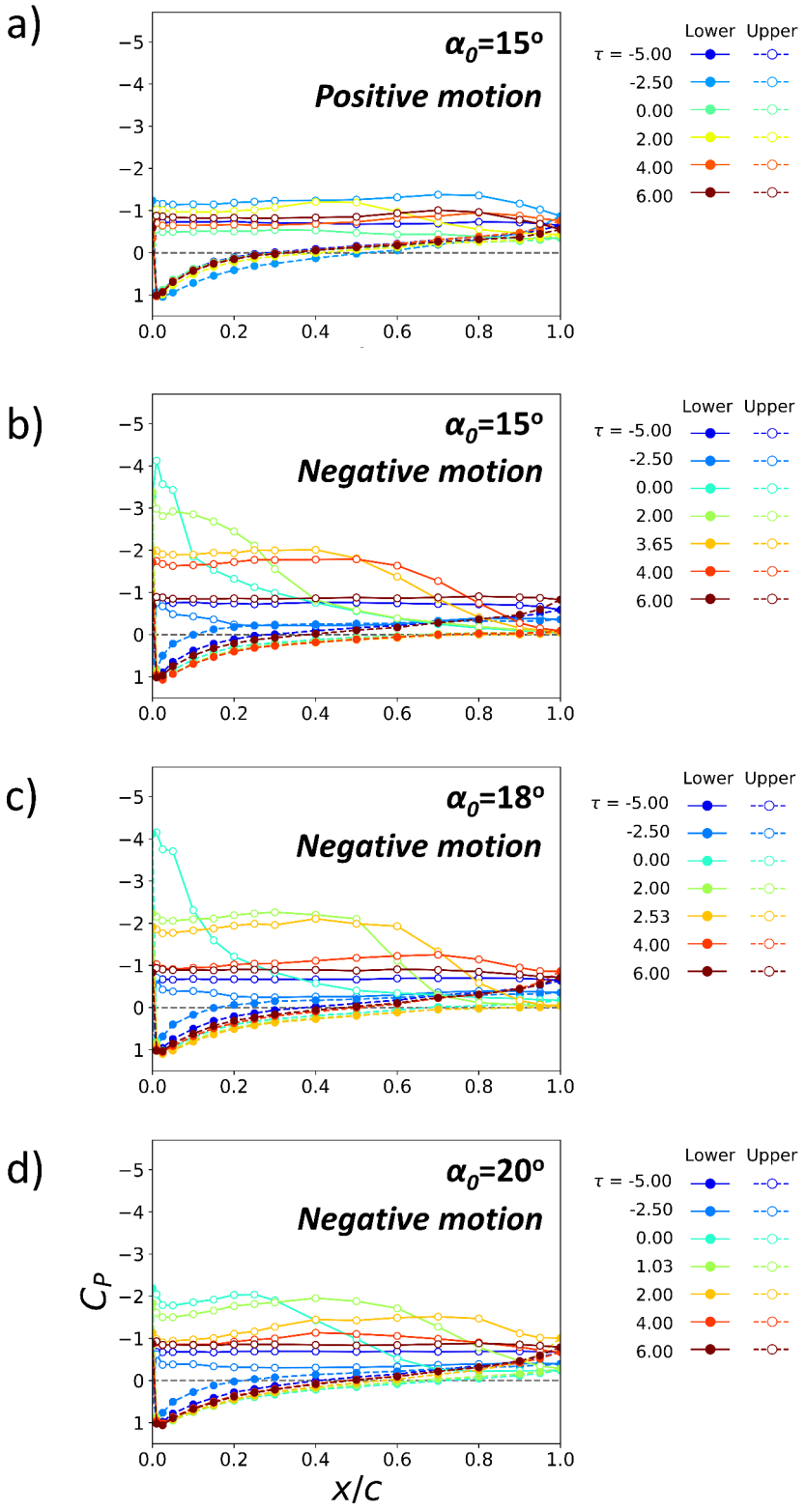

Figure 6-8: Pressure coefficient distribution at $Re = 150K$; corresponding to Figures 6-4,6-5, 6-6 and 6-7.

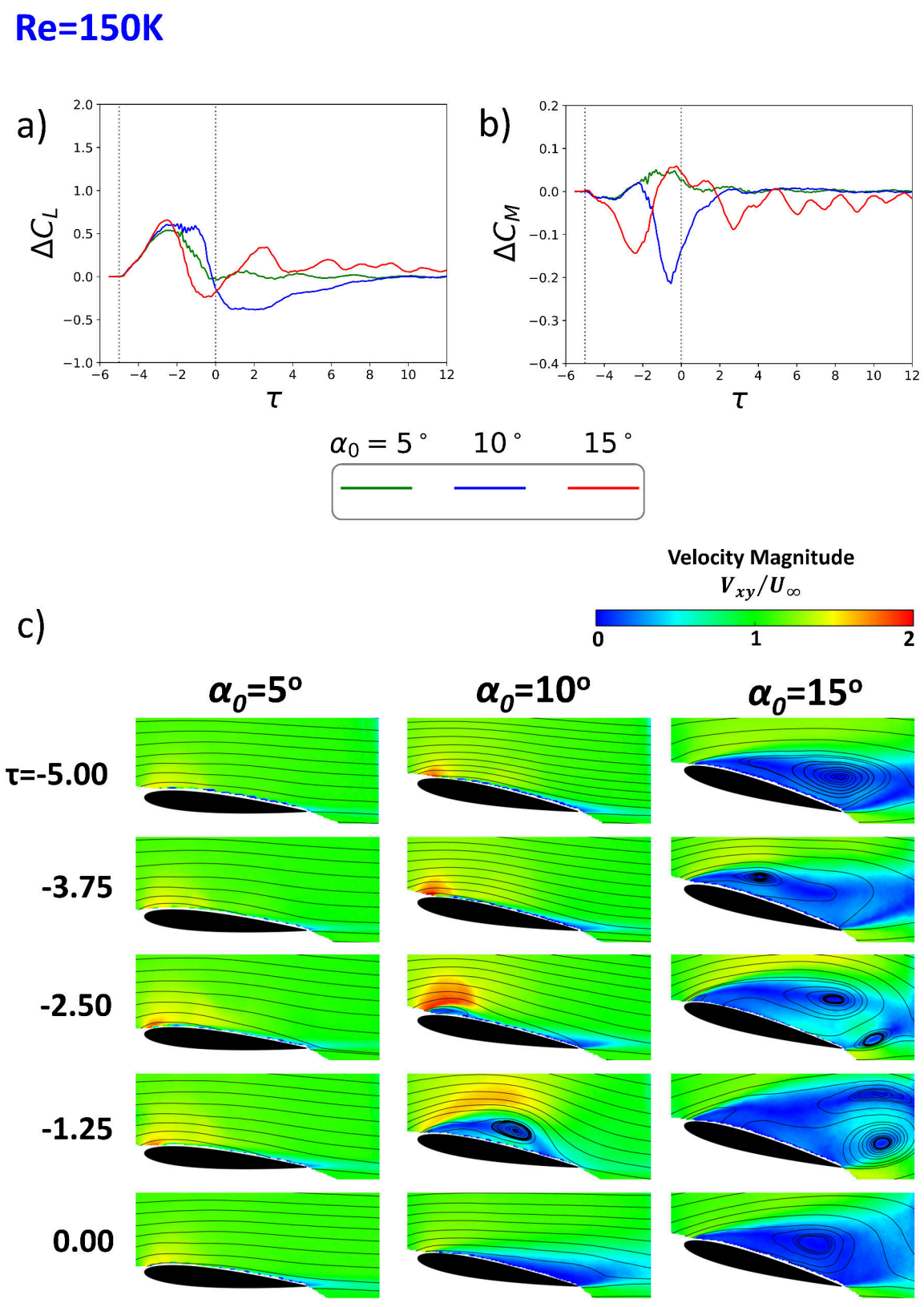

Figure 6-9: a) Relative lift, b) relative pitching moment and c) velocity magnitude plots at $Re = 150K$ for $\alpha_0 = 5, 10, 15°$, $T = 5.0$ and $\alpha_{pl,max} = 8°$.

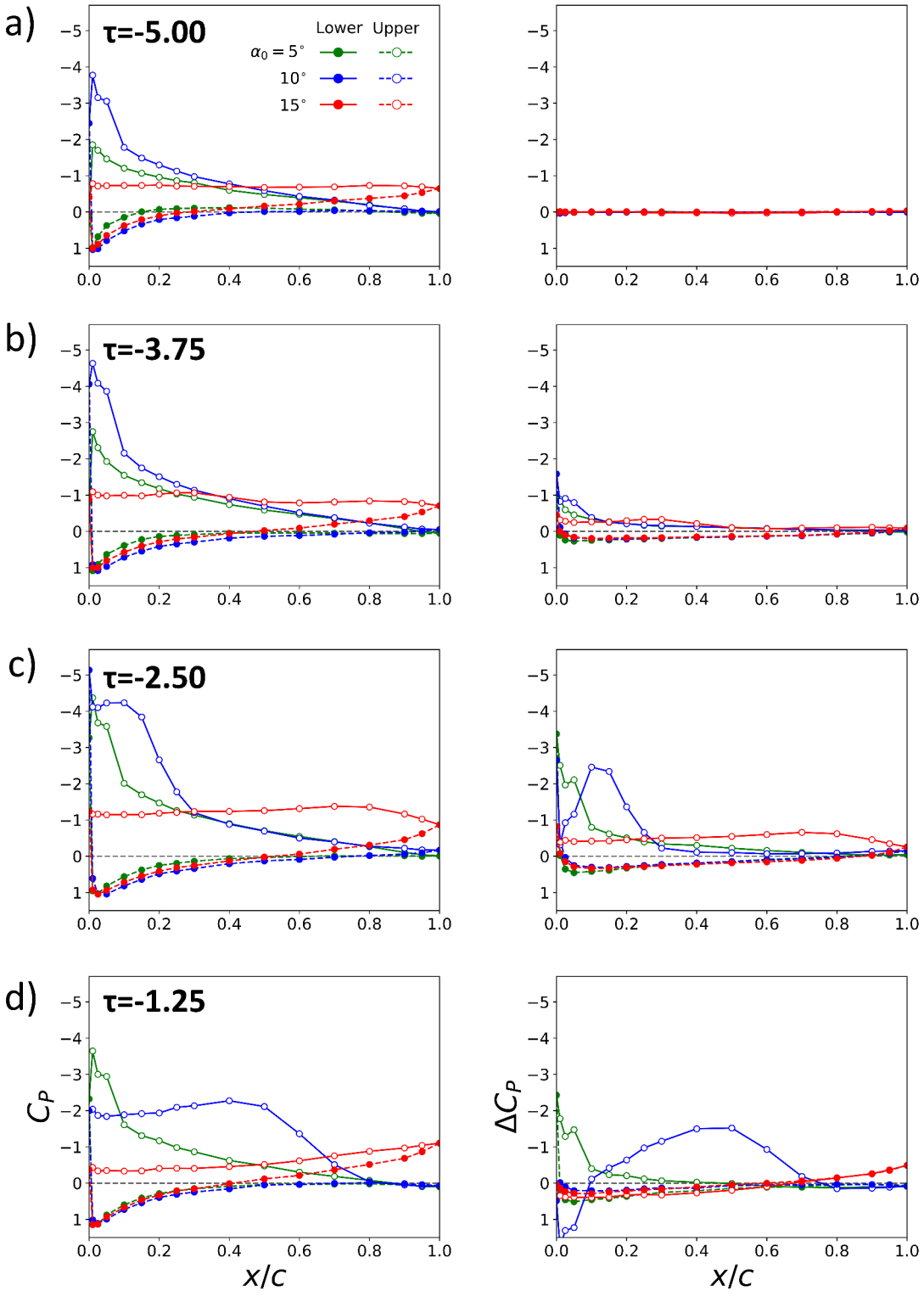

Figure 6-10: Pressure coefficient distribution at $Re = 150K$; corresponding to the cases presented in Figure 6-9.

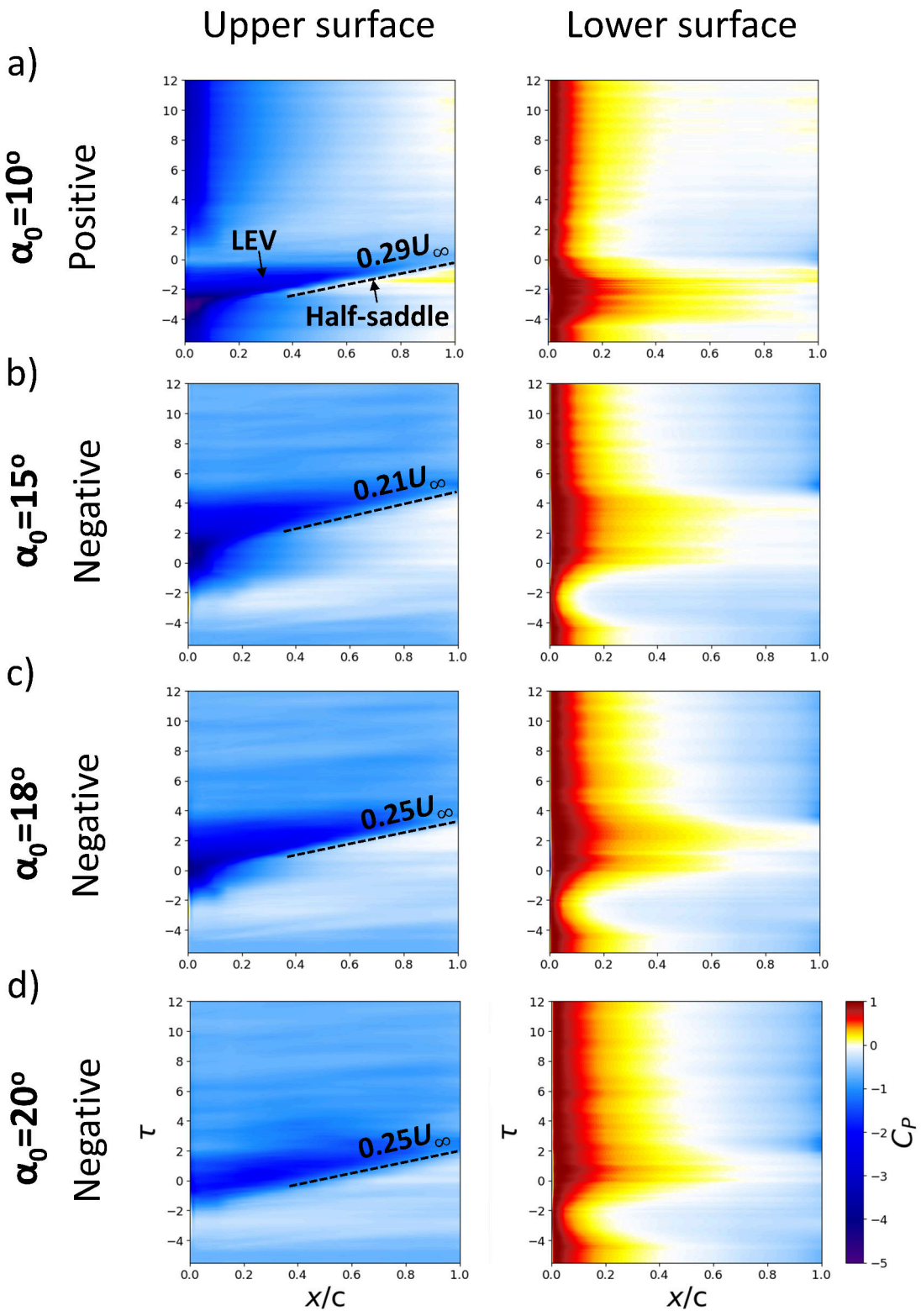

Figure 6-11: Pressure contour maps of the airfoil upper and lower surface.

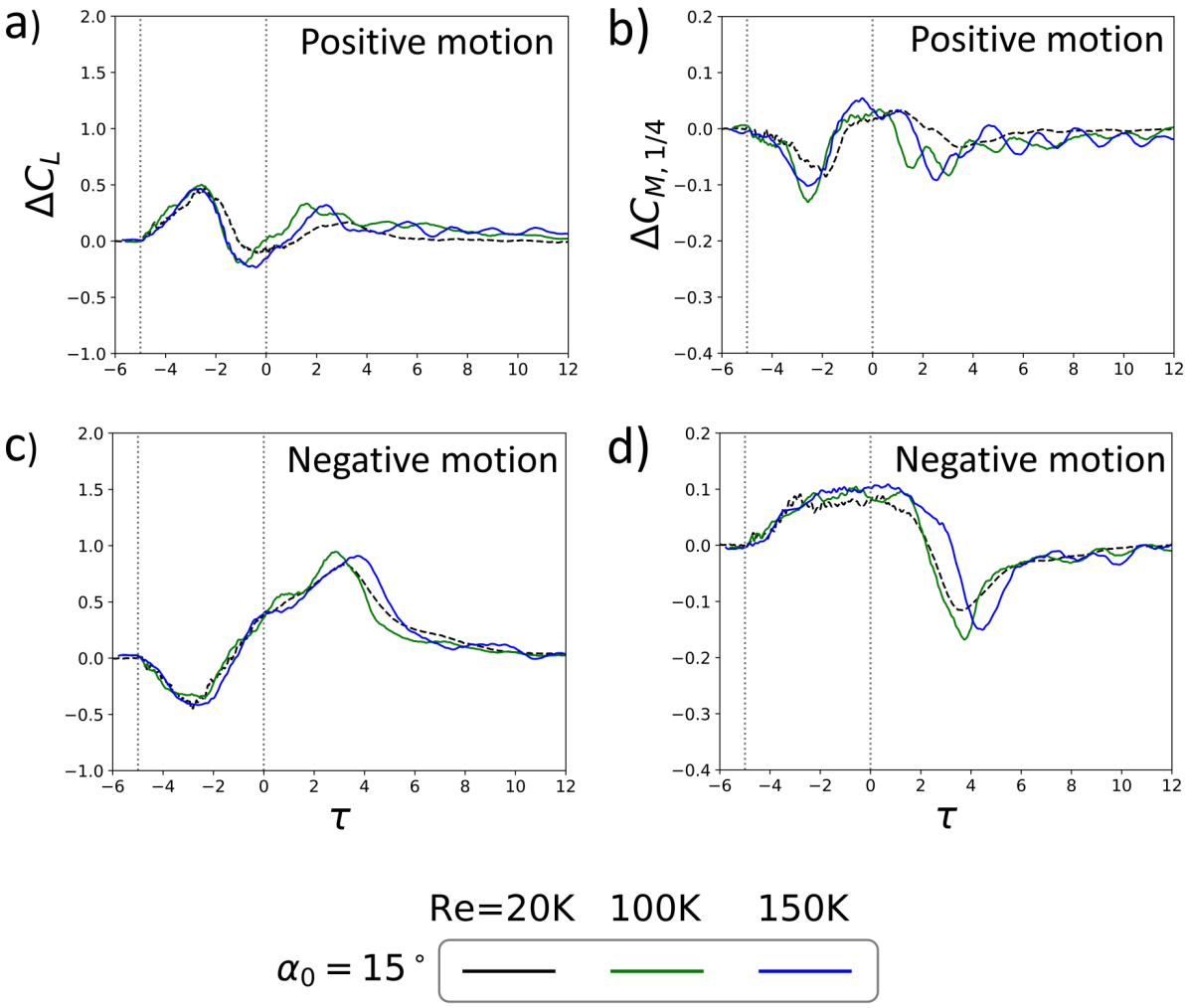

Figure 6-12: Comparison between $Re = 20K, 100K$ and $150K$ at $T = 5.0$ and $\alpha_{pl,max} = \pm 6°$ with $\alpha_0 = 15°$. a) relative lift for positive motion, b) relative pitching moment for positive motion, c) relative lift for negative motion, d) relative pitching moment for negative motion.

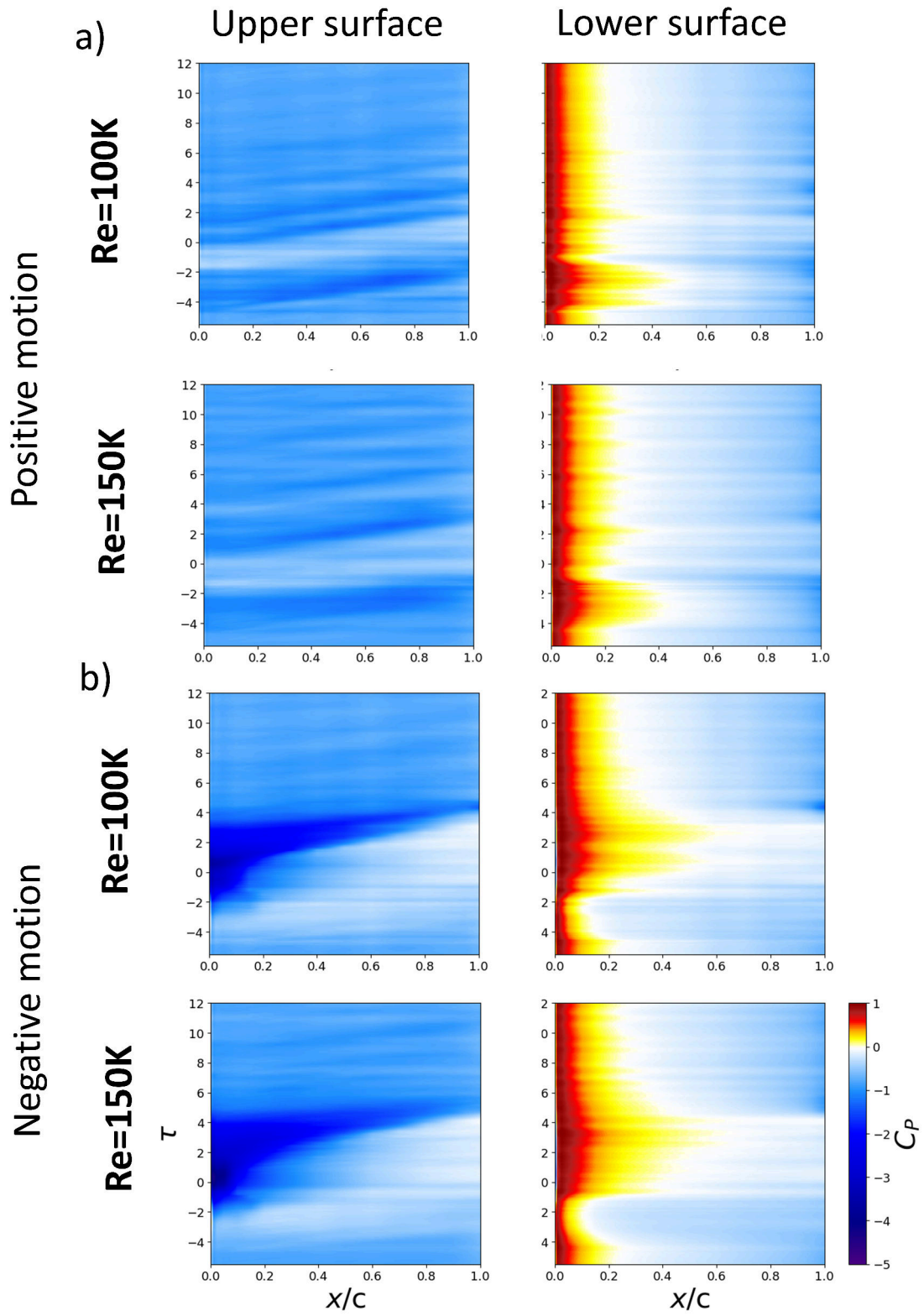

Figure 6-13: Pressure contour maps of the airfoil upper and lower surface at $Re = 100, 150K$ for positive and negative motion.

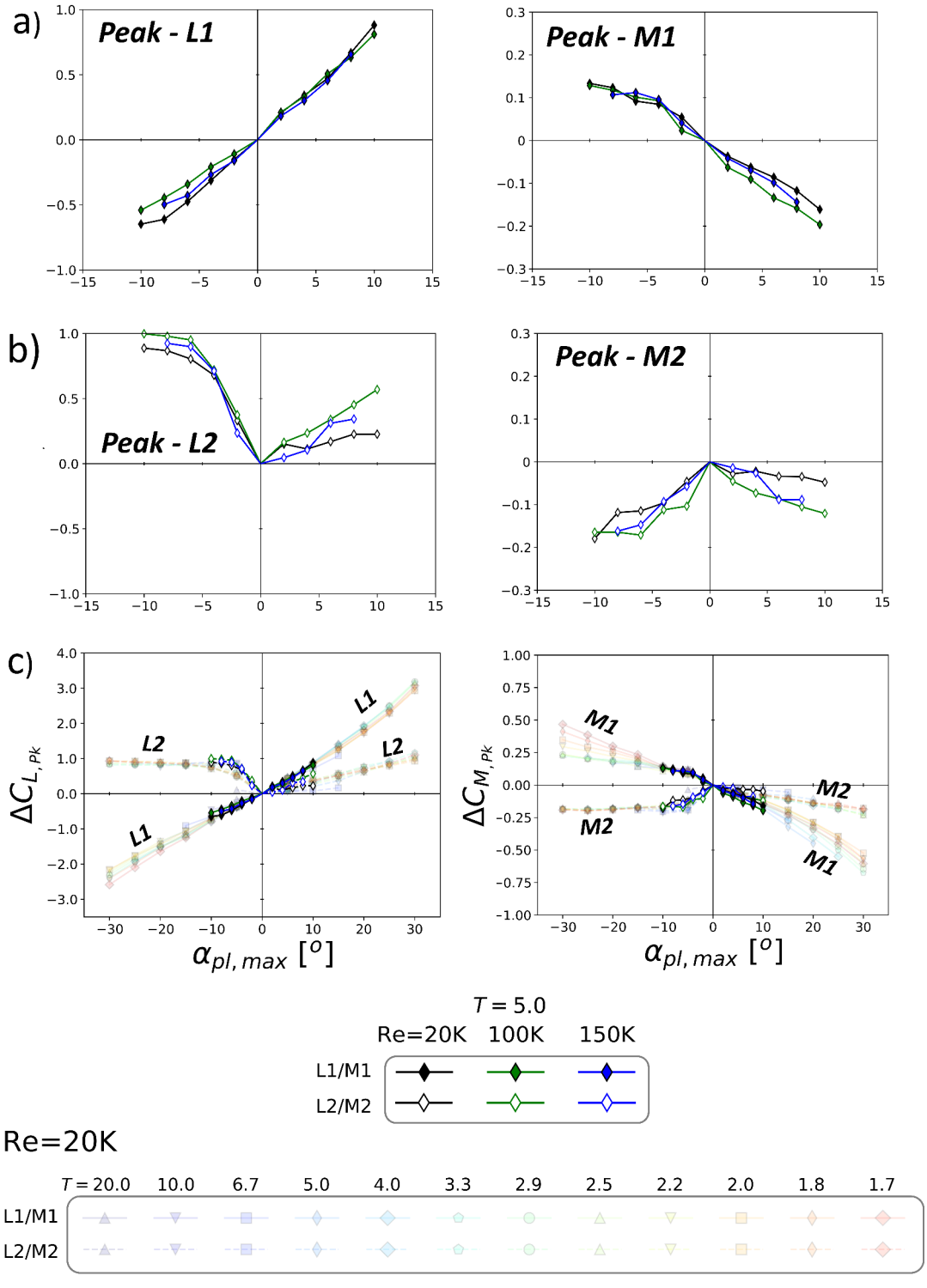

Figure 6-14: Relative lift and pitching moment peaks comparison between $Re = 20K, 100K$ and $150K$ for $\alpha_0 = 15°$. a) L1/M1, b) L2/M2, c) Peaks superposed onto Figure 4-8 at $\alpha_0 = 15°$.

Chapter 7

Loads Reduction Through Passive Device

7.1 Summary

Aircraft of all scales experience their highest loads during extreme manoeuvres, gust encounters or turbulence; the suppression of which is highly beneficial from a structural and control view point. A novel approach to reduce the peak lift and pitching moment on a plunging airfoil was investigated through force, moment, and velocity measurements. This study investigates a device that can be activated for short time intervals during a gust encounter or unsteady manoeuvre at the expense of potential short-duration drag increase. The approach, unlike previous investigations of delayed flow separation and leading-edge (dynamic stall) vortex, uses forced separation through deployment of a mini-tab (flow fence) near the leading-edge. Depending on the frequency and the amplitude of the wing motion the mini-tab can delay the roll-up of vorticity through the prevention of shear layer reattachment during the motion cycle. This change in the vortex dynamics provides effective lift and moment alleviation for post-stall angles of attack and low reduced frequencies. In contrast, at low angles of attack the separated shear layer emanating from the mini-tab can reattach downstream and roll-up, resulting in vortex shedding and lift/moment

increase. These two distinct flow regimes cause (positive) maximum and (negative) minimum in the lift reduction, with optimal frequencies roughly scaling with the reduced frequency. In contrast the borderline between the two regions approximately scales with the Strouhal number based on amplitude, and in particular with the minimum effective angle of attack during the cycle. The transient response was studied by investigating impulsively started plunging oscillations. In most cases, periodic response is reached within one cycle. During the first cycle, lift reduction is achieved for all frequencies within the range tested in the experiments, which is highly beneficial for a device operating in a more realistic gust or manoeuvre scenario.

7.2 Static Lift and Pitching Moment

Figure 7-1a presents the static lift coefficient for the "baseline" NACA 0012 and the "control" NACA 0012 with mini-tab alongside relevant examples of the NACA 0012 in literature at comparable Reynolds numbers. The lift coefficient of the baseline NACA 0012 shows excellent agreement with previous measurements taken at the University of Bath using both the current lift measurement system [70] and a binocular strain gauge configuration [137]. A substantial amount of non-linearity can be seen in the lift curve slope, which is characteristic of a NACA 0012 airfoil at low Reynolds numbers [138–140]. The observed plateau between $\alpha_0 = 0$ to 2° is attributed to laminar separation of the boundary layer followed by an abrupt reattachment at around 4° [138], causing the sharp increase in lift curve slope. As the angle of attack increases the gradient begins to decrease, hinting at the formation of a laminar separation bubble on the upper surface [139]. This is highlighted in Figure 7-1c, where a closed region of separation can be observed at $\alpha_0 = 5°$ on the baseline airfoil. The streamlines deviate from the contour of the airfoil which leads to the non-linearity in the lift curve slope. Despite the agreement with literature at low to moderate angles of attack, differences begin to manifest beyond stall. It has been shown that at low Reynolds numbers, $\mathcal{O}(10^4)$, the lift curve is highly sensitive to both turbulence intensity and Reynolds number [114, 139].

Considering the static lift of the "control" airfoil in Figure 7-1a, the mini-tab drastically reduces the lift across the majority of the α_0 range. This is shown in Figure 7-1c as a result of forced

flow separation at the mini-tab location which extends across the chord [110]. At post-stall conditions the mini-tab becomes less effective as the baseline airfoil is also in a fully separated state. Interestingly a positive lift coefficient is observed at $\alpha_0 = 0°$. This was not seen in the study by Heathcote *et al.* [110] and is most likely related to the difference in Reynolds numbers between the studies ($Re = 20K$ to $Re = 660K$), rather than the difference in lift measurement systems. At negative angles of attack the mini-tab's effect is reduced, in line with the measurements by Heathcote *et al.* [110].

In Figure 7-1b the static pitching moment for the baseline airfoil shows excellent agreement with Ohtake *et al.* [140] at a similar Reynolds number. The causes of the undulations is not fully understood, but is most likely related to the laminar boundary layer behaviour responsible for the non-linearity in the lift curve. The mini-tab suppresses the undulations in the pitching moment at positive, pre-stall angles of attack but leads to a more negative, nose-down value. At post-stall angles the control airfoil exhibits a less negative, nose-down pitching moment. Similar to the lift response, the pitching moment is less effected by the mini-tab at negative angles of attack.

7.3 Dynamic Loads and Mini-tab Performance

The test matrix for dynamic loads measurements includes a wide range of reduced frequencies, amplitudes and geometric angles of attack. This is reduced to a single performance parameter each for the lift, δC_L, and pitching moment, δC_M, that is calculated from the phase-averaged response. This is illustrated in Figure 7-2a and Figure 7-2b which presents the phase-averaged lift and pitching moment respectively at $\alpha_0 = 15°$, $A/c = 0.5$, $k = 0.24$ for both the baseline and control airfoils. In this case the baseline airfoil displays a distinct peak in lift and nose-down pitching moment at $t/T = 0.23$ which corresponds to the formation and shedding of a coherent LEV, see Figure 7-2c. The LEV induces a low pressure over the airfoil upper surface which is the mechanism of the lift increase. As the vortex is approaching the trailing-edge, the low pressure centre acts at large distance from the quarter-chord axis resulting in the large nose-down pitching moment. For the control case the mini-tab suppresses the formation of the LEV and therefore

displays significantly reduced magnitudes of both peak lift and pitching moment. The parameter that determines the mini-tab effectiveness as a loads control device is therefore defined as the difference between these peaks:

$$\delta C_L = max(C_{L,control}) - max(C_{L,baseline}) \tag{7.1}$$

$$\delta C_M = max(|C_{M,control}|) - max(|C_{M,baseline}|) \tag{7.2}$$

The quantity δC_L in Equation 7.1 is defined as the difference in maximum phase-averaged lift coefficient between the control and baseline airfoils, illustrated in Figure 7-2a, as the magnitude of peak lift suppression is paramount for a loads control device. Peak lift reduction and hence beneficial performance will occur when $\delta C_L < 0$. For the pitching moment, δC_M is defined as the difference in maximum absolute phase-averaged pitching moment between the control and baseline airfoils, as shown in Figure 7-2b. Any large excursion in pitching moment regardless of its sign is undesirable from a loads control perspective, thus the absolute term in Equation 7.2.

The performance of the mini-tab with respect to lift, δC_L, is shown in Figure 7-3 for the entire test matrix. For the symmetry case at $\alpha_0 = 0°$ the lift performance is fairly insensitive to both reduced frequency and amplitude, residing primarily in the "detrimental" region which is defined as $\delta C_L > 0$, i.e. the mini-tab increases the peak lift. The value of δC_L remains close to the static performance of the mini-tab at $k = 0.0$ and only begins to deviate into the beneficial region from $k = 0.9$ to 1.1, depending on the amplitude. For the pre-stall angles of attack,$\alpha_0 = 3, 5, 7°$, the lift performance becomes more sensitive to k and A/c. At $k = 0.0$ the value of δC_L varies in accordance with the static lift curves (Figure 7-1a) and therefore monotonically decreases with α_0 up to 9°. In this regime there is a strong amplitude dependence. For $\alpha_0 = 3, 5, 7°$ δC_L consistently increases with A/c; for the stall angle $\alpha_0 = 9°$ at the largest amplitude, $A/c = 0.5$, δC_L initially decreases with k before increasing so that the monotonic trend is lost. Superposed onto this general trend of increasing δC_L with k and A/c are maxima. For $\alpha_0 = 5°$ these occur

at $k = 0.4, 0.52, 0.52, 0.6$ and 0.8 for $A/c = 0.5, 0.3, 0.2, 0.1$ and 0.05 respectively, suggesting a dependence on Strouhal number based on peak-to-peak amplitude, St_A. The highest amplitudes tend to converge towards $\delta C_L = 0.0$ at high reduced frequencies indicating a reduced effect of the mini-tab in extreme unsteadiness, this will be explored later. All angles in the pre-stall regime appear to show a quasi-static region, beyond which δC_L begins to deviate from the static performance. The reduced frequency which this deviation occurs at increases proportionally with α_0 from approximately $k = 0.1$ at $\alpha_0 = 3°$ to $k = 0.25$ at $\alpha_0 = 9°$.

For post-stall angles, $\alpha_0 = 11, 13, 15°$, the inflection with amplitude becomes stronger, with distinct minima present between $k = 0.20$ and 0.40. The magnitude of lift reduction in this region increases with α_0 and at $\alpha_0 = 15°$ the mini-tab is capable of suppressing lift by up to $\delta C_L = -1.5$. Similar to the pre-stall α_0, δC_L exhibits minor variations with k at $A/c = 0.05$ and shows greater sensitivity to k as the amplitude is increased. It is interesting to note the absence of quasi-static behaviour for the post-stall cases and deviations from the static performance occur at very low reduced frequencies. Once again the influence of the mini-tab deteriorates at high reduced frequencies and amplitudes resulting in a convergence towards $\delta C_L = 0.0$.

The performance of the mini-tab with respect to the pitching moment, δC_M, is shown in Figure 7-4. At $k = 0.00$ the value of δC_M varies in accordance with the static values. For the symmetry case and pre-stall angles, $\alpha_0 = 0, 3, 5, 7, 9°$, the response remains somewhat quasi-static at low reduced frequencies. In this regime δC_M lies primarily within the detrimental region for all pre-stall α_0 and tends to deviate from the quasi-static performance at lower reduced frequencies. As k is increased, distinct maxima can be seen for the higher amplitudes at comparable reduced frequencies to δC_L which suggests the same mechanism is responsible. The same amplitude effects are also present, where δC_M displays greater sensitivity to k as A/c is increased. At $\alpha_0 = 9°$ the response shows an inversion which becomes more distinct with increasing α_0. Post-stall α_0 display the same minima as δC_L at higher amplitudes, but also show a distinct maxima at higher k of almost equal magnitude between $k = 0.63$ and 0.71. The trends then appear to tend towards $\delta C_M = 0.0$ at comparatively higher reduced frequencies.

Figure 7-3 and Figure 7-4 show several distinct regimes of behaviour. To understand the cause an extensive PIV campaign was conducted, however for the sake of brevity only representative cases will be shown in this article. The selection is based on four distinct flow field types:

- *Type A*: the baseline **and** control flow shows no coherent LEV formation.
- *Type B*: the baseline flow exhibits coherent LEV formation, whereas the control flow shows **no** significant roll-up.
- *Type C*: the baseline flow has **no** coherent LEV formation, whilst the control flow exhibits coherent LEV formation.
- *Type D*: the baseline **and** control flows exhibit coherent LEV formation.

The following figures will present PIV that illustrates these flow types and the corresponding locations of the cases are marked in Figure 7-3 and Figure 7-4 with the label 'A', 'B', 'C' or 'D'.

7.4 Flow Field Types

7.4.1 Type A

Figure 7-5 presents the phase-averaged lift (Figure 7-5a) and pitching moment (Figure 7-5b) along with streamlines overlaid onto normalised velocity magnitude (Figure 7-5c) at select phases in the motion for $\alpha_0 = 9°$, $A/c = 0.05$, $k = 0.94$. This is a representative case for the Type A flow field where no coherent vortex shedding or roll-up is seen for the baseline and control airfoils. The added-mass component of the lift and pitching moment is also plotted in Figure 7-5a and Figure 7-5b. This is calculated based on the expressions derived by Theordorsen [2] and uses the acceleration measured during the experiments. This provides a reliable estimate of the added-mass force even in highly separated, vortical flows [15]. For this case the performance of δC_L and δC_M remains close to the static case, which is highlighted with the label 'A' in Figure 7-3 and Figure 7-4. The flow fields in Figure 7-5c show that the baseline flow remains attached throughout the period and displays increased velocity at the leading-edge at $t/T = 0.250$, corresponding to the maximum plunge velocity, V_{pl}, and hence induced angle of attack, α_{pl}. The control case

however shows the mini-tab enforcing separation across the chord throughout. Minor velocity variations can be seen towards the trailing-edge between $t/T = 0.375$ and 0.750, which appears to be due to weak roll-up, indicated by the development of singularities in the streamlines. For both airfoils the lift variation is virtually sinusoidal with small amplitude and is primarily comprised of the circulatory component. A constant offset can be observed between the baseline and control cases which is close to the difference in static lift. The pitching moment on the other hand is solely governed by the added-mass component for attached flows [2] and as such, the baseline closely agrees well with this estimation whilst the control case deviates somewhat due to flow separation, particularly between $t/T = 0.125$ and $t/T = 0.500$ where the weak roll-up can be seen. Despite the weak roll-up on the control airfoil, this case is classified as a Type A flow field as it leads to no significant change in δC_L and δC_M compared with the static performance. Although subjective, the roll-up is not classed as "coherent" relative to the examples of greater coherency shown later.

7.4.2 Type B

Figure 7-6 presents the phase-averaged lift (Figure 7-6a) and pitching moment (Figure 7-6b) along with plots of normalised spanwise vorticity (Figure 7-6c) at select phases in the motion period for $\alpha_0 = 15°$, $A/c = 0.50$, $k = 0.24$. This is a representative case for the Type B flow field, in which the baseline flow exhibits coherent vortex shedding and reattachment, whereas the control flow shows no significant roll-up. For this case δC_L and δC_M show a drastic reduction as highlighted by the label 'B' in Figure 7-3 and Figure 7-4. At $t/T = 0.00$ the baseline flow begins the period with fully attached flow. As the period progresses and α_{pl} increases the flow begins to roll-up aft of the quarter-chord ($t/T = 0.125$) and has grown into a coherent LEV by $t/T = 0.250$, mirroring the shape of a typical dynamic stall vortex [14]. At this point the LEV is approaching the trailing-edge and corresponds to the peak lift and the distinct nose-down pitching moment spike. Note that the added-mass contribution to both C_L and C_M for this low frequency case is virtually negligible. At $t/T = 0.375$ the LEV has been shed from the trailing-edge into the wake, inducing a TEV. The lift response displays a secondary peak around $t/T = 0.400$. This is due to the shedding of a secondary, less coherent vortical structure which is well documented in

dynamic stall literature [40, 47]; however this is not discernible from the vorticity plots in Figure 7-6c. From $t/T = 0.500$ to 0.875 the flow begins to progressively reattach from the leading-edge as α_{pl} decreases. In stark contrast the control airfoil exhibits a separated leading-edge shear layer throughout the cycle and subsequently suppressed lift and pitching moment. The difference between the two airfoils is emphasised in Figure 7-6c at $t/T = 0.250$ in the streamline plots, where the control case shows no sign of shear layer roll-up. It appears that a prerequisite for coherent vortex shedding for this case is flow reattachment on the upper surface, something that the mini-tab prevents throughout the cycle.

7.4.3 Type C

Figure 7-7 presents the phase-averaged lift (Figure 7-7a) and pitching moment (Figure 7-7b) along with streamline and normalised velocity magnitude plots (Figure 7-7c) for $\alpha_0 = 3°$, $A/c = 0.50$, $k = 0.40$. This is a representative case for the Type C flow field in which the baseline flow shows no separation, whereas the control flow shows reattachment and coherent vortex formation. For this case δC_L and δC_M display a distinct maxima in the detrimental region and is highlighted with the label 'C' in Figure 7-3 and Figure 7-4. For the baseline airfoil, the flow is attached throughout the cycle. The lift response is almost sinusoidal and the pitching moment agrees well with the added-mass estimation, with some deviation around the top of the stroke ($t/T = 1.00$ and 0.00). For the control airfoil, the shear layer emanating from the mini-tab reattaches just downstream around $x/c = 0.5$ at $t/T = 0.00$, forming a closed area of recirculation behind the mini-tab. As the airfoil plunges downwards and α_{pl} increases, the area of recirculation begins to grow as the vorticity accumulates. At $t/T = 0.250$ the flow displays a noticeable increase in velocity above the mini-tab shear layer. The corresponding vorticity plot shows shear layer roll-up around the mid-chord position into a coherent vortical structure. This is responsible for the increased lift peak in Figure 9 a and the nose-down pitching moment peak in Figure 7-7b (at a slightly later phase). As the vortex is shed into the wake the lift drops below the baseline case and the pitching moment begins to recover towards the added-mass estimate. This case illustrates the detrimental behaviour of forced separation during unsteady motion at low α_0, as shear layer reattachment and roll-up can occur downstream of the separation point resulting in

lift increase for the control case.

7.4.4 Type D

A Type D flow field is achieved when both the baseline and control flow display coherent vortex shedding and reattachment. Multiple PIV cases were selected here to fully illustrate LEV behaviour. This flow field type is associated with near zero δC_L but a wide range of δC_M. As will be shown, the sensitivity of the pitching moment to the reduced frequency is due to the phase at which the LEV is shed. The selected cases are highlighted in Figure 7-3 and Figure 7-4 with the label 'D'.

Figure 7-8 presents the phase-averaged lift (Figure 7-8a) and pitching moment (Figure 7-8b) along with plots of normalised spanwise vorticity (Figure 7-8c) for $\alpha_0 = 5°$, $A/c = 0.50$, $k = 0.94$. This case was selected as it shows a near zero δC_L and δC_M. In general, the flow fields are qualitatively very similar and display coherent LEV formation and shedding. From $t/T = 0.00$ to 0.125 the baseline airfoil displays fully attached flow. At $t/T = 0.250$ the baseline shows the onset of LEV formation at the leading-edge region. Conversely, the mini-tab shear layer begins to roll-up much earlier in the cycle and by $t/T = 0.250$ the LEV has already convected to the mid-chord position. This has virtually no effect on the magnitude of the lift peak but results in a slightly earlier peak time. The added-mass estimation is more significant at such a high amplitude and frequency combination, however the peak lift for both cases occur when this is close to zero, highlighting the dominance of the circulatory component in peak lift [70]. The pitching moment on the other hand is more significantly affected by the LEV formation phase. For the control case the LEV reaches the trailing-edge at around $t/T = 0.625$ which produces a large deviation from the added-mass estimate in Figure 7-8b. The LEV and added-mass components are in direct opposition which results in a relatively low magnitude pitching moment response at the point of LEV shedding [70]. For the baseline airfoil the pitching moment follows the added-mass estimate up to $t/T = 0.500$, after which it begins to show similar deviations which correspond with the later formation and convection of the LEV. In terms of pitching moment performance, δC_M is calculated from the maximum absolute pitching moment which in this case corresponds

to the top of the stroke region ($t/T = 0.95$ and 0.10) for both airfoils.

The effect of LEV formation and shedding phase is highlighted in Figure 7-9, which presents the phase-averaged lift (Figure 7-9a) and pitching moment (Figure 7-9b) along with plots of normalised spanwise vorticity (Figure 7-9c) for $\alpha_0 = 9°$, $A/c = 0.50$, $k = 0.47$. This case was selected as it shows distinct differences in both δC_L and δC_M performance. Similar to the previous case in Figure 7-9, the control airfoil displays roll-up and convection from $t/T = 0.00$ (Figure 7-9c). The LEV reaches the trailing-edge at a comparatively earlier than the previous case due to the lower reduced frequency, and as such the induced nose-down pitching moment is observed at $t/T = 0.250$ which occurs where the added-mass contribution is zero. For the baseline airfoil on the other hand, LEV formation occurs later in the cycle. At $t/T = 0.250$ a small region of concentrated vorticity can be seen. This greatly contrasts against the flow field above the control airfoil, yet interestingly produces the same lift peak magnitude ($\delta C_L \approx 0.0$). Between $t/T = 0.250$ and 0.500 the LEV convects across the chord, creating a low pressure wave that is responsible for the sustained lift increase seen in Figure 7-9a. The nose-down pitching moment peak at $t/T = 0.500$ marks the arrival of the LEV at the trailing-edge which occurs comparatively later in the cycle. At this phase the added-mass estimate produces a maximum nose-up pitching moment, directly opposing the nose-down moment induced by the LEV. Figure 7-4 displays a detrimental δC_M, yet the amplitude of deviation from the added-mass estimation for both airfoils is very similar, indicating comparable LEV influences. This highlights the sensitivity of δC_M to the added-mass component, which itself is highly dependent on the airfoil kinematics.

Figure 7-10 further demonstrates the sensitivity of δC_M to the added-mass component and shows where δC_M is at a maximum. Phase-averaged lift (Figure 7-10a) and pitching moment (Figure 7-10b) along with plots of normalised spanwise vorticity (Figure 7-10c) are presented for $\alpha_0 = 15°$, $A/c = 0.50$, $k = 0.63$. The pitching moment response of the baseline airfoil is relatively flat, despite the coherent LEV produced during the downstroke. In this case the added-mass component is sufficient in magnitude to almost completely suppress the pitching moment induced by the LEV as it convects and approaches the trailing-edge ($t/T = 0.250$ to 0.500). The

control airfoil on the other hand shows drastically different vortical behaviour. At $t/T = 0.00$ the shear layer is already exhibiting roll-up and by $t/T = 0.250$ the LEV is already approaching the trailing-edge. Similar to the previous case the phasing of the LEVs arrival at the trailing-edge induces a large nose-down pitching moment where the added-mass component is zero, leading to a largely detrimental δC_M in Figure 7-4. At this phase the flow field difference between the airfoils is substantial, yet the lift magnitudes are similar. Interesting vortical interactions begin to take place on the control airfoil from $t/T = 0.250$. A second vortical structure starts to form behind the mini-tab which then interacts strongly with the downstream LEV. At $t/T = 0.375$ the newly formed LEV has been lifted away from the surface as the downstream LEV is stretched and pulled underneath; similar to the behaviour documented in Chapter 5. By $t/T = 0.500$ the two structures have merged together into a single structure which approaches the trailing-edge, inducing an additional, less substantial dip in the pitching moment response.

Finally, Figure 7-11 presents a case on the upper extremity of the test matrix in terms of frequency, amplitude and geometric angle of attack. In this extreme regime the mini-tab on the control airfoil has very little effect on the loads and is dwarfed by the size of the separation present in the flow field. Small differences in flow fields can be seen during the downstroke from $t/T = 0.00$ to 0.375. A similar vortex merging is present above the control airfoil, which again has seemingly little influence on the aerodynamic loads. By $t/T = 0.500$ the LEV coherency and position begin to agree between the two airfoils and produce comparable nose-down pitching moment excursions at the same phase. The LEV strength in this case appears sufficient enough to counteract the large nose-up pitching moment contribution from the added-mass component. Generally the flow fields and C_L time history are very similar between baseline and control. The pitching moment is also similar but offset by a constant amount.

7.5 Flow Field Type Identification

The flow field types in the previous sections were defined qualitatively from select flow field measurements. In order to give a quantitative delineation between type A, B, C and D, a modified pitching moment coefficient is proposed:

$$C_{M,mod} = C_M - C_{M,am} - C_{M,\alpha_0} \tag{7.3}$$

where $C_{M,am}$ is the estimated added-mass contribution and C_{M,α_0} is the measured static component. The modified pitching moment, $C_{M,mod}$, in Equation 7.3 is therefore defined as the pitching moment response with the estimated added-mass and measured static components removed. This gives a comparable measure of how the pitching moment response deviates from the theoretical added-mass response. When an LEV forms and convects towards the trailing-edge it induces a nose-down pitching moment spike which results in a distinct deviation from the added-mass estimation. An example is shown in Figure 7-12, which presents $C_{M,mod}$ for the baseline airfoil at $\alpha_0 = 7°$, $A/c = 0.50$ and $k = 0.24$, 0.31. At $k = 0.24$ the relatively flat response indicates no coherent LEV formation; though their may be some flow separation present which causes excursions in $C_{M,mod}$. When k is increased to 0.31, the distinct signature of a coherent LEV is observed. Using this analysis, the boundary of coherent LEV formation can be estimated for each α_0 at each A/c tested, giving an approximation of the flow field type boundaries.

To extract the boundaries of coherent LEV formation the peak searching algorithm in the *SciPy* Python tool box was implemented, namely *scipy.signal.find_peaks* [160]. Two thresholds were used to determine the LEV signatures:

- *Peak prominence*: a measure of how much the detected peak stands out from the surrounding signal [160].
- *Peak width*: the width of the detected peak [160].

A sensitivity analysis was conducted over a range of appropriate peak prominence and peak width thresholds and compared against PIV flow fields for verification, the results of which can be found in Appendix A. A peak prominence threshold of $C_{M,mod} < -0.1$ was found to be a good indicator for coherent LEV formation, akin to the boundary between the light and deep dynamic stall examples given by McCroskey [40]. A maximum peak width of 3.5τ was set to fully encompass the array of vortex convection and shedding times whilst eliminating any broad

peaks induced by incoherent flow separation.

The boundaries of coherent LEV formation for the baseline (dashed lines) and control (solid lines) are shown in Figure 7-13. Each boundary is plotted as a band which manifests from the discrete number of reduced frequencies tested, representing a level of uncertainty; an example of this is shown in Figure 7-12 where coherent LEV formation initiates between $k = 0.24$ and 0.31. Note that at $A/c = 0.05$ and 0.10, the boundary lines terminate where no $C_{M,mod}$ peak was detected, indicating that coherent LEV formation occurs beyond the maximum k tested. The areas of flow field type are indicated with the labels A, B, C and D. Additionally the PIV test cases are also shown and are grouped based on qualitative assessment of the flow field type. Finally, this is overlayed onto contour plots of the performance data from Figure 7-3 to better elucidate the effect of α_0. Consider first the amplitude extremes of A/c = 0.05 and 0.50. For A/c = 0.05 the majority of α_0 and k produce the Type A flow field, where the plunging velocity is insufficient to produce roll-up on either airfoil. The exception is for $\alpha_0 = 15°$ at $k = 0.94$ where both flow field assessment and $C_{M,mod}$ peak detection show a Type B flow field. At low α_0, δC_L is detrimental across the frequency range, quickly transitioning to slightly beneficial around $\alpha_0 = 3°$. This behaviour is in line with the static data with minimal effect of k. At $A/c = 0.50$ the parameter space consists of all flow field types (A, B, C and D) and their partition is made apparent by the LEV formation boundaries. The Type A flow field occurs for all α_0 as k approaches zero. This quickly transitions to either a Type C (low α_0) or Type B (high α_0) flow field as k is increased. For low α_0 the transition from Type C to Type D is highly dependent on α_0, occurring approximately at $k = 0.79$ at $\alpha_0 = 0°$ and $k = 0.24$ at $\alpha_0 = 7°$. For high α_0 boundary between Type B and Type D is less sensitive to α_0, occurring approximately at $k = 0.31$ at $\alpha_0 = 9°$ and $k = 0.39$ at $\alpha_0 = 15°$. Also presented in Figure 14 is the intermediate amplitudes which illustrate how the Type A, B, C and D flow fields develop.

Equivalent contour plots for δC_M are presented in Figure 7-14. For $A/c = 0.50$ the boundary of $\delta C_M = 0.0$ encapsulating the Type B flow field is well defined and is in agreement with the LEV formation boundaries. The development of this region can be seen as the amplitude is increased from $A/c = 0.05$ to 0.5.

It is clear that the desired flow field types for loads control are Type A and B, where full separation is maintained over the upper surface of the control airfoil. However, a detrimental δC_L boundary exists within the Type A region, see Figure 7-13. This boundary of $\delta C_L = 0.0$ is presented in Figure 7-15 for all A/c. Figure 7-15a shows no significant collapse of thes boundaries with k. The gradient dependence on A/c at low k suggests that scaling with St_A may be more appropriate, see Figure 7-15b. A reasonable amount of collapse can be see at low St_A and α_0, where the boundary between beneficial and detrimental performance increases almost linearly with α_0. Figure 7-15c presents the boundaries in terms of the maximum induced angle of attack during motion $\alpha_{pl,max}$. Interestingly the performance boundary lines up well with the line of $\alpha_0 = \alpha_{pl,max}$, indicating that the switch to detrimental performance (due to shear layer reattachment) occurs when the total effective angle of attack reduces to zero during the motion (for this particular mini-tab configuration). The contours then begin to deviate in the post-stall regime, where the beneficial performance is defined by the boundary between Type B and Type D flow field, see Figure 7-13.

An interesting feature in Figure 7-3 is the maxima and minima of δC_L displayed in the pre- and post-stall regimes respectively. Figure 7-16 presents the approximate locations of these with respect to k and St_A. A reasonable degree of collapse can be observed in Figure 7-16a with respect to k. The maxima for all A/c occur across a particular frequency band of $k = 0.35$ to 0.60; the large outliers for $A/c = 0.2$ and 0.3 are most likely due to a lack of resolution in k when extracting the maxima. A monotonic increase is present for the post-stall minima occurrences, increasing from $k = 0.2$ to 0.5 as α_0 is increased. In contrast, no distinct scaling can be seen with St_A in Figure 7-16b.

7.6 Transient Response

The study has so far considered the mini-tab's performance under periodic conditions, however it is also essential to consider the transient response to such disturbances, analogous to a discrete gust or extreme manoeuvre, for a more complete picture. Further experiments were conducted to examine the response to impulsively started plunging oscillations. Figure 7-17 presents this data for select frequencies at $\alpha_0 = 15^\circ$ and $A/c = 0.5$. The motion starts at $t/T = 0.00$.

Consider first the lift signal at $k = 0.24$ in Figure 7-17. A striking difference in baseline airfoil response can be seen between the first and second motion cycle. The peak lift increases by around 100% from $t/T = 0.25$ to $t/T = 1.25$ which then holds for subsequent cycles. In contrast, the control airfoil response displays no significant cycle to cycle variation. This is also reflected in the pitching moment responses, where a large nose-down pitching moment spike emerges at the same phase, $t/T = 1.25$, indicating a distinct change in vortex formation and shedding. This is typical of a Type B flow field. As k is increased, the lift amplitude over consecutive cycles becomes more similar whilst the mean lift increases significantly. At $k = 0.94$ the lift response takes multiple cycles for the increase in mean to asymptote which suggests that periodic conditions are achieved at a critical convective time rather than cycle number. Similar dependence on convective time is present in the pitching moment responses.

The parameters δC_L and δC_M were extracted from the transient signals to determine the mini-tab's performance for impulsively started oscillations. Figure 7-18 presents this data for $\alpha_0 = 5, 9$ and 15° at $A/c = 0.5$. The first four cycles are compared against the periodic response shown in black. Interestingly the mini-tab performance shows relatively little variation with k during the first cycle, with the exception of δC_M for $\alpha_0 = 9^\circ$, and all α_0 tested exhibit beneficial performance in δC_L and δC_M compared to the periodic counterpart; a promising result for performance during discrete gust encounters. At low values of k the mini-tab performance agrees well with the periodic performance after the first cycle. At high values of k more cycles are required to approach the periodic response.

To show the cause of this transience, Figure 7-19c presents the flow field measurements for $\alpha_0 = 15^\circ$ at $A/c = 0.5$ and $k = 0.24$. Lift and pitching moment are shown in Figure 7-19a and Figure 7-19b respectively for reference. Peak lift and nose-down pitching moment in the first cycle is achieved around $t/T = 0.25$ for both airfoils. Relatively weak roll-up can be seen over the aft portion of the baseline airfoil and the control airfoil displays largely separated flow. During the upstroke the induced angle of attack is sufficient to reattach the flow over the baseline airfoil, which causes an increase in lift beyond the static value. In contrast, the control airfoil maintains a separated shear layer. This has significant consequences for the subsequent cycle. A coherent

LEV is present over the baseline airfoil at $t/T = 1.25$, in stark contrast to the same phase of the previous cycle ($t/T = 0.25$). Flow reattachment prior to LEV formation is a significant factor to vortex coherency and induced loads, potentially stemming from an increased circulation due to attached flow during the upstroke combined with the inherent lag in the flows response. The control airfoil at $t/T = 1.25$ matches that of $t/T = 0.25$ and is highlighted by the similarity in the loads, see Figure 7-19a and Figure 7-19b. At $t/T = 1.50$ the wake of the baseline airfoil shows less momentum deficit than at $t/T = 0.50$ which corresponds with the small secondary peak in Figure 7-19a.

A more extreme case is presented in Figure 7-20, which displays the normalised spanwise vorticity for $\alpha_0 = 15°$ at $A/c = 0.5$ and $k = 0.94$. For both airfoils a coherent LEV begins to form in the first cycle, $t/T = 0.25$, along with a coherent TEV. During the second cycle however there is a notable lack of TEV during the down-stroke at $t/T = 1.25$, which corresponds with the drastic increase in lift for both airfoils, see Figure 7-20a. The pitching moment is largely unaffected by the TEVs absence. At the bottom of the stroke ($t/T = 1.50$) the LEV appears larger and significantly closer to the upper surface. The LEVs proximity to the upper surface during the cycle combined with the absence of a TEV during down-stroke produces the increase in mean lift and pitching moment observed in Figure 7-20a and Figure 7-20b.

7.7 Conclusions

A passively deployed mini-tab (flow fence) device was tested to determine the efficacy of forced flow separation at the leading-edge of a NACA 0012 airfoil to alleviate high loads during extreme unsteady events, particularly where organised vortical structures can form. The performance of the device was compared to a clean "baseline" NACA0012 airfoil and was determined through steady and unsteady lift, pitching moment and flow field measurements. In static conditions the mini-tab enforces flow separation across the chord, leading to a free-shear layer. During dynamic plunging oscillations, the mini-tab's performance depended drastically on the behaviour of the free-shear layer, which varies greatly with the geometric angle of attack, amplitude and reduced frequency. The mini-tab performance has been classified into four types depending on shear layer

behaviour.

- *Type A*: the baseline **and** control flow shows no coherent LEV formation.
- *Type B*: the baseline flow exhibits coherent LEV formation, whereas the control flow shows **no** significant roll-up.
- *Type C*: the baseline flow has **no** coherent LEV formation, whilst the control flow exhibits coherent LEV formation.
- *Type D*: the baseline **and** control flows exhibit coherent LEV formation.

Type A and B are associated with beneficial load control behaviour and occur at low plunge velocities and low k. Shear layer reattachment behind the mini-tab is the primary cause of the performance degradation and precedes coherent shear layer roll-up. The boundaries delineating each flow field type were estimated through a modified pitching moment coefficient, $C_{M,mod}$, that isolated the LEV signature. A peak detection algorithm was applied on $C_{M,mod}$ to determine where coherent LEV formation occurred for both airfoils, resulting in contours that elucidated the flow field type boundaries. The switch from beneficial and detrimental lift performance was found to scale with St_A and occur when the induced angle of attack during motion was approximately equal to the geometric angle of attack, i.e. the total effective angle of attack reaches zero. Type B and C flow fields show distinct maxima/minima that scale primarily with the reduced frequency for all amplitudes tested. Finally, the transient response to impulsively started plunging oscillations revealed the importance of wake development on the mini-tab performance. Across the majority of the tests, the performance was significantly more beneficial during the first motion cycle, which is highly beneficial for a device operating in a more realistic gust or manoeuvre scenario.

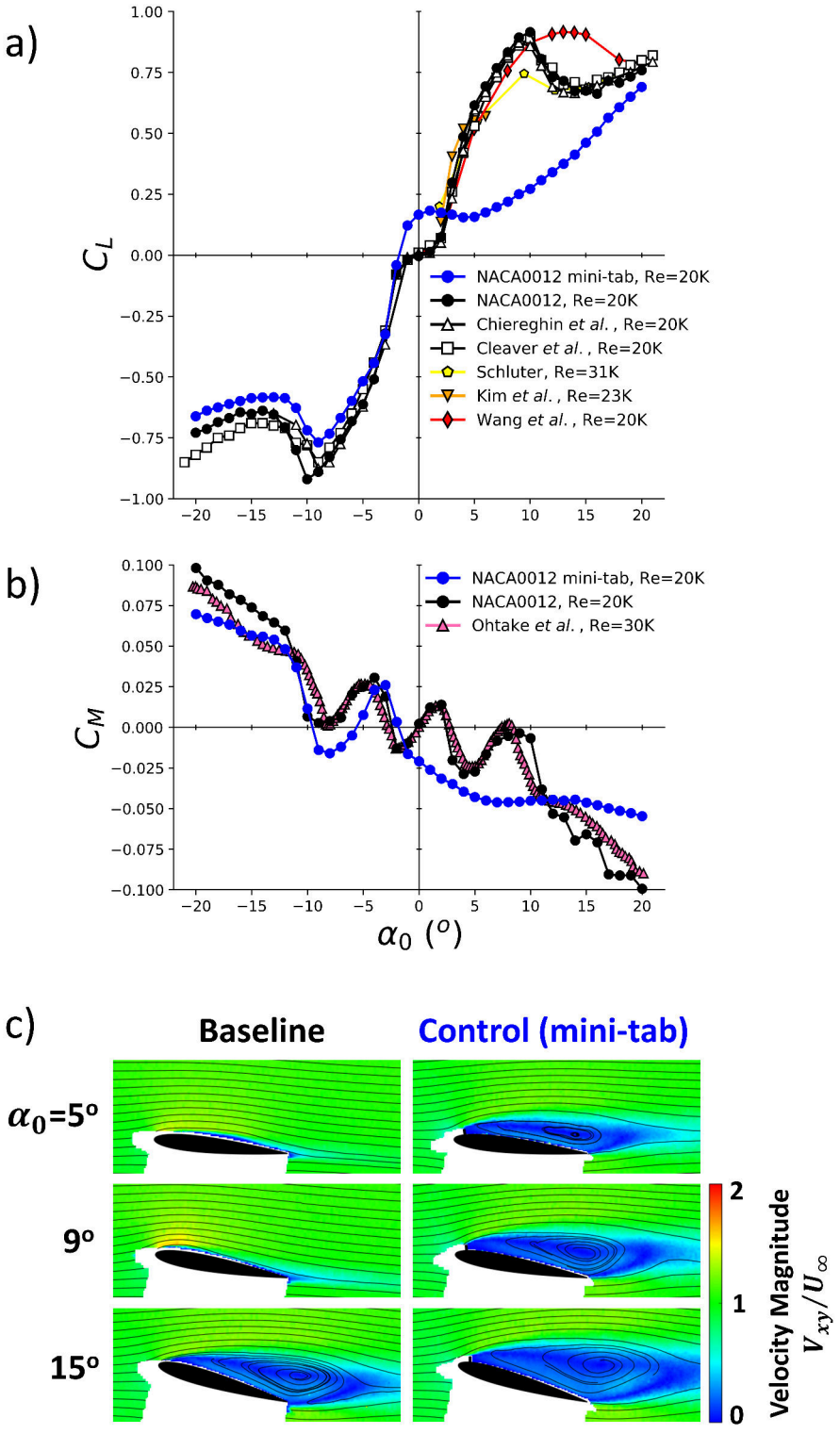

Figure 7-1: a) Static lift coefficient, b) static pitching moment coefficient and c) velocity magnitude plots for select α_0.

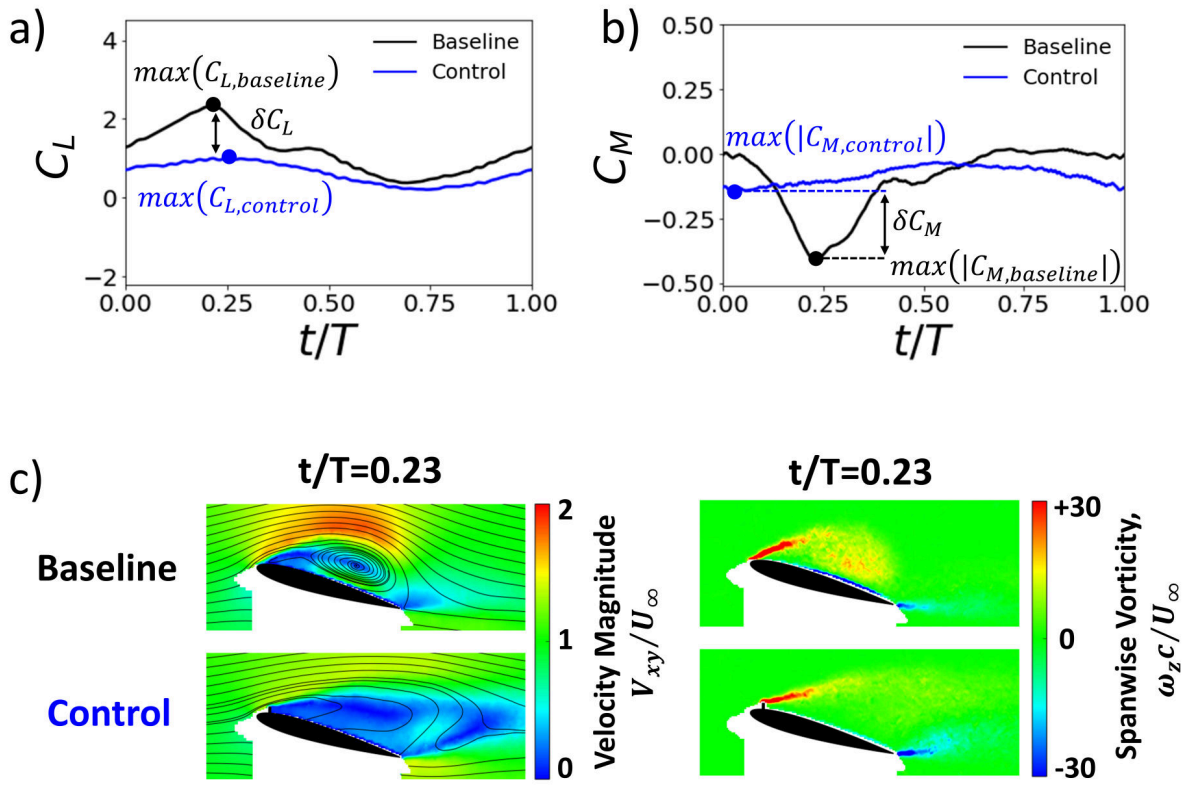

Figure 7-2: Example case: $\alpha_0 = 15°$, $A/c = 0.5$, $k = 0.24$; a) phase-averaged lift coefficient, b) phase-averaged pitching moment coefficient, c) normalised velocity and vorticity flow fields.

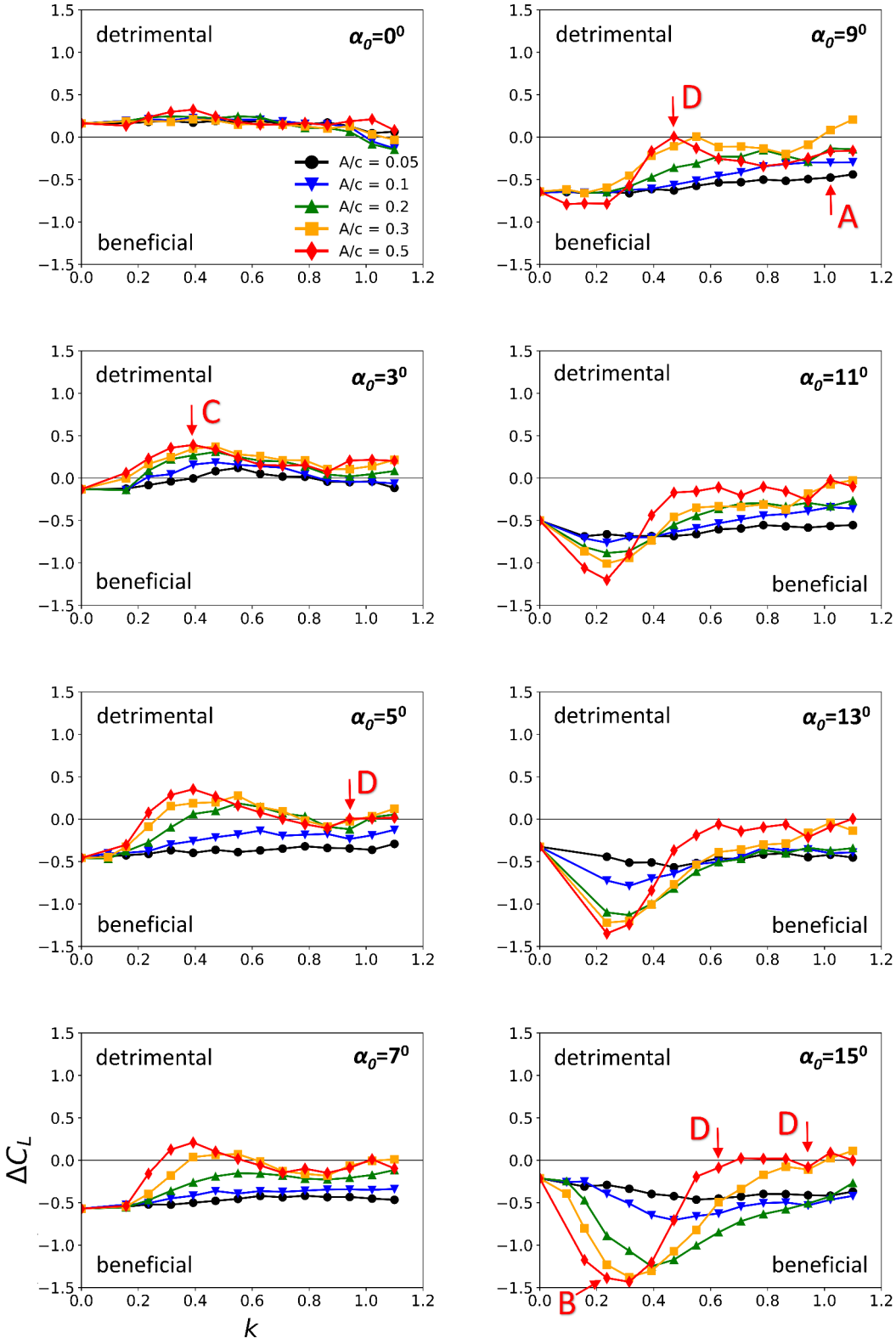

Figure 7-3: Lift performance of mini-tab.

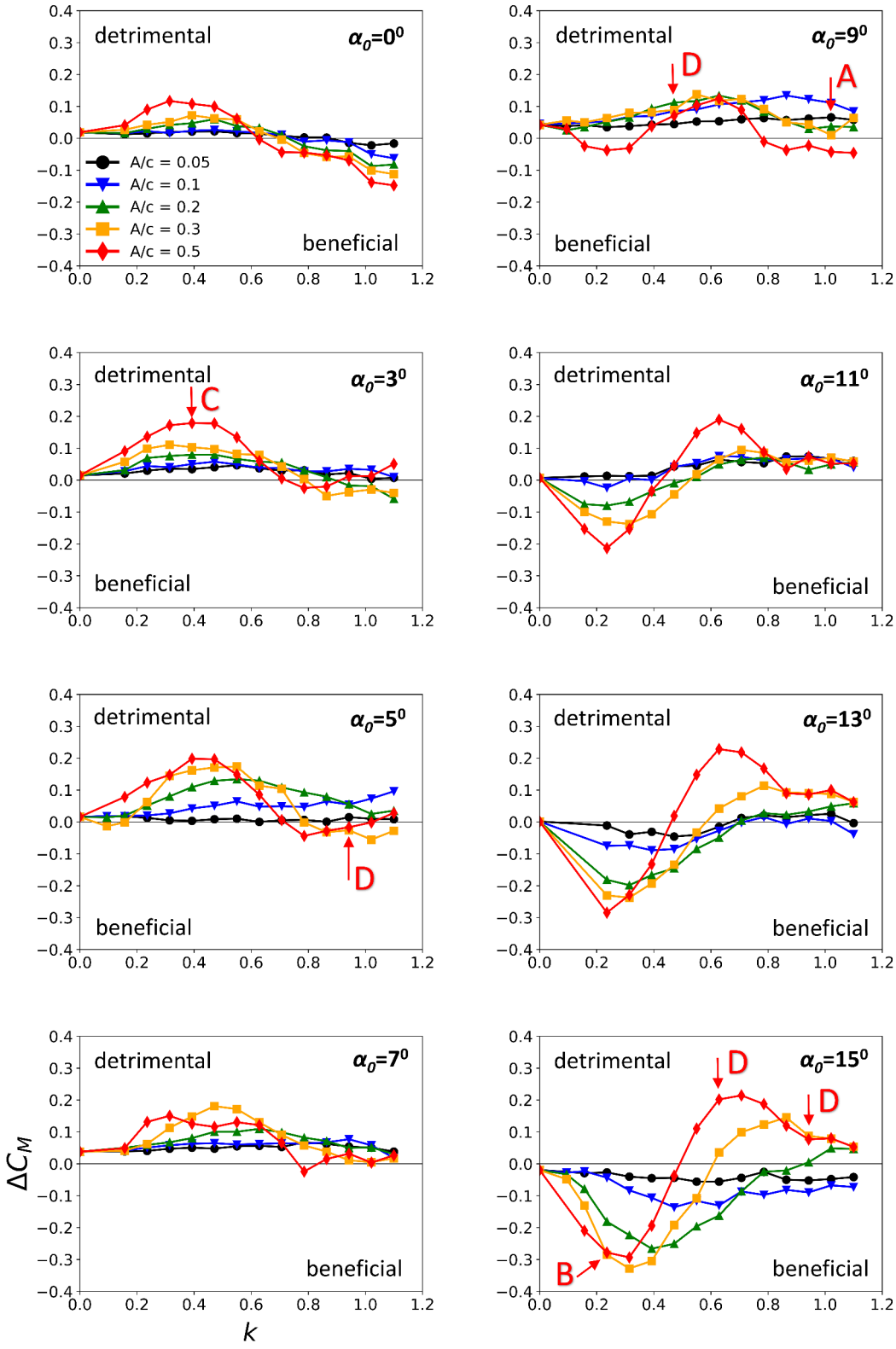

Figure 7-4: Pitching moment performance of mini-tab.

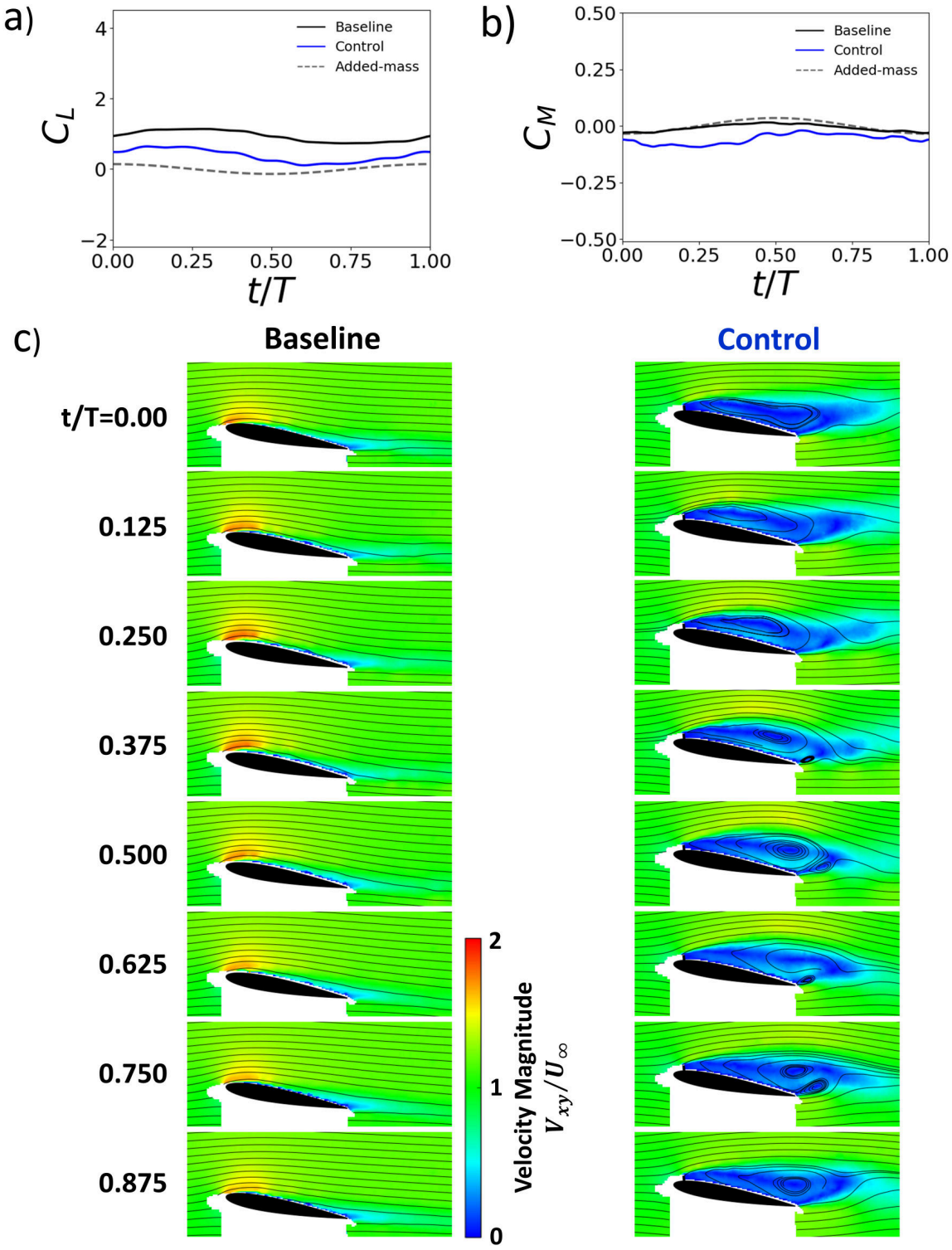

Figure 7-5: Type A flow field - $\alpha_0 = 9°$, $A/c = 0.05$, $k = 0.94$: a) phase-average lift coefficient, b) phase-average pitching moment coefficient, c) normalised velocity magnitude with streamlines.

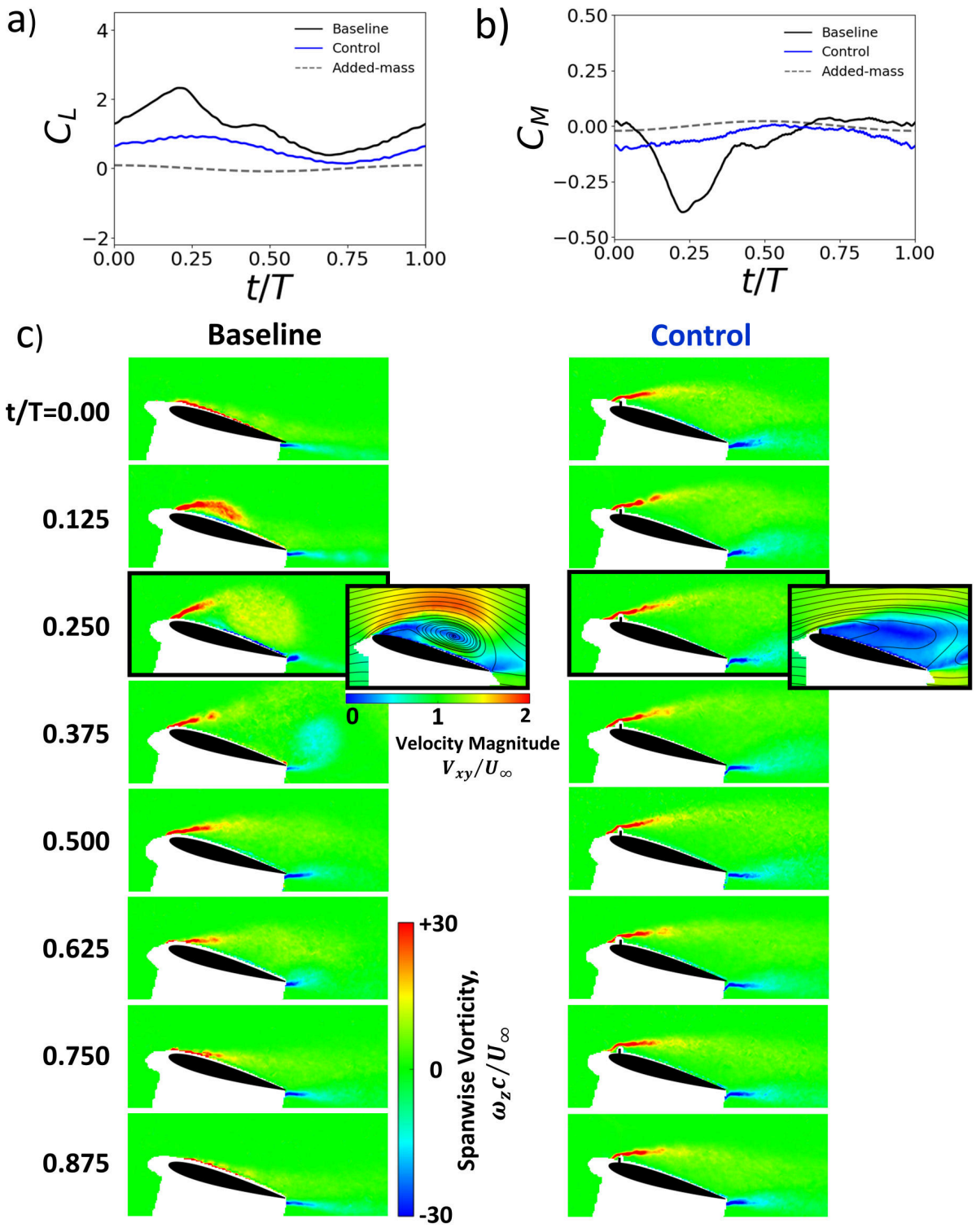

Figure 7-6: Type B flow field - $\alpha_0 = 15°$, $A/c = 0.5$, $k = 0.24$: a) phase-average lift coefficient, b) phase-average pitching moment coefficient, c) normalised spanwise vorticity.

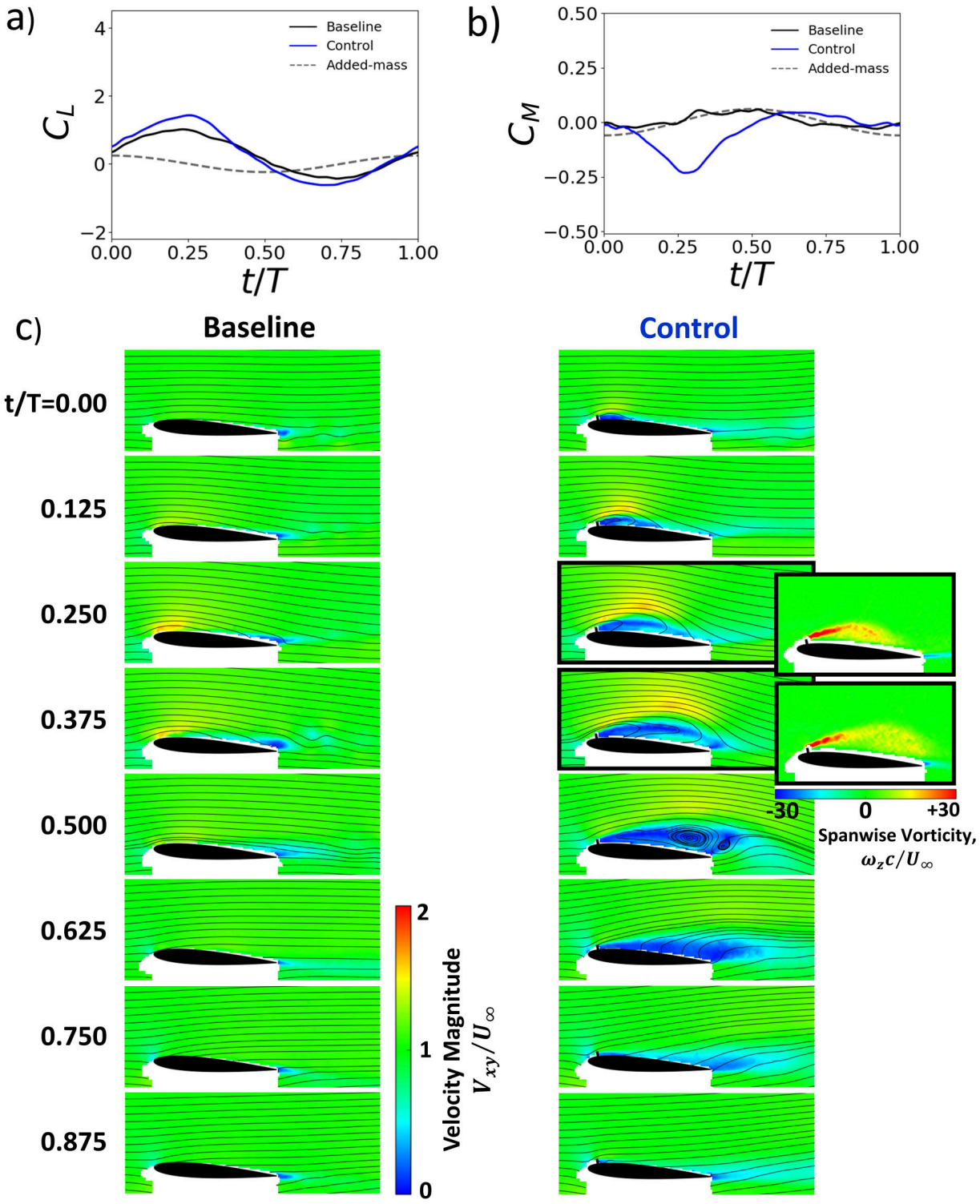

Figure 7-7: Type C flow field - $\alpha_0 = 3°$, $A/c = 0.5$, $k = 0.40$: a) phase-average lift coefficient, b) phase-average pitching moment coefficient, c) normalised velocity magnitude with streamlines.

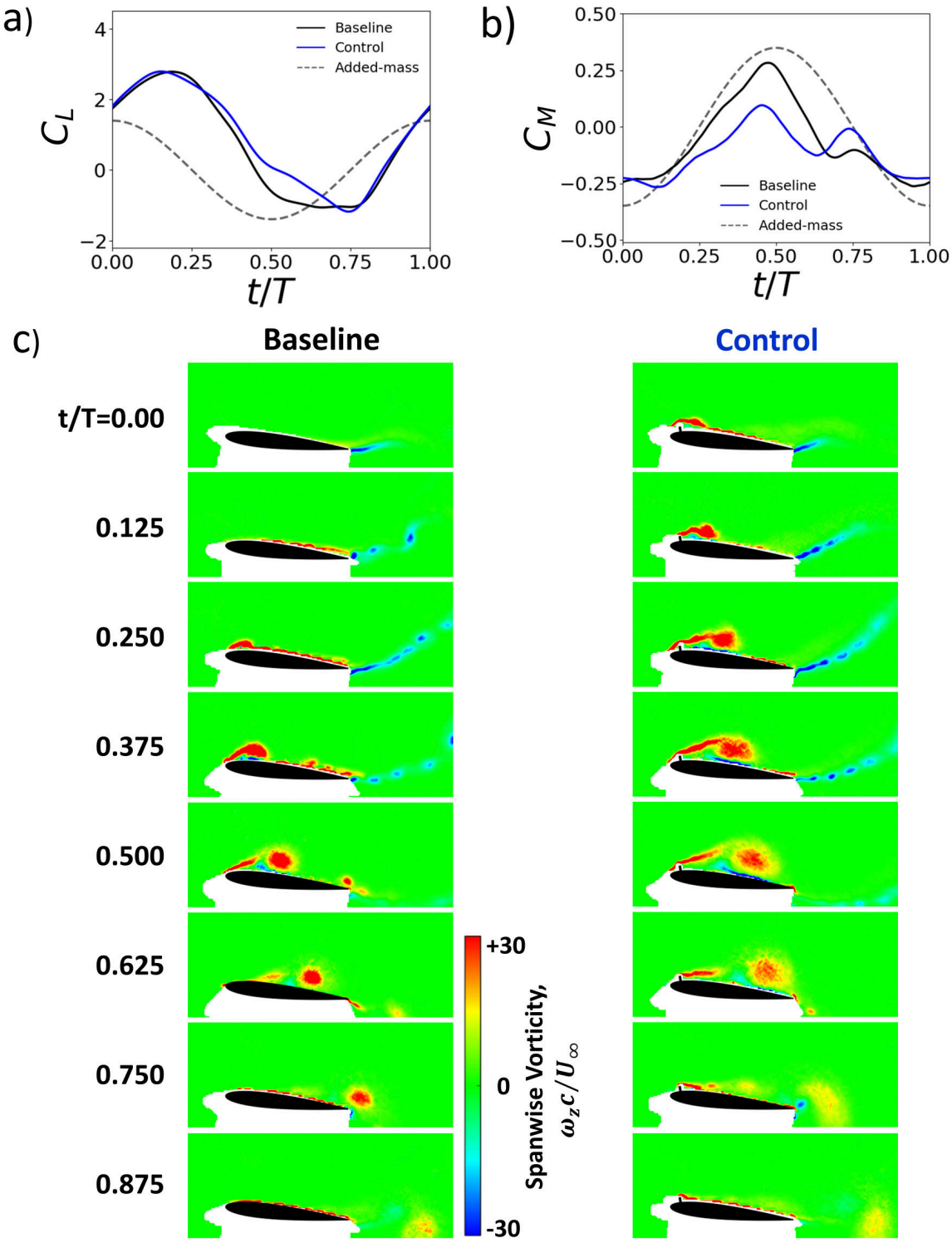

Figure 7-8: Type D flow field - $\alpha_0 = 5°$, $A/c = 0.5$, $k = 0.94$: a) phase-average lift coefficient, b) phase-average pitching moment coefficient, c) normalised spanwise vorticity.

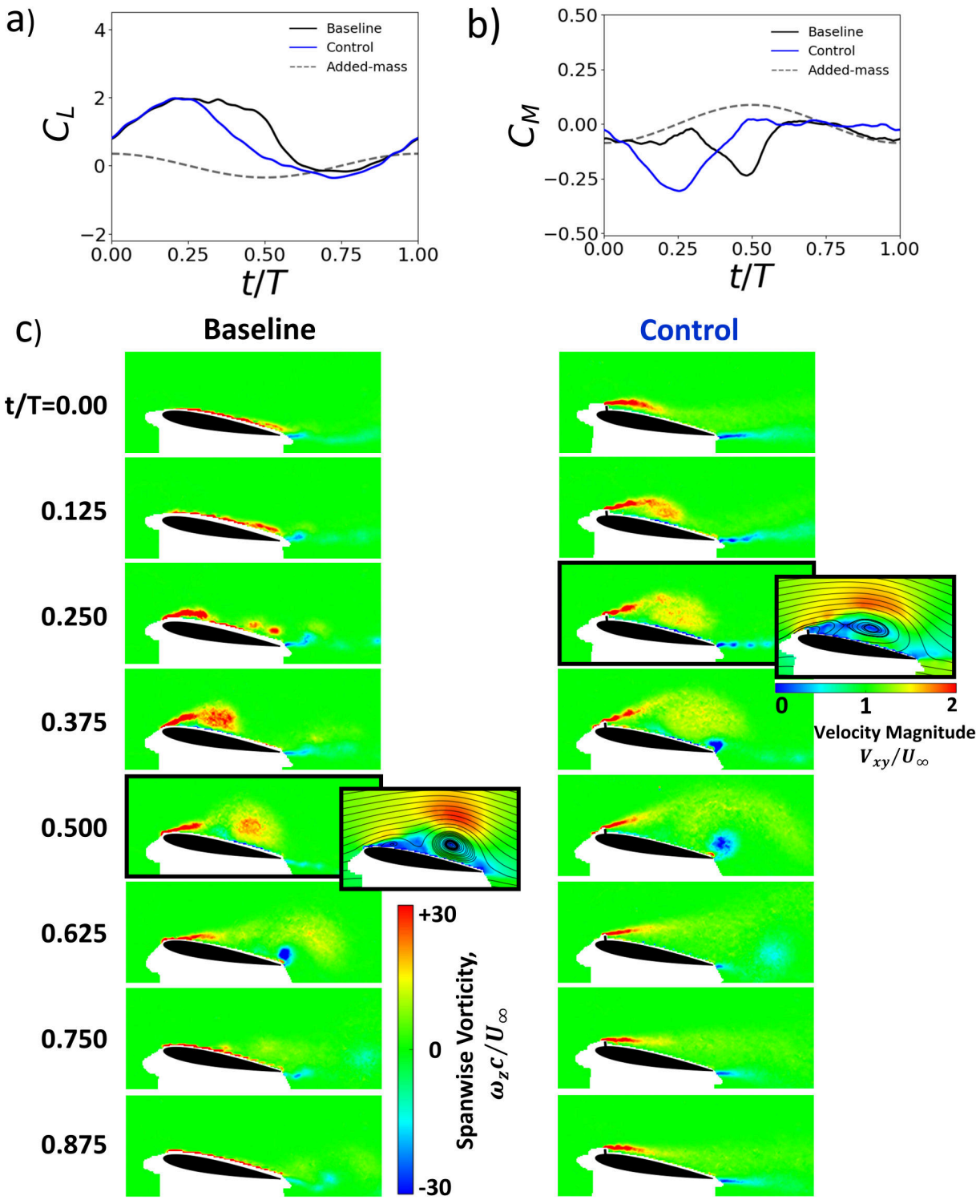

Figure 7-9: Type D flow field - $\alpha_0 = 9°$, $A/c = 0.5$, $k = 0.47$: a) phase-average lift coefficient, b) phase-average pitching moment coefficient, c) normalised spanwise vorticity.

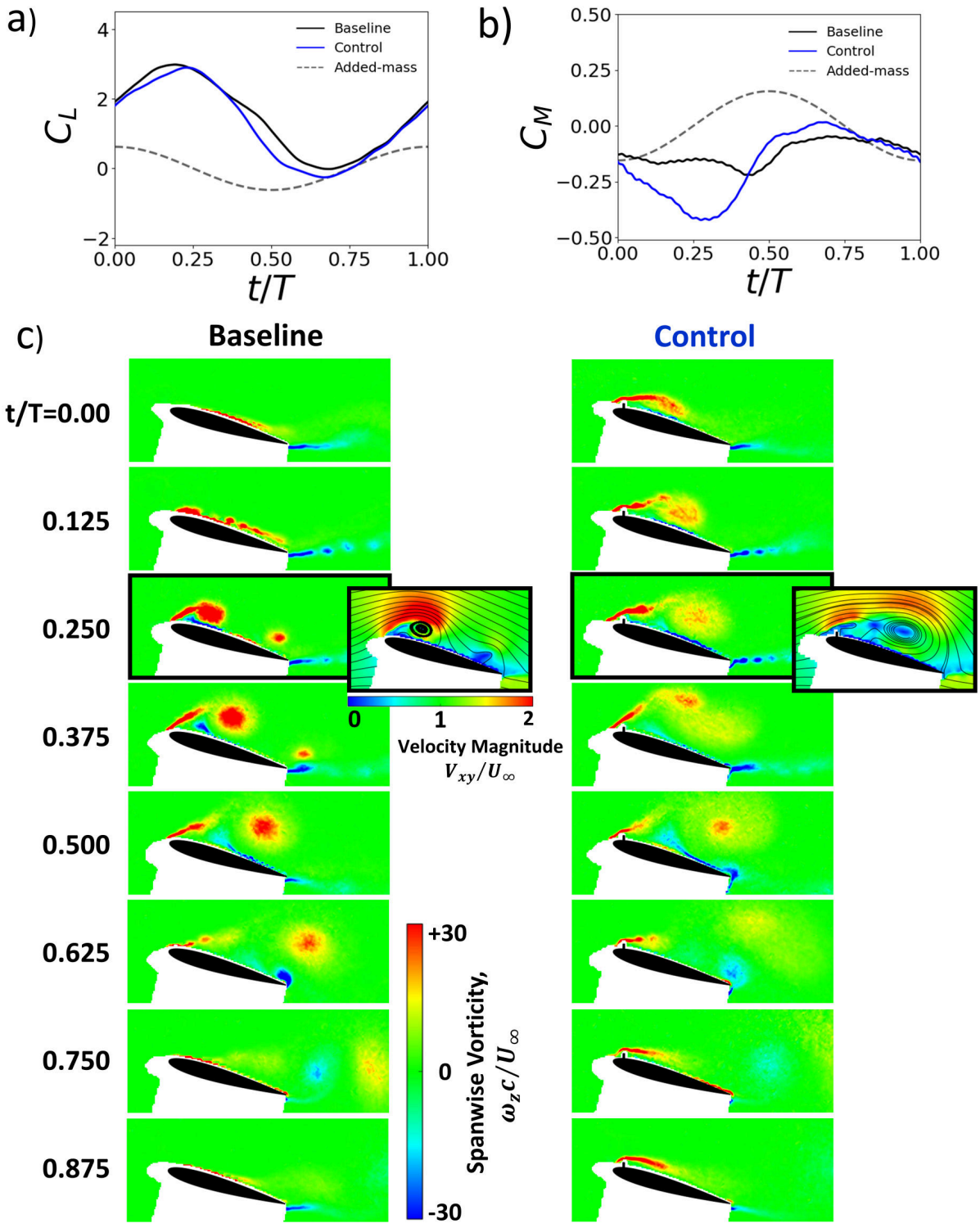

Figure 7-10: Type D flow field - $\alpha_0 = 15°$, $A/c = 0.5$, $k = 0.63$: a) phase-average lift coefficient, b) phase-average pitching moment coefficient, c) normalised spanwise vorticity.

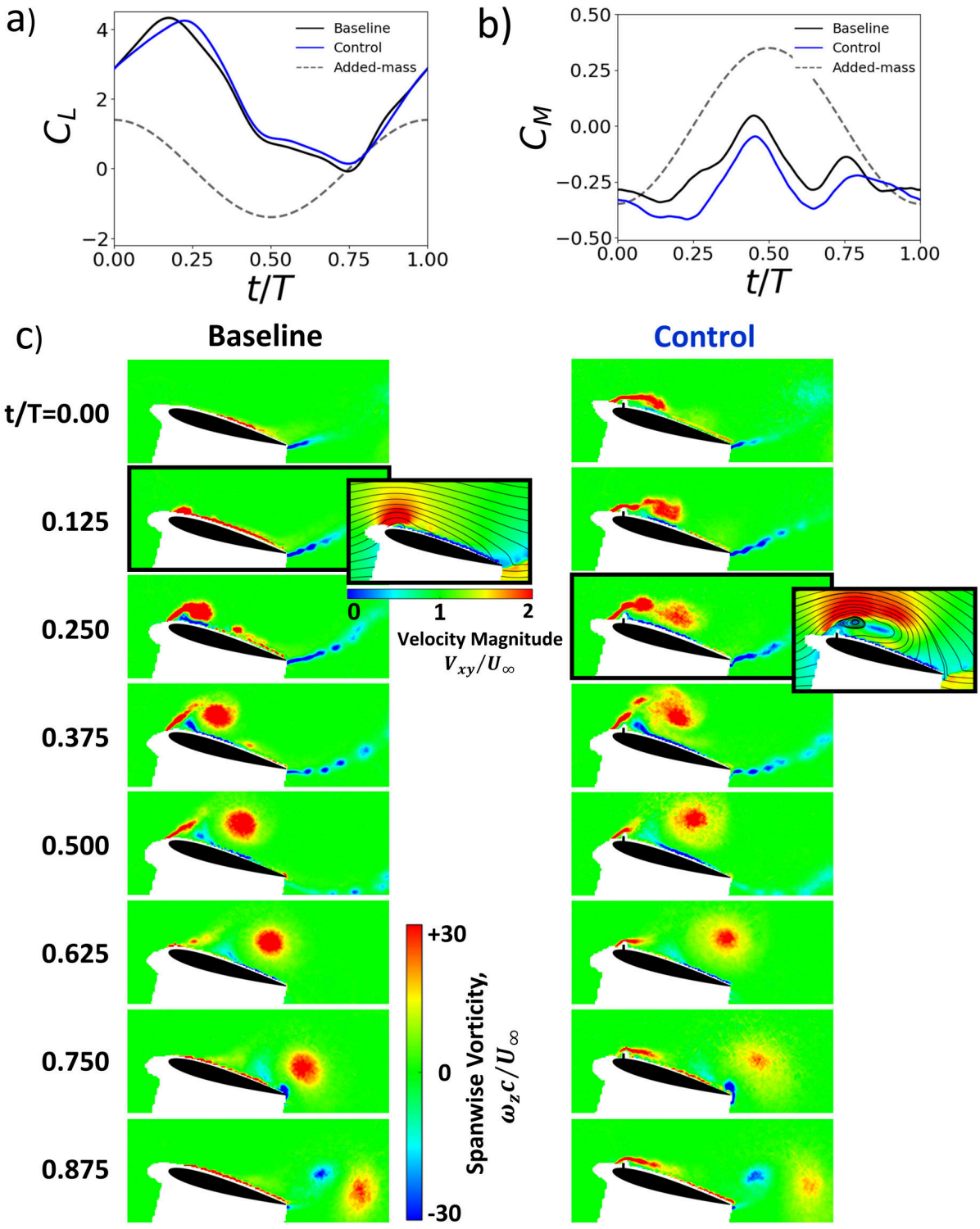

Figure 7-11: Type D flow field - $\alpha_0 = 15°$, $A/c = 0.5$, $k = 0.94$: a) phase-average lift coefficient, b) phase-average pitching moment coefficient, c) normalised spanwise vorticity.

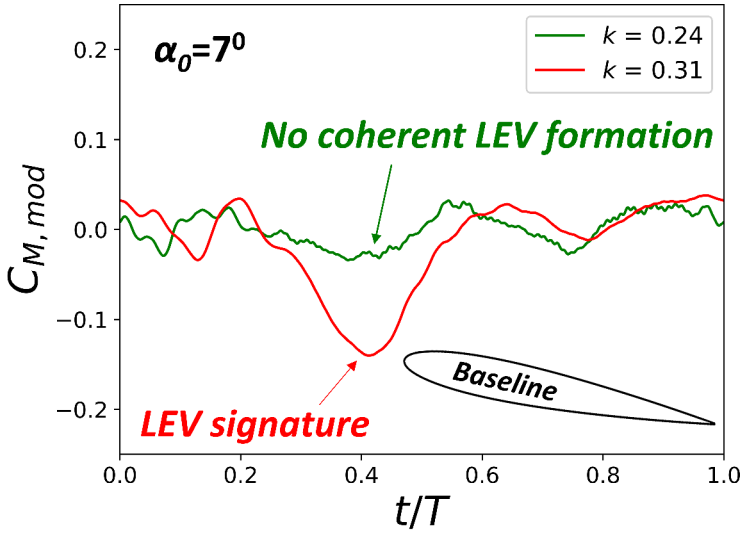

Figure 7-12: LEV signature detection through modified pitching moment coefficient, $C_{M,mod}$: Baseline airfoil at $\alpha_0 = 7°$, $A/c = 0.5$, $k = 0.24$,0.31.

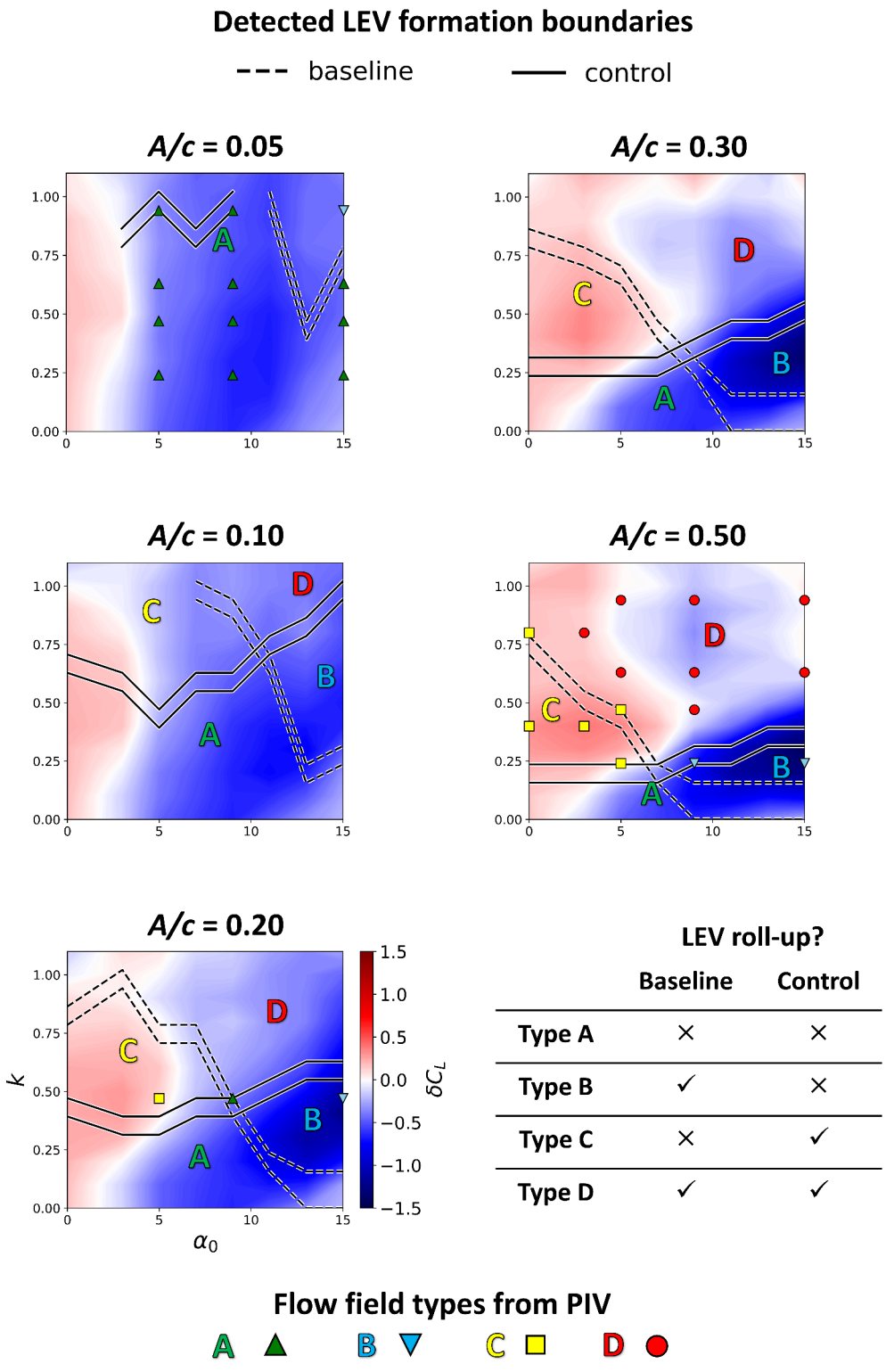

Figure 7-13: Contour plots of mini-tab lift performance with detected LEV formation boundaries and qualitative PIV flow field types.

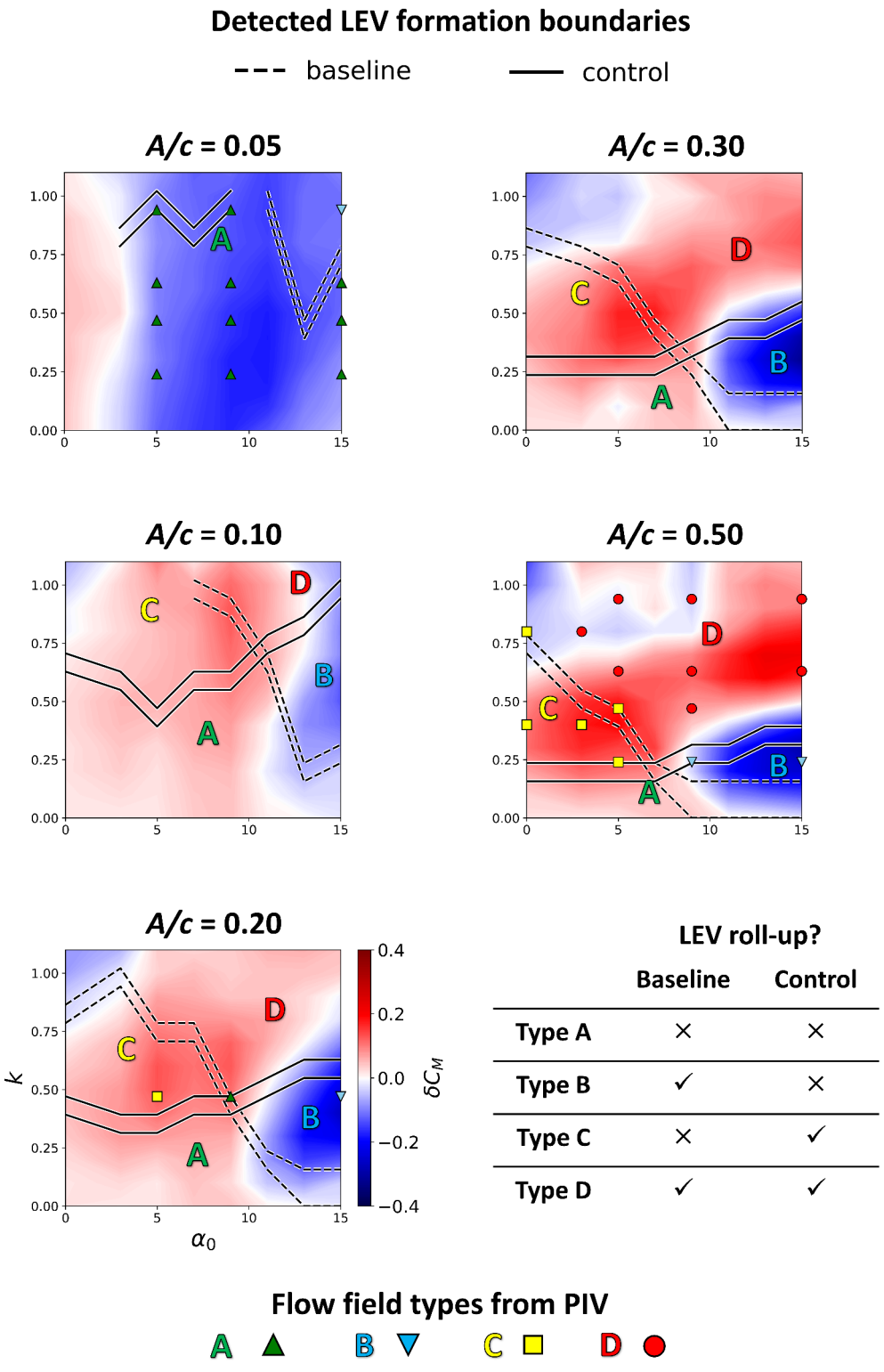

Figure 7-14: Contour plots of mini-tab pitching moment performance with detected LEV formation boundaries and qualitative PIV flow field types.

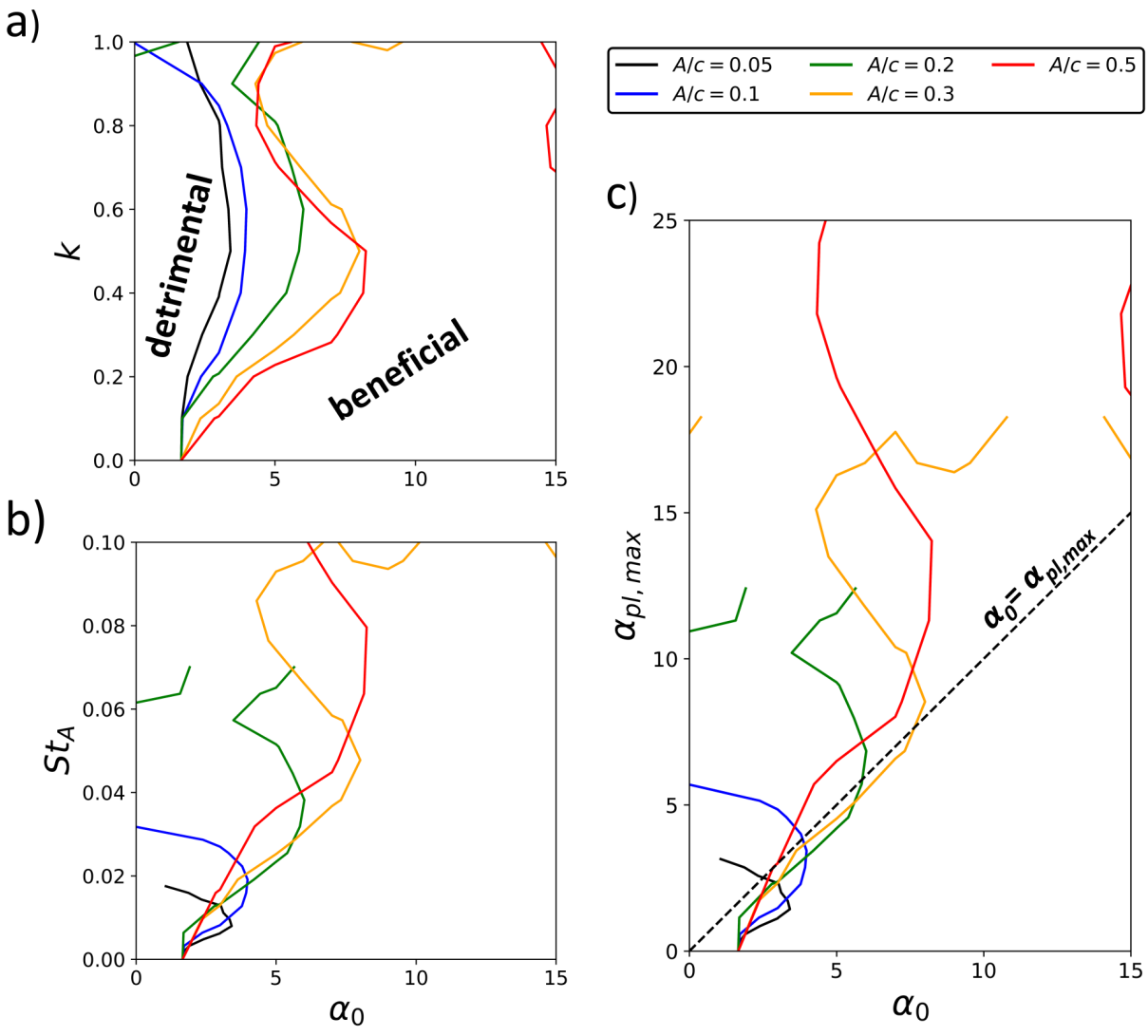

Figure 7-15: Boundary of $\delta C_L = 0.0$.

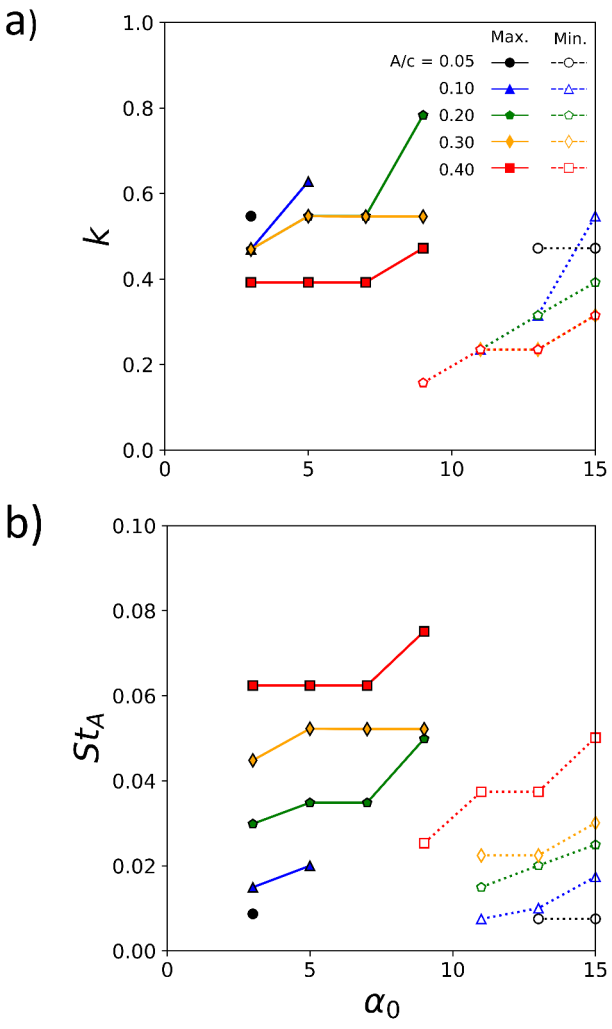

Figure 7-16: Extracted minima/maxima of δC_L.

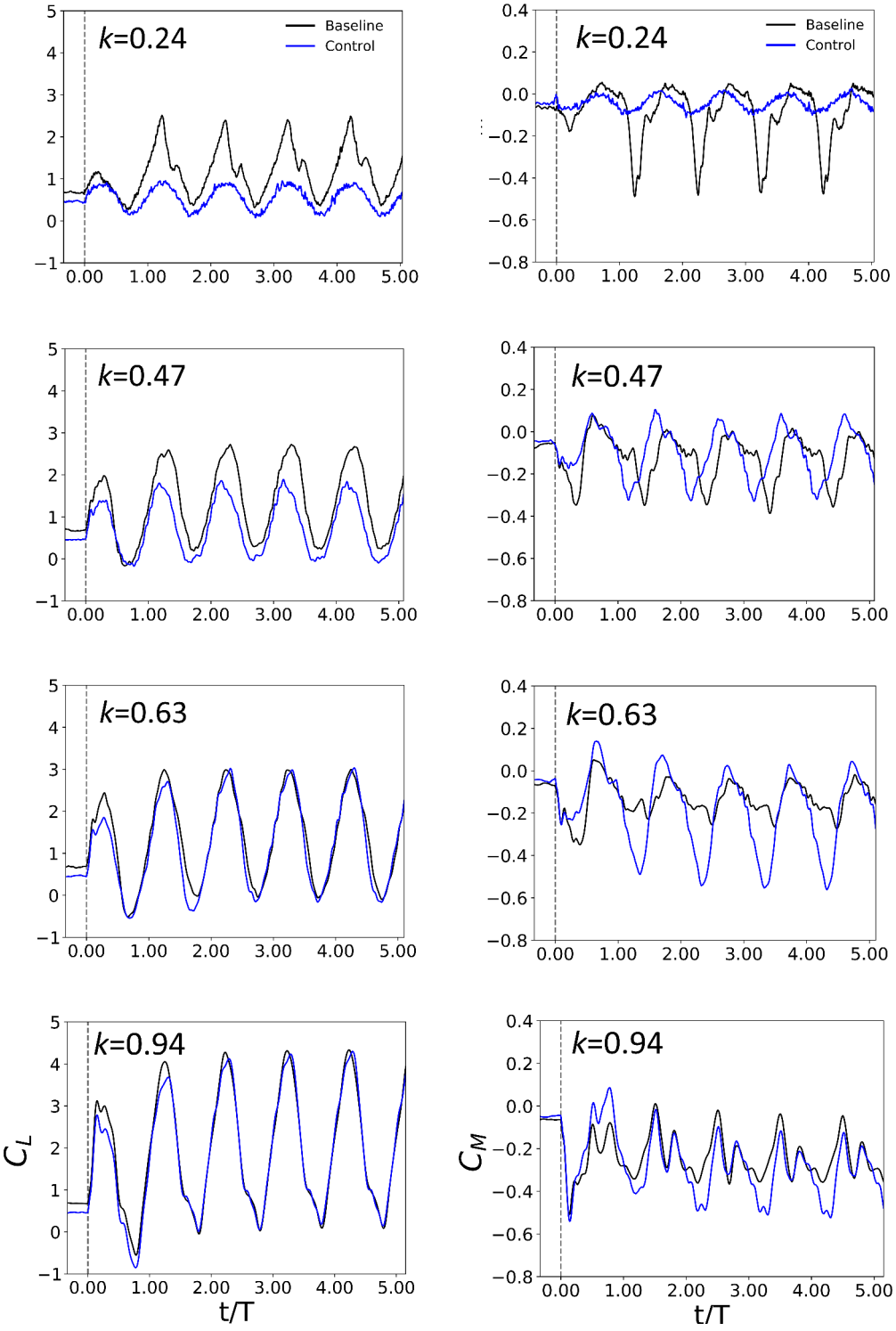

Figure 7-17: $\alpha_0 = 15°$, $A/c = 0.5$ - Lift and pitching moment response for impulsively started plunging oscillations at different k.

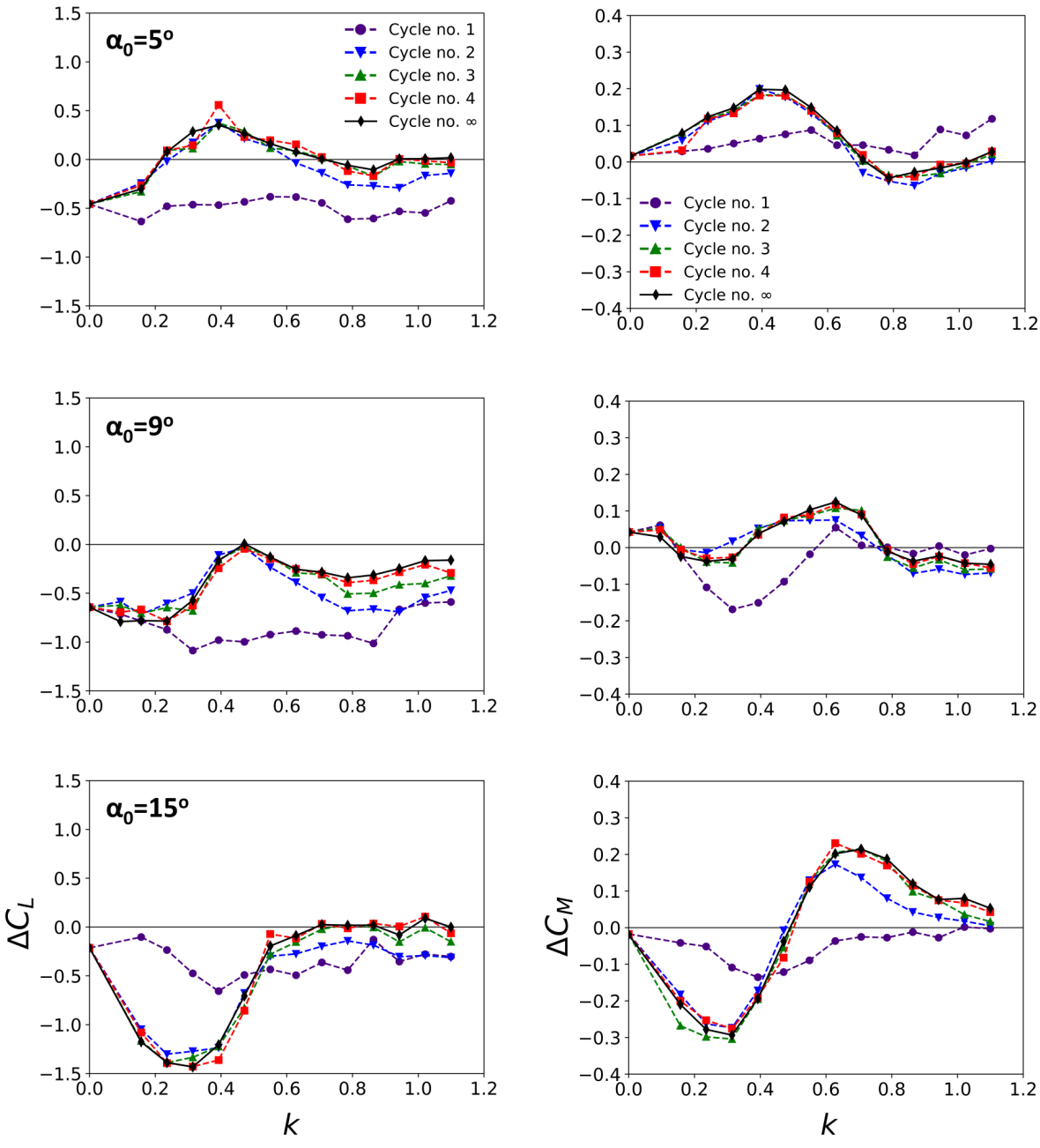

Figure 7-18: $A/c = 0.5$ - Transient lift and pitching moment performance.

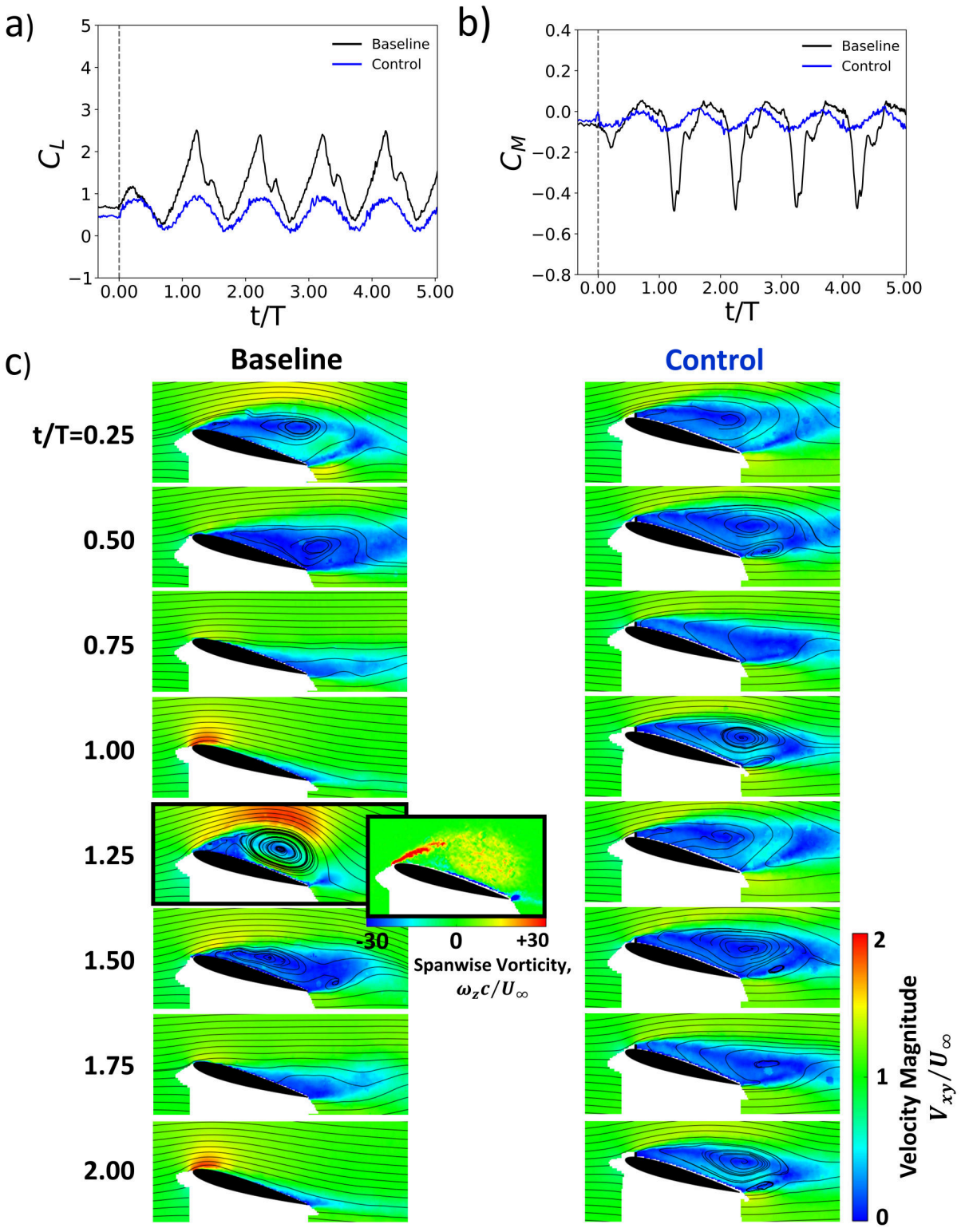

Figure 7-19: $\alpha_0 = 15°$, $A/c = 0.5$, $k = 0.24$; a) transient lift coefficient, b) transient pitching moment coefficient, c) normalised velocity magnitude with streamlines.

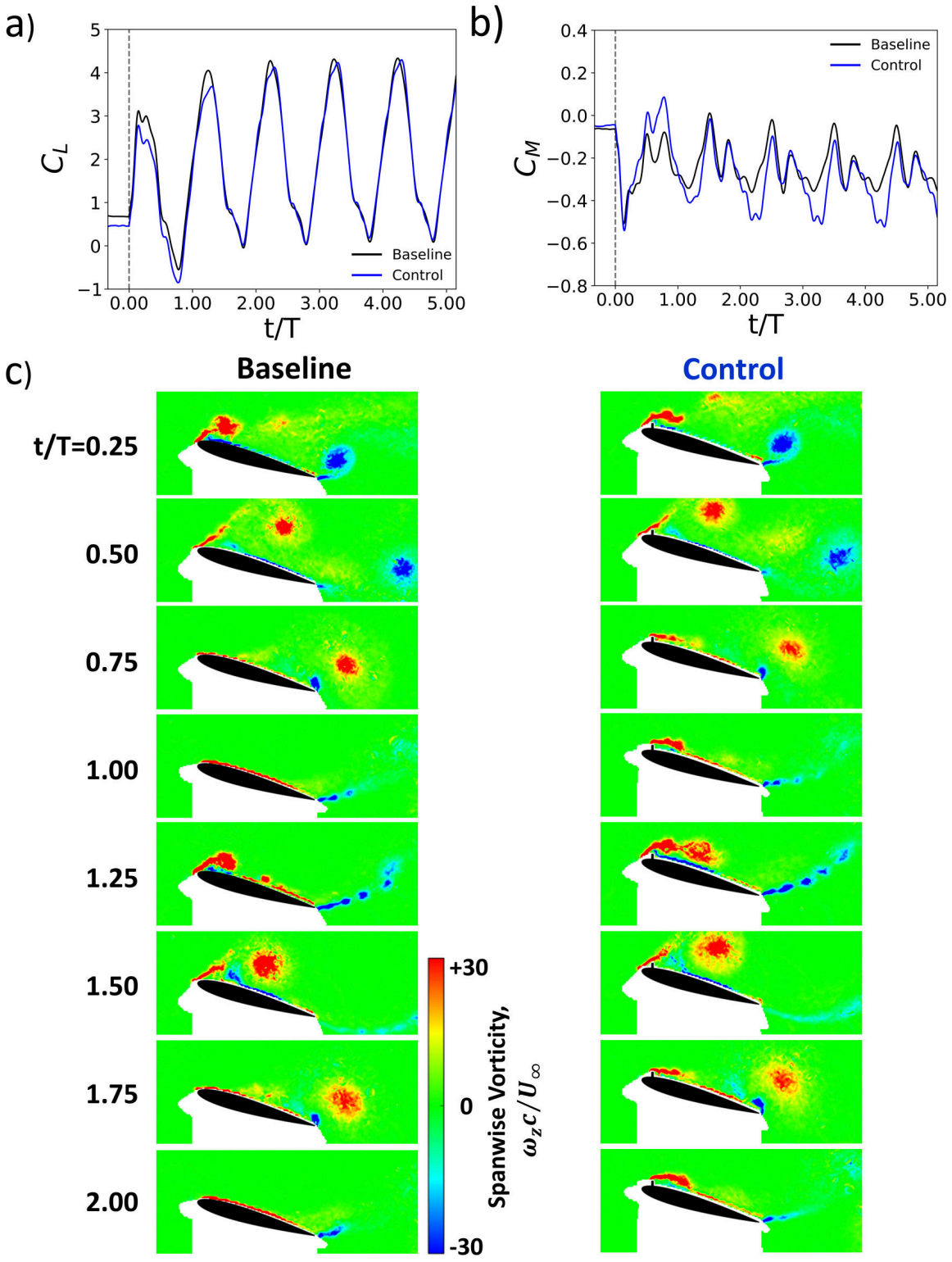

Figure 7-20: $\alpha_0 = 15°$, $A/c = 0.5$, $k = 0.94$; a) transient lift coefficient, b) transient pitching moment coefficient, c) normalised vorticity magnitude.

Chapter 8

Conclusions

The unsteady aerodynamics of a transient plunging airfoil was investigated through lift, pitching moment and flow field measurements. Peak loads were experienced during the motion for all cases which showed strong dependence on motion amplitude, yet remained insensitive to motion period. Significant loads oscillations were observed after the end of motion at post-stall angles of attack. These were shown to be caused by large-scale vortex shedding, where alternate vortices form and shed at the leading and trailing-edge of the airfoil and display a decay in magnitude with time. The frequency of the first vortex shedding cycle was shown to occur at the sub-harmonic of the airfoils static shedding frequency, which displayed little sensitivity to motion period and amplitude. After the first shedding cycle, the frequency showed an asymptotic increase to the static shedding frequency within 10 to 15 convective times. A potential relationship between peak magnitude and subsequent cycle frequency was found to follow a linear trend to a reasonable level of correlation, $R^2 = 0.70$.

The introduction of a second transient motion in the large-scale vortex shedding window produced a significant increase in peak lift and pitching moment. It was found that the loads response could be accurately estimated through linear superposition of the single motion response, which coincided with the merging of two distinct vortices over the airfoil upper surface. Breakdown of this linear behaviour occurred when the separation distance between the two vortices reached the

critical separation distance of a chord length, controlled through a time delay between the two motions. Linear superposition held valid for up to four transient motions, but showed increasing sensitivity on the time delay parameter. To test this further, the linear superposition of a single sinusoidal cycle was compared against the true periodic experiment. It could predict the mean lift and amplitude reasonable well for lower frequencies, where weaker vortical flow was present.

The effect of Reynolds number change from $\mathcal{O}(10^4)$ to $\mathcal{O}(10^5)$ was investigated through equivalent water and wind tunnel measurements. The loads and flow-fields were qualitatively similar and only minor differences were observed, stemming from the unsteady shear layer behaviour. During large-scale vortex shedding, unsteady pressure measurements revealed the maximum loads to occur when the chord-wise area exposed to the induced low pressure was maximised, which correlated with the significant aftward movement of the lower surface stagnation region. Leading-edge vortex growth and convection rates were estimated from the movement of the low pressure frontier across the chord and shown to vary between 21 and 29%. This frontier is a reasonable approximation of the airfol half-saddle point, a topological flow point on the surface that divides forward and reversed flow. The half-saddle marks the shedding of the upper surface vortex and subsequent loss of suction when it reaches the trailing-edge. The peak loads showed excellent agreement with equivalent water tunnel measurements at $Re = 20K$, adding confidence in the use of low Re measurements for the high Reynolds number applications.

The effect of a passively deployed mini-tab (flow fence) device at the airfoils leading-edge was investigated for lift and pitching moment suppression in unsteady conditions. This device forces separation over the upper surface of the airfoil in order to reduce the aerodynamic loads. Depending on the frequency and the amplitude of the wing motion the mini-tab can delay the roll-up of vorticity through the prevention of shear layer reattachment during the motion cycle. This change in the vortex dynamics provides effective lift and moment alleviation for post-stall angles of attack and low reduced frequencies. In contrast, at low angles of attack the separated shear layer emanating from the mini-tab can reattach downstream and roll up, resulting in vortex shedding and lift/moment increase. These two distinct flow regimes cause (positive) maximum and (negative) minimum in the lift reduction, with optimal frequencies roughly scaling with the

reduced frequency. In contrast the borderline between the two regions scales with the Strouhal number based on amplitude, and in particular with the minimum effective angle of attack during the cycle. The transient response was studied by investigating impulsively started plunging oscillations. In most cases, periodic response is reached within one cycle. During the first cycle, lift reduction is achieved for all frequencies within the range tested in the experiments.

8.0.1 Future Work

The work presented in this thesis opens up interesting avenues for future research:

- *Large-scale vortex shedding* - A study aimed at tracking both the leading and trailing-edge vortex strengths and trajectories could elucidate the mechanism for the shift in vortex shedding frequency from large-scale to bluff body vortex shedding.

- *Compound transient motions* - More compound transient motions need to be investigated for different wing kinematics to look for any commonality in LEV behaviour. Does the principle of linear superposition hold true in different unsteady conditions?

- *Dynamically deployed mini-tab* - A logical extension of Chapter 7 is the dynamic deployment of the mini-tab device. This could prove beneficial or detrimental depending on deployment phase and profile. Methods for dynamic stall detection could be integrated to give an active feedback for the mini-tab device, such as the leading-edge suction parameter [161] which has been experimentally determined in a recent study by Deparday and Mulleners [162].

Bibliography

[1] Michael W Kehoe. A Historical Overview of Flight Flutter Testing. *NASA Technical Memorandum*, (4720), 1995.

[2] Theodore Theodorsen. General theory of aerodynamic instability and the mechanism of flutter. *NACA Report*, No. 496:413–433, 1935.

[3] R.L. Bisplinghoff, H. Ashley, and R.L. Halfman. *Aeroelasticity*. Addison-Wesley Publishing Co., Reading, MA, 1955.

[4] Jeff D. Eldredge and Anya R. Jones. Leading-Edge Vortices: Mechanics and Modeling. *Annual Review of Fluid Mechanics*, 51(1):75–104, 2019.

[5] J. Gordon Leishman. *Principles of Helicopter Aerodynamics*. Cambridge University Press, Cambridge, 2nd edition, 2006.

[6] Doug McLean. *Understanding Aerodynamics: Arguing from the Real Physics*. John Wiley & Sons, Chichester, first edition, 2013.

[7] Jie-Zhi J.-Z. J.-M. Jain-Ming Wu, Xi-Yun Lu, Andrew G. Denny, Meng Fan, and Jie-Zhi J.-Z. J.-M. Jain-Ming Wu. Post-stall flow control on an airfoil by local unsteady forcing. *Journal of Fluid Mechanics*, 371:21–58, 1998.

[8] D J Cleaver, Z Wang, I Gursul, and M R Visbal. Lift Enhancement by Means of Small-Amplitude Airfoil Oscillations at Low Reynolds Numbers. *AIAA Journal*, 49(9):2018–2033, 2011.

[9] P. Rojratsirikul, M. S. Genc, Z. Wang, and I. Gursul. Flow-induced vibrations of low aspect ratio rectangular membrane wings. *Journal of Fluids and Structures*, 27(8):1296–1309, 2011.

[10] R.F. Huang and C.L. Lin. Vortex shedding and shear-layer instability of a cantilever wing at low reynolds numbers. *33rd Aerospace Sciences Meeting and Exhibit*, 33(8):1398–1403, 1995.

[11] J. Panda and K. B. M. Q. Zaman. Experimental investigation of the flowfield of an oscillating airfoil. *NASA Technical Memorandum*, 105675:1–18, 1992.

[12] J.E. Cooper and J.R. Wright. *Introduction to Aircraft Aeroelasticity and Loads*. John Wiley & Sons, Chichester, 2007.

[13] Y.C. Fung. *An introduction to the theory of aeroelasticity*. Courier Dover Publications, Mineola, 2002.

[14] W J McCroskey. Unsteady airfoils. *Annual Review of Fluid Mechanics*, 14:285–311, 1982.

[15] S. J. Corkery, H. Babinsky, and W. R. Graham. Quantification of added-mass effects using particle image velocimetry data for a translating and rotating flat plate. *Journal of Fluid Mechanics*, 870:492–518, 2019.

[16] Abe Silverstein and Upshur T. Joyner. Experimetnal Verification of the Theory of Oscillating Airfoils. Technical Report 673, National Advisory Committe for Aeronautics, 1939.

[17] R. L. Halfman. Experimental Aerodynamic Derivatives of a Sinusoidally Oscillating Air-foil in Two-Dimensional Flow. *NACA Technical Report*, 1108:1–44, 1952.

[18] Elliott G. Reid and W Vincenti. An Experimental Determination of the Lift of an Oscillating Airfoil. *Journal of the Aeronautical Sciences*, 8(1):1–6, 1940.

[19] A. Gerald Rainey. Measurement of aerodynamic forces for various mean angles of attack on an airfoil oscillating in pitch and on two finite-span wings oscillating in bending with emphasis on damping in the stall. *NACA*, 1305:1–33, 1956.

[20] Bodapati Satyanarayana and Sanford Davis. Experimental Studies of Unsteady Trailing-Edge Conditions. *AIAA Journal*, 16(2):125–129, 1978.

[21] S. H. Chen and C. M. Ho. Near wake of an unsteady symmetric airfoil. *Journal of Fluids and Structures*, 1:151–164, 1987.

[22] M. F. Platzer, K. D. Jones, J. Young, and J. C. S. Lai. Flapping Wing Aerodynamics: Progress and Challenges. *AIAA Journal*, 46(9):2136–2149, 2008.

[23] I.E. Garrick. Propulsion of a Flapping and Oscillating Airfoil. *NACA Report*, 567:1–14, 1936.

[24] Manoochehr M. Koochesfahani. Vortical patterns in the wake of an oscillating airfoil. *AIAA Journal*, 27(9):1200–1205, 1989.

[25] James D. DeLaurier and J. M. Harris. Experimental Study of Oscillating-Wing Propulsion. *Journal of Aircraft*, 19(5):368–373, 1982.

[26] K. D. Jones, C. M. Dohring, and M. F. Platzer. Experimental and computational investigation of the Knoller-Betz effect. *AIAA Journal*, 36(7):1240–1246, 1998.

[27] D J Cleaver, Z Wang, and I Gursul. Bifurcating flows of plunging aerofoils at high Strouhal numbers. *Journal of Fluid Mechanics*, FirstView:1–28, 2012.

[28] J Young and J C S Lai. Oscillation frequency and amplitude effects on the wake of a plunging airfoil. *AIAA Journal*, 42(10):2042–2052, 2004.

[29] Ramiro Godoy-Diana, Jean-Luc Aider, and Jose Eduardo Wesfreid. Transitions in the Wake of a Flapping Foil. *Pysical Review E*, 77:1–6, 2008.

[30] D. G. Bohl and M. M. Koochesfahani. MTV measurements of the vortical field in the wake of an airfoil oscillating at high reduced frequency. *Journal of Fluid Mechanics*, 620:63–88, 2009.

[31] M. S. Triantafyllou, G. S. Triantafyllou, and R. Gopalkrishnan. Wake mechanics for thrust generation in oscillating foils. *Physics of Fluids A: Fluid Dynamics*, 3(12):2835–2837, 1991.

[32] Graham K Taylor, Robert L Nudds, and Adrian L R Thomas. Flying and swimming animals cruise at a Strouhal number tuned for high power efficiency. *Letters To Nature*, 425:707–711, 2003.

[33] K. D. von Ellenrieder and S. Pothos. PIV measurements of the asymmetric wake of a two dimensional heaving hydrofoil. *Experiments in Fluids*, 44:733–745, 2008.

[34] D. E. Calderon, D. J. Cleaver, I. Gursul, and Z. Wang. On the absence of asymmetric wakes for periodically plunging finite wings. *Physics of Fluids*, 26:1–15, 2014.

[35] E. Reissner and John E. Stevens. Effect of Finite Span on the Airload Distributions For Oscillating Wings. *NACA Technical Note*, 1195:1–97, 1947.

[36] Raymond L. Bisplinghoff, Holt Ashley, and Robert L. Halfman. *Aeroelasticity*. Dover Publications, Inc., New York, first edition, 1983.

[37] By Edward Widmayer, Sherman A Clevenson, and Sumner A Leadbetter. Some Measurements of Aerodynamic Forces and Moments at Subsonic Speeds on a Rectangular Wing of Aspect Ratio 2 Oscillating About the Midchord. *NACA Research Memorandum*, L53F19:1–45, 1953.

[38] M. F. Neef and D. Hummel. Euler Solutions for a Finite-Span Flapping Wing. *Progress in Astronautics and Aeronautics*, 195:429–451, 2001.

[39] X He and I Gursul. Point Vortex Model of Deflected Wakes of Oscillating Airfoils. *AIAA Journal*, 54(11):3647–3651, 2016.

[40] W. J. McCroskey. The Phenomenon of Dynamic Stall. *NASA Technical Memorandum*, 81264:1–28, 1981.

[41] J. M. Anderson, K. Streitlien, D. S. Barrett, and M. S. Triantafyllou. Oscillating foils of high propulsive efficiency. *Journal of Fluid Mechanics*, 360:41–72, 1998.

[42] D. Rival and C. Tropea. Characteristics of Pitching and Plunging Airfoils Under Dynamic-Stall Conditions. *Journal of Aircraft*, 47(1):80–86, 2010.

[43] Peter Freymuth. Propulsive Vortical Signature of Plunging and Pitching Airfoils. *AIAA Journal*, 26(7):881–883, 1988.

[44] C. Maresca, D. Favier, and J. Rebont. Experiments on an aerofoil at high angle of incidence in longitudinal oscillations. *Journal of Fluid Mechanics*, 92(4):671–690, 1979.

[45] Ismet Gursul and Chih-Ming Ho. High Aerodynamic Loads on an Airfoil Submerged in an Unsteady Strem. *AIAA Journal*, 30(4):1117–1119, 1992.

[46] Thomas C. Corke and Flint O. Thomas. Dynamic Stall in Pitching Airfoils: Aerodynamic Damping and Compressibility Effects. *Annual Review of Fluid Mechanics*, 47:479–505, 2015.

[47] Karen Mulleners and Markus Raffel. The onset of dynamic stall revisited. *Experiments in Fluids*, 52:779–793, 2012.

[48] Kenneth W. McAlister, Lawrence W. Carr, and McCroskey William J. Dynamic Stall Experiements on the NACA 0012 Airfoil. *NACA Technical Paper*, 1100:1–161, 1978.

[49] Kazuo Ohmi, Madeleine Coutanceau, Olivier Daube, and Ta Phuoc Loc. Further experiments on vortex formation around an oscillating and translating airfoil at large incidences. *Journal of Fluid Mechanics*, 211:37–60, 1990.

[50] Cheng Hsiung Kuo and J. K. Hsieh. Unsteady flow structure and vorticity convection over the airfoil oscillating at high reduced frequency. *Experimental Thermal and Fluid Science*, 24:117–129, 2001.

[51] WJ McCroskey, KW McAlister, and LW Carr. An experimental study of dynamic stall on advanced airfoil sections. Volume 1: Summary of the experiment. Technical report, NASA, Moffet Field, 1982.

[52] H Oshima and B R Ramaprian. Velocity Measurements over a Pitching Airfoil. *AIAA Journal*, 35(1):119–126, 1997.

[53] Scott J Schreck and Hank E Helint. Unsteady Vortex Dynamics and Surface Pressure Topologies on a Finite Pitching Wing. *Journal of Aircraft*, 31(4):899–907, 1994.

[54] D M Tang and E H Dowell. Experimental investigation of three-dimensional dynamic stall model oscillating in pitch. *Journal of Aircraft*, 32(5):1062–1071, 1995.

[55] A. Spentzos, G. Barakos, K. Badcock, B. Richards, P. Wernert, S. Schreck, and M. Raffel. Investigation of Three-Dimensional Dynamic Stall Using Computational Fluid Dynamics. *AIAA Journal*, 43(5):1023–1033, 2005.

[56] A Spentzos, G N Barakos, K J Badcock, B E Richards, and F N Coton. Computational Fluid Dynamics Study of Three-Dimensional Dynamic Stall of Various Planform Shapes. *Journal of Aircraft*, 44(4), 2007.

[57] Antonella Ferrecchia. *Analysis of Three-Dimensional Dynamic Stall*. PhD thesis, University of Glasgow, 2002.

[58] F.O. Carta. A Comparison of the Pitching and Plunging Response of an Oscillating Airfoil. *NASA Contractor Report*, 3172:1–153, 1979.

[59] Shin-Hsing Chen. *The Unsteady Aerodynamic of a Plunging Airfoil*. PhD thesis, University of Southern California, 1985.

[60] T. Lee and Y. Y. Su. Surface Pressures Developed on an Airfoil Undergoing Heaving and Pitching Motion. *Journal of Fluids Engineering*, 137:1–11, 2015.

[61] T. Fukushima and L.U. Dadone. Comparison of Dynamic Stall Phenomena For Pitching and Vertical Translation Motions. Technical report, Boeing Vertol Company, Washington, D.C., 1977.

[62] Christian A. Maresca, Daniel J. Favier, and Jean M. Rebont. Unsteady aerodynamics of an aerofoil at high angle of incidence performing various linear oscillations in a uniform stream. *Journal of the American Helicopter Society*, 26(2):40–45, 1981.

[63] Miguel R. Visbal. Numerical Investigation of Deep Dynamic Stall of a Plunging Airfoil. *AIAA Journal*, 49(10):2152–2170, 2011.

[64] Michael V. Ol, Luis Bernal, Chang Kwon Kang, and Wei Shyy. Shallow and deep dynamic stall for flapping low Reynolds number airfoils. *Animal Locomotion*, 46:883–891, 2009.

[65] Ismail H. Tuncer, Ralf Walz, and Max F. Platzer. A computational study on the dynamic stall of a flapping airfoil. In *16th AIAA Applied Aerodynamics Conference*, pages 1–7, Albuquerque, 1998. AIAA.

[66] K. B. Lua, T. T. Lim, K. S. Yeo, and G. Y. Oo. Wake-Structure Formation of a Heaving Two-Dimensional Elliptic Airfoil. *AIAA Journal*, 45(7):1571–1583, 2007.

[67] John Young and Joseph C. S. Lai. On the aerodynamic forces of a plunging airfoil. *Journal of Mechanical Science and Technology*, 21:1388–1397, 2007.

[68] G. C. Lewin and H. Haj-Hariri. Modelling thrust generation of a two-dimensional heaving airfoil in a viscous flow. *Journal of Fluid Mechanics*, 492:339–362, 2003.

[69] I H Tuncer and M F Platzer. Computational study of flapping airfoil aerodynamics. *Journal of Aircraft*, 37(3):514–520, 2000.

[70] N. Chiereghin, D. J. Cleaver, and I. Gursul. Unsteady Lift and Moment of a Periodically Plunging Airfoil. *AIAA Journal*, 57(1):208–222, 2019.

[71] M. R. Soltani and Faezeh Rasi Marzabadi. Effect of plunging oscillation on an offshore wind turbine blade section. *The Aeronautical Journal*, 70:571–581, 2007.

[72] D Rival, Jochen Kriegseis, and Pascal Schaub. A criterion for vortex separation on unsteady aerodynamic profiles. In *51st AIAA Aerospace Sciences Meeting including the New Horizons Forum and Aerospace Exposition*, pages 1–11, Grapevine, 2013. AIAA.

[73] Mehdi Ghoreyshi and Russell M. Cummings. Challenges in the aerodynamics modeling of an oscillating and translating airfoil at large incidence angles. *Aerospace Science and Technology*, 28:176–190, 2013.

[74] Jean Yves Andro and Laurent Jacquin. Frequency effects on the aerodynamic mechanisms of a heaving airfoil in a forward flight configuration. *Aerospace Science and Technology*, 13:71–80, 2009.

[75] Jeesoon Choi, Tim Colonius, and David R. Williams. Dynamics and Energy Extraction of a Surging and Plunging Airfoil at Low Reynolds Number. *Journal of Fluid Mechanics*, 763:237–253, 2013.

[76] John Young and Joseph C.S. Lai. Vortex Lock-In Phenomenon in the Wake of a Plunging Airfoil. *AIAA Journal*, 45(2):485–490, 2007.

[77] Azar Eslam Panah and James H J Buchholz. Parameter dependence of vortex interactions on a two-dimensional plunging plate. *Experiments in Fluids*, 55:1687, 2014.

[78] D J Cleaver, Zhijin Wang, and Ismet Gursul. Investigation of high-lift mechanisms for a flat-plate airfoil undergoing small-amplitude plunging oscillations. *AIAA Journal*, 51(4):968–980, 2013.

[79] Joel E. Guerrero. Aerodynamic Performance of Cambered Heaving Airfoils. *AIAA Journal*, 48(11):2694–2698, 2010.

[80] Chang-kwon Kang, Yeon Sik Baik, Luis Bernal, Michael V. Ol, and Wei Shyy. Fluid Dynamics of Pitching and Pluging Airfoils of Reynolds Number between 1x10ˆ4 and 6x10ˆ4. In *47th AIAA Aerospace Sciences Meeting Including The New Horizons Forum and Aerospace Exposition*, number January, pages 1–20, 2009.

[81] Miguel Visbal, Turgut O. Yilmaz, and Donald Rockwell. Three-dimensional vortex formation on a heaving low-aspect-ratio wing: Computations and experiments. *Journal of Fluids and Structures*, 38:58–76, 2013.

[82] Turgut O. Yilmaz and Donald Rockwell. Three-dimensional flow structure on a maneuvering wing. *Experiments in Fluids*, 48:539–544, 2010.

[83] D. E. Calderon, Z. Wang, I. Gursul, and M. R. Visbal. Volumetric measurements and simulations of the vortex structures generated by low aspect ratio plunging wings. *Physics of Fluids*, 25(6), 2013.

[84] N Chiereghin, S Bull, D J Cleaver, and I Gursul. Three-Dimensionality of Leading Edge Vortices on High Aspect Ratio Plunging Wings. *Physical Review Fluids [IN REVIEW]*, 2020.

[85] J. H. Strickland and G. M. Graham. Dynamic stall inception correlation for airfoils undergoing constantpitch rate motions. *AIAA Journal*, 24(4):678–680, 1986.

[86] P. F. Lorber and F. O. Carta. Airfoil dynamic stall at constant pitch rate and high Reynolds number. *Journal of Aircraft*, 25(6):548–556, 1988.

[87] Miguel R. Visbal. Dynamic stall of a constant-rate pitching airfoil. *Journal of Aircraft*, 27(5):400–407, 1990.

[88] D. G. Daley and E. J. Jumpert. Experimental investigation of dynamic stall for a pitching airfoil. *Journal of Aircraft*, 21(10):831–832, 1984.

[89] J. M. Walker, H. E. Helin, and J. H. Strickland. An experimental investigation of an airfoil undergoing large-amplitude pitching motions. *AIAA Journal*, 23(8):1141–1142, 1985.

[90] Amanullah Choudhry, Maziar Arjomandi, and Richard Kelso. Methods to control dynamic stall for wind turbine applications. *Renewable Energy*, 86:26–37, 2016.

[91] Charles P. Ellington, Coen van den Berg, Alexander P. Willmott, and Adrian L. R. Thomas. Leading-edge vortices in insect flight. *Letters To Nature*, 384:626–630, 1996.

[92] Michael V. Ol, Jeff D. Eldredge, and Chengjie Wang. High-Amplitude Pitch of a Flat Plate: an Abstraction of Perching and Flapping. *International Journal of Micro Air Vehicles*, 1(3):203–216, 2009.

[93] David E. Rival, Jochen Kriegseis, Pascal Schaub, Alexander Widmann, and Cameron Tropea. Characteristic length scales for vortex detachment on plunging profiles with varying leading-edge geometry. *Experiments in Fluids*, 55(1):1–8, 2014.

[94] C. W. Pitt Ford and H. Babinsky. Lift and the leading-edge vortex. *Journal of Fluid Mechanics*, 720:280–313, 2013.

[95] H. Babinsky and P. R. R. J. Stevens. Low Order Modelling of Lift Forces for Unsteady Pitching and Surging Wings . In *54th AIAA Aerospace Sciences Meeting*, pages 1–12, San Diego, 2016.

[96] Field Manar, Peter Mancini, David Mayo, and Anya R Jones. Comparison of Rotating and Translating Wings : Force Production and Vortex Characteristics. *AIAA Journal*, 54(2), 2016.

[97] Michael V. Ol and Holger Babinsky. Unsteady Flat Plates: a Cursory Review (Invited - AVT202 special session). In *54th AIAA Aerospace Sciences Meeting*, number January, 2016.

[98] Gino Perrotta and Anya R. Jones. Quasi-Steady Approximation of Forces on Flat Plate due to Large-Amplitude Plunging Maneuvers. *AIAA Journal*, 56(11):4232–4242, 2018.

[99] Alexander Widmann and Cameron Tropea. Reynolds number influence on the formation of vortical structures on a pitching flat plate. *Interface Focus*, 7(1), 2017.

[100] Swathi Krishna, Melissa A. Green, and Karen Mulleners. Flowfield and Force Evolution for a Symmetric Hovering Flat-Plate Wing. *AIAA Journal*, 56(4):1360–1371, 2018.

[101] R. R. Leknys, M. Arjomandi, R. M. Kelso, and C. H. Birzer. Leading-edge vortex development on a pitching flat plate with multiple leading edge geometries. *Experimental Thermal and Fluid Science*, 96:406–418, 2018.

[102] A. R. Jones and H. Babinsky. Reynolds number effects on leading edge vortex development on a waving wing. *Experiments in Fluids*, 51(1):197–210, 2011.

[103] Karen Mulleners, Peter Mancini, and Anya R Jones. Flow Develpment on a Flat-Plate Wing Subjected to a Streamwise Acceleration. *AIAA Journal*, 55(6), 2017.

[104] E. J. Jumper, S. J. Schreck, and R. L. Dimmick. Lift-curve characteristics for an airfoil pitching at constant rate. *Journal of Aircraft*, 24(10):680–687, 1987.

[105] Sabrina Henne, Agastya Parikh, Julien Deparday, and Karen Mulleners. Dynamic stall vortex shedding and associated load fluctuations. In *19th International Symposium on the Applications of Laser and Imaging Techniques to Fluid Mechanics*, Lisbon, 2018.

[106] Marco E. Rosti, Mohammad Omidyeganeh, and Alfredo Pinelli. Direct numerical simulation of the flow around an aerofoil in ramp-up motion. *Physics of Fluids*, 28(2), 2016.

[107] Onur Son, Oksan Cetiner, P. R. R. J. Stevens, Holger Babinsky, Field Manar, Peter Mancini, Anya R. Jones, Michael V. Ol, and Arif C. Gozukara. Parametric Variations in Aspect Ratio , Leading Edge and Planform Shapes for the Rectilinear Pitch Cases of AVT-202. In *54th AIAA Aerospace Sciences Meeting*, number January, pages 1–17, San Diego, 2016.

[108] Louis N. (University of Florida) Cattafesta III and Mark (University of Florida) Sheplak. Actuators for Active Flow Control. *Annual Review of Fluid Mechanics*, 43:247–272, 2011.

[109] Eric Moreau. Airflow control by non-thermal plasma actuators. *Journal of Physics D: Applied Physics*, 40:605–636, 2007.

[110] D. J. Heathcote, I. Gursul, and D. J. Cleaver. Aerodynamic load alleviation using Minitabs. *Journal of Aircraft*, 55(5):2068–2077, 2018.

[111] A Zanotti, R Nilifard, G Gibertini, A Guardone, and G Quaranta. Assessment of 2D/3D numerical modeling for deep dynamic stall experiments. *Journal of Fluids and Structures*, 51:97–115, 2014.

[112] Wandon Joo, Bo-sung Lee, and Dong-ho Lee. Combining Passive Control Method for Dynamic Stall Control. *Journal of Aircraft*, 43(4):1120–1128, 2006.

[113] A. D. Gardner, S. Opitz, C. C. Wolf, and C. B. Merz. Reduction of dynamic stall using a back-flow flap. *CEAS Aeronautical Journal*, 8(2):271–286, 2017.

[114] Jorg U. Schluter. Lift Enhancement at Low Reynolds Numbers Using Self-Activated Movable Flaps. *Journal of Aircraft*, 47(1):348–351, 2010.

[115] L. W. Carr, M. S. Chandrasekhara, M. C. Wilder, and K. W. Noonan. Effect of compressibility on suppression of dynamic stall using a slotted airfoil. *Journal of Aircraft*, 38(2):296–309, 2001.

[116] Benjamin Heine, Karen Mulleners, Gilles Joubert, and Markus Raffel. Dynamic Stall Control by Passive Disturbance Generators. *AIAA Journal*, 51(9):2086–2097, 2013.

[117] D. J. Cleaver, D. E. Calderon, Z. Wang, and I. Gursul. Lift enhancement through flexibility of plunging wings at low Reynolds numbers. *Journal of Fluids and Structures*, 64:27–45, 2016.

[118] Ismet Gursul, D.J. Cleaver, and Z. Wang. Control of low Reynolds number flows by means of fluid-strucutre interactions. *Progress in Aerospace Sciences*, 64:17–55, 2014.

[119] M. Gad-el Hak. Flow control: The future. *Journal of Aircraft*, 38(3):402–418, 2001.

[120] T. Lee and Y. Y. Su. Unsteady airfoil with a harmonically deflected trailing-edge flap. *Journal of Fluids and Structures*, 27:1411–1424, 2011.

[121] R B Green, E A Gillies, and Y Wang. Trailing-edge flap flow control for dynamic stall. *Aeronautical Journal*, 115(1170):493–503, 2011.

[122] Tim Lee and Panayiote Gerontakos. Dynamic Stall Flow Control via a Trailing-Edge Flap. *AIAA Journal*, 44(3):469–480, 2006.

[123] P. Freymuth, S. Jackson, and W. Bank. Toward dynamic separation without dynamic stall. *Experiments in Fluids*, 7(3):187–196, 1988.

[124] A. Le Pape, M. Costes, G. Joubert, F. David, and J.-M. Deluc. Dynamic Stall Control Using Deployable Leading-Edge Vortex Generators. *AIAA Journal*, 50(10):2135–2145, 2012.

[125] A. D. Gardner, T. Knopp, K. Richter, and H. Rosemann. Numerical investigation of pulsed air jets for dynamic stall control on the OA209 airfoil. *CEAS Aeronautical Journal*, 1:1–69, 2011.

[126] Hanns Friedrich Muller-Vahl, Christian Navid Nayeri, Christian Oliver Paschereit, and David Greenblatt. Dynamic stall control via adaptive blowing. *Renewable Energy*, 97:47–64, 2016.

[127] M. Ahsanul Karim and Mukund Acharya. Suppression of dynamic-stall vortices over pitching airfoils by leading-edge suction. *AIAA Journal*, 32(8):1647–1655, 1994.

[128] D. Greenblatt and I. Wygnanski. Dynamic Stall Control by Periodic Excitation, Part 1: NACA 0015 Parametric Study. *Journal of Aircraft*, 38(3):430–438, 2001.

[129] John A. Ekaterinaris. Numerical investigations of dynamic stall active control for incompressible and compressible flows. *Journal of Aircraft*, 39(1):71–78, 2002.

[130] Thomas C. Corke, Patrick O. Bowles, Chuan He, and Eric H. Matlis. Sensing and control of flow separation using plasma actuators, 2011.

[131] A. A. Hassan. Applications of zero-net-mass jets for enhanced rotorcraft aerodynamic performance. *Journal of Aircraft*, 38(3):478–485, 2001.

[132] Daniel Heathcote, David Cleaver, and Ismet Gursul. Frequency Response of Aerodynamic Load Control through Mini-tabs. *55th AIAA Aerospace Sciences Meeting*, (January):1–22, 2017.

[133] Nader H. Al-Battal, David J. Cleaver, and Ismet Gursul. Lift reduction by counter flowing wall jets. *Aerospace Science and Technology*, 78:682–695, 2018.

[134] Nader H. Al-Battal, David J. Cleaver, and Ismet Gursul. Unsteady actuation of counter-flowing wall jets for gust load attenuation. *Aerospace Science and Technology*, 89:175–191, 2019.

[135] Samuel Francis Heathcote. *Flexible flapping airfoil propulsion at low Reynolds numbers*. PhD thesis, The University of Bath, Bath, England, U.K., 2006.

[136] Robert J. Moffat. Describing the uncertainties in experimental results. *Experimental Thermal and Fluid Science*, 1(1):3–17, 1988.

[137] David J Cleaver, Zhijin Wang, and Ismet Gursul. Vortex Mode Bifurcation and Lift Force of a Plunging Airfoil at Low Reynolds Numbers. *48th AIAA Aerospace Sciences Meeting*, pages 1–16, 2010.

[138] Dong-Ha Kim, Jo-Won Chang, and Joon Chung. Low-Reynolds-Number Effect on Aerodynamic Characteristics of a NACA 0012 Airfoil. *Journal of Aircraft*, 48(4):1212–1215, 2011.

[139] S Wang, Y Zhou, Mahbub Alam, H Yang, S Wang, Y Zhou, Mahbub Alam, and H Yang. Turbulent intensity and Reynolds number effects on an airfoil at low Reynolds numbers. *Physcis Of Fluids*, 115107(2014), 2014.

[140] T. Ohtake, Y. Nakae, and T. Motohashi. Nonlinearity of the aerodynamic characteristics of NACA 0012 aerofoil at low Reynolds number (In Japanese). *The Japan Society for Aeronautical and Space Science*, 55(644):439–445, 2007.

[141] A. K. Prasad. Particle image velocimetry. *Current Science*, 79(1):51 – 60, 2000.

[142] John J. Charonko and Pavlos P. Vlachos. Estimation of uncertainty bounds for individual particle image velocimetry measurements from cross-correlation peak ratio. *Measurement Science and Technology*, 24(6), 2013.

[143] TSI. Uncertainty Analysis for PIV Measurement. *ITTC Recommended Procedures and Guidelines*, 017:2013–2014, 2008.

[144] Daniel James Heathcote and Daniel James Heathcote. *Aerodynamic Loads Alleviation Using Mini-tabs*. PhD thesis, 2019.

[145] X. Amandolèse and E. Széchényi. Experimental study of the effect of turbulence on a section model blade oscillating in stall. *Wind Energy*, 7(4):267–282, 2004.

[146] Deman Tang and Earl H. Dowell. Aerodyamic Flow Control of an Airfoil with Small Trailing-Edge Strips. *Journal of Aircraft*, 43(6):1854–1866, 2006.

[147] K. Rinoie and N. Takemura. Oscillating behaviour of laminar separation bubble formed on an aerofoil near stall. *Aeronautical Journal*, 108(1081):153–163, 2004.

[148] G. B. Gilyard S. A. Whitmore, W. T. Lindsey, R. E. Curry. Experimental Characterization of the Effects of Pneumatic Tubing on Unsteady Pressure Measurements. *NASA Technical*, 4171:1–26, 1990.

[149] Jaime G. Wong, Ali Mohebbian, Jochen Kriegseis, and David E. Rival. Rapid flow separation for transient inflow conditions versus accelerating bodies: An investigation into their equivalency. *Journal of Fluids and Structures*, 40:257–268, 2013.

[150] Jordan M Leung, Jaime G Wong, and Ontario Kl. Modeling Transverse Gusts Using Pitching , Plunging , and Surging Airfoil Motions. 56(8), 2018.

[151] Ismet Gursul and David Cleaver. Plunging Oscillations of Airfoils and Wings: Progress, Opportunities, and Challenges. *AIAA Journal*, pages 1–18, 2018.

[152] J. Panda and K. B. M. Q. Zaman. Experimental investigation of the flow field of an oscillating airfoil and estimation of lift from wake surveys. *Journal of Fluid Mechanics*, 265:65–95, 1994.

[153] Morteza Gharib, Edmond Rambod, and Karim Shariff. A universal time scale for vortex ring formation. *Journal of Fluid Mechanics*, 360:121–140, 1998.

[154] Miguel R. Visbal and Daniel J. Garmann. Numerical Investigation of Spanwise End Effects on Dynamic Stall of a Pitching NACA 0012 Wing. In *55th AIAA Aerospace Sciences Meeting*, number January, pages 1–22, 2017.

[155] Thomas Leweke, Stéphane Le Dizès, and Charles H.K. Williamson. Dynamics and Instabilities of Vortex Pairs. *Annual Review of Fluid Mechanics*, 48(1):507–541, 2016.

[156] R. R. Trieling, O. U. Velasco Fuentes, and G. J.F. van Heijst. Interaction of two unequal corotating vortices. *Physics of Fluids*, 17(8):1–17, 2005.

[157] H.-T. Liu, P. A. Hwang, and R. A. Srnsky. Physical modeling of ground effects on vortex wakes. *Journal of Aircraft*, 29(6):1027–1034, 2008.

[158] Yaping Wang, Peiqing Liu, Tianxiang Hu, and Qiulin Qu. Investigation of co-rotating vortex merger in ground proximity. *Aerospace Science and Technology*, 53(March):116–127, 2016.

[159] Gino Perrotta and Anya R. Jones. Unsteady forcing on a flat-plate wing in large transverse gusts. *Experiments in Fluids*, 58(8):1–11, 2017.

[160] SciPy Community. SciPy, 2019.

[161] Kiran Ramesh, Ashok Gopalarathnam, Jack R. Edwards, Michael V. Ol, and Kenneth Granlund. An unsteady airfoil theory applied to pitching motions validated against experiment and computation. *Theoretical and Computational Fluid Dynamics*, 27(6):843–864, 2013.

[162] Julien Deparday and Karen Mulleners. Critical evolution of leading edge suction during dynamic stall. (June), 2018.

Appendix A

A.1 Chapter 5 - Pitching Moment Responses

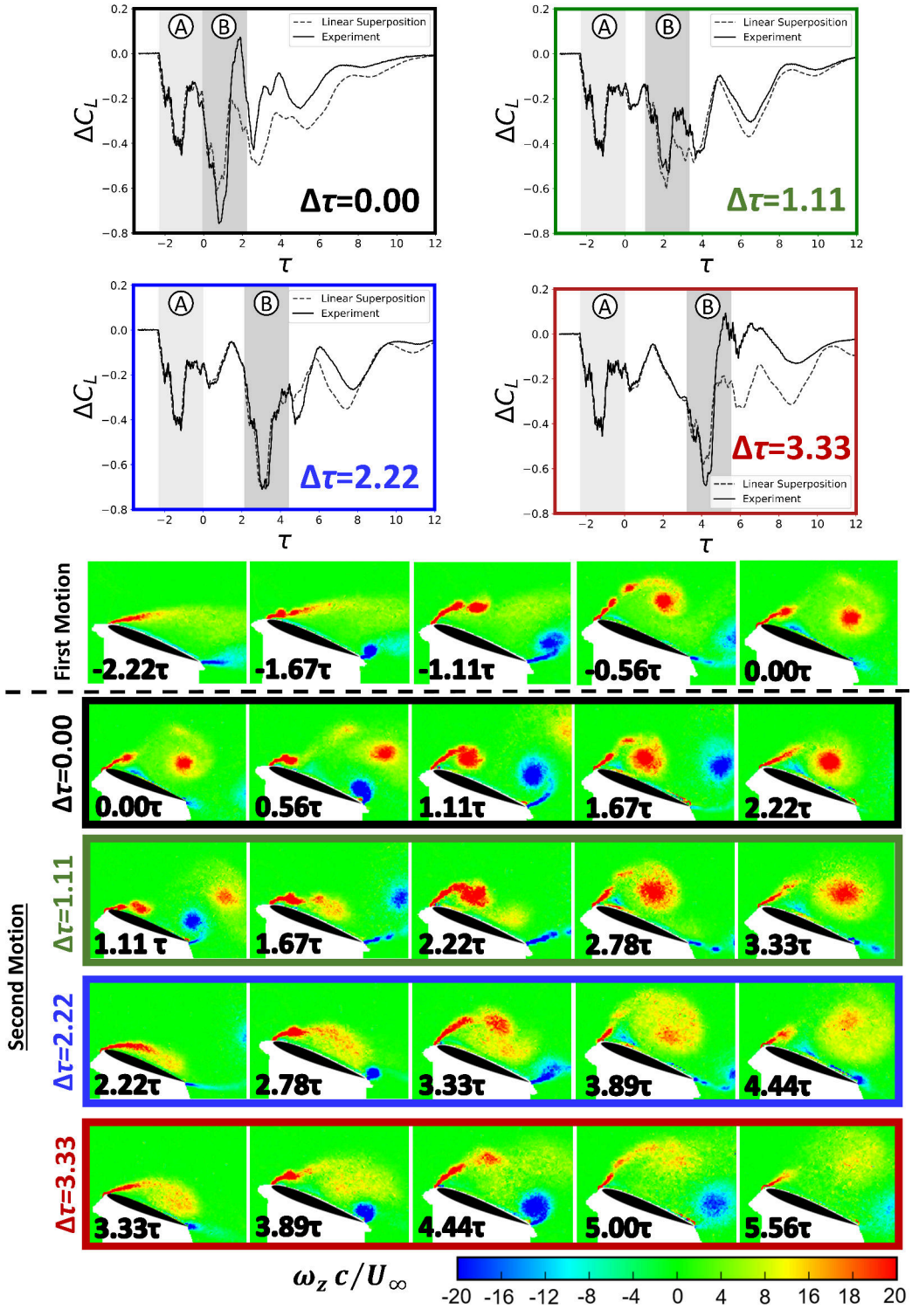

A.2 Chapter 7 - LEV boundary sensitivity

Peak prominence = 0.100
Peak window = 0.0 to 3.5τ

OPTIMUM VALUES

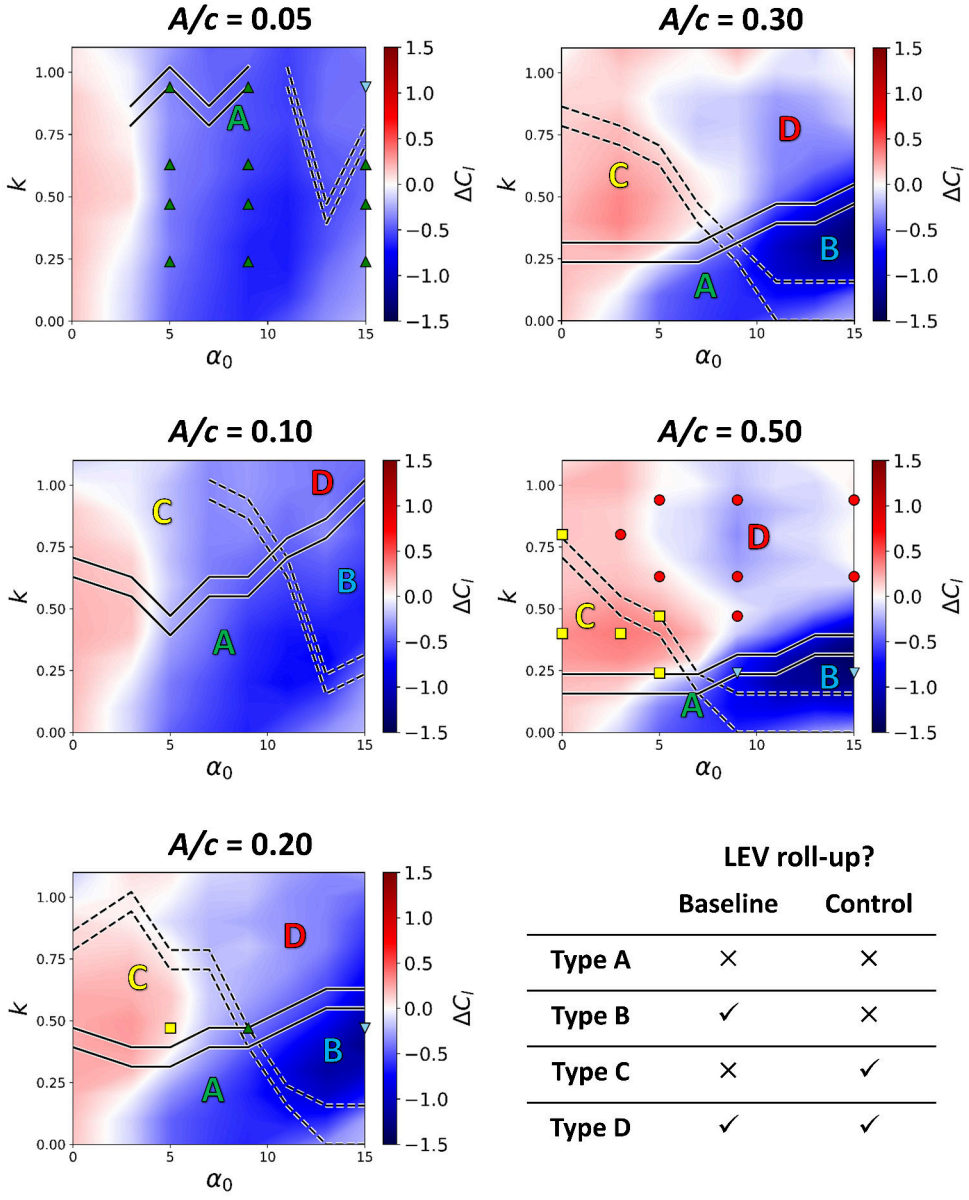

LEV roll-up?

	Baseline	Control
Type A	×	×
Type B	✓	×
Type C	×	✓
Type D	✓	✓

Peak prominence = 0.130
Peak window = 1.0 to 3.5τ

INCREASE PROMINENCE

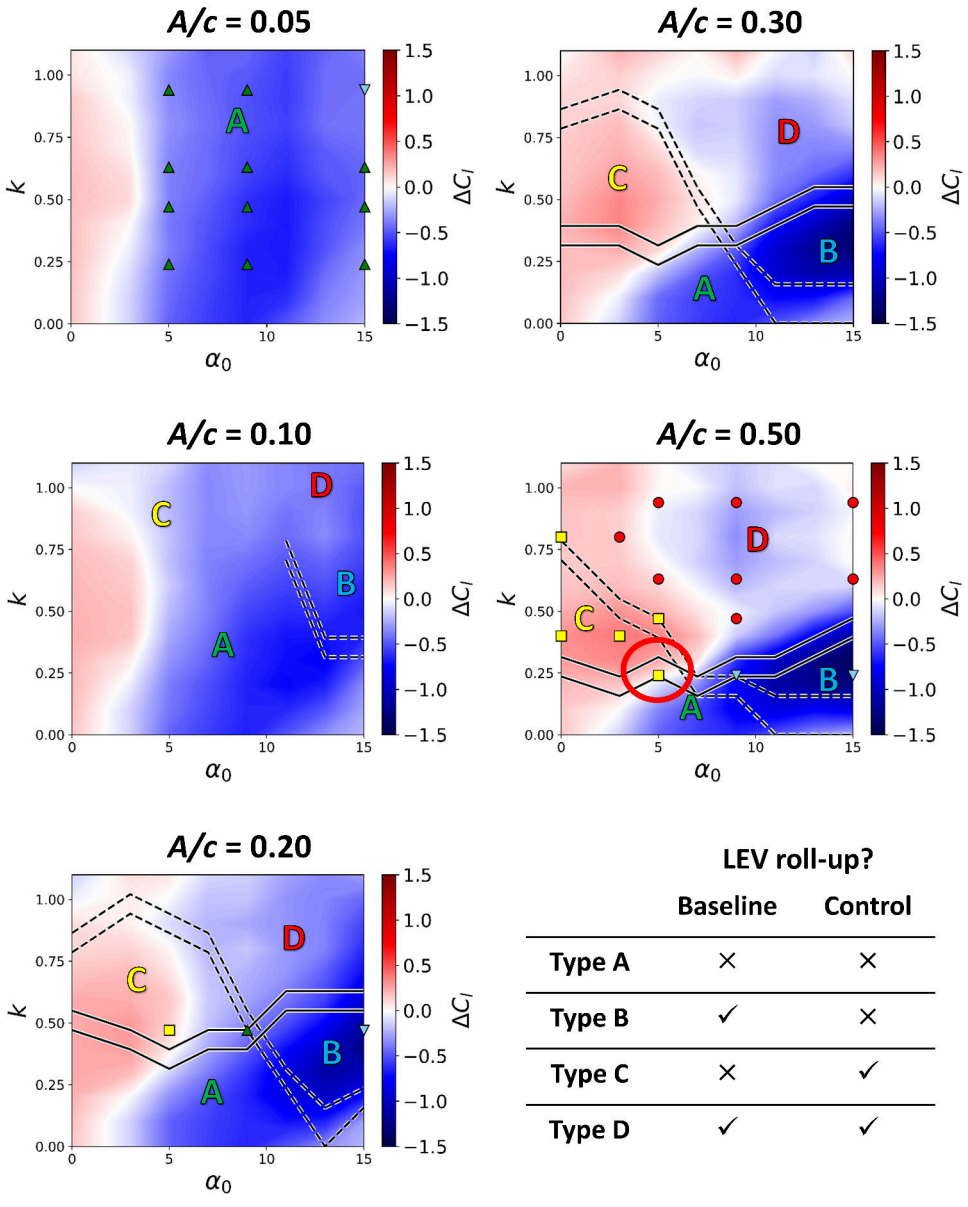

LEV roll-up?	Baseline	Control
Type A	×	×
Type B	✓	×
Type C	×	✓
Type D	✓	✓

Peak prominence = 0.090
Peak window = 1.0 to 3.5τ

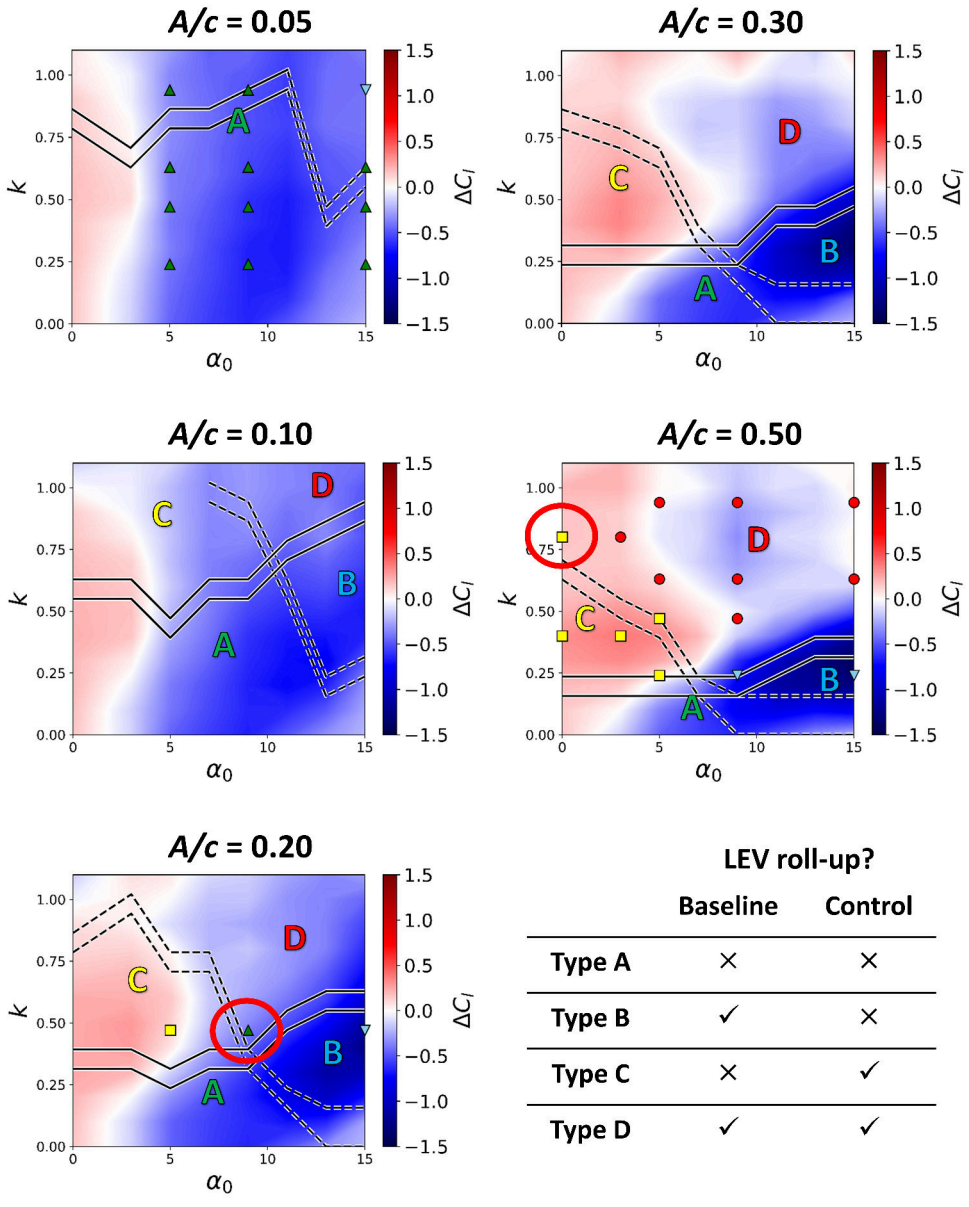

LEV roll-up?

	Baseline	Control
Type A	×	×
Type B	✓	×
Type C	×	✓
Type D	✓	✓

Peak prominence = 0.100
Peak window = 1.0 to 4.0τ **INCREASE UPPER PEAK WIDTH LIMIT**

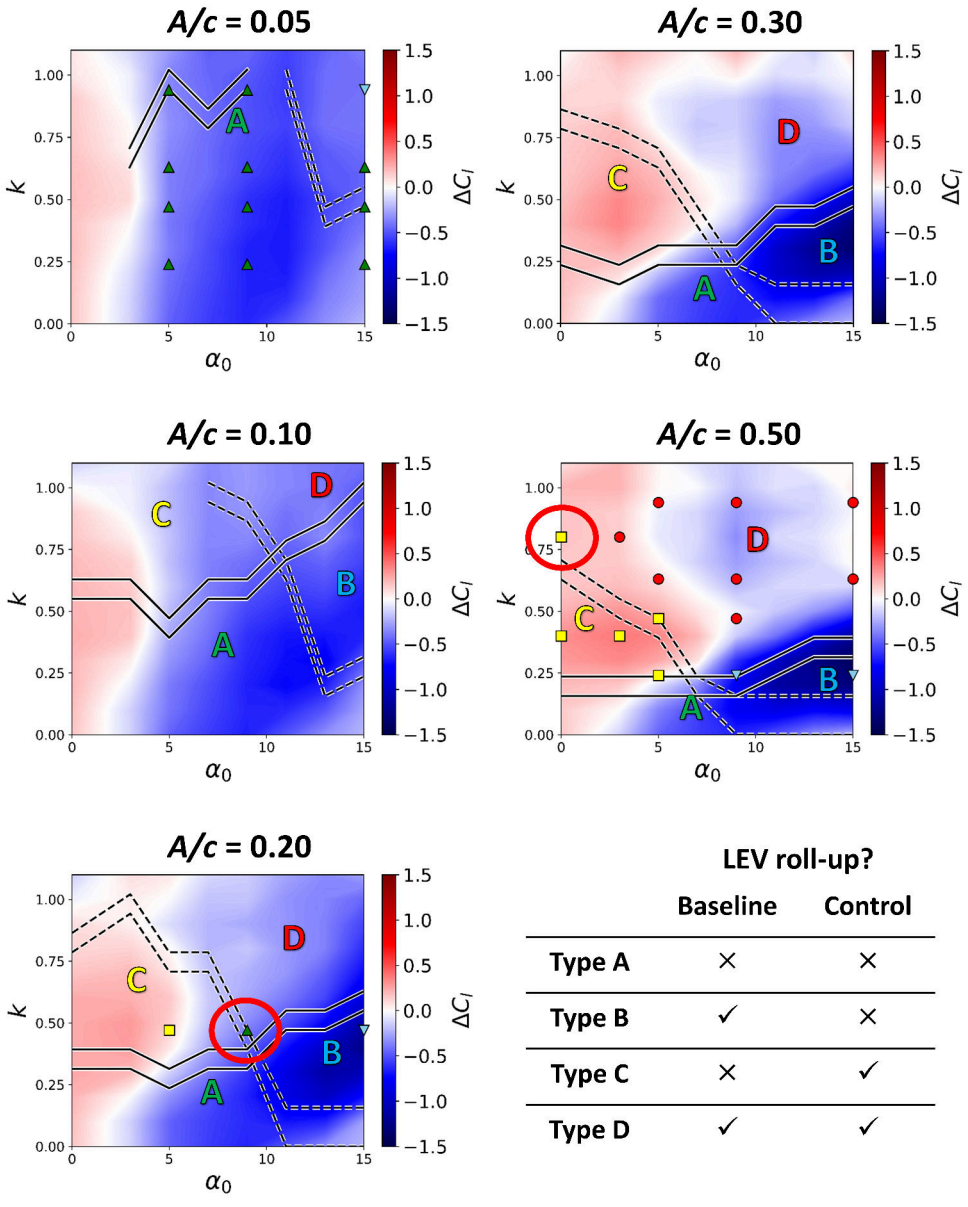

	LEV roll-up?	
	Baseline	Control
Type A	×	×
Type B	✓	×
Type C	×	✓
Type D	✓	✓

Peak prominence = 0.100
Peak window = 1.0 to 3.0τ **REDUCE UPPER PEAK WIDTH LIMIT**

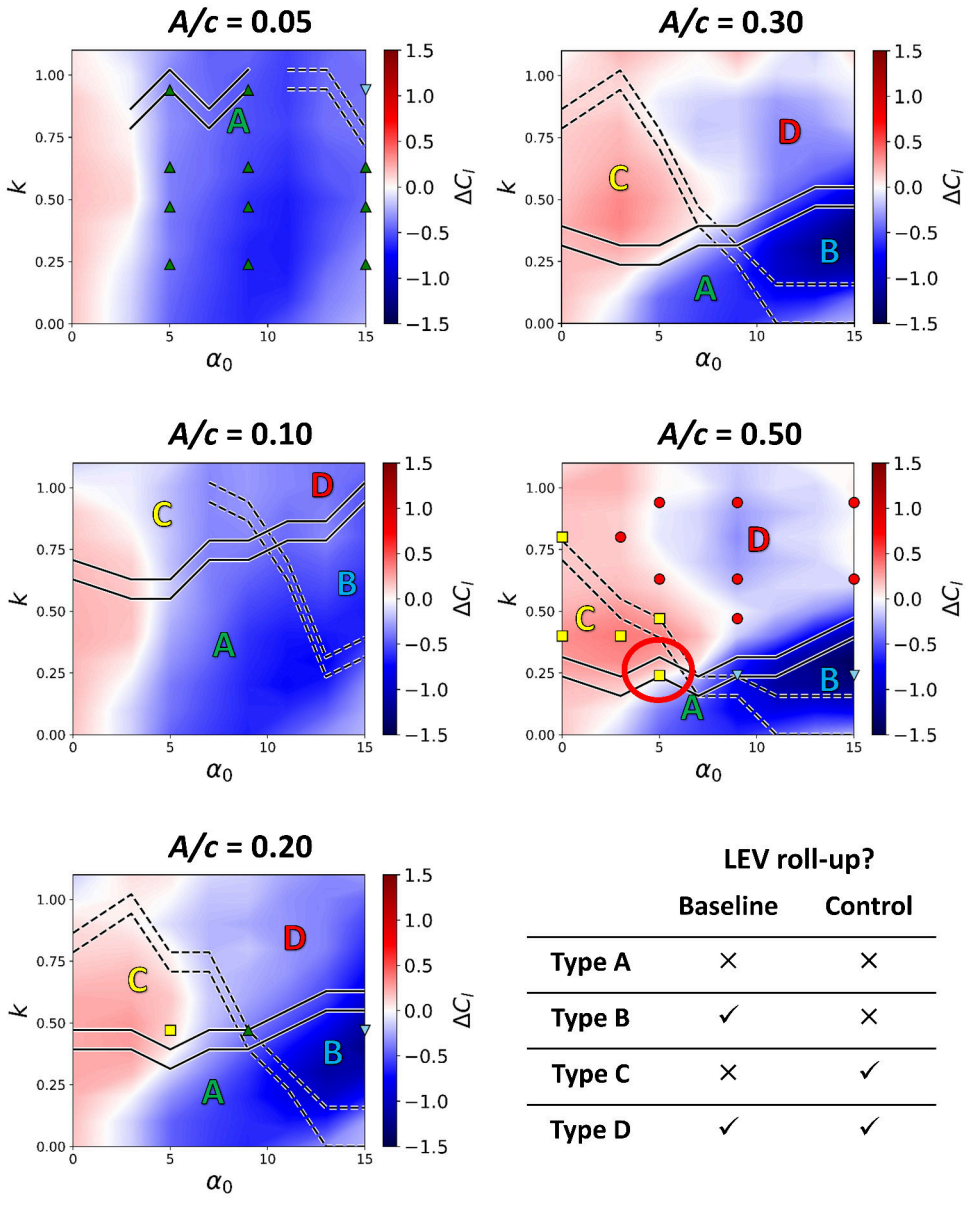

LEV roll-up?

	Baseline	Control
Type A	×	×
Type B	✓	×
Type C	×	✓
Type D	✓	✓

Peak prominence = 0.100
Peak window = 0.0 to 3.5τ **CHANGING LOWER LIMIT: NEGLIGABLE**

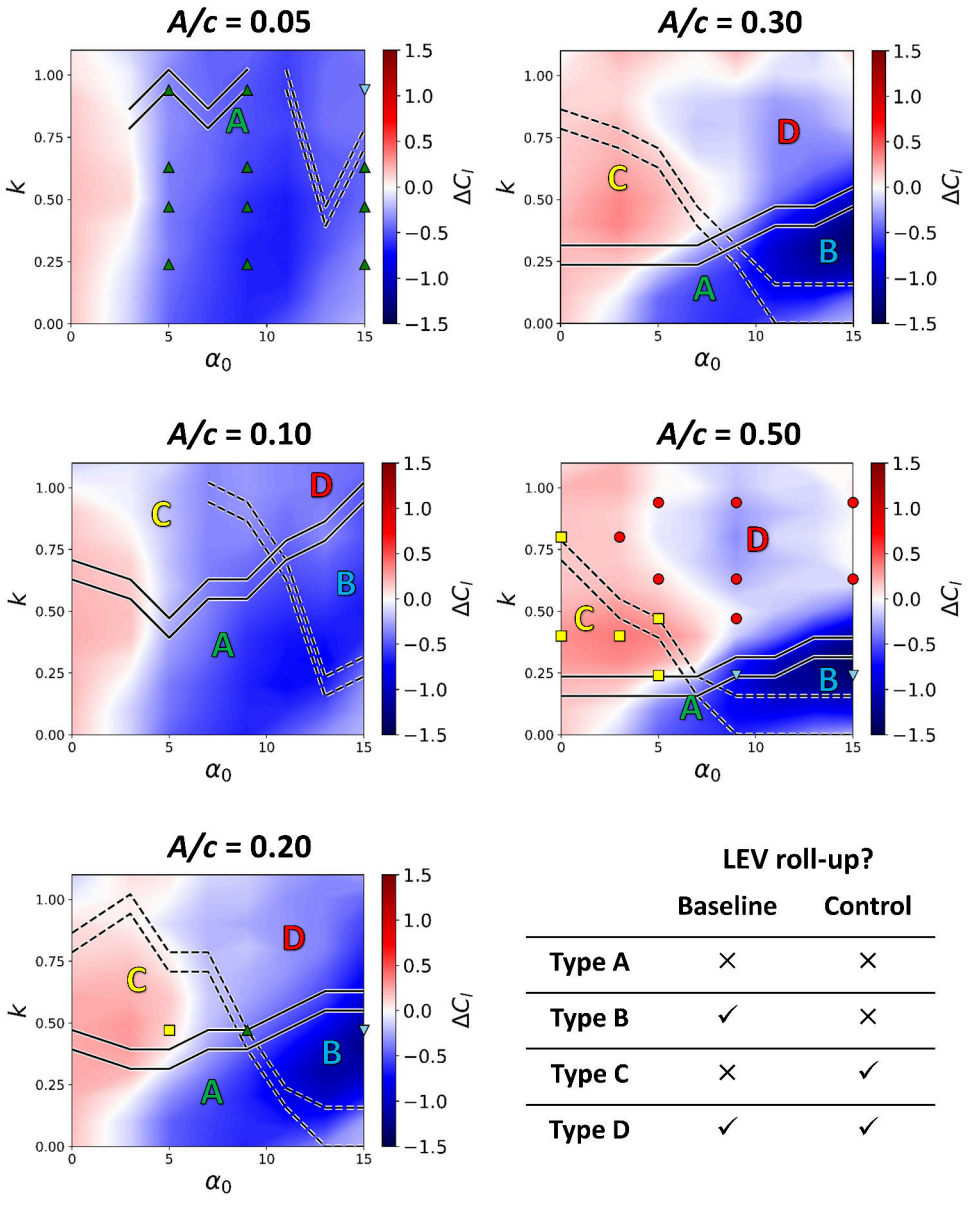

LEV roll-up?	Baseline	Control
Type A	×	×
Type B	✓	×
Type C	×	✓
Type D	✓	✓

Appendix B

B.1 Uncertainty Analysis

The uncertainties were calculated, where possible, based on the methods outlined by Moffat [136]. The principle is to combine all possible sources of error into a single uncertainty value that represents a 95% confidence level. Equation B.1 describes the premise of this method, where the uncertainty in the quantity of interest δR is calculated from the root square sum of the errors due each contributing variable. The δ term here represents uncertainty and is not to be confused with Chapter 7, where it was used to represent a performance metric.

$$\delta R = \sqrt{\left(\frac{\partial R}{\partial x_1}\delta x_1\right)^2 + \left(\frac{\partial R}{\partial x_2}\delta x_2\right)^2 + ... \left(\frac{\partial R}{\partial x_n}\delta x_n\right)^2} \tag{B.1}$$

B.2 Lift Coefficient Uncertainty: Water Tunnel

The lift coefficient is defined as:

$$C_L = \frac{L}{\frac{1}{2}\rho b c U_\infty^2} = \frac{L}{Q} \tag{B.2}$$

The error in lift coefficient, δC_L, is then:

$$\delta C_L = \sqrt{\left(\frac{\partial C_L}{\partial L}\delta L\right)^2 + \left(\frac{\partial C_L}{\partial Q}\delta Q\right)^2} = \sqrt{\left(\frac{1}{\partial Q}\delta L\right)^2 + \left(\frac{\partial L}{Q^2}\delta Q\right)^2} \tag{B.3}$$

Where L is the lift force and Q is the product of the dynamic head and the wing area (aerodynamic constant). The following sections will treat the errors in L and Q separately.

B.2.1 Total Measured Lift Force Uncertainty

The total measured lift force has three main errors associated;

1. *Calibration Uncertainty, δC* - The voltage is converted to newtons through a calibration constant. The error associated with this constant was determined through Microsoft Excel's LINEST function. The calibration error was found to be small, $\delta C = 0.001N/V$: where V is volts and N is newtons.

2. *Drift Uncertainty, δD* - The drift was continually monitored between runs and was found to be small, $\delta D = 0.005N$.

3. *Averaging Uncertainty* - The error associated with an average of multiple runs is given as:

$$\delta N = \frac{1.96 \cdot \sigma}{\sqrt{N}} \tag{B.4}$$

The averaging uncertainty changes with the standard deviation of the signal, σ at each time instant. A typical uncertainty is around $\delta N = 0.03N$.

These components combine to give a total measured lift uncertainty of:

$$\delta L_{total} = \sqrt{\left(\frac{\partial L_{total}}{\partial C}\delta C\right)^2 + \left(\frac{\partial L_{total}}{\partial D}\delta D\right)^2 + \left(\frac{\partial L_{total}}{\partial N}\delta N\right)^2} \tag{B.5}$$

B.2.2 Inertial Lift Force Uncertainty

To isolate the uncertainty of the aerodynamic lift, as per Chapter 3, the errors of the inertial force and wire components must be calculated.

The inertial lift force, $L_{inertial}$, is calculated through the product of the moving mass, m, and the acceleration, a. Therefore the error associated with $L_{inertial}$ is:

1. ***Moving Mass uncertainty,*** δm - This was found to be $0.05Kg$.

2. ***Acceleration Uncertainty,*** δa - This is composed of calibration, drift and averaging uncertainties. Using the same methods as outlined above, the error was found to be $0.02m/s^2$.

These components combine to give an inertial lift uncertainty of:

$$\delta L_{inertial} = \sqrt{\left(\frac{\partial L_{inertial}}{\partial m}\delta m\right)^2 + \left(\frac{\partial L_{inertial}}{\partial a}\delta a\right)^2} \tag{B.6}$$

B.2.3 Wire Lift Force Uncertainty

The wire force uncertainty was calculated from the uncertainty in the force sensor and the standard deviation of 5 repeats and was found to be $0.005N$.

B.2.4 Aerodynamic Lift Force Uncertainty

Combining the errors above gives a dynamic aerodynamic lift force uncertainty:

$$\delta L_{aero} = \sqrt{(L_{total})^2 + (L_{inertial})^2 + (L_{wires})^2} \tag{B.7}$$

B.2.5 Aerodynamic Constant Uncertainty

The aerodynamic constant is comprised of the density (ρ), free-stream velocity (U_∞), chord length (c) and wing span (b). Each variable has an associated uncertainty, which then combine using the root square sum method.

1. ***Density Uncertainty,*** $\delta\rho$ - The density is primarily a function of water temperature, which was measured to fluctuate no more than $\pm 0.5°$ across each run. This gives density uncertainty of $< 0.6 Kg/m^3$.

2. ***Free-Stream Velocity Uncertainty,*** δU_∞ - The water tunnel velocity has been calibrated using PIV measurements and the uncertainty associated is estimated to be $< 0.005 m/s$.

3. ***Chord and Span Uncertainty,*** $\delta c, \delta b$ - The error in length due to manufacturing was no greater than $0.5mm$

Combining the errors above gives a aerodynamic constant uncertainty of:

$$\delta Q = \sqrt{\left(\frac{\partial Q}{\partial \rho}\delta\rho\right)^2 + \left(\frac{\partial Q}{\partial U_\infty}\delta U_\infty\right)^2 + \left(\frac{\partial Q}{\partial c}\delta c\right)^2 + \left(\frac{\partial Q}{\partial b}\delta b\right)^2} \tag{B.8}$$

B.3 Pitching Moment Coefficient Uncertainty: Water Tunnel

The lift coefficient is defined as:

$$C_M = \frac{M}{\frac{1}{2}\rho b c^2 U_\infty^2} = \frac{M}{Q} \tag{B.9}$$

The error in lift coefficient, δC_M, is then:

$$\delta C_M = \sqrt{\left(\frac{\partial C_M}{\partial L}\delta L\right)^2 + \left(\frac{\partial C_M}{\partial Q}\delta Q\right)^2} = \sqrt{\left(\frac{1}{\partial Q}\delta M\right)^2 + \left(\frac{\partial M}{Q^2}\delta Q\right)^2} \tag{B.10}$$

Where M is the moment and Q is the aerodynamic constant. As the uncertainty in Q has previously been discussed, the next sections will focus on the uncertainty of M.

B.3.1 Total Measured Moment Uncertainty

The total measured moment has two main errors associated:

1. *Calibration Uncertainty,* δC - The voltage is converted to newton meters through a calibration constant. The error associated with this constant was determined through Microsoft Excel's LINEST function. The calibration error was found to be $0.001 Nm/V$: where V is volts and Nm is newton meters.

2. *Drift Uncertainty,* δD - The drift was continually monitored between runs and was found to be small, $\delta D = 0.001 Nm$.

3. *Averaging Uncertainty* - The error associated with an average of multiple runs is given as:

$$\delta N = \frac{1.96 \cdot \sigma}{\sqrt{N}} \tag{B.11}$$

The averaging uncertainty changes with the standard deviation of the signal, σ at each time instant. A typical uncertainty is around $\delta N = 0.03 Nm$.

These components combine to give a total measured lift uncertainty of:

$$\delta M_{total} = \sqrt{\left(\frac{\partial M_{total}}{\partial C}\delta C\right)^2 + \left(\frac{\partial M_{total}}{\partial D}\delta D\right)^2 + \left(\frac{\partial M_{total}}{\partial N}\delta N\right)^2} \tag{B.12}$$

B.3.2 Inertial Moment Uncertainty

To isolate the uncertainty of the aerodynamic moment, the errors of the inertial force must be calculated.

The inertial lift force, $M_{inertial}$, is calculated through the product of the moving mass about the sensor, m, and the acceleration, a. Therefore the error associated with $M_{inertial}$ is:

1. ***Moving Mass Uncertainty,*** δm - This was estimated to be $0.00005 Kg \cdot m$.

2. ***Acceleration Uncertainty,*** δa - Previously defined to be $0.02 m/s^2$.

These components combine to give an inertial lift uncertainty of:

$$\delta M_{inertial} = \sqrt{\left(\frac{\partial M_{inertial}}{\partial m}\delta m\right)^2 + \left(\frac{\partial M_{inertial}}{\partial a}\delta a\right)^2} \tag{B.13}$$

B.3.3 Aerodynamic Moment Uncertainty

Combining the errors above gives a dynamic aerodynamic lift force uncertainty:

$$\delta M_{aero} = \sqrt{(M_{total})^2 + (M_{inertial})^2} \tag{B.14}$$

B.4 Pressure Coefficient Uncertainty: Wind Tunnel

The pressure coefficient is defined as:

$$C_P = \frac{P - P_\infty}{\frac{1}{2}\rho U_\infty^2} = \frac{P - P_\infty}{Q} \tag{B.15}$$

The error in pressure coefficient, δC_P, is then:

$$\delta C_P = \sqrt{\left(\frac{\partial C_P}{\partial P}\delta P\right)^2 + \left(\frac{\partial C_P}{\partial P_\infty}\delta P_\infty\right)^2 + \left(\frac{\partial C_P}{\partial Q}\delta Q\right)^2} \tag{B.16}$$

$$= \sqrt{\left(\frac{1}{\partial Q}\delta P\right)^2 + \left(\frac{1}{\partial Q}\delta P_\infty\right)^2 + \left(\frac{P - P_\infty}{Q^2}\delta Q\right)^2}$$

Where P is the static pressure measured by the individual transducer, P_∞ is the static pressure of the free-stream and Q is the aerodynamic constant. The following sections will treat the errors in P, P_∞ and Q separately.

B.4.1 Static Pressure Uncertainty

The static pressure has five main errors associated:

1. ***Calibration Uncertainty,*** δC - The 14 bit number is converted to pascals through a calibration constant. The error associated with this constant was determined through Microsoft Excel's LINEST function and was found to be virtually negligible.

2. ***Drift Uncertainty,*** δD - The drift was continually monitored between runs and was found to be small, $\delta D = 0.15Pa$.

3. ***Averaging Uncertainty*** - The error associated with an average of multiple runs is given as:

$$\delta N = \frac{1.96 \cdot \sigma}{\sqrt{N}} \tag{B.17}$$

The averaging uncertainty changes with the standard deviation of the signal, σ at each time instant. A typical uncertainty is around $\delta N = 0.05Pa$.

4. ***Vibration Uncertainty,*** δV - Although the transducer diaphragms were aligned perpendicular with the plunging axis, the vibrational loads they are subjected to could still have an effect. This was measured through a number of sinusoidal motion tests and determined to be $0.008Pa$.

5. ***Tubing Uncertainty,*** δT - As described in Chapter 3, the tubing introduces an error (1.5%) on the magnitude of pressure measured, which is a function of frequency. A typical error this incurs is around $2Pa$.

These components combine to give a total measured lift uncertainty of:

$$\delta P = \sqrt{\left(\frac{\partial P}{\partial C}\delta C\right)^2 + \left(\frac{\partial P}{\partial D}\delta D\right)^2 + \left(\frac{\partial P}{\partial N}\delta N\right)^2 + \left(\frac{\partial P}{\partial V}\delta V\right)^2 + \left(\frac{\partial P}{\partial T}\delta T\right)^2} \tag{B.18}$$

B.4.2 Free-Stream Static Pressure Uncertainty

The free-stream static pressure was measured across a range of tunnel conditions to give a calibration curve of static pressure vs. Reynolds number which collapsed with excellent agreement onto a power curve, $5.04e-09Re^{1.92}$. The uncertainties with this method are:

1. ***Calibration Uncertainty,*** δC - The error associated with the calibration constant estimated to be $0.1Pa$.

2. ***Drift Uncertainty,*** δD - The drift was continually monitored between runs and was found to be $0.3Pa$.

3. ***Power Curve Uncertainty,*** δE - An error is associated with the correlation of the fit as well as the Reynolds number input, which is a function of the temperature. This was calculated to give a power curve uncertainty of $1Pa$.

These components combine to give a total measured lift uncertainty of:

$$\delta P_\infty = \sqrt{\left(\frac{\partial P_\infty}{\partial C}\delta C\right)^2 + \left(\frac{\partial P_\infty}{\partial D}\delta D\right)^2 + \left(\frac{\partial P_\infty}{\partial E}\delta E\right)^2} \tag{B.19}$$

B.4.3 Aerodynamic Constant Uncertainty

The aerodynamic constant is comprised of the density (ρ), free-stream velocity (U_∞) and chord length (c). Each variable has an associated uncertainty, which then combine using the root square sum method.

1. ***Density Uncertainty,*** $\delta\rho$ - The density is primarily a function of water temperature, which was measured to fluctuate no more than $\pm 0.5^\circ$ across each run. This gives density uncertainty of $0.005Kg/m^3$.

2. ***Free-Stream Velocity Uncertainty,*** δU_∞ - The velocity is measured through the dynamic pressure, which is a function of pressure and density uncertainty; the typical uncertainty associated with the free stream velocity is $0.05m/s$.

3. ***Chord Uncertainty,*** δc - The error in length due to manufacturing was no greater than $2mm$

Combining the errors above gives a aerodynamic constant uncertainty of:

$$\delta Q = \sqrt{\left(\frac{\partial Q}{\partial \rho}\delta\rho\right)^2 + \left(\frac{\partial Q}{\partial U_\infty}\delta U_\infty\right)^2 + \left(\frac{\partial Q}{\partial c}\delta c\right)^2} \tag{B.20}$$

B.5 Lift and Moment Uncertainty: Wind Tunnel

The lift and moment coefficient uncertainties were estimated based on stochastic analysis where the error of each pressure transducer was permitted to fluctuate randomly within its own uncertainty bounds. The uncertainty of this analysis ($C_{L,stoch.}$, $C_{M,stoch.}$) was combined with the free-stream uncertainty, δQ, and the averaging uncertainty, δN, associated with each repeat using the root square sum method:

$$\delta C_L = \sqrt{(\delta C_{L,stoch.})^2 + \left(\frac{\partial C_L}{\partial Q}\delta Q\right)^2 + \left(\frac{\partial C_L}{\partial N}\delta N\right))^2} \tag{B.21}$$

$$\delta C_M = \sqrt{(\delta C_{M,stoch.})^2 + \left(\frac{\partial C_M}{\partial Q}\delta Q\right)^2 + \left(\frac{\partial C_M}{\partial N}\delta N\right))^2} \tag{B.22}$$